
# TECHNISCHE UNIVERSITÄT MÜNCHEN

PHYSIK-DEPARTMENT

Lehrstuhl für Funktionelle Materialien (E13)
Forschungs-Neutronenquelle Heinz Maier-Leibnitz


# Thermal Conductivity of High-Density Uranium-Molybdenum Fuels for Research Reactors


**Tanja Kathrin Huber**


Vollständiger Abdruck der von der Fakultät für Physik der Technischen Universität München zur Erlangung des akademischen Grades eines

**Doktors der Naturwissenschaften (Dr. rer. nat.)**

genehmigten Dissertation.

| | |
|---|---|
| Vorsitzende(r): | Univ.-Prof. Dr. Martin Zacharias |
| Prüfer der Dissertation: | 1. Univ.-Prof. Dr. Winfried Petry |
| | 2. Univ.-Prof. Dr. Katharina Krischer |
| | 3. Prof. Dr. Olivier Tougait, Université Lille Nord de France (nur schriftliche Beurteilung) |


Die Dissertation wurde am 21.12.2015 bei der Technischen Universität München eingereicht und durch die Fakultät für Physik am 26.01.2016 angenommen.

Des is wia bei jeda Wissenschaft, am Schluss stellt sich dann heraus,
dass alles ganz anders war.
*Karl Valentin*

**Abstract**

The evolution of the thermal conductivity of research reactor fuel during in-pile irradiation plays a significant role for the performance of the fuel element. To correctly simulate the heat fluxes and temperatures in the fuel meat during normal reactor operation and also off-normal scenarios, it is crucial to investigate the change in thermal properties. Especially the thermal conductivity depends on the fission density and temperature.

Two different U-Mo fuel types, dispersion and monolithic design, have to be considered. The thermal conductivity of fresh dispersion fuel lies between 25 $^{W}/_{m \cdot K}$ and 70 $^{W}/_{m \cdot K}$ depending on the particle size and shape, matrix material composition and Uranium loading. In contrast, the thermal conductivity of non-irradiated monolithic fuel is below 17 $^{W}/_{m \cdot K}$ due to the lack of a highly conductive Aluminum matrix.

The thermal conductivity is a composition of the thermal diffusivity, specific heat capacity and density. The specific heat capacity was measured with a Differential Scanning Calorimeter. It is mainly dependent on the atomic, i.e. material composition, and does not vary significantly for the different fuel types and not even during irradiation. The density was obtained with the Immersion Method and Pycnometry. Like specific heat capacity, it does not vary much for the different fuel types, but it slightly decreases due to the formation of fission gas bubbles during irradiation. The thermal diffusivity was determined using the Laser Flash Method. This quantity is strongly dependent on the material's microstructure and is the parameter with the largest variation between the different fuels. During irradiation the material's crystal lattice is destroyed by the high energetic fission products and fission gas bubbles. This decreases the thermal diffusivity of the irradiated material drastically down to 30 % of the fresh material. Therefore, it has the highest impact on the change of the thermal conductivity during irradiation.

At the beginning of irradiation, the thermal conductivity of the dispersion fuel strongly decreases from 60 $^{W}/_{m \cdot K}$ down to 19 $^{W}/_{m \cdot K}$ which is about 30 % of its original value. In this phase, the highly thermal conductive matrix material is replaced by the low thermal conducting interdiffusion layer that grows during irradiation between the U-Mo particle and Aluminum matrix. In contrast, the decrease of the monolithic fuel from 17 $^{W}/_{m \cdot K}$ down to 12 $^{W}/_{m \cdot K}$ which is about 70 % of its original value. This decrease is less rapid than for the dispersion fuels, due to the lack of the effects in the matrix material. In the U-Mo itself, the decrease of the thermal conductivity is mainly caused by the formation of fission gas bubbles and crystal lattice decomposition from the fission products. In the second phase, when all matrix material in the dispersion fuel is consumed, the thermal conductivity of the dispersion fuel follows the flatter trend of the thermal conductivity of the monolithic U-Mo and is further reduced down to 10 $^{W}/_{m \cdot K}$ which is only 10 % of the original value.

The behavior of the fuel under irradiation can be described by the combination of an empirical model, derived from metallurgical investigations of irradiated U-Mo fuels, and the Hsu model for the calculation of the thermal conductivity of dispersed materials that is extended by the Badrinarayan model for coated spheres.

Compared to $U_3Si_2$, the thermal conductivity of U-Mo fuel is roughly in the same range for a similar fuel loading. To replace the highly enriched $U_3Si_2$ fuel by low enriched U-Mo fuel, a higher Uranium loading is needed which reduces the thermal conductivity of the fuel as a big amount of the highly conductive Al matrix material is replaced by low conductive U-Mo.

# Contents

# CHAPTER 1

## Motivation

### 1.1 FRM II and RERTR - A Short Historical Review

In 1953 Dwight D. Eisenhower announced the program "Atoms for Peace", providing research reactors and fuels for civilian uses [Wac07, Eis14]. These first reactors were operated with low enriched uranium fuels (LEU), i.e. containing less than 20 % of U-235.

***Figure 1.1:*** *Forschungsreaktor München (FRM) [KP97]*

A few years later in August 1955, during the first International Conference on the Peaceful Uses of Atomic Energy in Geneva, the Federal Republic of Germany got the approval for the civilian use of nuclear energy. Shortly afterwards, end of 1956, the construction of the first German research reactor, the Forschungsreaktor München (FRM) was launched. It was bought from the American Machine & Foundry Corporation, N.Y. (AFM) in the design of an open swimming pool reactor using 20 % enriched dispersed $UAl_x$ fuel and operating at a power of 1 MW [KP97].

But within very short time, the international scientific community demanded higher specific powers and neutron fluxes. This could be obtained by increasing the enrichment of the reactor fuel. In the course of this, in 1960, the FRM converted its fuel from LEU to highly enriched uranium (HEU), i.e. $\sim 90$ % U-235 [KP97]. This allowed for an increase of its power to 4 MW.

In the late 1970's, the US was exporting about 700 kg of HEU to foreign research and test reactors per year. To counter the risk of proliferation, the US Department of Energy (DoE) initiated the Reduced Enrichment for Research and Test Reactors (RERTR) program in August 1978 [Wac07]. The scope of this program was the investigation of new high-density reactor fuels to replace existing fuels with lower uranium densities and thereby reduce the U-235 enrichment. Reducing the amount of the U-235 isotope in the uranium, requires an increase of the total amount of uranium in the fuel to retain the reactor performance at a comparable level. The

U-238 isotope is a neutron absorber, which has to be compensated by an overproportionally higher total amount of uranium in the fuel. Often, additional measures, such as an increased power level, are necessary to compensate flux losses. The effort for such a conversion ranges, depending on reactor core design, regarding the various influences of the fuel on the reactor operation, technically from a simple fuel exchange to a greater challenge and is sometimes even not feasible at all.

However, the International Nuclear Fuel Cycle Evaluation (INFCE) conference conceded the further use of HEU for high-flux reactors, such as the FRM, for which a conversion is challenging or not feasible.

But rising scientific standards demanded significant higher neutron fluxes, which were impossible for the FRM to cope with. A reconstruction of the FRM was hardly feasible due to the necessity for extensive structural alteration works. As a consequence in 1981, the Technische Universität München (TUM) developed the concept for the new high-flux neutron source FRM II, the Forschungs-Neutronenquelle Heinz Maier-Leibnitz. In 1985 the final design was a cylindrical compact core with involute plates in the style of the High Flux Reactor (HFR) at the Institute Laue-Langevin (ILL) and the High Flux Isotope Reactor (HFIR) at the Oak Rich National Laboratory (ORNL) [BAS01].

At the time being, a LEU design of the new reactor was no option. With the hitherto known fuels, a sufficient neutron flux could only be reached using HEU [BGR95, MHM95]. So, in April 1996 the first partial permission was granted and the construction of the new reactor started. The FRM was finally shut down in July 2000, while the construction of the FRM II was still ongoing.

In the meanwhile, the investigations of new high-density reactor fuels in the framework of the RERTR progressed. The uranium concentration of the two main fuel types used in western designed reactors, $UAl_x$ and $U_3O_8$ could be increased from $1.7\,gU/cm^3$ and $1.3\,gU/cm^3$ to $2.3\,gU/cm^3$ and $3.2\,gU/cm^3$, respectively [Wac07]. Further new promising fuel types based on $U_3Si$, $U_3Si_2$ and $U_6Me$ (Me- transition metal) were examined. Their higher density would allow higher uranium loading in the fuel meat. But $U_3Si$ testplates failed at high burnup and were dropped from the US, French and German programs. Instead, $U_3Si_2$ dispersed in Al (see Figure 1.2) with a uranium density of up to $4.8\,gU/cm^3$ was found to be very stable under irradiation. After successful irradiation testing of a full-size LEU $U_3Si_2 - Al$ dispersion fuel element, in 1988, this fuel type received generic approval by the US Nuclear Regulatory Commission (NRC) in the form of a Safety Evaluation Report (NUREG 1313) [Wac07, Com88]. Finally the decision for the type of fuel to operate the new FRM II fell on dispersed $U_3Si_2 - Al$ using HEU.

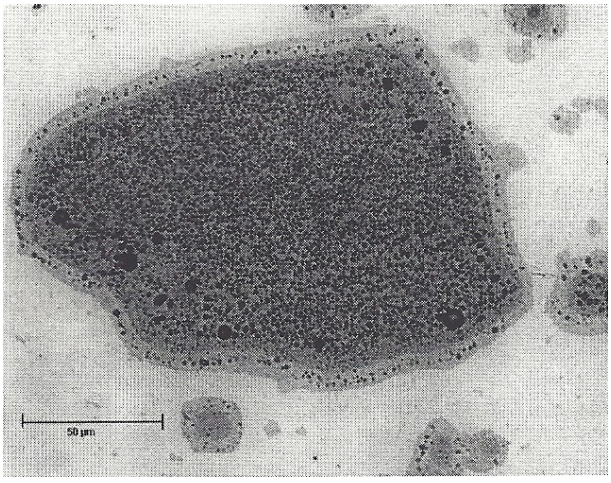


***Figure 1.2:*** *Optical microsope image of a* $U_3Si_2$ *fuel particle in the Al matrix after irradiation.*

Since 1988, these new kinds of $UAl_x$ and $U_3O_8$ fuels helped more than 30 research reactors world wide to convert from HEU to LEU. But its density was still too low to convert the high

performance research reactors (HPRR), like the Advanced Test Reactor (ATR) in Idaho, USA, or the High Flux Reactor (HFR) in Grenoble, France. For this purpose, LEU fuel densities must be in the range of $(8 - 10\,\mathrm{gU/cm^3})$. For the FRM II in Munich, Germany, even higher LEU fuel densities of $> 15\,\mathrm{gU/cm^3}$ are mandatory.

Most promising candidates for this challenge were metallic uranium compounds with low alloy content or $U_6Me$ intermetallics, like $U_6Fe$ or $U_6Mn$ [HDC87, MWHH00]. But both intermetallics showed poor irradiation behavior, as swelling already started at low burnup, rapidly leading to breakaway swelling. This leads to the assumption that other intermetallics behave in a similar manner. So, the attention was turned to metallic uranium alloys. After considering several criterias, like metallurgic phase-stability and knowledge about irradiation behaviors, two alloys remained: U-Nb-Zr and U-Mo.

Since there was only little knowledge of the irradiation behavior of these fuels, selected metallic fuel alloys of this kind, dispersed in an aluminum matrix, were chosen for irradiation screening tests at different irradiation temperatures from 65 °C up to 200 °C [MHS$^+$00, Wac07] with variable U-235 burnup between $\sim 20$ at.% to almost 80 at.% in the Advanced Test Reactor (ATR) at the Idaho National Laboratory (INL) in Idaho, USA, between 1997 and 2001 [Wac07]. The post irradiation examinations (PIEs) proofed that U-Nb-Zr fuels and U-Mo fuels with less than 6 wt.% are less suitable, as they indicated breakaway swelling. But the U-Mo alloys with Mo contents over 6 wt.% Mo and uranium loadings up to $8\,\mathrm{gU/cm^3}$ hitherto showed stable irradiation behavior and acceptable swelling.

***Figure 1.3:*** *Forschungs-Neutronenquelle Heinz Maier-Leibnitz (FRM II)*

These irradiation tests pointed out that there is a potential candidate for an alternative high-density fuel with reduced enrichment. So in 2003, it was stated in the third partial license ("Dritte Teilerrichtungsgenehmigung") that the FRM II is obliged to convert its fuel from currently 93 at.% enrichment to a lower level (max. 50 at.%), once such a fuel is available and qualified.

The conversion is further bound to the condition that there is no significant penalty in safety, performance (i.e. neutron flux density) and costs.

But, further irradiation tests, meanwhile also conducted in Europe in the OSIRIS reactor in Saclay, France, and the High Flux Reactor (HFR) in Petten, Netherlands, exhibited significant problems, mainly breakaway swelling, in fuel performance under the irradiation conditions required by most high-performance research reactors. In 2001, a new approach with a monolithic fuel design, i.e. a pure U-Mo foil sealed in Al cladding, which, due to the lack of matrix material, increased the uranium loading significantly to over $14\,\mathrm{gU/cm^3}$, was tested for the first time. Most failures were mainly caused by difficulties on the fabrication side, like debonding on the intersection between cladding and U-Mo.

In the meanwhile the construction of the FRM II was completed and the reactor achieved its first criticality in March 2004 using $U_3Si_2 - Al$ dispersion fuel with 93 % enrichment. Already since 2003, the FRM II was supporting the development of high-density U-Mo fuel in several international collaborations and was in parallel working on its own conversion program, e.g. feasibility studies and simulation of changes in the reactor performance depending on new fuel designs.

## 1.2 Fuel Qualification

The new lower enriched fuel for the FRM II has to pass through a qualification process, before it can be used for regular reactor operation.

Fuel development and qualification is a phased process. At the beginning, the main focus lies on the research and development until a preferred fuel is selected. Parallel neutronic and thermohydraulic calculations have to pave the way for an eventual changed fuel element geometry. Finally it is to proof that the fuel meets the desired performance and required specifications for a safe reactor operation.

First, several considerations have to be made to work out a fuel design concept. This includes multiple factors like technical improvements with the goal to enhance the reactor performance, backend issues, as well as strategic aspects like material supply. With respect to these points, the fuel performance expectations, design requirements and also the safety expectations need to be stated. For this, neutronic and thermal-hydraulic requirements have to be taken into account and in what extent the fuels crystallographic structure and chemical behavior influences these parameters. Besides manufacturing techniques, backend options have to be assessed as well.

Based on these considerations, first fuel specimens are fabricated to test different fuel compositions and manufacturing techniques. Out of pile testing gives then information about the basic properties of the unirradiated fuel. These include the fuel material's chemical and phase composition, mainly affecting the mechanical properties, thermal conductivity and, depending on the fuel type, fuel powder or foil properties. These data will provide important information for the interpretation of the fuel behavior during fabrication and further on irradiation.

Once these characteristics are determined, a test reactor has to be chosen for irradiation testing of the specimen. Thereby the test reactor should meet the irradiation conditions of the reactor, for which the fuel is designed, as close as possible to representative burnup, although the initial irradiation should be performed at lower power and fuel temperature to avoid premature failure and enhance the safety of the experiment. If the fuel shows adequate behavior the irradiation conditions can be exacerbated to higher power, temperature and burnup to determine the limiting conditions of the fuel.

Destructive and non-destructive post-irradiation examinations (PIE) will provide further information, for example if the fuel can retain the fission products, maintain mechanical integrity and changes of the thermal conductivity.

Embedded in this qualification process is this thesis' topic: The thermal conductivity of U-Mo fuels that are promising candidates for the conversion of the FRM II reactor. The thermal properties have been determined for dispersion and monolithic fuels that have been fabricated for irradiation tests. Each type of fuel was analysed in the as-fabricated and post-irradiation

state to determine the evolution of the thermal conductivity during reactor operation. Based on this data, the fuel meat temperature and heat fluxes in the fuel meat during reactor operation can be calculated. This can finally be used to simulate the fuel elements cooling system.

# Part I

# Scientific Background

# CHAPTER 2

## Uranium-Molybdenum Fuels

As already discussed, the efforts to reduce the enrichment of reactor fuel require higher uranium loading in the fuel. The loading that is necessary for FRM II to keep the reactor performance at the same level of high enriched uranium fuel, cannot be achieved with the current $U_3Si_2$ fuel for a reduction of the enrichment to low enriched uranium (LEU), i.e. an enrichment of less than 20 % U-235.
The uranium-molybdenum (U-Mo) alloy has a higher chemical uranium density than the $U_3Si_2$ compound. So, higher uranium loading in the fuel meat can be achieved with similar volume loading. Furthermore, $U_3Si_2$ is a ceramic and therefore brittle. So, in general, aluminum is used as matrix material for fuels based on $U_3Si_2$. The soft aluminum compensates the brittle ceramic and partly assimilates the swelling caused by the fission products during irradiation, but most of the swelling is assimilated by porosity that is generated during fabrication in the fuel meat. Increasing the fraction of $U_3Si_2$ in the fuel meat reduces the mechanical integrity. With the higher Uranium density of the U-Mo alloy, the uranium loading is already higher at equal fuel volume loading. But even an increase of the fuel loading reduces the mechanical integrity of the U-Mo fuel less than $U_3Si_2$ fuel.
Finally, the uranium loading can be further increased by completely removing the matrix material, so that the fuel meat only consists of a U-Mo foil, called monolithic fuel.

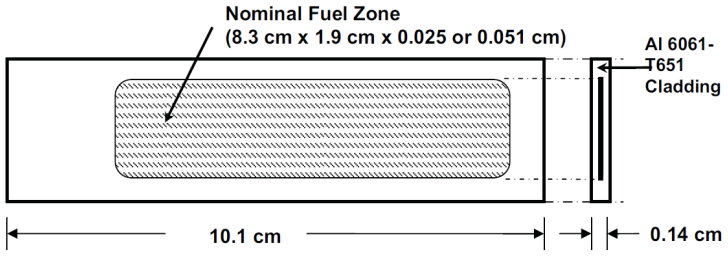


***Figure 2.1:*** *Schematic drawing of a typical minisize fuel plate designed for test irradiations [RCK+09].*

Most High Performance Research Reactors (HPPRs) require plate type fuel. New fuels are tested first in mini-size plates, as shown in Figure 2.1 for the case of US test plates. If this irradiation test was successful, the size of the plate is scaled up to a full size plate with the same geometry, but bigger dimensions (nominal fuel zone: 52.4 cm × 3.7 cm × 0.097 cm). The fuel meat of those

plates either consists of dispersion or monolithic U-Mo fuel with 6 wt.% to 12 wt.% molybdenum in the U-Mo alloy. From the metallurgical view, this U-Mo composition can stabilize the $\gamma$-phase, which at room temperature has a bcc crystal structure that is characterized by the same lattice parameters in each direction with a very low linear expansion coefficient ($12 \cdot 10^{-6}/\mathrm{K}$), compared to $\alpha$-U-Mo [Zwe14] which expands anisotropically due to its hexagonal structure. So, the fuel expands isotropically and therefore well predictably, which makes it very suitable for the use in a reactor.
Finally, the fuel meat is embedded in cladding material to contain the fission products and prevent a release to the cooling agent and the contact of the U-Mo with water. Most commonly, an aluminum alloy is used for plate type fuels. They provide good heat transfer between the fuel meat and the cooling agent. The oxidation, respectively hydration, of the aluminum during irradiation presents a challenge. Hydroxides grow on the surface, which have extremely low thermal conductivities ($< 1\,\mathrm{W/m \cdot K}$). This restrains the heat transfer from the meat to the coolant. The US manufacturers mainly use the aluminum alloy 6061, while the European manufacturers preferentially use the aluminum alloys AlFeNi or AG3NE which react less with water.

Some reactors have the design of pin-type fuel, but this is not further discussed in this work.
In the following, the two different plate type fuel designs, dispersion and monolithic, and their irradiation behavior is discussed, focusing on the results from the European irradiation test program.

## 2.1 Dispersion Fuels

The meat of dispersion fuels consists of U-Mo powder in matrix material. The U-Mo powder can be either produced by grinding or centrifugal atomization.
Production by atomization [SPS+13] results in almost perfectly shaped U-Mo spheres. According to the process, the fuel is called “atomized powder”. While there are several variants of the process, TUM focuses on the “rotating electrode process” [SPS+13, SSP+15]. During this process, high voltage is applied between a fast rotating pin of U-Mo alloy and an electrode, generating an electric arc. The heat from the arc is sufficient to melt the U-Mo alloy. Due to the rotation, small particles are ejected from the pin. In flight the particles cool down and form almost perfect spheres due to the surface tension in the liquid state.
Another way to fabricate U-Mo powder is to pulverize cast U-Mo coupons using standard techniques like hammer milling or jaw crushers. As the U-Mo alloy is ductile, which makes the communition difficult, oxygen is added during the process. A rotary classifier systems holds back the oversized particles and allows the final powdered product to leave the grinding chamber. Powder that is produced with this method is called “ground powder”. It has an irregular shape and contains minor oxygen contamination [Lee14].
Another type, called “Canadian ground powder” is fabricated by machining and milling under oxygen addition. This leads also to irregular shaped particles, but with smoother surface and variable oxygen content [KH10].

Then the U-Mo powder is blended with the matrix material in form of powder. The matrix material should have a high thermal conductivity to allow for a good transfer of the heat from the fission in the particles to the cladding, where the heat goes into the coolant agent. If the heat transfer is restrained, the temperature in the fuel increases which could in the worst case lead to melting of the fuel meat. To guarantee a good thermal contact, the material needs to follow the

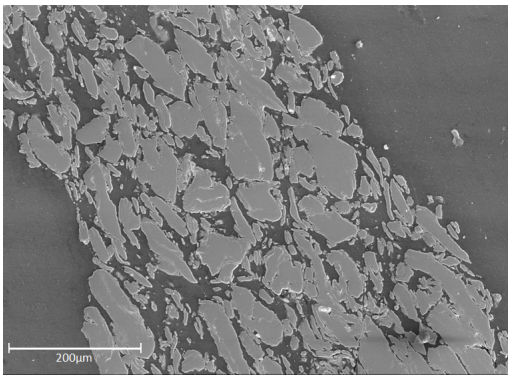


***Figure 2.2:*** *Magnification of ground powder fuel meat. The randomly shaped light dark areas are the U-Mo particles.*

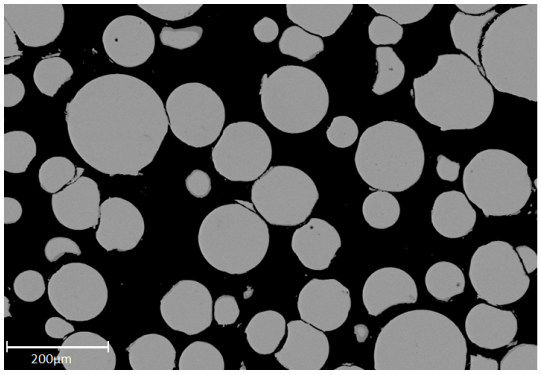


***Figure 2.3:*** *Magnification of atomized powder fuel meat. The spherical light dark areas are the U-Mo particles.*

swelling of the fuel particles and contain the gaseous fission products. Brittle materials would generate cracks that restrain the heat flux. Further the material should have low cross-sections for neutron absorption. The higher the absorption, the more reactivity and cycle length would be lost.
Usually, pure aluminum was used for the matrix, as it has a high thermal conductivity ($\sim 200\,\mathrm{W/m{\cdot}K}$) and is a soft material with good creeping properties. But in case of U-Mo fuels, the uranium reacts with the aluminum during irradiation disadvantageously [BL14] and forms an interaction or also called inter-diffusion layer (IDL) on the interface between fuel particle and aluminum matrix. Gaseous fission products conglomerate in this amorphous layer, growing to large voids that lead to pillowing and further on to break-away swelling during in-pile irradiation under high and low power conditions at already relatively low burnup ($2.0 \cdot 10^{21}\,\mathrm{f/cm^3}$) [BL14], as it happened in the IRIS-1 and IRIS-2 irradiation experiments. Details to the different irradiation tests can be found in Table 2.1.
Post irradiation tests on US plates with AA6061 cladding, which contains a small amount of silicon, showed reduced interaction layer formation at the interface between fuel particles and cladding. This was not observed on European test plates with AG3NE or AlFeNi cladding, not containing silicon. Consequently, the aluminum of the matrix material was mixed with different fractions of silicon. Annealing of the fuel plate enhances the silicon diffusion towards the U-Mo-Al interface, forming a Si rich layer around the fuel particles [Jun11]. The effect of the Si was tested with atomized U-Mo powder in the IRIS-3 and E-FUTURE and E-FUTURE II irradiation experiments and with ground powder in the IRIS-TUM experiment. This retards the formation of the interaction layer, but does not completely suppress the formation. At high irradiation temperatures and burnup, the formation of this layer still occurs.

Silicon additions up to 12 wt.% have been tested. But a higher silicon content in the aluminum reduces the creeping of the matrix material. It is assumed, that this leads to a destabilization of the matrix material during irradiation until the fuel plate looses mechanical integrity and the plate fails [BL14].
Tests have also been performed on magnesium based matrix materials [Jun11, HHKS13, KWR+12]. Irradiation tests showed good performance and no formation of interaction layers, but fabrication and fuel handling is difficult due to the pyrophoric properties of the magnesium. In general, magnesium could react disadvantageously with the aluminum of the cladding material, but this has not been observed yet [CDP+14, Chi14].

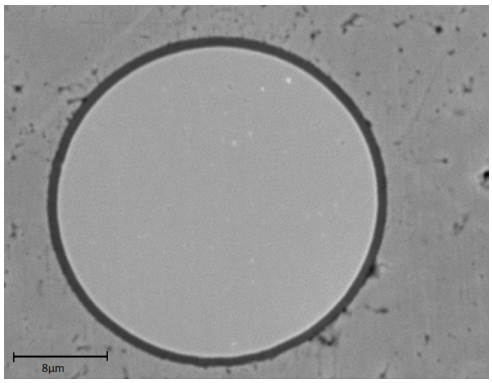


***Figure 2.4:*** *The black line around the spherical U-Mo fuel particle is zirconium-nitride coating [LBD13].*

Another option is to directly coat the fuel particles, to physically avoid the contact with the aluminum matrix. The first approach was oxidation of the fuel particles [CRA+09] in the IRIS-4 irradiation experiment. The particles were covered with a thin layer of $\sim 1$ $\mu$m uranium oxide by thermal treatment of the U-Mo powder under oxygen atmosphere. Similar to uranium-silicide, the uranium oxide undergoes less interaction with the aluminum. Irradiation test showed good behavior, as long as the oxide layer stays intact. However, the oxide is a ceramic and therefore brittle, which leads to cracks in the oxide layer during fabrication and irradiation. At these cracks, the U-Mo gets into contact with the Aluminum of the matrix and interaction starts [Zwe14].

Further approaches are silicon or zirconium-nitride coatings [LBD13] applied on the U-Mo kernels by sputter-coating, see Figure 2.4. This technique has been tested in the SELENIUM experiment showing that the coating does not completely suppresses the intermixing, especially at higher burnups. However, at such high burnups ($4.5 \cdot 10^{21}$ f/cm³), the recrystallization in the U-Mo particles becomes more a problem than the IDL formation. During irradiation, fission gases preferably conglomerate in the amorphous interaction layer or on grain boundaries inside the U-Mo particles. The fission gases remain on the grain boundaries of the fuel particle and grow to large bubbles, leading to accelerated swelling of the entire fuel plate.

| Irradiation Experiment | U-Mo Powder Type | Matrix | Max. Heat Flux [W/cm²] | Max. Fission Density (U-Mo) [$\cdot 10^{21}$ f/cm³] |
|---|---|---|---|---|
| IRIS-1 | ground | Al | 124 - 145 | 0.9 - 3.2 |
| FUTURE | atomized | Al | 351 - 353 | 1.8 |
| IRIS-2 | atomized | Al | 214 - 238 | 2.0 - 2.7 |
| IRIS-3 | atomized | Al + 0.3 − 2.1 wt.%Si | 163 - 201 | 1.4 - 4.1 |
| IRIS-TUM | ground | Al + 2.1 wt.%Si | 251 - 259 | 3.8 - 5.9 |
| IRIS-4 | atomized oxide coating | Al, Al + 2.1 wt.%Si | 249 - 269 | 2.8 - 3.6 |
| E-FUTURE | atomized | Al + 4.1 − 6.0 wt.%Si | 453 - 472 | 5.3 - 5.5 |
| E-FUTURE II | atomized | Al + 7 − 12 wt.%Si | 435 - 448 | |
| SELENIUM | atomized Si/ZrN coating | Al | 421 - 466 | 5.3 |

***Table 2.1:*** *Summary of the main European in-pile irradiation tests [BL14].*

## 2.2 Monolithic Fuels

The uranium loading can be increased to its maximum by simply removing the matrix material. This way, the interaction between matrix material and fuel particle is avoided, except for the interface between fuel foil and aluminum cladding. Different materials are suitable as barrier layers that prevent the contact between the U-Mo and the aluminum cladding [Chi14].
As the U-Mo has a rather low thermal conductivity ($\sim 15\,\mathrm{W/m{\cdot}K}$, see chapter 8), the transfer of the fission heat to the coolant is not as good as for dispersion fuels, so it is advantageously if the material of the barrier layer has a high thermal conductivity. Further, the barrier material's absorption cross-section for thermal neutrons should be as low as possible to minimize the loss of neutrons. To allow for mechanical stability, the material should be ductile and have an adequate thermal expansion coefficient. Finally, considering back-end issues, it should be possible to reprocess the material easily.

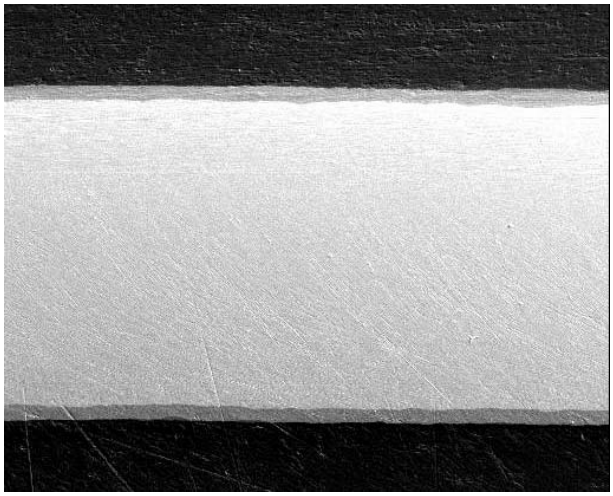

***Figure 2.5:*** *Cross section of a zirconium co-rolled monolithic U-Mo fuel plate [MRW+08]. The light gray inner zone is the U-Mo foil coated with the dark gray zirconium interlayer and clad in the almost black AA 6061 alloy.*

The fabrication of this type of fuel plays a significant role in the fuels' performance. For example, thin cracks in the barrier layer can lead to a reaction of the fuel with the aluminum cladding. The fission gases conglomerate there, which can lead to blisters. But even worse are debond areas, where the interlayer either does not adhere to the cladding or the fuel. Again, fission gases conglomerate there preferably and grow to large bubbles until breakaway swelling occurs.
Different techniques have been developed to fabricate monolithic fuel plates [RCK+09]. Typically, a thin U-Mo alloy ingot is cast through arc-melting or induction melting in a book mold. Then the ingot is subsequently hot rolled to an intermediate thickness. Then the decision has to be made, how the inter-layer is applied to the U-Mo foil. Either the ingot is then cold rolled to a foil to be coated by thermal spray coating or sputter coating or it is hot co-rolled with the diffusion barrier material. Zirconium barriers, applied by co-rolling, showed good processibility and good irradiation performance.
A very important step is the fuel-cladding bonding. The most commonly used technique is Hot Isostatic Pressing [MRW+09]. The coated fuel foil is put between two aluminum cladding plates into a hermetically sealed and evacuated canister. High pressure ($\sim 100\,\mathrm{MPa}$) and temperature $> 550\,^{\circ}\mathrm{C}$ is applied to the stack of foils for a certain time (about 1 h).
In collaboration, the Technische Universität München and AREVA-NP (CERCA) have developed a welding technique called "C2TWP" ("CEA CERCA TUM Welding Process") to apply the cladding by hot rolling [SGC+14].

# CHAPTER 3

## Thermal Conductivity

The subject of this thesis is to investigate the thermal conductivity of the different U-Mo fuels that have been presented in the previous chapter, as well as the evolution of their thermal conductivity during reactor operation.
This chapter gives now information about the theoretical background of the thermal conductivity and its calculation.

The thermal conductivity $\lambda$ is typically not assessed directly. Rather it is a composition of the material's thermal diffusivity $\alpha$, specific heat capacity $c_p$ and density $\rho$.

$$\lambda = \alpha \cdot c_{\mathrm{p}} \cdot \rho \tag{3.1}$$

Each of these parameters can be measured separately. As well, each parameter is dependent on the temperature and the increasing burn-up during reactor operation, finally influencing the thermal conductivity. In the following, each parameter, their changes and impacts on the thermal conductivity are discussed separately.

### 3.1 Thermal Diffusivity

The thermal diffusivity $\alpha$ is a quantity for the reaction of a material to a temperature change. It is used to describe the unsteady heat conduction and serves as diffusion coefficient for the heat transport in the heat Equation 3.2 [Tou70c].

$$\frac{\partial T(\boldsymbol{x},t)}{\partial t} = \boldsymbol{\nabla}\left(\alpha(\boldsymbol{x},t)\,\boldsymbol{\nabla} T(\boldsymbol{x},t)\right) \tag{3.2}$$

The thermal diffusivity strongly depends on the material and its microstructure. Due to this, the thermal diffusivity of the reactor fuel is very sensitive on microstructural changes in the material during irradiation. Fission products have an average kinetic energy of 80 MeV and cause heavy distortion and changes in the crystal lattice. The gaseous fission products conglomerate to microscopic voids that intersperse the bulk material. Both effects lead in general to a decrease of

the thermal diffusivity.
The thermal diffusivity is also dependent on the temperature. For most materials it increases with temperature. In general, the behavior is non-linear.

There is no general mathematical model to calculate the thermal diffusivity of a mixture of different composites. However, several models have been developed to calculate the thermal diffusivity of dispersed and layered materials. In principle, those models are based on the calculation of the thermal conductivity, but together with the knowledge of the specific heat capacity and density, it is possible to obtain the thermal diffusivity. More details about these models are discussed in Chapter 3.4.

## 3.2 Specific Heat Capacity

The heat capacity $C$ is the ratio of heat $\Delta Q$ that is applied to a body to the resulting temperature change $\Delta T$.

$$C(T) = \frac{\delta Q}{\mathrm{d}T} \tag{3.3}$$

It depends on the body's mass, its chemical composition and its thermodynamic state.

The specific heat capacity can be derived from the thermodynamic relations. The first law of thermodynamics, Equation 3.4, states that the internal energy of a system can only be changed by adding heat $\delta Q$ or performing work $\delta W$.

$$\mathrm{d}U = \delta Q + \delta W = \delta Q - p\,\mathrm{d}V \tag{3.4}$$

During an isochoric process, heat is added to the system without changing the volume ($\mathrm{d}V = 0$). This process defines the heat capacity for a constant volume $C_V$.

$$\left(\frac{\partial U}{\partial T}\right)_V = \left(\frac{\partial Q}{\partial T}\right)_V = C_\mathrm{V} \tag{3.5}$$

Adding energy to a system at constant pressure ($\mathrm{d}p = 0$), changes its volume and is called an isobaric process. This change of the system's energy content is then related to the enthalpy $H$.

$$\mathrm{d}H = \delta Q + V\,\mathrm{d}p \tag{3.6}$$

Those isobaric processes ($\mathrm{d}p = 0$) lead to the heat capacity for constant pressure $C_\mathrm{p}$.

$$\left(\frac{\partial H}{\partial T}\right)_P = \left(\frac{\partial Q}{\partial T}\right)_P = C_\mathrm{p} \tag{3.7}$$

Dividing $C_\mathrm{V}$ and accordingly $C_\mathrm{p}$ by the body's mass $m$, one obtains its specific heat capacity $c_\mathrm{p}$, accordingly $c_\mathrm{V}$.

$$c_\mathrm{p} = \frac{C_\mathrm{p}}{m} \tag{3.8}$$

In the experiment for the determination of the specific heat capacity, it is more viable to measure solid materials under constant pressure than of constant volume. $c_\mathrm{p}$ can be converted to $c_\mathrm{V}$. Writing Equation 3.5 and 3.7 in terms of the entropy by using the second law of thermodynamics, the Maxwell relations can be applied. This leads to following equation:

$$C_\mathrm{p} - C_\mathrm{V} = T \left.\frac{\partial p}{\partial T}\right|_V \left.\frac{\partial V}{\partial T}\right|_p = TV\frac{\gamma^2}{\kappa_\mathrm{T}} \tag{3.9}$$

with $\gamma^2$ the isobaric thermal expansion coefficient and $\kappa_\mathrm{T}$ the isothermal compressibility.

As the specific heat capacity is dependent on the material composition, the specific heat capacity of uranium-molybdenum fuels is at first depending on the fuel type, monolithic or dispersion. For dispersion fuels different fuel loadings and matrix materials have to be considered. The specific heat capacity of a composite $c_\mathrm{p}$, like dispersion fuels, can be approximated with the Neumann-Kopp rule by adding the specific heat capacity of each component $c_\mathrm{p,i}$ weighted with its mass fraction $\omega_\mathrm{i}$.

$$c_\mathrm{p} = \sum_\mathrm{i} \omega_\mathrm{i} c_\mathrm{p,i} \tag{3.10}$$

During in-pile irradiation, the specific heat can change, as a result of the change in the material composition, as $^{235}$U is consumed leading to a build up of various fission and neutron capture products.

## 3.3 Density

The density $\rho$ is the ratio of a body's mass $m$ to its volume $V$.

$$\rho = \frac{m}{V} \tag{3.11}$$

The volume of a body is temperature dependent. So, according to Equation 3.11, thermal expansion has to be considered. The temperature dependent volume $V(T)$ is given by Equation 3.12 assuming that the expansion coefficient $\gamma$ is independent of the temperature and the volume expansion is isotropic.

$$V(T) = V_0 \cdot (1 + \gamma \Delta T)^3 \tag{3.12}$$

In $\gamma$-U-Mo, fcc and bcc crystal structures are found that undergo isotropic volume expansion, so Equation 3.12 is valid for monolithic U-Mo fuels and the temperature dependent density is given by:

$$\rho\left(T\right) = \frac{\rho_0}{\left(1+\gamma\Delta T\right)^3} \tag{3.13}$$

For dispersion fuels, U-Mo particles are embedded in aluminum that also has a fcc crystal structure undergoing isotropic volume expansion. So, in first approximation, Equation 3.13 is valid for dispersion fuels as well.

Monolithic uranium-molybdenum has high Uranium densities of about $15\,\mathrm{g/cm^3}$ depending on the Mo content. In contrast, dispersion fuel is mixed with aluminum which is a material with a rather low density ($2.7\,\mathrm{g/cm^3}$), as well as other low-density materials, like silicon. This further decreases the density of the composite of fuel and matrix material to densities even below $10\,\mathrm{g/cm^3}$. With the rule of mixture (Equation 3.14), it is possible to estimate the density $\rho$ of the composite.

$$\rho = \frac{1}{\sum_\mathrm{i} \frac{\omega_\mathrm{i}}{\rho_\mathrm{i}}} \tag{3.14}$$

$\omega_\mathrm{i}$ is the mass fraction of each component and $\rho_\mathrm{i}$ its density.
In principle it is only valid for homogenous mixtures, but it can also be used as a good approximation for dispersion fuel.

During in-pile irradiation fission gas bubbles are formed and increase the total volume.
Equation 3.14 can also be written as a function of the volume fractions $\nu_\mathrm{i}$. As the density of the fission gas in the bubbles is much lower than the solid fission products and the meat, the density of the fission gas bubbles can be assumed to be zero. During irradiation their volume fraction increases and so it is obvious that the fuel's density decreases with increasing burn-up.

$$\rho = \sum_\mathrm{i} \nu_\mathrm{i} \cdot \rho_\mathrm{i} \tag{3.15}$$

## 3.4 Models for Composite Materials

The fuel is clad in aluminum. In the case of irradiated fuel, either monolithic or disperse, it is not possible to remove the cladding before the measurement of the thermal properties, as the fuel segments are due to the irradiation effects very porous and would loose their mechanical integrity during handling and measurement. In this case, the composite of fuel meat and cladding has to be measured. To derive the thermal conductivity of only the meat from the measurement of the composite, theoretical models need to be found, because thermal conductivities can not simply be added together for non-stationary scenarios.

Two different types of materials need to be considered.
A typical fuel plate segment consists of three layers, meat with cladding on the top and the down

side. For the measurement of fresh fuel, the cladding can be removed and the segment is reduced to a one layer system. So, the measurements can be evaluated with standard methods. But for in-pile irradiated fuel this is not possible. Therefore, different models for layered materials have been developed, see Chapter 3.4.1.
Further, especially regarding dispersion fuels, the fuel particles are randomly distributed in the aluminum matrix. The heat transfer through the material depends on the shape, density and thermal diffusivity of the fuel particles. So, different models need to be found for the different dispersion fuels. Several models exist for different particle shapes and boundary conditions. The most adaptive model [BCH15] for dispersion fuel has been selected for the calculation of the investigated dispersion fuel and is presented in Chapter 3.4.2.

### 3.4.1 Layered Materials

Mainly two different models have been developed to calculate the thermal conductivity, respectively thermal diffusivity, of layered materials from measurements using the Laser Flash Method. Here, a short intense heat pulse, usually from a laser, hits the front surface of the investigated material. The heat is transferred through the material in a certain time and heats up the rear surface. The temperature rise can be measured with an infrared detector. Finally, the thermal diffusivity of the material can be calculated from the temperature rise on the rear surface. More details to the measurement technique are provided in Chapter 4.1.
The models are denoted as the TUM and the PNNL model, developed at Technische Universität München (TUM) and accordingly Pacific Northwest National Laboratory (PNNL) [BCC+15a]. Both models have been crosschecked against each other by comparing the results of the two models for a three and a five layer system. The samples for the test originate from an in-pile irradiated monolithic fuel plate, for details to the sample see Chapter 5.1.3.

The data in this work have been exceptionally evaluated with the TUM model, so, the description of the PNNL model is rather short, while the TUM model will be explained more in detail in the following. The direct comparison of the two models is shown in Chapter 6.

#### 3.4.1.1 PNNL Model

Both models are based on the solution of the one dimensional heat diffusion equation for a three layer system:

$$\frac{\partial^2 T_j\,(x,t)}{\partial z^2} = \frac{1}{\alpha_j}\frac{\partial T_j\,(x,t)}{\partial t} \tag{3.16}$$

The PNNL model assumes no heat losses from the sample surface, no interfacial contact resistance, homogeneous layers and a uniform absorption of the incoming heat pulse. Further, the thermal conductivity of two layers has to be known, as well as the specific heat capacity and density of the layer of interest. It is the goal of the model to calculate the thermal diffusivity of the this layer to finally be able to calculate the thermal conductivity of this layer together with its already from other measurements obtained specific heat capacity and density.
Finally, the analytical solution of Equation 3.16 follows the derivation of Lee [Lee77]. It is

based on the solution of the differential equation by applying the Laplace transformation and the determination of the characteristic equation. This leads to an equation of the normalized temperature rise on the back face following a heat pulse to the front face. The equation depends on the shape of the incoming heat pulse, the thermal properties of the different layers, their thickness and the thermal diffusivity of the composite material. The thermal diffusivity of the composite is obtained from the laser flash measurement, assuming the material as a one layer system for a simplified evaluation.
Given this, the only unknown parameter is the thermal diffusivity of one layer. The model iterates upon this parameter until the thermal diffusivity of the unknown layer is determined.

#### 3.4.1.2 TUM Model

The TUM model does not use the solution of the one layer evaluation, as the multiple layers have an impact on the shape of the temperature curve and the one layer model does not correctly calculate the composite thermal diffusivity. So, the TUM model solves the one dimensional heat diffusion Equation 3.16 numerically.

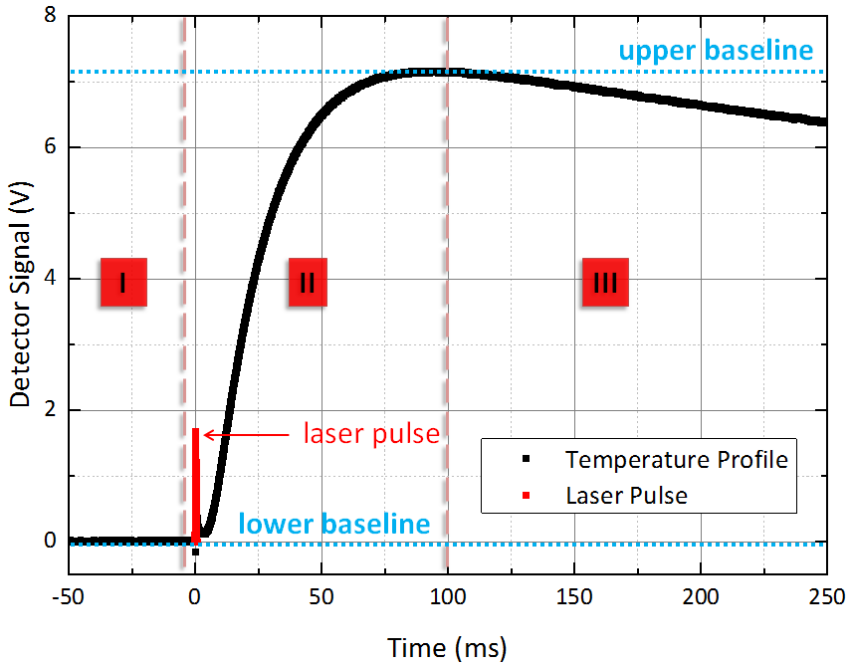


***Figure 3.1:*** *Example of a typical time-temperature profile (black data points) obtained from a LFA measurement. The red line shows the laser pulse that causes the temperature rise in part (II). The dashed green lines represent the upper and lower baselines.*

Figure 3.1 shows a typical temperature profile over time from a laser flash measurement. It displays the temperature of the rear surface of the material that is hit by a laser shot on the front surface. In the first part (I) of the curve, called lower baseline or $T_0$, the material is in equilibrium with the temperature of the environment. When the laser shot hits the front surface, heat is transfered to the rear side, resulting in a temperature rise, which can be seen in the second part (II) of the curve. Finally, the temperature saturates in a maximum temperature $T_{\max}$, called upper baseline. But, as can be seen in the third part (III), the temperature decreases again due to (mainly radiative and convectional) heat loss into the environment.

In the first step, the program determines the lower and upper baselines from the data to calculate the minimum and maximum temperature $T_0$ and $T_{\max}$) at the sample backside.

The backside temperature curve for an isolated one-layer system can be approached by the analytical solution of the heat diffusion equation (Parker model) [PJBA61], as it is used in the PNNL model to obtain a starting value for the thermal diffusivity of the composite. In the TUM model, the results are used as start values for the numerical simulation, which takes additional properties into account.

$$T_{\text{norm}}(L,t) = \frac{T(L,t) - T_0}{T_{\max} - T_0} = 1 + 2 \cdot \sum_{n=1}^{\infty} (-1)^n \cdot \exp\left(-n^2 \frac{\pi\alpha\,(t - t_0)}{L^2}\right) \tag{3.17}$$

In Equation 3.17, $T_{\text{norm}}(L,t)$ is the normalized temperature derived from the ratio between the actual backside temperature $T(L,t)$ at time $t$ and position $L$, where $L$ is the thickness of the sample, and the maximum temperature $T_{\max}$. As only the temperature interval is of relevance, the baseline temperature $T_0$ is subtracted from $T(L,t)$ and $T_{\max}$.
The sum has to be cut off after some term to avoid numerical instability during the calculation of the solution of Equation 3.17. However, in this case for $t \leq t_0$, the function for the normalized temperature does not yield $T_{\text{norm}}(t_0)$, but rather approaches negative infinity at $t_0$ with a sharp bend. Taking more terms into account, the sharp bend moves closer to $t_0$ and away from the relevant data points. Twenty-five terms are usually a good choice to sum over, more terms take longer computing time, but do not significantly improve the result. For a very large number of terms, the solution may become numerically unstable due to the exponential factor in the sum. To avoid this, the actual implementation does not allow for $T_{\text{norm}}(L,t) < 0$, i.e. $T_{\text{norm,impl.}}(L,t) = \max(0, \mathrm{T}_{\text{norm}})(L,t)$.
This solution is only valid for single layers and does not take into account the time-dependent intensity of the laser flash and heat losses. However, it is sufficient to calculate the initial values for the simulation-based fit, i.e., the average thermal diffusivity of the whole sample and the time of the laser shot $t_0$. As the $t_0$ parameter and the thermal diffusivity are strongly linked in the parameter correlation matrix, it is of great advantage to specify $t_0$ manually if it is known in advance. Often, $t_0 = 0$.
Figure 3.2 shows the fit of the sum compared to the fit resulting from the advanced numerical results, which will be explained in the following.

This analytical pre-solution is then improved by the numerical solution of the 1D heat diffusion Equation 3.18 using the explicit Euler rule.

$$T_{n,i}^{k+1} = T_{n,i}^{k} + \frac{\alpha_i \Delta t}{\Delta x_i^2}\left(T_{n+1,i}^{k} - 2T_{n,i}^{k} + T_{n-1,i}^{k}\right) \tag{3.18}$$

$\Delta x_i$ is the spatial discretization in layer $i = 0$, which may be different from layer to layer, $\Delta t = (t_{k+1}) - t_k$ is the time discretization. $n$ is the index of the spatial descretization $n = 0...N$. Therefore, $T_{n,i}^{k}$ is the temperature at point $n$ in layer $i$ at time $k$.

The discretized heat equation is solved with the following boundary conditions, given by Equations 3.19 to 3.25:

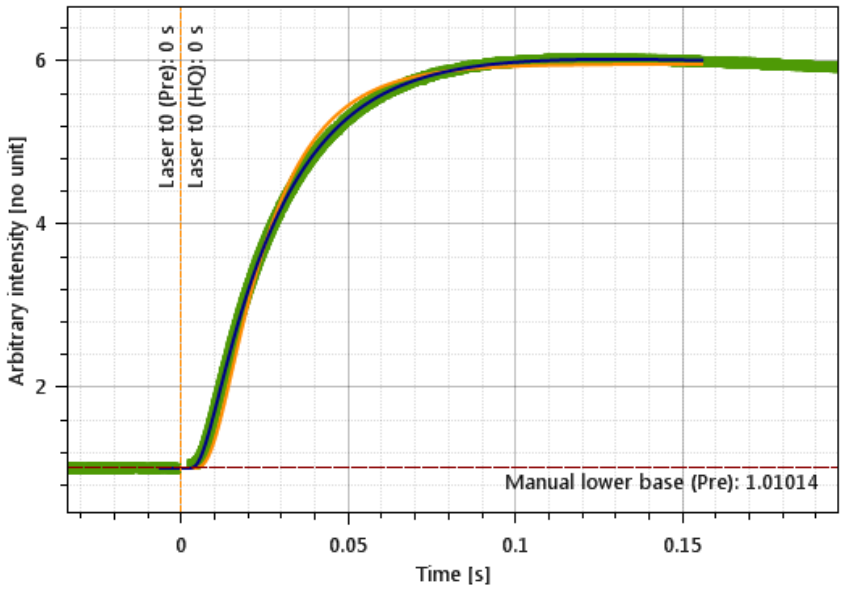


***Figure 3.2:*** *A typical time-temperature profile (green data points) obtained from a LFA measurement. The red dashed line shows the lower baseline, i. e. the minimum temperature. The orange line is the result of a one-layer fit that provides start values, the blue line represents the numerical fit.*

1. Incoming heat flux from the laser pulse hits the sample on the front side and convective and radiative cooling

$$T_{0,0}^{k+1} = T_{0,0}^{k} + \frac{2\alpha_0 \Delta t}{\Delta x_0^2}\left[T_{1,0}^{k} - T_{0,0}^{k} + \underbrace{\Delta x_0 S_0\left(k\right)}_{\text{laser}} + \underbrace{a_1\left(T_{0,0}^{k} - T_{0,0}^{0}\right)}_{\text{convective}} + \underbrace{a_4\left(T_{0,0}^{k} - T_{0,0}^{0}\right)^4}_{\text{radiative}}\right] \tag{3.19}$$

with $\mathrm{S_0\,(t)}$ the normalized laser signal:

$$S_0\left(k\right) = \frac{\Delta T_{\text{norm}}}{\lambda_0} \cdot \frac{\int_k^{k+1} \text{Laser}\left(t\right) dt}{\int_0^{\infty} \text{Laser}\left(t\right) dt} \cdot \sum \frac{\lambda_i}{\alpha_i} d_i \tag{3.20}$$

for the unknown layer, the thermal conductivity $\lambda$ is calculated from the trial solution for the thermal diffusivity $\alpha$ and the known density $\rho$ and specific heat capacity $C_p$.

$$\Delta T_{\text{norm}} = T_{\max} - T_0 \tag{3.21}$$

2. Continuous boundary conditions at the layer interfaces A $\longleftrightarrow$ B, for heat flux and for temperature

$$T_{A,N}^{k+1} = T_{A,N}^{k} + \frac{2\alpha_A\alpha_B\Delta t}{(\alpha_B\lambda_A\Delta x_A + \alpha_A\lambda_B\Delta x_B)}\left(\frac{\lambda_B}{\Delta x_B}\left(T_{B,1}^{k} - T_{B,0}^{k}\right) - \frac{\lambda_A}{\Delta x_A}\left(T_{A,N}^{k} - T_{A,N-1}^{k}\right)\right) \tag{3.22}$$

$$T_{B,0}^{k+1} = T_{A,N}^{k+1} \tag{3.23}$$

3. Cooling conditions at the back of the sample

$$T_{M,N}^{k+1} = T_{M,N}^{k} + \frac{1\alpha_M\Delta t}{\Delta x_M^2}\left[\left(-T_{M,N}^{k} + T_{M,N-1}^{k}\right) + a_1\underbrace{\left(T_{M,N}^{k} - T_{M,N}^{0}\right)}_{\text{convective}} + a_4\underbrace{\left(T_{M,N}^{k} - T_{M,N}^{0}\right)^4}_{radiative}\right] \tag{3.24}$$

$N$ being the number of special discretization steps and $\lambda_i$ the thermal conductivity of the layer $i$. M is the outermost layer index. $a_1$ and $a_4$ are cooling factors that are assumed to be temperature independent and equal for both sides of the sample. Note that due to the cooling correction, the actual curve does not necessarily reach $T = T_{\max}$, which would correspond to the upper baseline in the Parker model. In the simulation, $T_{\max}$ serves as a free parameter for the normalization. Other free parameters are $T_0$, $t_0$, $T_{\max}$, $a_1$, $a_4$ and $\alpha_x$. All of these parameters, except $\alpha_x$, can optionally be fixed manually in teh actual implementation. It is recommended to fix especially $T_0$ and $t_0$ for higher accuracy.

4. Initial condition at $t_0$

$$T_{i,n}^{0} = T_0 \tag{3.25}$$

The result of the simulation $T_{\mathrm{M,N}}(t)$ is the temperature curve at the rear side of the sample that is actually measured in the experiment. An adapted version of the Levenberg-Marquardt algorithm [Mar63] is used to solve the inherent optimization problem by comparing the numerical solution from the differential equation to the actual data curve. In other words, the heat conduction equation is solved with continuously adapted parameters until the squared distance $X^2$ between the measured data and the solution from the simulation is minimal.
The model can be used for a variable number of layers, as long as the thermal conductivity of all but one layer is known, as well as the specific heat capacity and density of the unknown layer. In theory, it is possible to solve for multiple unknown diffusivities, however, this would require exceptional data quality that currently cannot be reached with measurements.

### 3.4.2 Dispersed Materials

There is a variety of models to calculate the thermal conductivity of dispersed composites. The three most common models to calculate the thermal conductivity of such materials are the Maxwell model [CJ59], the Bruggeman model [Bru35] and the Hsu model [HB85] that are all derived from the effective-medium theory [CJ73, Str75].
The models were compared with measured data of fuels with different volume fractions of 10 vol.% and 50 vol.% of U-Mo fuel particles in an aluminum alloy 1060 matrix [BCH15]. All models showed good agreement at 10 vol.%, but the Maxwell and Bruggeman model differed significantly at higher volume fractions, while the Hsu model was in good agreement with the measured data also at 50 vol.%.
The Maxwell model assumes a low concentration of the dispersed material, so that there is no interaction between the particles. The Bruggeman model neglects the interaction between the particles in much the same manner. So, these two models are only valid for low volume fractions of fuel particles in the matrix, which was proven by the measurement. In contrast, the Hsu model combines the effective-medium theory [CJ73, Str75] with the percolation theory [Kir73] and therefore also allows interaction between the particles. So, this model can be applied also for higher volume fractions of the dispersed phase, where the matrix and the fuel particles cluster and agglomerate.

Applying the Laplace Equation on the Hsu model, the thermal conductivity of a composite material is described with the following equation [HB85]:

$$\{1 - F(e)\}\,\lambda_\mathrm{c}^2 + \{\lambda_\mathrm{d}\,[F(e) - \nu_\mathrm{d}] + \lambda_\mathrm{m}\,[F(e) - \nu_\mathrm{m}]\}\,\lambda_\mathrm{c} - \lambda_\mathrm{d}\lambda_\mathrm{m}F(e) = 0 \tag{3.26}$$

$\lambda_\mathrm{i}$ is the thermal conductivity, $\nu_\mathrm{i}$ the volume fraction of phase i, the subscripts c, m and d represent the composite, matrix and dispersed phase and $F(e)$ is a function of the eccentricity $e$ of the dispersed phase. It takes into account the shape and orientation of the particles. In the case of dispersion fuels, this factor has to be calculated for spheres, which leads to $F(e) = \frac{1}{3}$ or prolate spheroids [HB85]:

$$F(e) = \frac{1}{e^2}\left[1 - \frac{\sqrt{1-e^2}}{e}\arctan\left(\frac{e}{\sqrt{1-e^2}}\right)\right] \tag{3.27}$$

For in-pile irradiated fuels, the model needs to be extended [BHC15], because of the growth of the IDL. This can be implemented by a model for coated spheres that are subjected to an axial heat flow. Equation 3.28 is the solution of the heat transport equation for a coated sphere and adapted boundary conditions [BB90].

$$\lambda_\mathrm{cs} = \frac{R}{\left\{\left(\frac{2R}{a}\right)\ln\left[\frac{(aR+b)}{(a(R-r)+b)}\right] + \left(\frac{b}{a^2}\right)\ln\left[\frac{(aR+b)}{(a(R-r)+b)}\right] + \left(\frac{R-r}{\lambda_\mathrm{IL}}\right) - \left(\frac{r}{a}\right)\right\}} \tag{3.28}$$

where

$$a = -\lambda_{\mathrm{fp}} \tag{3.29}$$

$$b = 2\,(R - r)\,\lambda_{\mathrm{IL}} + 2r\lambda_{\mathrm{fp}} \tag{3.30}$$

$\lambda_{\mathrm{cs}}$ is the thermal conductivity of the coated sphere, $\lambda_{\mathrm{IL}}$ the thermal conductivity of the interaction layer and $\lambda_{\mathrm{fp}}$ is the fuel particle's thermal conductivity, $R$ is the the total particle radius including the interaction layer and $r$ is the fuel particle radius. $\lambda_{\mathrm{fp}}$ substitutes $\lambda_{\mathrm{d}}$ in Equation 3.26.
The thermal conductivity of the fuel particle $\lambda_{\mathrm{fp}}$ depends on the operational temperature of the fuel meat $T_{\mathrm{op}}$ and burn-up $f_{\mathrm{d}}$. For U-Mo, following equation was determined from a multiple second-order polynomial regression on data from in-pile irradiated monolithic U-Mo fuels with a temperature range from 50 °C to 350 °C and a burnup of $(3.30 - 4.52) \cdot 10^{21}\,\mathrm{f/cm^3}$ [BCC+15b]. The equation already includes the influence of fission gas bubbles:

$$\begin{aligned}\lambda_{\text{U-Mo}}\left(T_{\mathrm{op}}, f_{\mathrm{d}}\right) = 1.29 \cdot 10^{-5}\left[\tfrac{W}{\mathrm{m \cdot K^3}}\right] \cdot T_{\mathrm{op}}^2 - 5.59 \cdot 10^{-3}\left[\tfrac{\mathrm{W \cdot cm^3}}{\mathrm{m \cdot K^2}}\right] \cdot T_{\mathrm{op}} \cdot f_{\mathrm{d}} - \\ -1.46 \cdot 10^{-2}\left[\tfrac{\mathrm{W \cdot cm^6}}{\mathrm{m}}\right] \cdot f_{\mathrm{d}}^2 + 4.11 \cdot 10^{-2}\left[\tfrac{W}{\mathrm{m \cdot K^2}}\right] \cdot T_{\mathrm{op}} - 0.74\left[\tfrac{\mathrm{W \cdot cm^3}}{\mathrm{m \cdot K}}\right] \cdot f_{\mathrm{d}} + 10.8\end{aligned} \tag{3.31}$$

Finally, the thickness of the interaction layer $Y_{\mathrm{IL}}^2$, which depends on the fuel meat fission density $f_{\mathrm{d}}$, the average operational temperature $T_{\mathrm{op}}$ and the duration of the irradiation $t$, needs to be considered.

$$Y_{\mathrm{IL}}^2 = Y_{\mathrm{IL},0}^2 \cdot r_{\mathrm{Si}} \cdot r_{\mathrm{Mo}} \tag{3.32}$$

with the thickness of the fission enhanced interaction layer of dispersion U-Mo with Al matrix $Y_{\mathrm{IL},0}^2$:

$$Y_{\mathrm{IL},0}^2 = 2.6 \cdot 10^{-8}\left[\mu\mathrm{m}^2\left(\mathrm{s \cdot cm^3}\right)^{0.5}\right] \cdot \dot{f}_{\mathrm{d}}{}^{0.5} \cdot \exp\left(\frac{-3850\left[\tfrac{\mathrm{K}}{\mathrm{s}}\right]}{T_{\mathrm{op}} + 273\,[\mathrm{K}]} \cdot t\right) \tag{3.33}$$

This relation is derived from the Arrhenius correlation for temperature enhanced interaction layer growth and adapted for fission enhanced interaction layer growth using measured data from post-irradiation examinations of multiple test irradiations of U-Mo/Al fuels [KHR+13]. It depends of course on the fuel meat fission density rate $\dot{f}_{\mathrm{d}}$ and is corrected with a reduction factor for Si in the matrix material, $r_{\mathrm{Si}}$, and the Mo content in the fuel, $r_{\mathrm{Mo}}$, as Equation 3.33 was derived for monolithic U-10 wt.%Mo, while most dispersion fuels contain U-7 wt.%Mo. Both

factors have been determined from measurements of the interaction layer of various irradiated fuels with different burnup and Si, respectively Mo, content [KHR+13].

$$r_{\mathrm{Si}} = \left[1.201 - 0.00062\left[\tfrac{1}{K}\right] \cdot (T_{\mathrm{op}} + 273\,[\mathrm{K}])\right] \cdot \exp\left\{-\left[10.333 - 0.021\left[\tfrac{1}{K}\right] \cdot (T_{\mathrm{op}} + \right.\right.$$
$$\left.\left. + 273\,[\mathrm{K}])\right] \cdot W_{\mathrm{Si}}\right\} + \left[0.00062\left[\tfrac{1}{K}\right] \cdot (T_{\mathrm{op}} + 273\,[\mathrm{K}]) - 0.201\right] \cdot \exp\left\{-\left[0.00081\left[\tfrac{1}{K}\right] \cdot \right.\right. \quad (3.34)$$
$$\left.\left. \cdot (T_{\mathrm{op}} + 273\,[\mathrm{K}]) - 0.302\right] \cdot W_{\mathrm{Si}}\right\}$$

$$r_{\mathrm{Mo}} = 1.35 - 0.05 \cdot W_{\mathrm{Mo}} \quad (3.35)$$

with $W_{\mathrm{Si}}$ and $W_{\mathrm{Mo}}$ being the weight fractions of the Si content in the matrix and Mo content in the fuel particle [KHR+13].

The interaction layer consumes both, fuel particle and matrix, but mostly matrix material [GKM+12] at relatively different rates depending upon a number of conditions. However, many studies have shown that the interaction layer mostly consists of (U,Mo)$\mathrm{Al_x}$ intermetallics, where x is generally 2, 3 or 4 [PE10]. This indicates that more matrix atoms must be consumed than fuel atoms. In this work, the interaction layer is assumed to be $\mathrm{UAl_3}$. As Uranium and Aluminum have similar particle densities ($N_{\mathrm{U}} = 5 \cdot 10^{22}\,\mathrm{f/cm^3}$ and $N_{\mathrm{Al}} = 6 \cdot 10^{22}\,\mathrm{f/cm^3}$), about 1/4 of fuel and 3/4 of the surrounding matrix can be expected to be consumed. So, with increasing burnup, 1/4 of the interaction layer growth needs to be subtracted from the fuel particle radius $r$ and 3/4 consume the matrix and increases the total fuel particle radius $R$ that considers the interaction layer. The amount of matrix material has to be reduced accordingly. For the results of the calculations, based on measured values, see Chapter 8.4.

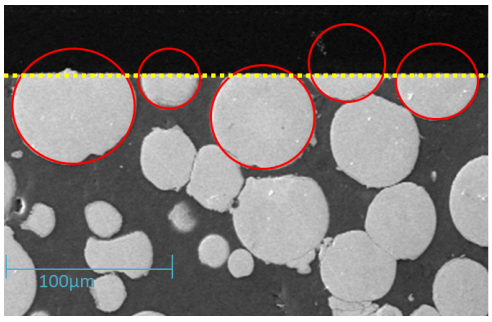


***Figure 3.3:*** *Cross-section of dispersion fuel meat.*

The parameters to calculate the thermal conductivity of the different as-fabricated or in-pile irradiated dispersion fuels can be obtained from the manufacturer's fuel fabrication sheets. There the initial contents of each component of the entire fuel plate is noted. So, it is possible to use this for the calculation of an average thermal conductivity of the fuel plate, but there might be deviations in the comparison of the theoretical values with measured values that origin from only small segments out of the entire fuel plate. Typically, in the case of mini-size plates, a segment is only about 2 % to 6 % of the plate. In the case of full-size plates the ratio is below 0.5 %.

The particle form and radius, as well as the thickness of the interdiffusion layer can be obtained by optical or scanning electronic microscopy. Here, it has to be denoted that the values have to be considered carefully and may only be used as average values, as long as multiple microscopy measurements have been performed.

The cross-section of a dispersion fuel meat in Figure 3.3 shows that the fuel particles are embedded in the matrix in different depths. Looking only from the top onto the surface without the knowledge of the cross-section, it is not possible to verify if the particle is cut through

its mid-plane. This effect falsifies the diameter or coating layer thickness. By taking a series of measurements of the thickest particles, it can be assumed that they are cut through their mid-plane. The average value of the measurement over multiple particles can be used as average diameter or coating layer thickness.

# Part II

# Experimental Techniques and Data Analysis

# CHAPTER 4

## Measurement Techniques and Data Analysis

This part describes the experimental techniques and the analysis of the measured data to calculate the parameters for the thermal conductivity, i.e. the thermal diffusivity, specific heat capacity and density. The thermal diffusivity was measured with a Laser Flash Apparatus (LFA) and the specific heat capacity with a power compensating Differential Scanning Calorimeter (DSC). For the measurement of the density, two different techniques have been adopted: Pycnometry and Immersion Method.

Besides the Laser Flash Technique, the thermal diffusivity can be obtained with another method: the Scanning Thermal Diffusivity Microscope [HFG+12, KH11, HSK13]. The thermal diffusivity of an in-pile irradiated dispersion and two in-pile irradiated monolithic fuel samples has been investigated. But the instrument, located in a hot cell, could not be sufficiently tested with standard or surrogate materials, as the electronics broke irreparably after these first measurements due to radiation damage in the hot cell. So, the measurements could not be completely verified and consequently are not further used in this work. Appendix B.4 gives an overview over the performed measurements.

## 4.1 Laser Flash Apparatus

### 4.1.1 Instrument

In Chapter 3.1, the thermal diffusivity has been discussed as one of the parameters to be determined for the calculation of the thermal conductivity. The standard technique to measure the thermal diffusivity is the Laser Flash method. A short energy pulse, typically a laser pulse, heats up the front surface of the material. The heat diffuses through the material and finally also heats up the rear surface of the material. The thermal diffusivity is related to the velocity of the temperature increase on the rear side. It can be obtained from the time dependent temperature profile of the rear surface [PJBA61]. Details about the analysis are provided in Chapter 4.1.3.

All measurements on fresh fuel were performed with an LFA 427 [NG14c], the measurements on the in-pile irradiated fuel with an LFA 457 MicroFlash [NG14b], both produced by Netzsch. The instruments are very similar and are both based on the same measurement principle. Figure 4.1 shows a schematic drawing of the instruments.
A carrier system holds the sample inside a sealed furnace which enables measurements in either

vacuum or inert atmospheres like argon or Helium. The sample holder is made of $Al_2O_3$, which is almost an insulator to avoid heat loss via the sample holder. A water cooled graphite heating element surrounds the sample holder to heat the sample from room temperature up to 1500 °C. Temperature sensors very close to the sample monitor its temperature and signalize the point of time when the sample reaches a predetermined temperature. A pulsed Nd:YAG (Neodymium: Yttrium Aluminum Garnet) laser is connected to the measurement chamber via a sheeted glass fiber. It emanates a very short ($< 1$ ms) burst of energy (maximum 25 Joule) which is absorbed on the front surface of the sample. The heat is transferred through the sample to the rear surface. A liquid Nitrogen cooled InSb infrared detector measures the temperature of the sample rear face as a function of time.
For the measurement of the irradiated samples, a sapphire disk was installed in the carrier system to place the sample on top of it. This prevents the sample from falling down into the instrument and precise orientation, as the irradiated samples were handled inside a hot cell with manipulators. Sapphire is transparent for laser light in the energy range of the used laser. Only a very small amount of heat from the sample is lost to the sapphire, as the sample only lightly bears on the sapphire disk. Further, compared to other isolating materials, sapphire is a thermal isolator with a relatively high thermal conductivity at room temperature ($\sim 42\,\mathrm{W/m{\cdot}K}$) that strongly decreases for higher temperatures. This way, only a negligible amount of heat gets lost in the sapphire disk. It was already shown in previous experiments that this is an adequate material for this purpose [SHMR98].

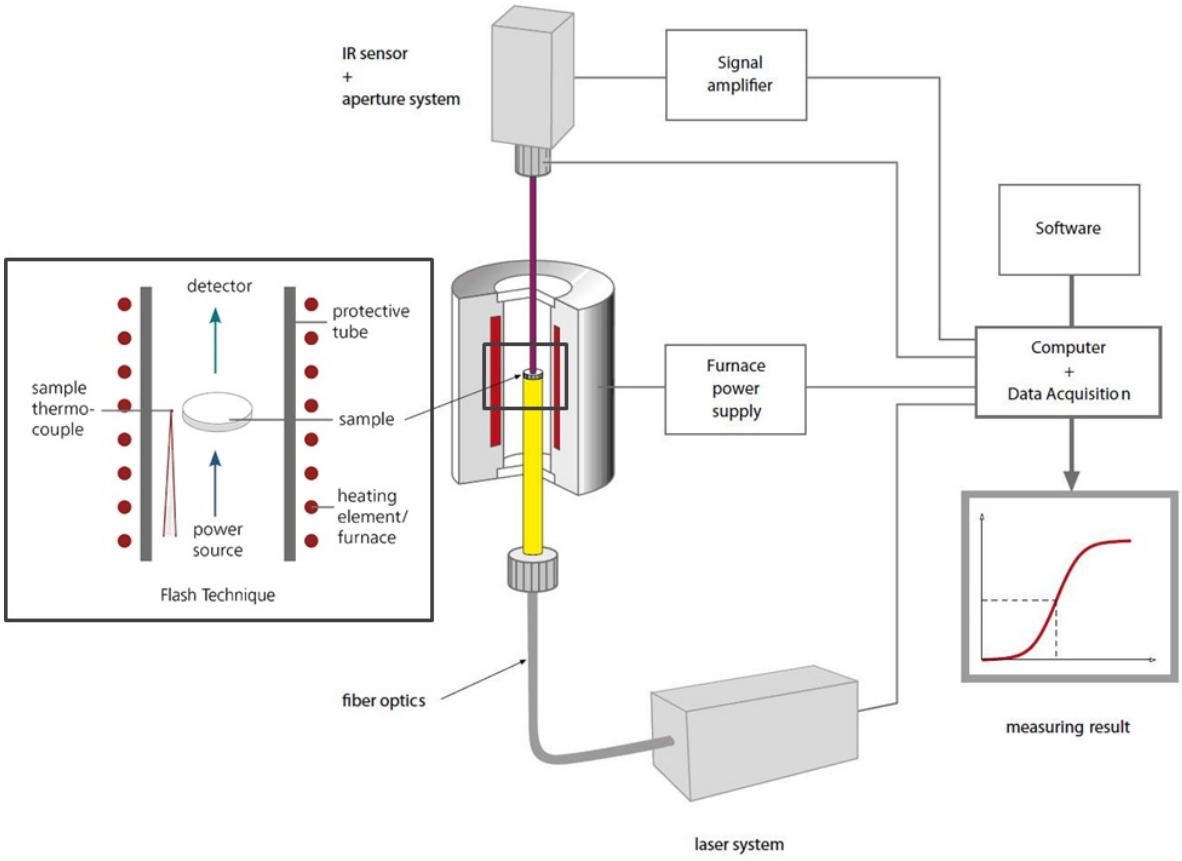


***Figure 4.1:*** *Scematic setup of a typical Laser Flash Apparatus [NG14c, NG14a].*

### 4.1.2 Measurement Procedure

The thermal diffusivity was measured over a temperature range from 25 °C to 350 °C in steps of 50 °C. Usually 5 laser shots were performed for each temperature step during the heating cycle and then another 5 per temperature step during the cooling cycle. This way, it is possible to look for hysteresis effects, e.g. if the heating induced changes in the material which would lead to a derivation of the thermal diffusivity values from the heating cycle (i.e. phase transition or degasing).
In case of the in-pile irradiated samples, the temperature program was modified, i.e. divided into two cycles, a low and a high temperature cycle. The low temperature cycle is ramped from room temperature to normal reactor operation temperature which is up to 125 °C for dispersion and up to 150 °C for monolithic fuel and back again to room temperature in intervals with 5 measurements per temperature step on the up- and down-ramp. It is safe to heat the samples up to these temperatures as during the irradiation the samples were exposed to similar temperatures inside the reactor without failure, like for example delamination, that would lead to a loss of the sample and valuable data points of the down-ramp. For the high temperature cycle, the sample is then heated in one step from room temperature to 150 °C, subsequent to the maximum temperature of the low temperature cycle and then again stepwise to up to 300 °C with again 5 measurements per temperature step on the up- and down-ramp.
Figure 4.2 shows an idealized plot of the different temperature programs. In real, the time for equilibrating the sample temperature between the measurements can take several minutes and delays the measurement.

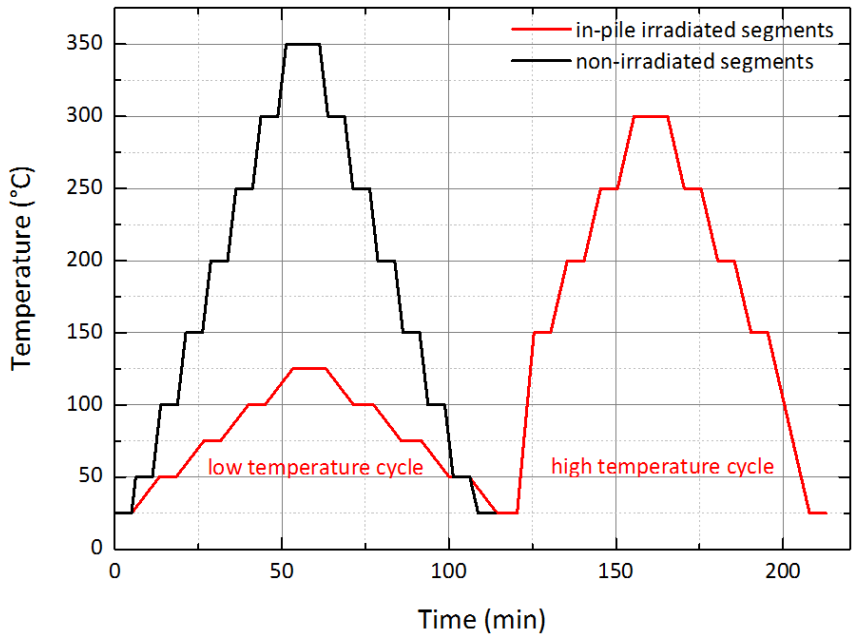


***Figure 4.2:*** *Plot of the different temperature programs. The in-pile irradiated temperature profile is an example for the measurement of a dispersion segment.*

### 4.1.3 Data Analysis

Each laser shot needs to be evaluated separately. The raw data can therefore be extracted from the Netzsch software as a .csv file. The header contains the main instrument and laser parameters, like e.g. the shot length and power, and sample temperature at the moment of the shot. The main file contains a list of time in [ms] and according sample temperature on the rear surface in [V], the unit of the detector. It is not necessary to convert voltage into °C, as only the relative temperature is relevant. In principle, LFA would be capable to also determine the specific heat of the sample, if the absolute temperatures and the integral absorbed power were known. As especially the latter is very difficult to determine and the specific heat capacity can easily be measured separately, it is sufficient to use relative temperatures.
This data list is imported into a software named "ThermoProp". This software is programmed by H. Breitkreutz and C. Reiter to execute the TUM model (Chapter 3.4.1 with the imported temperature curve.
First, the general sample description needs to be entered in the software. The number of layers of the material and their thickness, density and specific heat capacity need to be set. Besides, the thermal diffusivities of all layers, except the layer that is to be investigated, need to be set as well. As the LFA is sensitive to the order of the layers, in principle, it would be possible to determine the thermal diffusivities of several layers at the same time. However, such a determination needs extremely high quality signals that are not obtainable with today's hardware.
As soon as all parameters are set, the data fitting can be started.

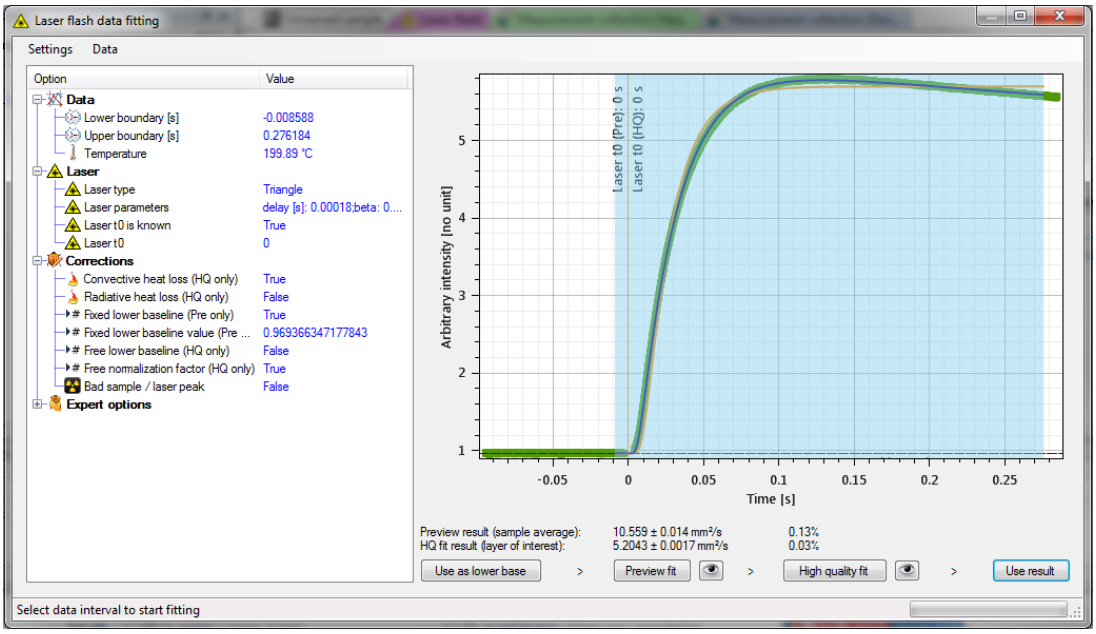


***Figure 4.3:*** *ThermoProp LFA module interface with settings.*

Figure 4.3 shows the interface of the fitting software. On the left side, the fitting parameters can be adjusted. The lower and upper baseline is automatically calculated. The temperature is the measurement temperature of the sample and is read from the input file during import. Further, the laser parameters can be adjusted manually. The correct pulse shape improves the result of the fit significantly. Each laser has its own characteristic pulse shape, see Figure 4.4, which needs to be determined for each laser separately, see the next paragraph. Finally, the user

can choose, if convective and radiative heat losses are considered in the fit. In the expert mode, parameters of the fitting algorithm can be changed. However, changing expert parameters might lead to systematically wrong results. Therefore, the standard parameter set was used.

The laser pulse shape differs between the LFA instruments. In Figure 4.4 the pulse shapes of the two instruments used for the measurements are shown. Their laser pulse shape varies and therefore needs different fitting functions.
The pulse shape for LFA 457, can be approximated by a triangle. The fitting function $f_{457}(t)$ is called piecewise, as it is composed of two straights.

$$f_{457}(t) = \begin{cases} 0 & \text{for } t < t_0, \\ A \cdot \frac{t-t_0}{\beta\cdot\tau} \cdot \frac{2}{\tau} & \text{for } t < (\beta \cdot \tau + t_0), \\ A \cdot \frac{\tau-(t-t_0)}{\tau-\beta\cdot\tau} \cdot \frac{2}{\tau} & \text{for } t < (\tau + t_0), \\ 0 & \text{for } t > (\tau + t_0). \end{cases} \tag{4.1}$$

$A$ is the amplitude and $\frac{2}{\tau}$ a normalization, so that $\int_{t_0}^{\tau} f_{457}(t) = 1$.

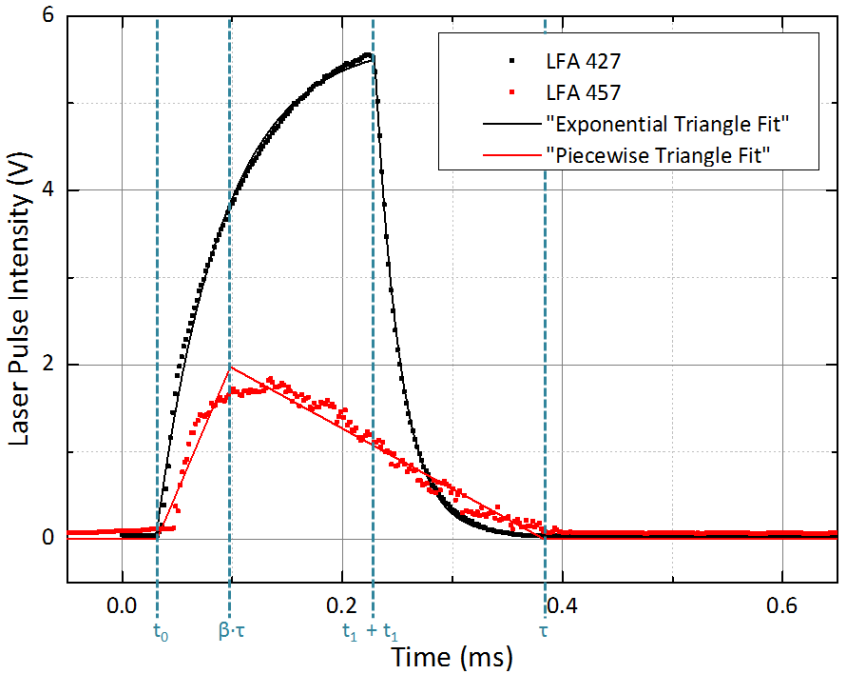


***Figure 4.4:*** *Shape of the laser shot of the two LFA instruments used for the measurement of the thermal diffusivity. LFA 427 was used for the measurement of fresh fuel, LFA 457 was installed in the hot cell for irradiated fuels.*

The pulse shape for LFA 427 cannot be accurately fitted by a triangle of two straights. There, a merged rising and a falling exponential function provide the best fit. The complete triangle function $f_{427}(t)$ is called "Exponential Triangle".

$$f_{427}(t) = \begin{cases} 0 & \text{for } t < t_0, \\ B \cdot \exp\left(\frac{t-t_0}{x_1}\right) - B & \text{for } t < (t_0 + t_1), \\ \left(B \cdot \exp\left(\frac{t_1}{x_1}\right) - B\right) \cdot \exp\left(\frac{t-(t_0+t_1)}{x_2}\right) & \text{for } t > (t_0 + t_1). \end{cases} \tag{4.2}$$

$B$ is the amplitude, $x_1$ rise factor and $x_2$ decay factor of the exponential functions.

The fit was executed with Origin 9.1 for several laser pulses of each LFA instrument. Table 4.1 shows the resulting parameters for each laser:

| LFA instrument | Parameter | Value | Comment |
|---|---|---|---|
| LFA 457 | $t_0$ | 0.032 | delay [s] |
| | $\beta$ | 0.189 | |
| | $\tau$ | 0.352 | pulse length [s] |
| | $A$ | 0.345 | Amplitude [V] |
| LFA 427 | $t_0$ | $3.0 \cdot 10^{-5}$ | delay [s] |
| | $t_1$ | $2.0 \cdot 10^{-4}$ | turnaround [s] |
| | $B$ | $-5.4$ | amplitude V |
| | $x_1$ | $-5.7 \cdot 10^{-5}$ | rise factor [s] |
| | $x_2$ | $2.3 \cdot 10^{-5}$ | decay factor [s] |

***Table 4.1:*** *Parameters for the laser shape of LFA instrument 457 and 427.*

Once all parameters are set, the temperature curve can be evaluated. The preview fit, fits the Parker Model, described in Chapter 3.4.1, on the data. It is not as accurate as the numeric fit (the TUM Model), but provides start values for the numeric or as in the software called "high quality fit", which reduces its computing time and improves stability of the algorithm.
The software finally calculates the thermal diffusivity, plus the uncertainty, $R^2$, adjusted $R^2$ and the residuals of the fit, as well as the covariance and correlation matrix of the fitting parameters. All these parameters can be exported as .csv file.

Finally, the thermal diffusivities of all temperature curves over the entire temperature interval, usually 25 °C to 350 °C, are evaluated and plotted in Origin 9.1, see Figure 4.5. The uncertainty of the data points are a Gaussian Error Propagation of the uncertainty of the ThermoProp fit and a 10 % layer thickness uncertainty, as ThermoProp does not yet evaluate the influence of the uncertainties of the data (density, specific heat capacity etc.) that it uses during the fitting process. These data points are then fitted with a polynomial function of third degree, weighted with the uncertainty of the data points.

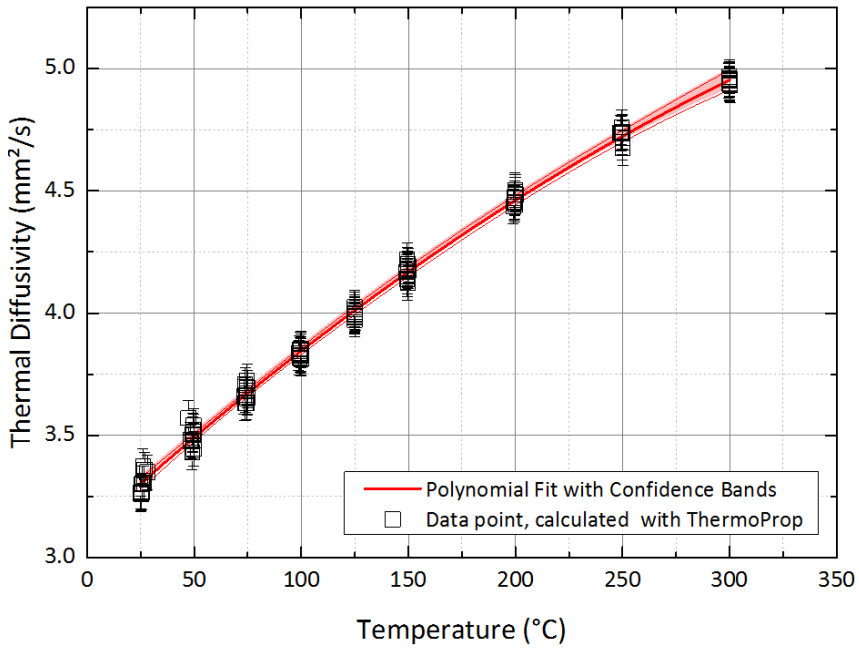


***Figure 4.5:*** *Result of an entire LFA measurement from* 25 °C *to* 300 °C*. The material is irradiated dispersion fuel with cladding. It was evaluated as a three layer composite. The black data points are the results from the high quality fits of the single temperature curves using ThermoProp. The red line is a polynomial fit of third degree together with its* 95 % *confidence interval.*

## 4.2 Differential Scanning Calorimetry

### 4.2.1 Instrument

In general, the specific heat was measured using a power-compensating Differential Scanning Calorimeter (DSC) type DSC8500, for the as-fabricated fuel segments at TUM, and type DSC1000, for the in-pile irradiated dispersion and monolithic fuel segments in the hot cell at PNNL, both produced by PERKIN ELMER with the same operating principle.
For the measurement of the as-fabricated AFIP-1 fuel segment at INL, a heat flux DSC type 404C produced by Netzsch has been used with a different operating principle that will not be discussed here, as only one sample was measured with this method. The method is well described in [HHF96]. The measurement of calibration standards yielded the same results as the power-compensating DSC and therefore the measurements are well comparable.

The DSC consists of two identical crucibles to which the same amount of heat is applied, see Figure 4.6. The different heat capacities of the materials inside the crucibles lead to a temperature difference, which is measured with a sensor on the bottom of the crucibles. To compensate this temperature difference, an additional amount of heat is applied to the cooler crucible. The resulting heat flux can be measured and is proportional to the heat capacity of the tested material. Both crucibles are connected to a cold head that constantly holds a temperature of −120°C. This leads to a stabilization of the measurement temperature, it guarantees a measurable positive heat flux even at constant measurement temperatures and it leads to very fast cooling rates (about 100 °C/min). But due to this low temperature, water condensates on the cold surfaces of the housing and forms thick layers of ice. To avoid this, the housing is purged with Nitrogen at a

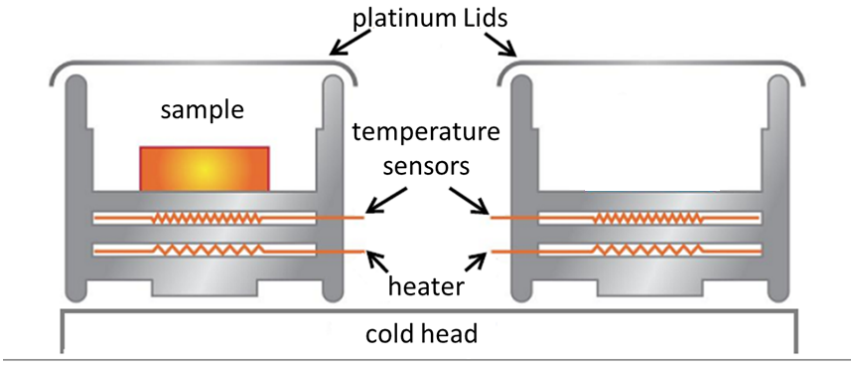


***Figure 4.6:*** *Schematic setup of the DSC instrument with a sample in one crucible. Two crucibles are mounted on a coldhead. Each crucible has its own heating element and temperature sensor for a separated regulation. Platinum lids cover each crucible.*

flow rate of 40 $^{ml}/_{min}$. The gas purges for example dust out of the crucibles, which influences the curvature of the heat flow, e.g. in the shape of peaks. But too high flow rates potentially move the light empty Al pans in the crucibles and therefore can falsify the measurement. Further the purging gas reduces the oxidation of the sample. As Uranium is a very reactive material, this is an important issue, especially at high temperatures.
The selection of the purging gas depends mainly on the measurement temperatures. For measurements below the condensation temperature of Nitrogen, Helium needs to be used. But in general Nitrogen is advantageous, as it is cost-efficient, compared to for example other noble gases like Argon, and it has a low thermal conductivity. Gases with a high thermal conductivity transfer the heat out of the crucibles too fast, which influences the measurement significantly especially at high temperatures.

The crucibles as well as their lids are fabricated from Platinum. The lids have two holes so that the crucibles are flooded with the purging gas, see Figure 4.7. It is mandatory to place these lids as accurately as possible on the same location for each measurement. Otherwise, there is a slight difference in the gas flow, which has a rather high impact on the heat flow. Marks on the lids and the crucibles are helpful for the alignment, see Figure 4.8.

***Figure 4.7:*** *Platinum lids with two holes to flood the crucibles with purging gas [Rei13].*

***Figure 4.8:*** *The red marks show how the lids are engraved for better alignment [Rei13].*

### 4.2.2 Operation

Before starting a measurement, the temperature and heat flux of the DSC need to be calibrated. This standard procedure is specified by the manufacturer PERKIN ELMER based on the melting points and melting enthalpies of Indium, Tin and Lead.
Figure 4.9 shows a calibration with Indium (In). The Indium is placed in an Al pan into one crucible. The other crucible only contains an empty Al pan. The melting point of In is 156.6 °C, so a temperature ramp from 120 °C to 180 °C with 70 °C/min is applied to the crucibles. At 156.6 °C the In melts and creates a peak in the heat flow over temperature diagram in Figure 4.9 due to the energy release during phase transition and its associated enthalpy. With the software, the onset of the peak can be determined, which is not necessarily to be found exactly at 156.6 °C for a non-calibrated instrument. But it is possible to correct this in the software via the calibration tool. The area under the peak is equivalent to the melting enthalpy, which is 28.45 J/g for In. Also this parameter can be adjusted in the software.

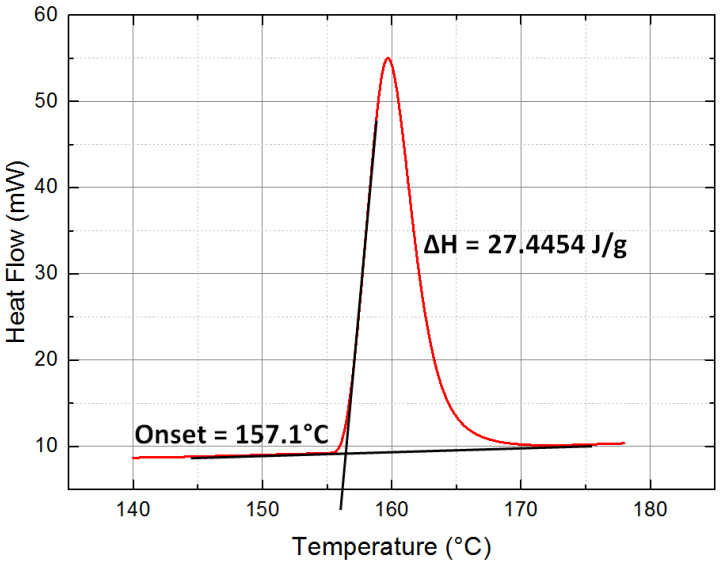


***Figure 4.9:*** *Heat flux diagram of a calibration with with Indium. The peak should start at* 156.6 °C *and the area under the peak should result in an enthalpy* $\Delta H$ *of* 28.5 J/g *for a calibrated DSC. So, for the measurement shown above, the values need to be adjusted in the software.*

This procedure is repeated also for Tin (melting point: 231.9 °C and melting enthalpy: 60.5 J/g) and Lead (melting point: 327.5 °C and melting enthalpy: 23.0 J/g) to calibrate the temperature and heat flux over a temperature range from 0 °C to 370 °C, which is the temperature range used for the experiments.

The basic measurement procedure consists in principle of 3 steps, see Figure 4.10:

1. Baseline measurement
2. Reference measurement
3. Sample measurement

Each step includes the use of Al pans inside the crucibles. These pans are necessary to contain the samples and therefore avoid a contamination of the crucibles.

Further, each step has the same temperature profile, which is defined by temperature cycles with certain heating and cooling rates.

The heating rate depends on the sample material and its characteristics, i.e. its specific heat $c_p$ and mass m. For the as-fabricated and annealed fuel with an expected specific heat between $0.2\,^{J}/_{gK}$ and $0.4\,^{J}/_{gK}$ and a typical sample mass between 20 mg and 50 mg, a heating rate of $70\,^{\circ C}/_{min}$ is chosen. For the measurements of the in-pile irradiated samples, performed with another power-compensating DSC, a heating rate of only $40\,^{\circ C}/_{min}$ has been chosen.
The ideal heating rates can vary for different instruments and depend on the mass and specific heat capacity of the sample. Usually, the heating rate needs to be determined for each DSC separately. In general, a high heating rate ($\gtrsim 70\,^{\circ C}/_{min}$) is optimal for samples with a low specific heat capacity ($< 0.3\,^{J}/_{gK}$) and low mass ($< 25$ mg) and a rather low heating rate ($\lesssim 40\,^{\circ C}/_{min}$) is optimal for samples with a high specific heat capacity ($> 0.6\,^{J}/_{gK}$) and high mass ($> 75$ mg) [Rei13]. Heavy samples with high specific heat capacity cannot follow the temperature gradient immediately which leads to a smearing of the heat flow signal and introduces systematic deviations.

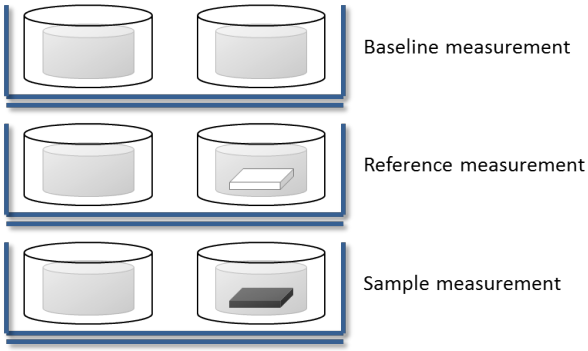


***Figure 4.10:*** *Pan configuration for baseline, reference and sample measurement.*

Baseline The first measurement is conducted with two empty Al pans in the crucibles. This measurement is finally used to compensate the structural induced difference between the crucibles as well as the mass difference of the Al pans.
This baseline is important for the quality of the measurement itself and should have an S-shaped flat curvature that needs to be adjusted with three parameters in the instrument software (Slope, Coarse Balance and Fine Balance) before starting the measurement.

Reference To correct the heat flux over the entire temperature range, a reference material is measured. The measured specific heat of the reference material is then compared to its literature values and serves as correction parameter in the calculation of the specific heat of the sample. Typically, a certified sapphire is used as reference material. For the measurement, the same Al pans are used in the same crucibles as for the baseline measurement, but one of the pans containing the sapphire. Using different Al pans leads to a slight change of the heat capacity and mass of the entire system and therefore affects the measurement.

Sample The same Al pan are used again. The sapphire is replaced by the material of interest.

### 4.2.3 Measurement Procedure

A typical measurement program begins with holding the start temperature for a few minutes to stabilize the instrument temperature. This part of the temperature curve is called start isothermal. Then the temperature is ramped to a higher temperature with a certain heating rate (see Chapter 4.2.2), while the differential heat flux between the two crucibles is measured. Finally the end temperature is held again for a few minutes for temperature stabilization, accordingly called end isothermal in the temperature curve.

For the measurements of the U-Mo fuel, a temperature range from 10 °C to maximal 350 °C is chosen. It covers general fuel handling, reactor operation and off-normal temperature excursions. As the Uranium starts to chemically react with the aluminum matrix (see Chapter 2.1) at temperatures above 400 °C within a few hours, the measurement temperature should not exceed this limit. It is advisable to set the upper limit for the measurement temperature to 370 °C to have a safety margin, in case there is a malfunction of the instrument at the highest temperature.

This wide temperature range cannot be measured in one step due to the behavior of the start and end isothermal. Theoretically these two curves of constant temperature should have the same heat flux value. But due to the inertia of the entire system, the position of the two curves deviates. This deviation was systematically examined [Rei13]. Temperature cycles from 10 °C to 400 °C with two empty Al pans in the crucibles were run, starting at 10 °C to 20 °C and then holding the temperature between two cycles for several minutes. The end temperature of each cycle was steadily increased by 10 °C, while the start temperature was fixed at 10 °C. This resulted in 39 intervals: 10 °C - 20 °C, 10 °C - 30 °C, . . . , 10 °C - 400 °C.
The red dotted upwards bended line in Figure 4.11 represents the position of the isothermals over the entire temperature range from 10 °C to 400 °C. Theoretically, they should be in one straight constant line. But by reducing the temperature intervals to 100 °C, the deviation can be approximated by a linear trend line as shown in Figure 4.12. So, the temperature interval between two isothermals may not exceed 100 °C.

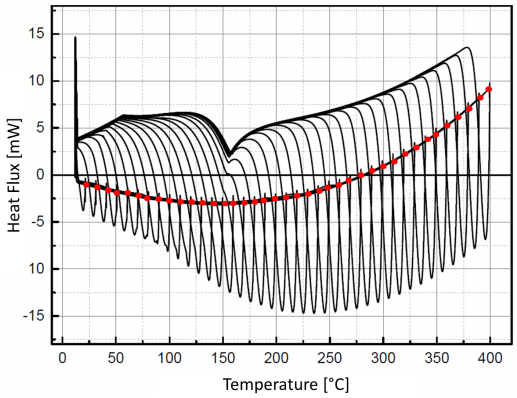


***Figure 4.11:*** *The test of isothermal behavior by running* 39 *temperature intervals from* 10 °C *to* 400 °C *with empty Al pans, constantly starting at* 10 °C *but increasing the end temperature for each cycle by* 10 °C *[Rei13].*

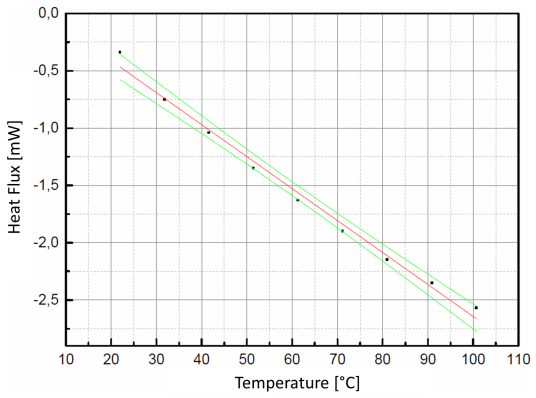


***Figure 4.12:*** *Plot of the position of the isothermals from* 20 °C *to* 100 °C *[Rei13]. The red line is a linear regression to the measured isothermal positions. The green line are the* 95% *upper and lower confidence bands.*

Finally considering all these impacts the measurement program was defined as shown in Figure 4.13.

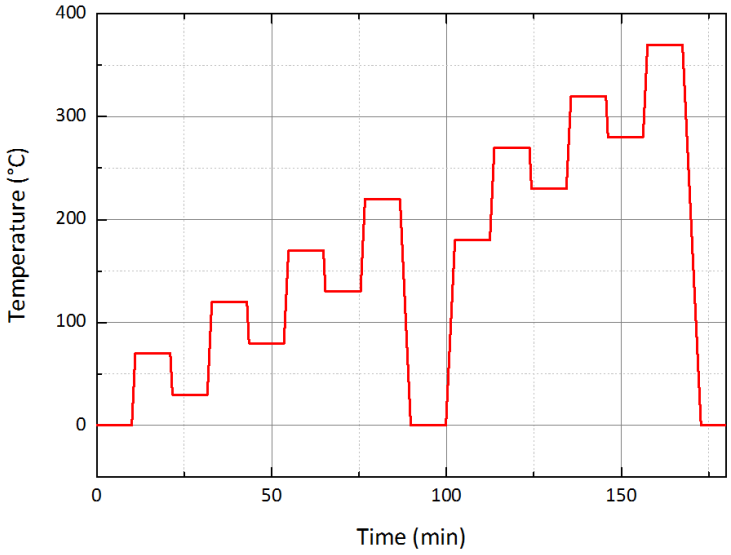


***Figure 4.13:*** *Final measurement program.*

After the forth cycle, the DSC is cooled down to 0 °C again. This is advised by the manufacturer PERKIN ELMER. They do not mention a precise reason, but it turns out that this cooling stabilizes the measurements at higher temperatures. Hysteresis effects are very possible to play a role in this behavior.
Further the single temperature intervals are chosen to be overlapping. The system of DSC and sample has a certain inertia, so that the temperature of the system cannot immediately follow the temperature gradient that is forced by the furnace. This leads to fluctuations of the heat flux at the beginning of each temperature range. This impacts roughly the first 20 °C of each cycle. To obtain a sufficient amount of data points, an overlap of 40 °C is chosen.

### 4.2.4 Data-Analysis

The measurements of the baseline, reference material and sample result in three separate heat flow curves in the shape of Figure 4.14 and 4.15.

The software ThermoProp that was used to evaluate the thermal diffusivity measurements is in principle also capable to evaluate DSC data, but was not completely developed at the time of the analysis of the data for this work. Yet, the new code is based on the previous software DSC8500CP that has also been developed by C. Reiter for the analysis of power compensating DSC measurements [Rei13] with some improvements in the calcuation of the uncertainty and usability. Both programs calculate the specific heat capacity depending on the temperature from the baseline, sapphire and sample measurement, including all necessary corrections.

In the first step, the program cuts the entire heat flow over time curve, as shown in Figure 4.14, into the different temperature cycles. Each cycle includes the temperature ramp and its start and end isothermal, see Figure 4.17 and 4.18. This needs to be done for all temperature cycles. So, the cutting points can be set manually as a list and be loaded into the software. The interface of the software can be seen in Figure 4.16. Then the raw data file can be loaded as well and

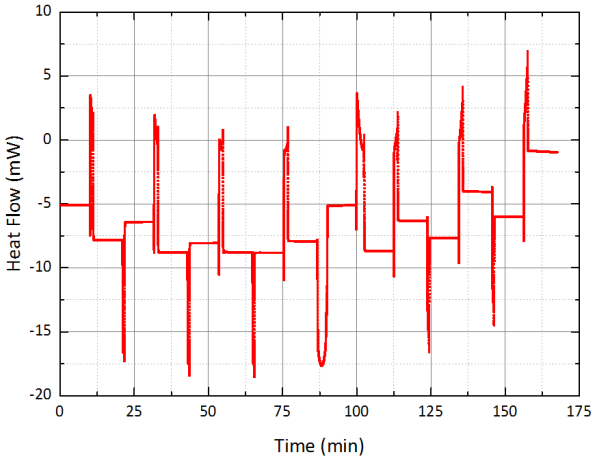


***Figure 4.14:*** *Diagram of the heat flow over the measurement time of a baseline measurement according to the measurement program from Figure 4.13.*

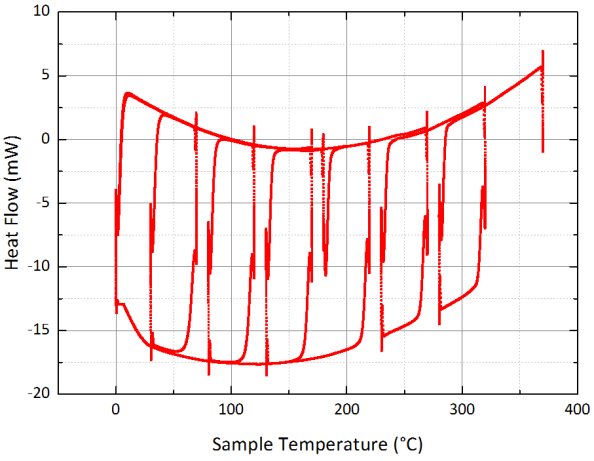


***Figure 4.15:*** *Diagram of the heat flow over the sample temperature of a baseline measurement. The temperature can be converted from time by multiplying with the heating rate, which is* $70\,^{\circ\mathrm{C}}/_{\mathrm{min}}$

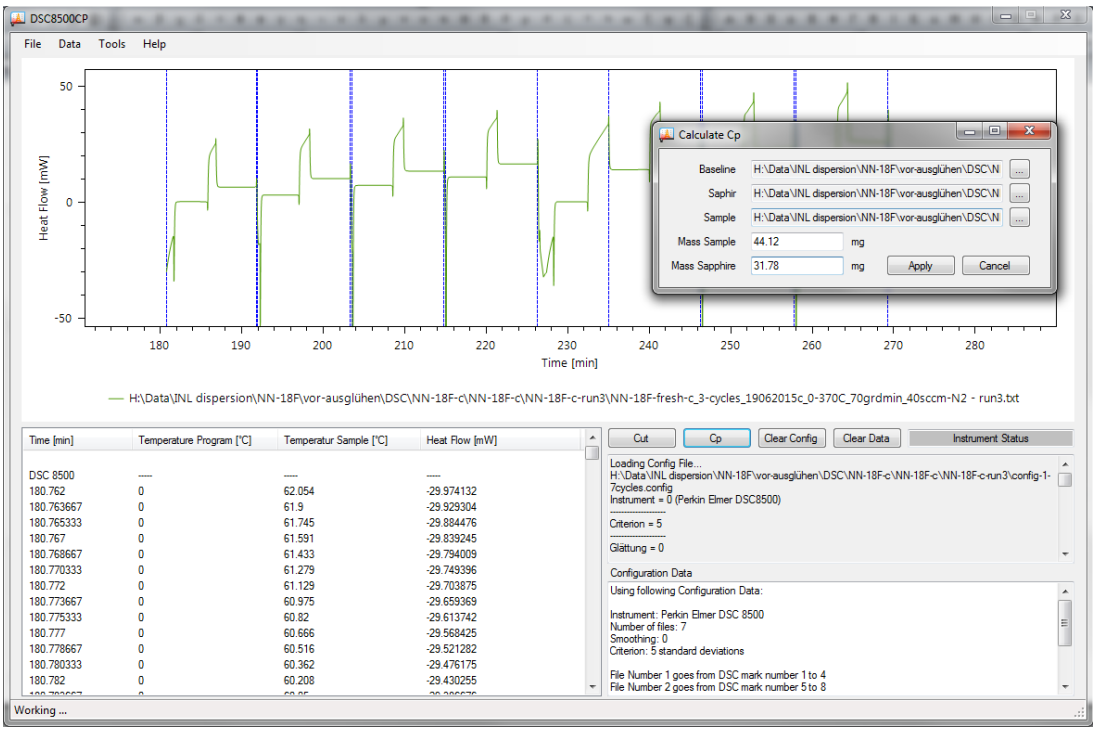


***Figure 4.16:*** *The interface of DSC8500CP for the analysis of DSC measurements.*

by pushing the button “cut”, the software separates the temperature cycles and stores them in separate files. This has to be done for the raw data files of the baseline, reference and sample measurement.

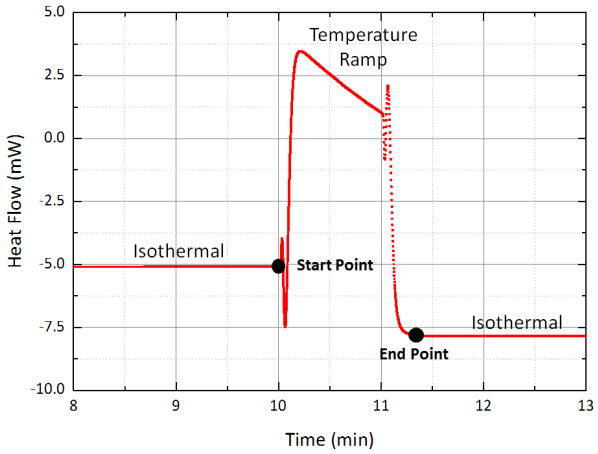


***Figure 4.17:*** *Diagram of the heat flow over the measurement time of a baseline measurement according to the measurement program from Figure 4.13.*

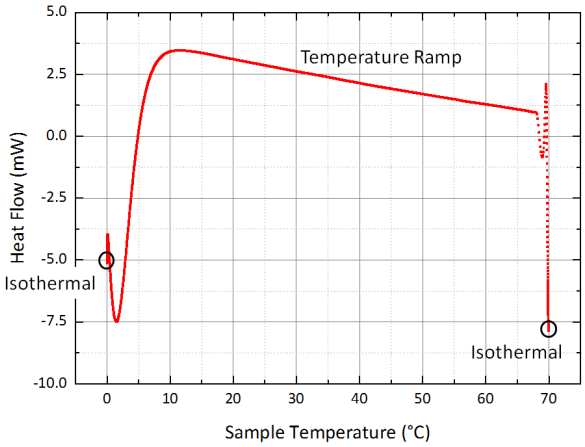


***Figure 4.18:*** *Diagram of the heat flow over the sample temperature of a baseline measurement. The temperature can be converted from time by multiplying with the heating rate, which is* $70\,^{\circ\mathrm{C}}/_{\mathrm{min}}$

Then, the button “Cp” can be selected and the window “Calculate Cp” (right upper edge in Figure 4.16) pops up. There, the baseline, reference and sample files can be uploaded and the masses of the sample and reference material used in the measurement need to be inserted. By clicking on “Apply” the software calculates the specific heat capacity for each temperature cycle from the cut files, including the isothermal correction, which has already been discussed before in Chapter 4.2.3.

At first, the isothermal correction is applied. Therefore the average heat flow of the start and end isothermal is calculated and then the end point of the start isothermal and start point of the end isothermal (see Figure 4.17) is determined. Therefore, the software scans the isothermal in direction to the temperature ramp until the data points start to deviate for a certain interval from the isothermal, which is the start or end point. A deviation interval of $4\sigma$ was found to be a good value. A straight line is calculated from these two points and subtracted from the temperature ramp, see Figure 4.19.

The isothermal correction is applied on all temperature cycles of all three measurements. From these corrected temperature cycles, the specific heat capacity can be calculated as shown in the following.

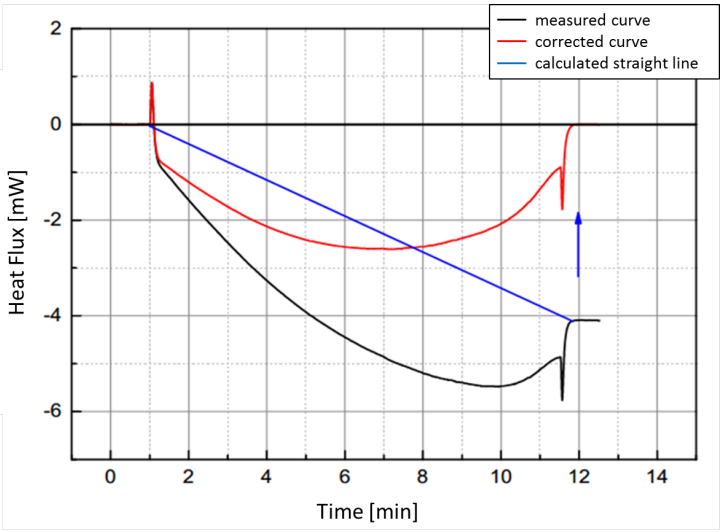


***Figure 4.19:*** *Graphic example for an isothermal correction [Rei13].*

The specific heat capacity $c_\mathrm{p}$ is the amount of heat $\mathrm{d}Q$ that needs to be added per mass $m$ of a body to heat it up a certain temperature interval $\mathrm{d}T$.

$$c_\mathrm{p} = \frac{\mathrm{d}Q}{m \cdot \mathrm{d}T} \tag{4.3}$$

The derivative with respect to time $t$ leads to:

$$c_\mathrm{p}(T) = \frac{\mathrm{d}Q/\mathrm{d}t}{m \cdot \mathrm{d}T/\mathrm{d}t}, \tag{4.4}$$

with $\phi = \mathrm{d}Q/\mathrm{d}t$ being the power that is needed to heat the sample to gain a temperature change of $\mathrm{d}T$ in the time interval $\mathrm{d}t$, which can be described as a heating rate $\beta$. Applying this expression to the DSC measurements, $\phi$ is the measured heat flux, $\beta = \mathrm{d}T/\mathrm{d}t$ the preset heating rate and m the sample mass. Due to the intrinsic heat capacity of the instrument, the heat flux $\phi_\mathrm{b}$ from the measurement of the baseline has to be subtracted from the heat flux $\phi_\mathrm{s}$ of the sample.

$$c_\mathrm{p}(T) = \frac{\phi_\mathrm{s} - \phi_\mathrm{b}}{\beta\, m} \tag{4.5}$$

In Equation 4.5 $\beta$ can be eliminated by using the calibration measurement with the reference material to improve the precision of the measurement:

$$\beta = \frac{\phi_\mathrm{r} - \phi_\mathrm{b}}{m_\mathrm{r} \cdot c_\mathrm{r}\,(T)}, \tag{4.6}$$

$$c_\mathrm{p}(T) = \frac{\phi_\mathrm{s} - \phi_\mathrm{b}}{\phi_\mathrm{r} - \phi_\mathrm{b}} \frac{m_\mathrm{r}}{m_\mathrm{s}} c_\mathrm{r}\,(T)\,, \tag{4.7}$$

with $\phi_\mathrm{r}$ the heat flux of the reference measurement, $m_\mathrm{r}$ the mass of the used certified reference sample and $c_\mathrm{r}$ its specific heat.

The software stores the resulting specific heat over time curves for the different temperature cycles in separate files, one for each cycle. In Figure 4.17 for example can be seen that the electronic produces peaks and spikes at the transitions between the isothermals and the temperature ramp. As the temperature cycles are chosen to be overlapping, it is useful to cut the curves, so that only the smooth part of the specific heat curves remains. This can also be done with the software by selecting "Adjust" in "Tool" in the tool bar in the main window. Another separate window pops up, where the calculated files can be loaded and cut, see Figure 4.20. The red and blue dotted lines can be moved and are used to select the cutting points.

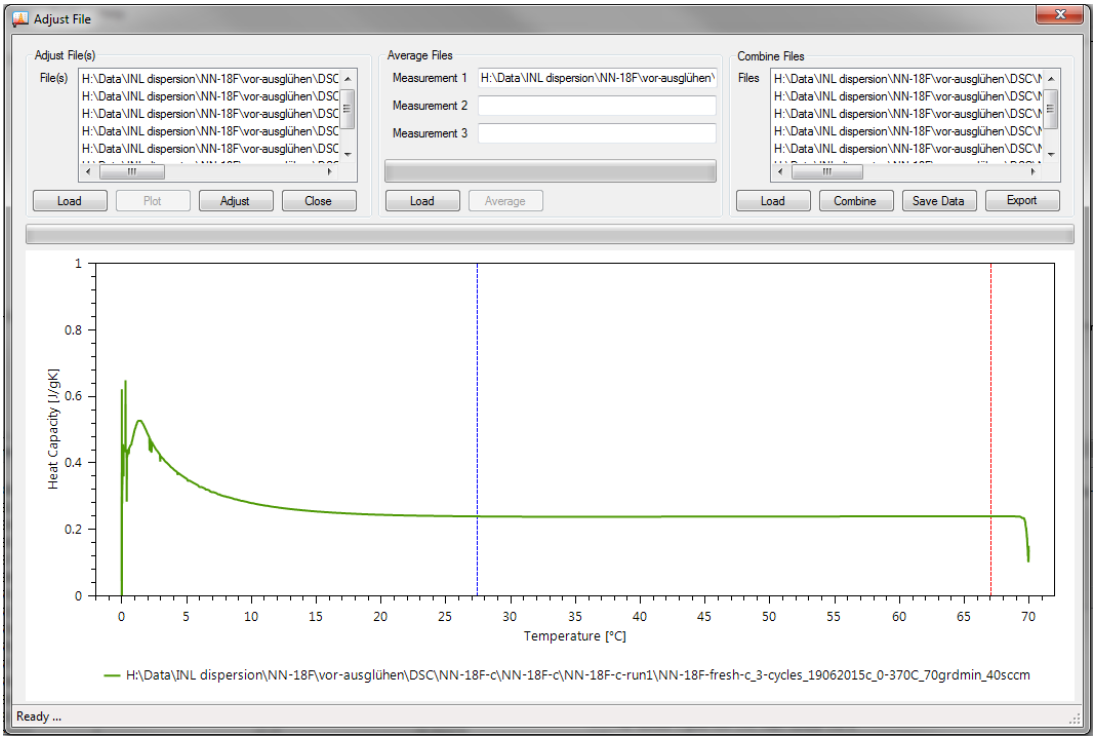


***Figure 4.20:*** *Interface to cut the evaluated data curves.*

In Figure 4.21, a sample has been measured five times (run 1 to 5). The curves are well conform to one another. This indicates the good performance of the instrument. Regarding statistics, the more data points and the more they are conform with one other, the lower is the statistical

error. Five measurements proved to be a good number, especially in the case one fails, there are enough others left for a good analysis.
For each fuel type, three samples have been prepared, because the fuel samples are very small ($\sim (3 \times 4 \times 0.5)$ mm$^3$) and the dispersion fuel can have inhomogeneous areas, where the fraction of fuel to matrix material deviated from the average. Figure 4.22 shows the results of three samples of the same fuel type, each type measured five times. The deviation of the curves indicate the homogeneity of the samples.
At least the three data curves (each data curve containing the five runs) are fitted with a polynomial function of third degree with the fitting parameters $A$, $B$, $C$ and $D$ to obtain a function for the specific heat capacity of the specific analyzed fuel. The 95% confidence bands are included in the plot, but due to the big amount of data points, they are so close to the fitted curve that they cannot be separated from it.

$$c_\mathrm{p}(T) = A + B \cdot T + C \cdot T^2 + D \cdot T^3 \tag{4.8}$$

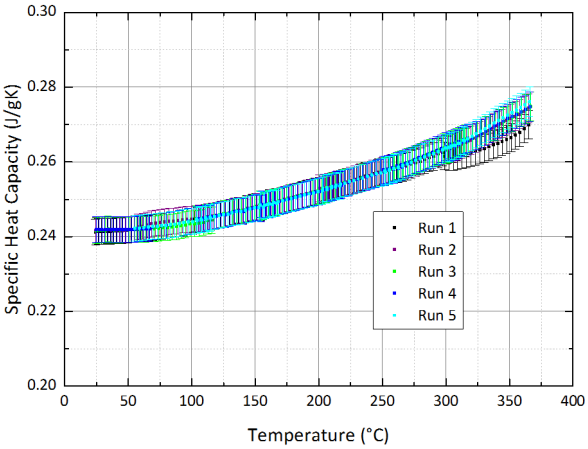


***Figure 4.21:*** *Diagram with the results of one dispersion fuel sample that has been measured five times (run1 to 5).*

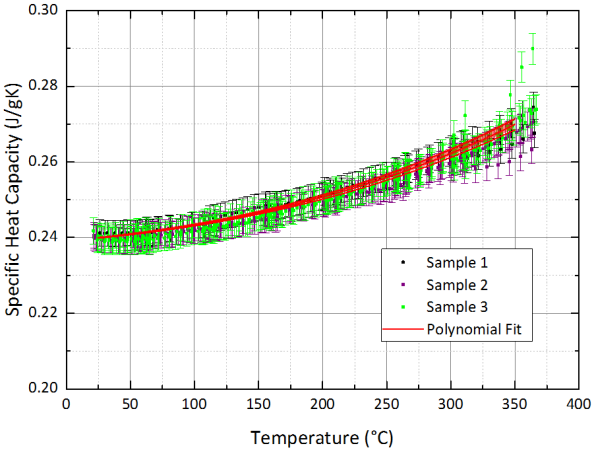


***Figure 4.22:*** *Diagram with the results of three samples of the same dispersion fuel. Each sample has been measured five times.*

The software DSC8500CP also considers and calculates uncertainties. In the following, a short summary of the uncertainties that need to be considered, is given. More details on the calculation can be found in [Rei13].

Temperature The uncertainty of the temperature $\Delta T$ consists of the uncertainty of the instrument $\Delta T_\mathrm{i}$ and the standard deviation of the temperature between the three data curves $\Delta T_\mathrm{d}$. Although the three curves are measured with the same temperature program, there is a marginal shift of a few ms. The total uncertainty of the temperature is calculated with Gaussian Error Propagation.

$$\Delta T = \sqrt{(\Delta T_\mathrm{i})^2 + (\Delta T_\mathrm{d})^2} \tag{4.9}$$

Heat Flow The uncertainty of the heat flow $\Delta\phi$ consists of the uncertainty of the instrument $\Delta\phi_\mathrm{i}$ and from the correction of the isothermals in the analysis $\Delta\phi_\mathrm{c}$. There, the straight line that is subtracted from the temperature ramp has an uncertainty, which goes into the uncertainty of the corrected heat flow of the temperature ramp. Again, both uncertainties are added with Gaussian Error Propagation.

$$\Delta\phi = \sqrt{(\Delta\phi_\mathrm{i})^2 + (\Delta\phi_\mathrm{c})^2} \tag{4.10}$$

Specific Heat Capacity The uncertainty of the heat fluxes has already been discussed above, but it is to mention that for each, the sample and the reference measurement, the heat flux of the baseline $\phi_\mathrm{b}$ is subtracted and therefore, needs to be considered in the error propagation.

$$\phi_\mathrm{(s,r-b)} := \phi_\mathrm{(s,r)} - \phi_\mathrm{b} \tag{4.11}$$

$$\Delta\phi_\mathrm{(s,r-b)} = \sqrt{\left(\Delta\phi_\mathrm{(s,r)}\right)^2 - (\Delta\phi_\mathrm{b})^2} \tag{4.12}$$

The uncertainty of the masses depend on the uncertainty of the balance and the uncertainty of the reference material. The latter can be neglected as this value is a literature value with in general negligible low uncertainty.

Regarding Equation 4.7, the uncertainty of the specific heat capacity $c_\mathrm{p}$ depends on the uncertainty of the heat flux of the sample $\Delta\phi_\mathrm{(s-b)}$ and reference $\Delta\phi_\mathrm{(s-b)}$ measurement, the masses of the sample $\Delta m_\mathrm{s}$ and reference $\Delta m_\mathrm{r}$ material and the specific heat capacity of the reference material $\Delta c_\mathrm{r}$.

$$\Delta c_\mathrm{p} = c_\mathrm{p} \cdot \sqrt{\left(\frac{\Delta\phi_\mathrm{(s-b)}}{\phi_\mathrm{(s-b)}}\right)^2 + \left(\frac{\Delta\phi_\mathrm{(r-b)}}{\phi_\mathrm{(r-b)}}\right)^2 + \left(\frac{\Delta m_\mathrm{s}}{m_\mathrm{s}}\right)^2 + \left(\frac{\Delta m_\mathrm{r}}{m_\mathrm{r}}\right)^2 + \left(\frac{\Delta c_\mathrm{r}}{c_\mathrm{r}}\right)^2} \tag{4.13}$$

## 4.3 Density Measurement

There are two different techniques to measure the material's density: Immersion Method and Pycnometry. For the Immersion Method Archimedes' Principle is used, while Pycnometry is based on Boyle's law. In the following, the two methods are described in detail.

### 4.3.1 Immersion Method

The measurement of the density via Archimedes' Principle is based on the balance of forces of a body in air or liquid. The total force $\boldsymbol{F}$ that affects a body in a medium is the weight $\boldsymbol{G}$ and the buoyancy $\boldsymbol{F}_{\mathbf{buoy}}$. In general, the absolute value $F$ of the force on the body is:

$$F = G - F_{\mathrm{buoy}} = mg - g\rho_{\mathrm{M}}V_{\mathrm{b}} \tag{4.14}$$

$\rho_{\mathrm{M}}$ is the density of the medium, $V_{\mathrm{b}}$ the body's volume and $g$ the gravitational acceleration. The density is given by the ratio of the body's mass $m$ and volume $V$:

$$\rho_{\mathrm{b}} = \frac{m_{\mathrm{b}}}{V_{\mathrm{b}}} \tag{4.15}$$

So, Equation 4.14 can be written as:

$$m_{\mathrm{M}} = \frac{F}{g} = V_{\mathrm{b}}\left(\rho_{\mathrm{b}} - \rho_{\mathrm{M}}\right), \tag{4.16}$$

with $\rho_{\mathrm{b}}$ being the body's density. The ration $\frac{F}{g}$ is equivalent to an apparent immersed weight $m_{\mathrm{M}}$ that a balance indicates, when the body is immersed in medium $M$.
The determination of a body's volume is in general rather difficult due to complex geometries. Therefore it is possible to eliminate it by weighing the body in two different media ($M$,1 and $M$,2). This results in two equations:

$$m_{\mathrm{M},1} = \frac{F}{g} = V_{\mathrm{b}}\left(\rho_{\mathrm{b}} - \rho_{\mathrm{M},1}\right) \tag{4.17}$$

$$m_{\mathrm{M},2} = \frac{F}{g} = V_{\mathrm{b}}\left(\rho_{\mathrm{b}} - \rho_{\mathrm{M},2}\right) \tag{4.18}$$

Equations 4.17 and 4.18 can be solved for the body's density $\rho_{\mathrm{b}}$:

$$\rho_{\mathrm{b}} = \frac{m_{\mathrm{M},1}\rho_{\mathrm{M},2} - m_{\mathrm{M},2}\rho_{\mathrm{M},1}}{m_{\mathrm{M},1} - m_{\mathrm{M},2}} \tag{4.19}$$

In general, the mass measured in air $m_{\mathrm{a}}$ is compared to the mass measured in liquid $m_{\mathrm{l}}$, which changes Equation 4.20 to:

$$\rho_{\mathrm{b}} = \frac{m_{\mathrm{a}}\rho_{\mathrm{l}} - m_{\mathrm{l}}\rho_{\mathrm{a}}}{m_{\mathrm{a}} - m_{\mathrm{l}}} \tag{4.20}$$

Figure 4.23 shows schematic the setup that is used to determine the mass of body in air and in liquid.

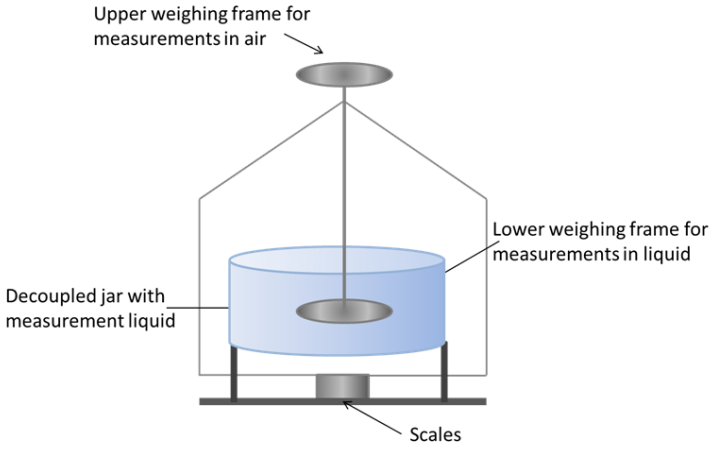


***Figure 4.23:*** *Setup for the measurement of the density using Archimedes' Principle.*

The setup consists of a upper and a lower weighing frame that are connected to scales. The upper weighing frame serves for the measurement in air, while the lower weighing frame is immersed in liquid that is in a jar that is decoupled from the scales. This way, the body's weight can be measured in liquid.

For the measurement, the sample is first weighed in air on the upper weighing frame and then in successively in three different liquids with known density (in this case: distilled water, Isopropanol and Ethanol) in the lower weighing frame. As the densities of the media are temperature dependent, a thermometer is placed in the jar to determined the temperature of the liquids, the air temperature is measured by the laboratory ventilation system.
By applying weight to the lower weighing frame, the supporting rods are further immersed into the liquid and receive further buoancy. So, Equation 4.20 has to be corrected by a factor $C = 0.99983$ that can be calculated from the geometry of the setup [A.G01].

$$\rho_b = \frac{m_\mathrm{a}\,(\rho_\mathrm{l} - \rho_\mathrm{a})}{C \cdot (m_\mathrm{a} - m_\mathrm{l})} + \rho_\mathrm{a} \tag{4.21}$$

As each sample is weighed in air, distilled water, Isopropanol and Ethanol, the density of each measurement in liquid is calculated in reference to the same sample measurement in air. Finally, the weighted average $\overline{\rho_\mathrm{b}}$ of the three densities ($\rho_\mathrm{i}$) is calculated.

$$\overline{\rho_\mathrm{b}} = \frac{\sum_{i=1}^{3} w_\mathrm{i} \cdot \rho_\mathrm{i}}{\sum_{i=1}^{3} \rho_\mathrm{i}} \tag{4.22}$$

The index $i$ stands for the three measurements in the different liquids.
The uncertainty $\Delta\overline{\rho_\mathrm{b}}$ of the weighted average is:

$$\Delta\overline{\rho} = \sqrt{\frac{1}{\sum_{i=1}^{3} w_\mathrm{i}}} \tag{4.23}$$

$w_\mathrm{i}$ is the weighting factor, that is calculated from the uncertainties $\Delta\rho_\mathrm{i}$ of the single measurements.

$$w_\mathrm{i} = \frac{1}{\Delta\rho_\mathrm{i}^2} \tag{4.24}$$

The statistical uncertainty $\Delta\rho_\mathrm{i}$ of the density $\rho_\mathrm{i}$ can be calculated using Gaussian error propagation [WW99].

$$\Delta\rho_\mathrm{i} = \sqrt{\left(\frac{\partial\rho_\mathrm{i}}{\partial m_\mathrm{a}}\Delta m_\mathrm{a}\right)^2 + \left(\frac{\partial\rho_\mathrm{i}}{\partial m_\mathrm{l}}\Delta m_\mathrm{l}\right)^2 + \left(\frac{\partial\rho_\mathrm{i}}{\partial\rho_\mathrm{a}}\Delta\rho_\mathrm{a}\right)^2 + \left(\frac{\partial\rho_\mathrm{i}}{\partial\rho_\mathrm{l}}\Delta\rho_\mathrm{l}\right)^2} \tag{4.25}$$

The density of the air $\rho_\mathrm{a}$ and the liquid $\rho_\mathrm{l}$, as well as the sample mass in air $m_\mathrm{a}$ and in liquid $m_\mathrm{l}$ are statistically independent. Therefore, it is not necessary to consider covariances between the parameters. [Rei13] showed that the uncertainty of the masses $\Delta m_\mathrm{a}$ and $\Delta m_\mathrm{l}$ are much bigger than the uncertainty of the densities of the air $\Delta\rho_\mathrm{a}$ and the liquids $\Delta\rho_\mathrm{l}$ due to temperature fluctuations. So: $\Delta\rho_\mathrm{a} = \Delta\rho_\mathrm{l} = 0$.
By insertion of the partial derivatives, the uncertainty $\Delta\rho_\mathrm{i}$ is given by:

$$\Delta\rho_\mathrm{i} = \sqrt{\left(\frac{(\rho_\mathrm{a}-\rho_\mathrm{l})\,m_\mathrm{l}}{(m_\mathrm{a}-m_\mathrm{l})}\Delta m_\mathrm{a}\right)^2 + \left(\frac{(\rho_\mathrm{l}-\rho_\mathrm{a})\,m_\mathrm{a}}{(m_\mathrm{a}-m_\mathrm{l})^2}\Delta m_\mathrm{l}\right)^2} \tag{4.26}$$

The mass has been measured three times in air and each liquid. The uncertainty of the mass $\Delta m_\mathrm{a,i}$ and $\Delta m_\mathrm{l,i}$ of each single measurement is $\pm 0.01\,\mathrm{mg}$, which is the uncertainty of the scale [A.G00]. Finally, the uncertainty of the mass is given by:

$$\Delta m_\mathrm{a/l} = \tau \cdot \left(\sum_{i=1}^{3} \frac{1}{\left(\Delta m_\mathrm{a/l,i}\right)^2}\right)^{-\frac{1}{2}} \tag{4.27}$$

$\tau = 1.32$ is the factor of the Student t-Distribution for three measurements.

By immersion of the specimen into the liquid, small gas bubbles can adhere to the sample surface, especially for samples with rough surfaces. These bubbles create a buoyant force that marginally affects the measurement. This effect can be reduced by polishing of the surfaces, but is not completely eliminated [Wol14]. The effect can be avoided by using pycnometry, which is

presented in the following Chapter 4.3.2. The immersion method is a very simple and cost saving method and therefore optimal for benchtop experiments with fresh fuels. But for the use in hot cells, gas pycnometry is the better solution, as it is difficult to polish the specimen and it avoids the use of liquids.

### 4.3.2 Pycnometry

In general, pycnometry is used to determine the volume of a body. But, together with the body's mass, its density can be calculated with Equation 4.15 in chapter 4.3.1.

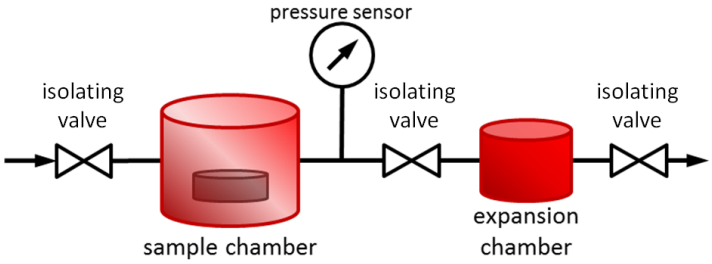


***Figure 4.24:*** *Setup for the measurement of the density using Pycnometry.*

Figure 4.24 shows the measurement setup. The sample with unknown volume $V_b$ is located in the sample chamber which has a known volume $V_{sc}$ and both chambers are evacuated to reduce additional uncertainties due to remaining gas. Then Helium gas is inserted via the locking valve 1, while locking valve 2 is closed. Then also valve 1 is closed and the gas in the sample chamber has a certain pressure $p_1$ (between 0.5 and 1.5 bar), which is measured with the pressure sensor, which is initially only connected to the sample chamber. Then, the locking valve 2 is opened, while valve 1 and 3 remain closed. So, the Helium can expand into the expansion chamber, which also has a known volume $V_{ec}$. So, in the combined volume $(V_{sc} - V_b) + V_{ec}$, there is a new pressure $p_2$.
The volume of the sample $V_b$ can be calculated using Boyle's law. It says that for ideal gases (Helium can be assumed to be an ideal gas) the pressure is in inverse proportion to the volume for an isothermal change of state, i.e. the temperature and the amount of substance, is constant.

$$\frac{V_1}{V_2} = \frac{p_2}{p_1} \tag{4.28}$$

With

$$V_1 = V_{\mathrm{sc}} - V_{\mathrm{b}} \tag{4.29}$$

and

$$V_2 = (V_{\mathrm{sc}} - V_{\mathrm{b}}) + V_{\mathrm{ec}} \tag{4.30}$$

Equation 4.28 results in:

$$V_\mathrm{b} = V_\mathrm{sc} + \frac{V_\mathrm{ec}}{1 - p_1/p_2} \tag{4.31}$$

With Equation 4.15 and the sample's mass $m_\mathrm{b}$, its density $\rho_\mathrm{b}$ is given by:

$$\rho_\mathrm{b} = \frac{m_b}{V_b} \tag{4.32}$$

The measurements have been performed with a Micrometrics AccuPyc 1300 and a Quantachrome Upyc 1200e. Both instruments have the same mode of operation. The instruments have an additional balance, so that the both mass and volume can be obtained in one measurement. The included software calculates the density automatically. Usually, the measurement of one specimen is repeated between five to ten times to reduce the statistical uncertainty. Finally, the software calculates the average density of the multiple measurements together with its standard deviation.

The pycnometer that was used to conduct the experiments is not equipped with a heating element, so the measurements were only performed at room temperature. Else, temperature dependent volume expansion of the sample and Helium gas would need to be considered.

# CHAPTER 5

## Sample Selection and Preparation Techniques

## 5.1 Sample Selection

### 5.1.1 As-fabricated Dispersion Fuels

The main focus of this work lies on the various dispersion fuel types. Therefore, usually an alloy of Uranium with 7 wt.% molybdenum is used for powder production, except for IRIS-TUM, which is fabricated from U-8 wt.%Mo.

As already discussed in Chapter 2.1, two different U-Mo powder types need to be distinguished: ground powder (IRIS-TUM fuel) with its irregular shape that has higher porosity than the atomized powder with its almost perfect spherical shape. Different kinds of sputter-coating may be applied on the atomized powder, like Si or ZrN (SELENIUM fuel), to prevent the disadvantageous reaction of the U-Mo particles with the aluminum of the matrix. Another way of coating is simply the oxidation of the particle surface (IRIS-4 fuel), as the Uranium-oxide does not react with the aluminum of the matrix in the same way as metallic U-Mo does. If no coating is applied on the U-Mo powder, the most convenient way is to mix the aluminum of the matrix with silicon (E-FUTURE, E-FUTURE II and AFIP-1), which forms a silicon rich layer around the U-Mo particles during annealing at $400 - 450\,^{\circ}\mathrm{C}$.
Table C.1 in Appendix A gives an overview over the investigated U-Mo fuels chosen from siblings of plates tested during in-pile experiments.

### 5.1.2 In-pile Irradiated Dispersion Fuel - AFIP-1 Experiment

Table C.1 contains a plate named AFIP-1. It originates from the US irradiation experiment: The Advanced Test Reactor (ATR) Full size plate In center flux trap Position (AFIP) experiment (AFIP-1).
One as-fabricated sample has been investigated, as well as two in-pile irradiated segments. Table 5.1 shows details of the as-fabricated fuel plate.

This full size test plate has a prototypic scale with a length of 54.6 cm, width 5.75 cm and a thickness of 0.13 cm. It was irradiated in the center flux trap position in the Advanced Test Reactor (ATR) at the Idaho National Laboratory (INL) in Idaho, USA, in three full reactor cycles in 2008 and 2009 (means 158 days) at a center flux trap power of 25 MW. In

| Plate | Fabrication | Roll Bond Process |
|---|---|---|
| Fuel | Fabrication | Atomized U-7 wt.%Mo Powder |
| | U-235 Enrichment | 19.85 % |
| | Molybdenum Content | 7.0 wt.% |
| | Uranium Density | 8.76 $g_U/cm^3$ |
| Matrix | Composition | Al/Si |
| | Silicon Content | 1.9 wt.% |
| Meat | Porosity | 3.1 vol.% |
| | Fuel Loading | 57.2 vol.% |
| Caldding | Material | AA 6061 |

***Table 5.1:*** *Summary of the as-fabricated AFIP-1 1T2 test plate [KHJ11, PLC⁺11a].*

this position it is possible to obtain a gradient in burnup along the length of the plate. Figure 5.1 shows the fuel fission density along the length of the plate, calculated with MCNP [PLC⁺11a].

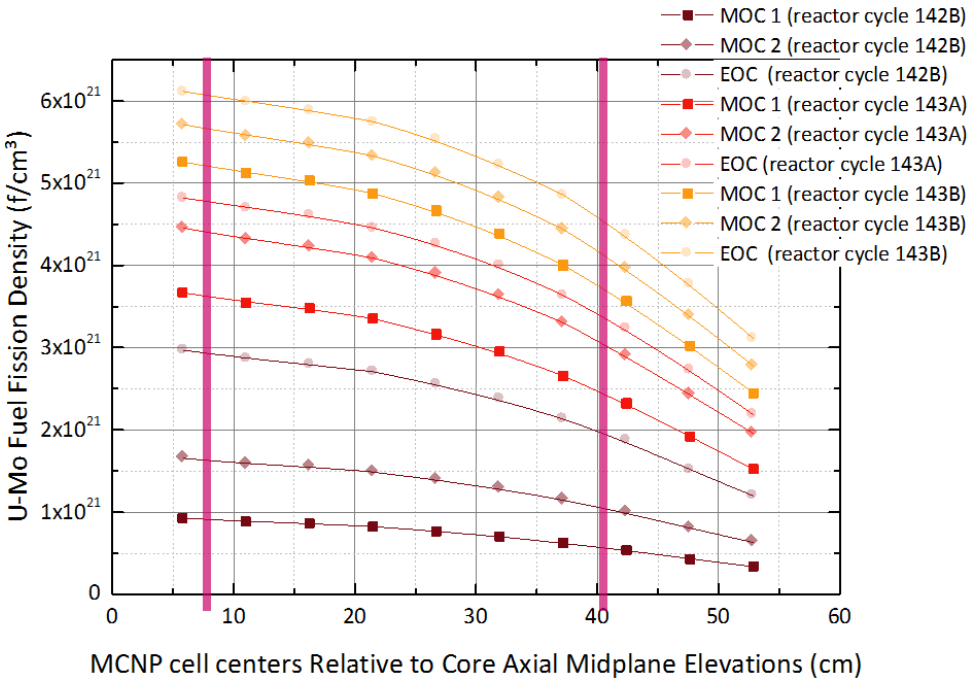


***Figure 5.1:*** *Axial fuel fission density distribution history of the AFIP-1 1T2 plate during each irradiation cycle [PLC⁺11a]. The zero position is the directing to midplane of the reactor core. The two vertical purple lines in the diagram above indicate the position of the examined samples. MOC stands for middle of cycle and EOC stands for end of cycle.*

Two segments, one with moderate and one with high burnup, have been cut 23 cm from the top and 4.5 cm from bottom edge of the fuel zone. Table 5.2 gives details to the segments.

| | AFIP-1 TL<br>Low Burnup Segment | AFIP-1 TK<br>High Burnup Segment |
|---|---|---|
| U-Mo Fuel Fission Density | $4.86 \cdot 10^{21}$ f/cm³ | $6.12 \cdot 10^{21}$ f/cm³ |
| BOL Heat Flux | 210 W/cm² | 315 W/cm² |
| Total Average Plate Thickness | 1.31 mm | 1.32 mm |
| Fuel Content in Meat | 51 vol.% | 49 vol.% |
| Matrix Content in Meat | 13 vol.% | Completely Consumed |
| IDL Content in Meat | 36 vol.% | 51 vol.% |

***Table 5.2:*** *Characteristics of the two investigated in-pile irradiated AFIP-1 1T2 dispersion segments. The fuel, matrix and IDL contents have been determined from optical microscopy [PLC⁺11a, BCB⁺14b].*

Figure 5.2 and 5.3 show an optical microscope image of the low burnup segment AFIP-1 TL and the high burnup segment AFIP-1 TK. From these microscopy examinations, the volume fractions of the fuel, matrix and IDL, as well as the thickness of the cladding and meat have been obtained, see Table A.2 [BCB⁺14a, BCB⁺14b].

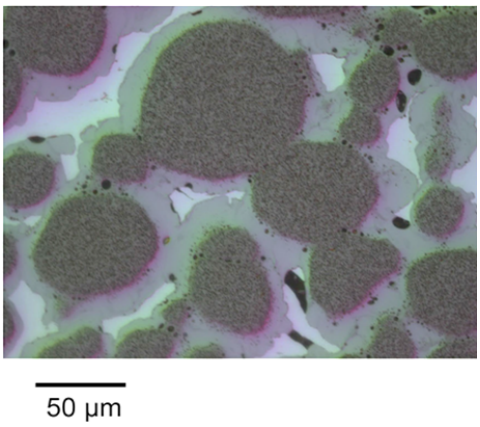


***Figure 5.2:*** *Microscopy image of the segment AFIP-1 TL [BCB⁺14a].*

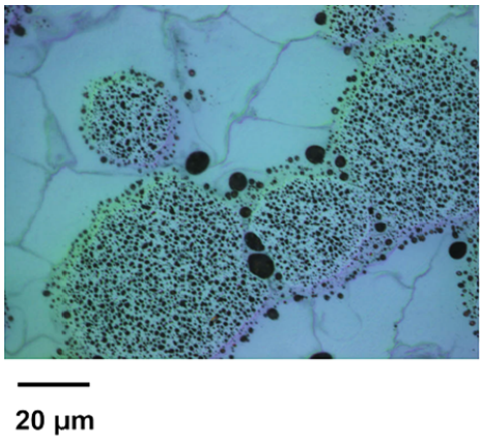


***Figure 5.3:*** *Microscopy image of the segment AFIP-1 TK [BCB⁺14a].*

### 5.1.3 In-pile Irradiated Monolithic Fuel

Besides the dispersion fuel, monolithic fuel and its behavior during irradiation has been investigated. Usually the monolithic fuels contain 10 wt.% Molybdenum in the Uranium alloy.
The in-pile irradiated fuel investigated here originates from the AFIP-2BZ full size test plate. The plate contains a U-10 wt.%Mo monolihtic foil with a Zirconium diffusion barrier and is clad in AA6061, see Table 5.3 [Moo10]. Like AFIP-1, this plate was as well irradiated in the center flux trap of the ATR at the INL in Idaho, USA, in three full reactor cycles for 132 days at $105 - 116$ MW reactor power. Table A.3 in Appendix A gives details to the irradiation conditions [PLC⁺11d].

| Plate | Fabrication | Friction Bonding |
|---|---|---|
| Fuel | Fabrication | Hot Co-Rolling of a U-10 wt.%Mo alloy ingot with Zr |
| | U-235 Enrichment | 19.75 % |
| | Molybdenum Content | 10.21 wt.% |
| | Uranium Density | 15.84 $g_U/cm^3$ |
| Diffusion Barrier | Material | Zirconium Foil |
| | Purity | 99.8 % |
| Cladding | Material | AA 6061 |

***Table 5.3:*** *Summary of the as-fabricated AFIP-2BZ test plate [Moo10].*

| | |
|---|---|
| Fuel Fission Density | $3.25 \cdot 10^{21}$ $f/cm^3$ |
| BOL Heat Flux | 237 $W/cm^2$ |
| Total Average Plate Thickness | 1.34 mm |

***Table 5.4:*** *Characteristics of the investigated in-pile irradiated AFIP-2BZ dispersion segments. The fuel, matrix and IDL contents have been determined from optical microscopy [PLC+ 11d, BCB+ 13].*

Table A.3 in Appendix A gives an overview over the layer thicknesses from the top to the bottom layer that are needed for the calculation of the thermal diffusivity. The data have been obtained from optical microscope images [BCC+15a].

## 5.2 Sectioning

Usually, pieces of $(1 \times 5)$ cm$^2$ are punched from the fuel zone of the test plate for further sample preparation. The size of theses punches is too big for the instruments for the measurement of the thermal properties. So, smaller samples have to be cut out of it. The sample holders of the instruments allow only for small tolerances. To obtain good precision, for fresh fuels, a diamond wire saw can be used in a fume hood. In-pile irradiated fuels can only be handled in a hot cell. There, a commercially available low-speed saw has been modified to be operated with manipulators.
The LFA instrument for thermal diffusivity measurements requires samples of $(6 \times 6)$ mm$^2$ size, the DSC instrument requires samples of maximum $(4 \times 4)$ mm$^2$ size.

### 5.2.1 Non-irradiated Fuel

For the fresh fuels, a Vertical Precision Diamond Wire Saw Model 3242 from Well Diamantdrahtsaegen GmbH, see Figure 5.4, was used to cut the punched fuel segments. The advantage of the saw is the high precision due to the thin wire (0.22 mm diameter) and the marginal expenditure of energy which helps to prevent ruptures at the edges of the sample.
First, the cutting lines are marked with a permantent marker. Then the segment is mounted in the sample holder of the saw and adjusted according to the wire, see Figure 5.5.

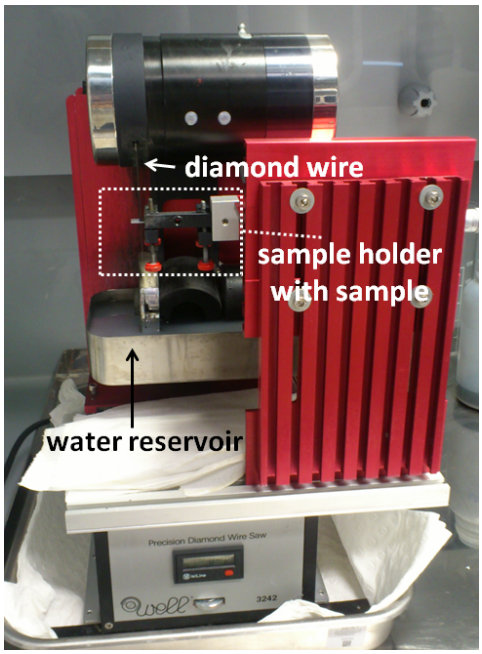


***Figure 5.4:*** *Photograph of the Vertical Precision Diamond Wire Saw Model 3242 from Well used for the preparation of the fresh fuel samples.*

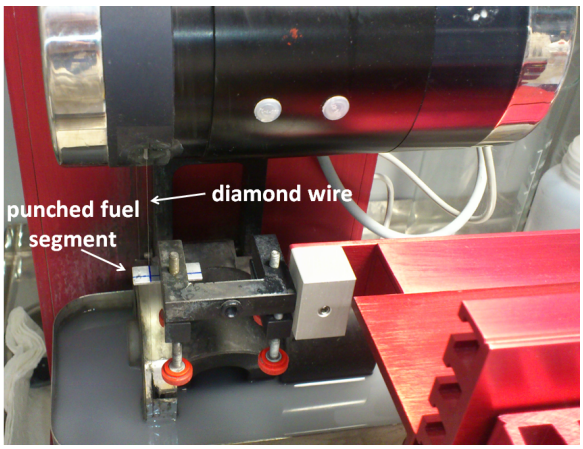


***Figure 5.5:*** *Magnification of the sample holder with punched fuel segment.*

### 5.2.2 In-pile Irradiated Fuel

From the in-pile irradiated AFIP-1 1T2 dispersion fuel plate, two fuel segments (see Figure 5.6 and 5.7) have been cut at different locations of the plate, see Chapter 5.1.2, of $(12.5 \times 12.5)$ mm$^2$ nominal size [BCB$^+$14a]. From the AFIP-2BZ plate, in total three segments have been cut from the plate, but only the segment 8.9 cm from the top edge of the plate (segment AFIP-2 TC) has been investigated here. Its dimensions are $(12.5 \times 27)$ mm$^2$ [BCB$^+$13].

For the further sectioning into the required dimensions for the different instruments, a specialized low-speed saw with a Buehler diamond-wafering blade is used. Figure D.1 to D.3 in Appendix D show the sectioning diagrams for the three fuel segments. AFIP-1 TL and TK were each sectioned into one LFA, one DSC sample, one for optical microscopy (OM), one for differential thermal analysis (DTA) and three spare parts. For the dimensions of the samples, see Figure D.1 and D.2 in Appendix D. The AFIP-2 TC segment is of double size, so more samples could be gained: Two LFA samples, four DSC samples, two OM samples and two samples for analytical chemistry, see Figure D.3 in Appendix D. The two LFA samples have been used to verify the multi-layer models (TUM model and PNNL model in Chapter 3.4.1) against each other, and used for the calculation of the thermal diffusivity of one layer out of a multi-layer system. DTA and AC have not been performed in the scope of this work.


***Figure 5.6:*** *Photograph of the AFIP-1 TL fuel segment before sectioning [BCB$^+$14a].*

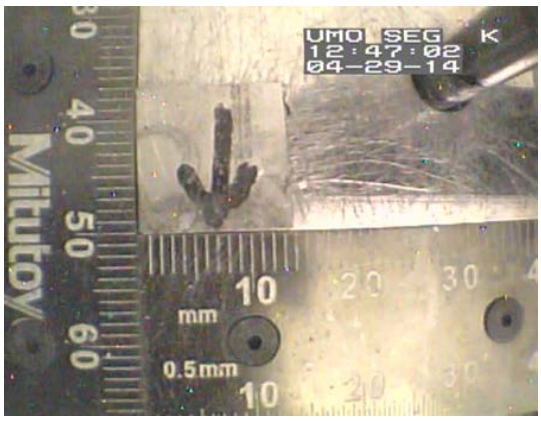


***Figure 5.7:*** *Photograph of the AFIP-1 TL fuel segment before sectioning [BCB$^+$14a].*

## 5.3 Polishing

### 5.3.1 Removing of Cladding

The analysis of measurements of a one-layer system is much easier and has a lower uncertainty than a three or more layer system, like a fuel segment consisting of meat and two layers of cladding on both sides or regarding especially monolithic fuel a five layer system, when considering the diffusion barrier. So, it is practicable to remove the cladding from the fuel zone before performing the measurements. Therefore, the cladding is grind down the meat with abrasive paper in a polishing machine. It is to remark, that this procedure is not applied on in-pile irradiated fuels, as they are brittle with much porosity, so that there is a risk that the fuel breaks, which means a destruction of the sample.
In the following, the procedure for removing the cladding from fresh fuel is described:

1. Placing a small block of metal on a hot plate at $\sim 200\,^{\circ}\mathrm{C}$
2. Melting a small spot of crystal bond (epoxy) on the hot metal surface
3. Placing the cut fuel sample on the epoxy spot (see Figure 5.8)
4. Removing the metal block with the fuel sample from the heater and putting it into a bowl of cold water to cool the metal block and to harden the liquid epoxy
5. Grinding off the upper cladding surface using fine grained sandpaper (see Figure 5.9) until the darker grey dotted fuel zone appears on the surface (see Figure 5.10)
6. Removing the sample from the metal block using acetone (see Figure 5.11)
7. Repeating the procedure from (1) to (6) for the rear side of the fuel sample

Figure 5.12 shows finally the resulting pure meat zone. The resulting thickness is measured with a micrometer caliper and lies between 0.25 mm and 0.50 mm depending on the fuel. In this case, an ATM SAPHIR 520/530 polishing machine was used.

***Figure 5.8:*** *Fuel sample glued in an Al block with hardened crystal bond.*

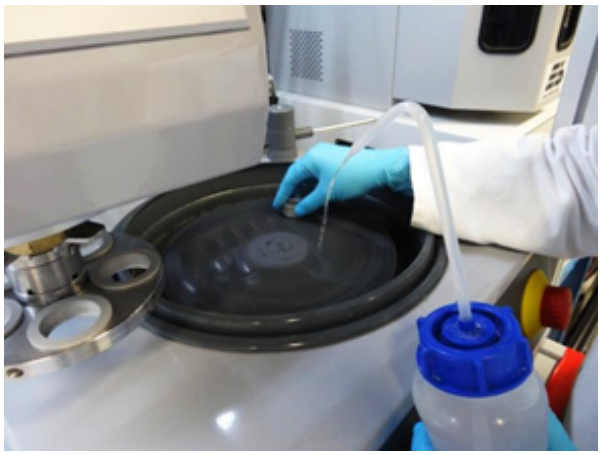

***Figure 5.9:*** *Grinding off the cladding from the fuel with fine grained sandpaper.*

### 5.3.2 Preparation of SEM Samples

To determine the thickness of the inter-diffusion layer after annealing, Scanning Electron Microscopy (SEM) is used to obtain images with high resolution. Therefore, the surface of the samples need to be very flat without scratches.
First step is to embed the sample in resin. Then, the polishing procedure starts with rough sandpapers and water to remove deep scratches from the sectioning, successively using finer sandpapers in each step. Finally, the sandpaper is replaced by cloth with diamond suspension, again starting with 9$\mu$m diameter diamonds, going down to 1$\mu$m Table E.1 in Appendix E gives a detailed description of the polishing procedure for an ATM SAPHIR 520/530 polishing machine.

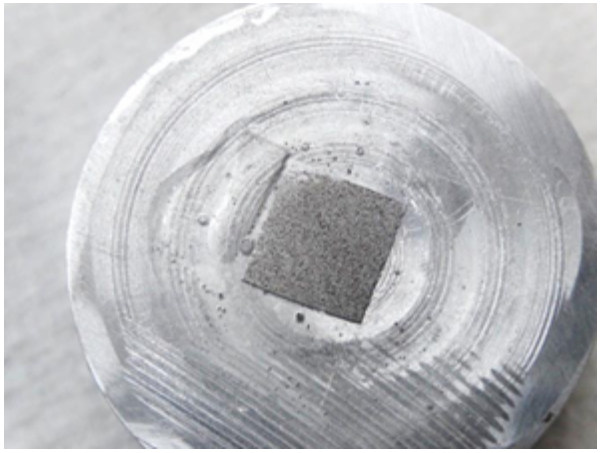

***Figure 5.10:*** *Fuel sample on the Al block after grinding off the cladding. The dark gray dots are the fuel particles in the lighter gray matrix.*


***Figure 5.11:*** *Removing the fuel sample from the Al block with acetone.*

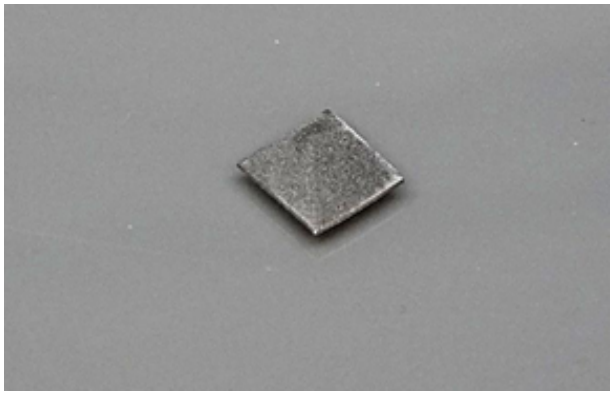

***Figure 5.12:*** *Pure fuel meat after removing the cladding.*

# Part III

# Results and Discussion

# CHAPTER 6

## Comparison of the Results from the TUM and PNNL Model

In Chapter 3.4.1 the TUM and the PNNL model for the evaluation of the thermal diffusivity, respectively the thermal conductivity, of layered materials have been presented.
To compare the models with each other, the raw data of two LFA measurements of separate samples have been evaluated independently from each other, but with the same input parameters, like layer thickness, density and specific heat of the single layers. A segment of irradiated monolithic fuel samples from the AFIP-2BZ testplate with a Zr diffusion barrier (see Chapter 5.1.3) has been cut in two segments and used for the measurement, see Chapter 5.2.2. This way, the segments have the same fabrication and irradiation history and the measurements of the two segments can be validated against each other as well.
The goal was to separate the thermal diffusivity of only the fuel meat from the data of the entire composite of cladding, Zr barrier layer and U-Mo that have been obtained from the LFA measurements, see Figure 6.1.

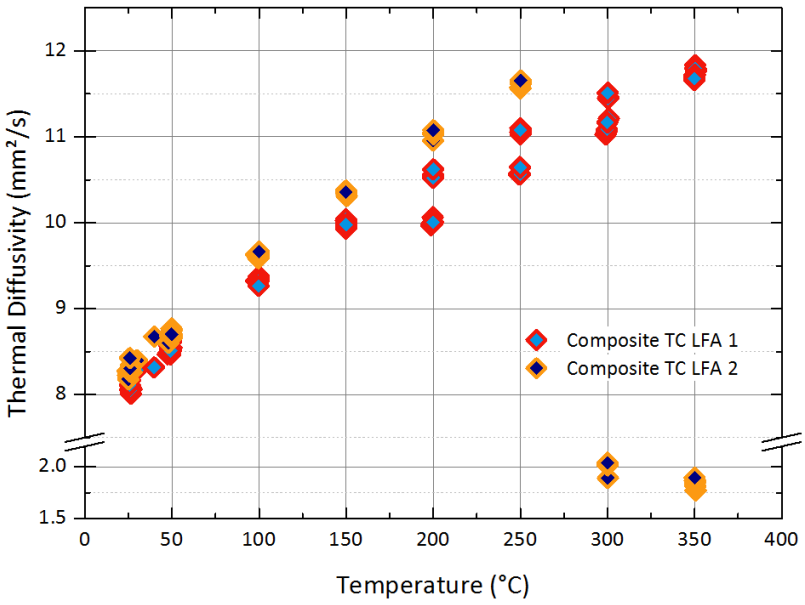


***Figure 6.1:*** *Thermal diffusivity of the composite, i.e. including the cladding and fuel meat, of the TC LFA 1 and TC LFA 2 segment of the in-pile irradiated AFIP-2BZ testplate, evaluated with the Netzsch LFA instrument software.*

The thermal diffusivity of the composite of both segments evaluated with the Netzsch software is in good agreement with each other between about 8 $mm^2/s$ at 25 °C and about 12 $mm^2/s$ at 350 °C. However, segment TC LFA 2 shows a slightly higher thermal diffusivity. The maximum deviation is 4.5 % at 250 °C, which can be explained by the deviation of the thickness over the entire segment, see Table F.2 in Appendix F.3.

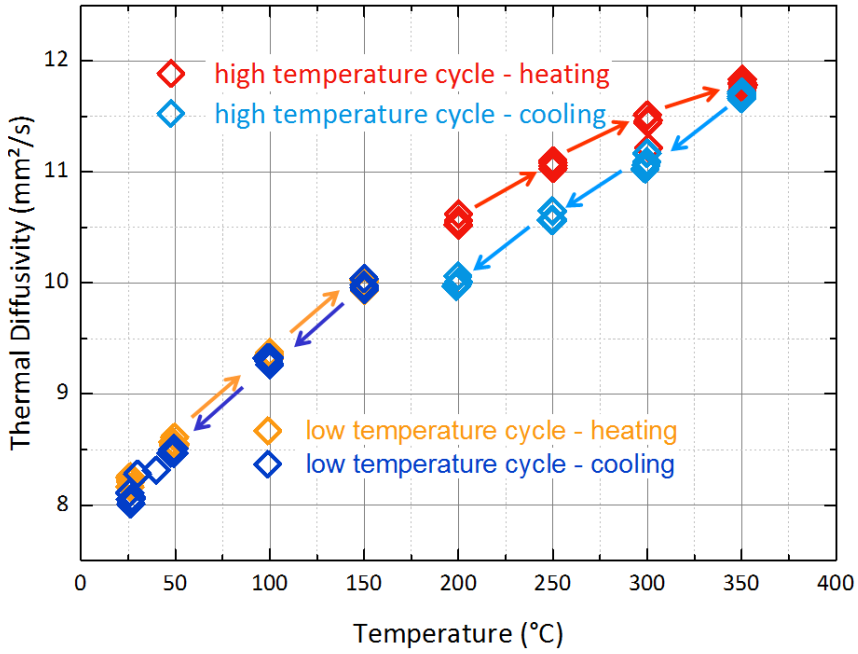


***Figure 6.2:*** *Thermal diffusivity of the composite of the TC LFA 1 segment. The arrows indicate the temperature cycles.*

The thermal diffusivity of the segment TC LFA 1 shows a significant spread of the data points between 200 °C and 350 °C. The measurement was performed in 2 cycles in steps of 50 °C: the first from 25 °C to 150 °C and again down to 25 °C and then heating in one step to 150 °C and then in 50 °C steps to 350 °C and again down to 150 °C, see Figure 6.2.
The first cycle does not show deviations and the second cycle connects accordingly. But when cooling down from 350 °C the data points start to deviate from the data points from the heating ramp. Optical examination showed that the segment started to delaminate, i.e. the cladding peeled off the U-Mo + Zr layer. The resulting gap reduces the heat transfer and decreases the thermal diffusivity noticeable.
In principle, the same phenomenon can be observed for segment TC LFA 2 at 300 °C. The thermal diffusivity suddenly decreases drastically down to below 1 $mm^2/s$. Optical examination after the measurement showed that the segment completely delaminated. The resulting gap instantly reduced the heat transfer which led to a drastic decrease of the thermal diffusivity.

Now, the data can be evaluated in two ways: As a three or five layer system.
Zr has a similar thermal diffusivity as U-Mo and the diffusion barrier is on both sides only $\sim 30\mu m$ thick, which is about 15 % of the fuel meat thickness. So, the layer may be assumed to be part of the fuel layer. The three layers are then 1) the top AA 6061 cladding layer, 2) the U-Mo + Zr layer and 3) the bottom AA 6061 cladding layer. For the five layer system, the Zr barriers on top and bottom of the U-Mo are assumed to be separate layers as follows: 1) top

AA 6061 cladding layer, 2) top Zr barrier layer 3) U-Mo layer, 4) bottom Zr barrier layer and 5) bottom AA 6061 layer.

The thickness values of the layers can be found in Table A.3 in Appendix A. For the calculation, the density and specific heat capacity as well as the thermal diffusivity of all layers but the one that is of interest need to be known for both models. Appendix F gives details about the determination and values of the parameters.

## 6.1 Three-Layer System

At first, the three layer system has been evaluated with the TUM and the PNNL model. Figure 6.3 shows the results for the thermal diffusivity of the Zr + U-Mo from the TC LFA1 and TC LFA2 sample as a function of temperature.

The thermal diffusivity of both segments increase from about $4\,\mathrm{mm^2/s}$ at $25\,^\circ\mathrm{C}$ to about $6\,\mathrm{mm^2/s}$ at $350\,^\circ\mathrm{C}$. Especially the evaluation of the TUM model, compare the blue data points, shows that the thermal diffusivity of both segments is in very good agreement.
Also here, the deviation between $200\,^\circ\mathrm{C}$ and $350\,^\circ\mathrm{C}$ of the TC LFA 1 segment can be observed, as well as the sudden decrease down to below $1\,\mathrm{mm^2/s}$ of TC LFA 2 at $300\,^\circ\mathrm{C}$ due to complete delamination.

However, both models are in very good agreement until $150\,^\circ\mathrm{C}$, especially for the TC LFA 1 segment. Then, at $200\,^\circ\mathrm{C}$ and above, the PNNL model calculates slightly higher values. There, the difference between the two models is higher for the TC LFA 2 segment.

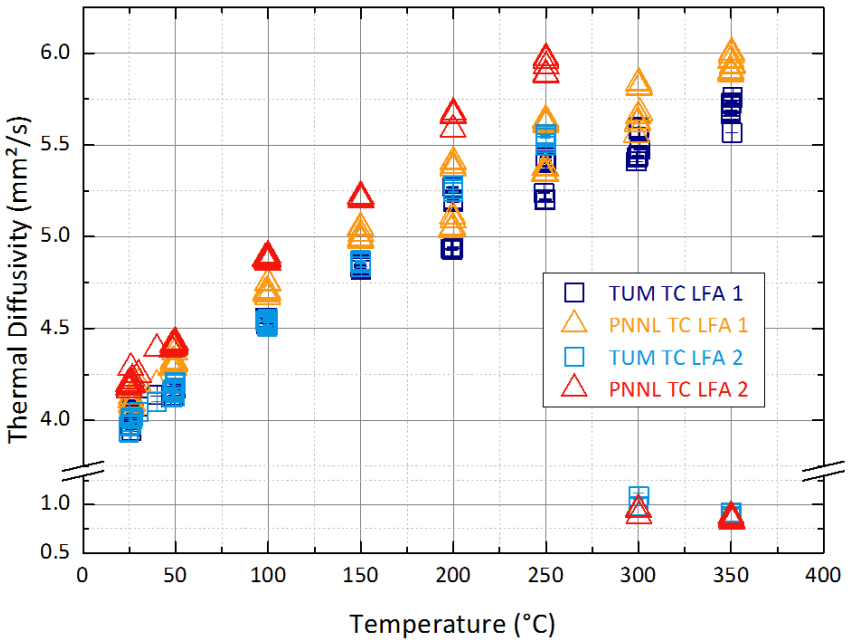


***Figure 6.3:*** *Thermal diffusivity of the Zr + U-Mo layer, evaluated with the TUM and PNNL model.*

Figure 6.4 shows a one-to-one comparison of the TUM and PNNL model for the TC LFA 1 and TC LFA 2 segment. The black line represents perfect agreement, the red lines represent a 10 % deviation between the values from the TUM and PNNL model.

In the case of the three layer system, the values are all above the black line, which indicates that the PNNL model calculates in general higher values than the TUM model. But the deviation of all values is still below 10 % for all values. The thermal diffusivity of the TC LFA 1 segment is closer to the black line and therefore, in this case, the values of the two models are in very good agreement. The deviation of the TC LFA 2 segment is slightly higher, but still below 10 %. By trend, the deviation of the TCA LFA 1 segment increases marginally to higher thermal diffusivity, but stays constant for the TC LFA 2 segment.
The data points in the range around 1 $mm^2/s$ represent the measurements after delamination of segment TC LFA2. Also here, the models are in good agreement. Yet, no model takes delamination into account.

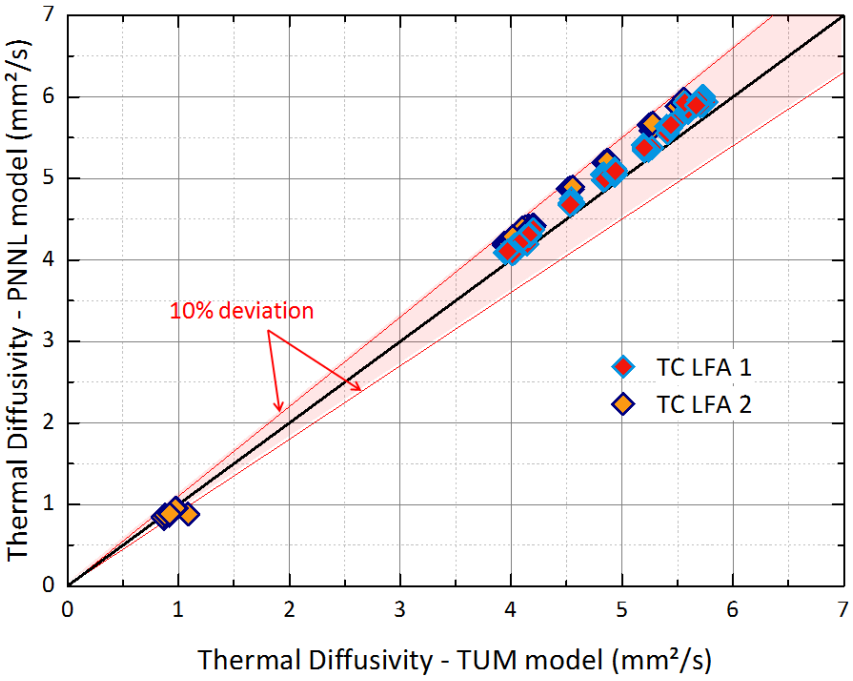


***Figure 6.4:*** *One-to-one comparison of the thermal diffusivity of the Zr + U-Mo layer, evaluated with the TUM and PNNL model. The black line represents perfect agreement, the red lines represent a 10 % deviation between the calculated values from the TUM and PNNL models.*

## 6.2 Five-Layer System

In the second step, the five layer system has been evaluated with the TUM and the PNNL model. Figure 6.5 shows the results for the thermal diffusivity of the U-Mo from the TC LFA1 and TC LFA2 sample as a function of temperature.

In general, the thermal diffusivity of the target layer of both segments is slightly lower than for the three layer system, as here the zirconium layer with the slightly higher thermal diffusivity than the U-Mo is not anymore included in the data points.
The thermal diffusivity increases here from about 3.5 $mm^2/s$ at 25 °C to also about 6 $mm^2/s$ at 350 °C. As already observed at the three layer system, the evaluation of the TUM model, compare the blue data points, shows that the thermal diffusivity of both segments is in very good agreement.

Also, the deviation between 200 °C and 350 °C of the TC LFA 1 segment can be observed, as well as the sudden decrease down to below 1 $mm^2/s$ of TC LFA 2 at 300 °C due to complete delamination.
Indeed, both models show the same trend, but the deviation between the data points is significantly higher than in the three layer case. The distance of the data points between the two models increases slightly with increasing temperature in the same way as already seen for the three layer system.

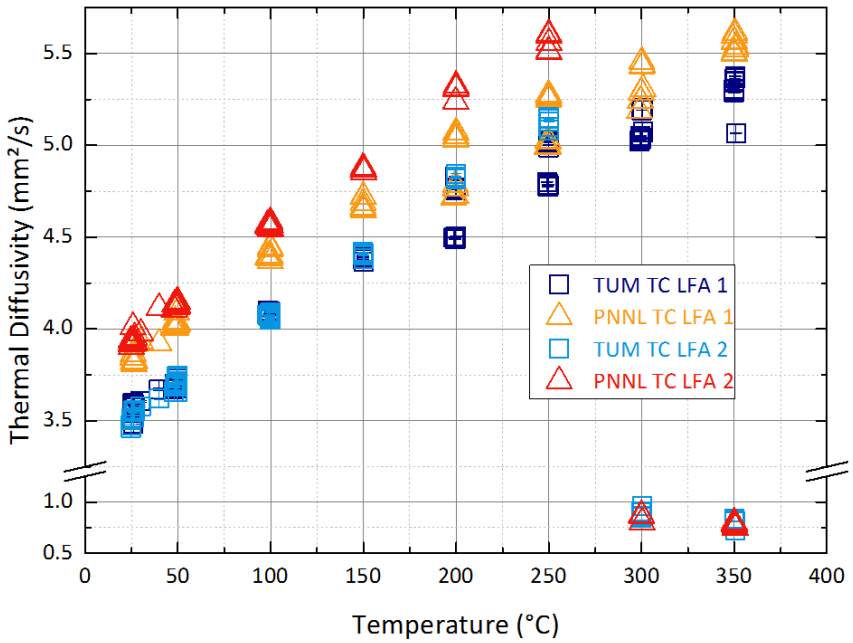


***Figure 6.5:*** *Thermal diffusivity of the U-Mo layer, evaluated with the TUM and PNNL model.*

Figure 6.6 shows a one-to-one comparison of the TUM and PNNL model for the TC LFA 1 and TC LFA 2 segment now for the five layer system. The black line again represents perfect agreement and the red lines represent a 10 % deviation between the values from the TUM and PNNL model.

Also here, the values are all above the black line indicating that the PNNL model calculates in general higher values than the TUM model. But, especially for segment TC LFA 2, the deviation of some values is almost above 10 % deviation. The thermal diffusivity of the TC LFA 1 segment is again closer to the black line and are therefore in better agreement, especially for higher thermal diffusivity values. Again the deviation of the TC LFA 2 segment thermal diffusivity stays more or less constant over the entire range.
The data points in the range around 1 $mm^2/s$ again represent the measurements after delamination of segment TC LFA2. Here, the models are in the same good agreement as in the three layer case.

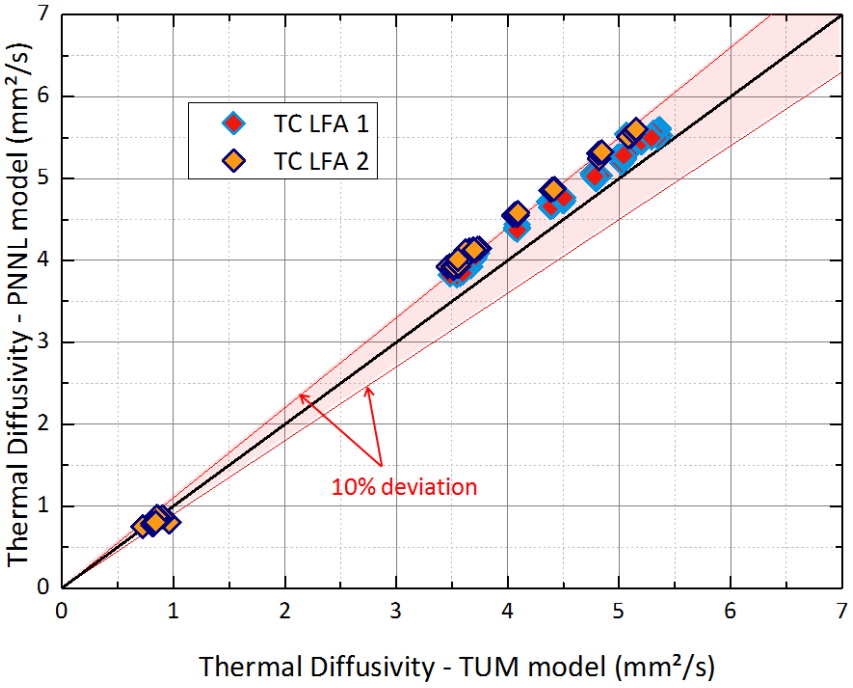


***Figure 6.6:*** *One-to-one comparison of the thermal diffusivity of the U-Mo layer, evaluated with the TUM and PNNL model. The black line represents perfect agreement, the red lines represent a* 10 % *deviation between the calculated values from the TUM and PNNL models.*

## 6.3 Discussion

The composite of cladding, Zr barrier layer and U-Mo has a thermal diffusivity of 8 $mm^2/s$ to 12 $mm^2/s$. In the first step, the thermal diffusivity of the U-Mo and the Zr barrier layer has been determined using the model for a three layer system. The resulting thermal diffusivity of about 4 $mm^2/s$ to 6 $mm^2/s$ without cladding is only about half of the thermal diffusivity of the composite. In the second step, the model for the five layer system was used to calculate the thermal diffusivity of only the U-Mo from the composite. In the case of the TUM model, this resulted in a thermal diffusivity of 3.5 $mm^2/s$ to 5.5 $mm^2/s$ for the U-Mo layer. The results for the PNNL model are slightly higher, but show roughly the same differences.

Figure 6.7 shows that both segments result in the same thermal diffusivity within 5 % deviation, which is within the uncertainty range, considering the uncertainty of the many parameters that are needed for the calculation and as well regarding the condition of a measurement on in-pile irradiated fuel in hot cells.
The thermal diffusivity of the in-pile irradiated U-10 wt.%Mo (see, segments TC LFA 1 and TC LFA 2 in Figure 6.7) is in general lower than the fresh U-10 wt.%Mo. Irradiation affects on the one hand the absolute value of the thermal, i.e. decreases the thermal diffusivity compared to fresh U-10 wt.%Mo, and on the other hand it influences the temperature dependence. Fresh U-10 wt.%Mo shows a steeper increase with increasing temperature than the irradiated U-10 wt.%Mo.

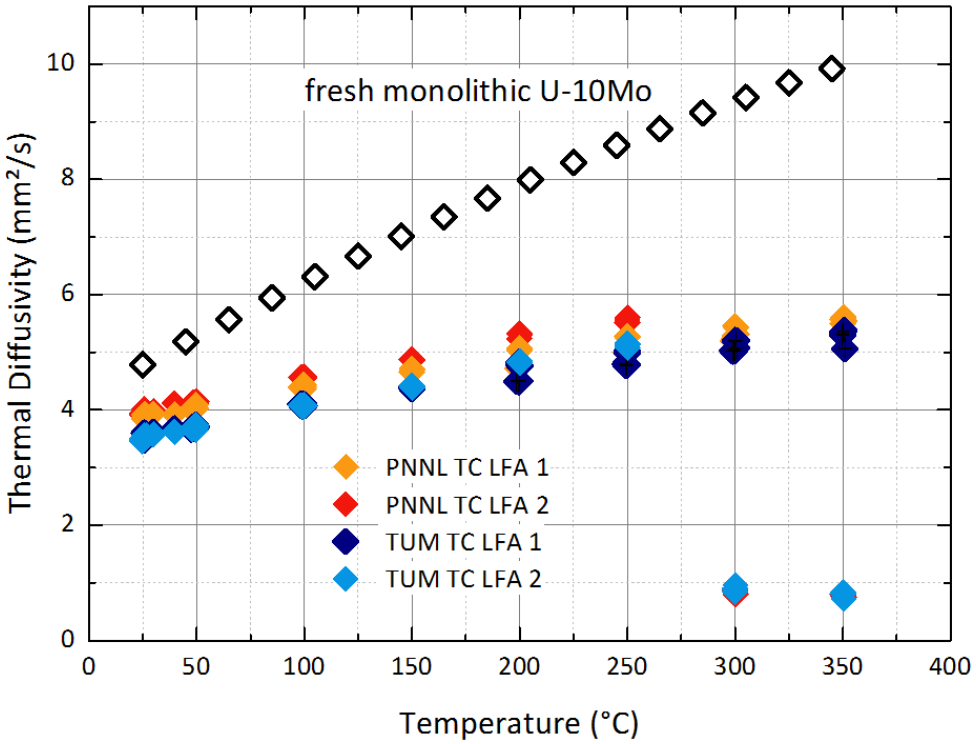


***Figure 6.7:*** *Thermal diffusivity of fresh and in-pile irradiated U-10 wt.%Mo [BCB+13, BCC+15b].*

Three-Layer System Comparing the TUM and PNNL model, there is only little deviation in the calculated thermal diffusivity using the three layer system.
The TUM model directly fits the raw data curve together with the exact information about the laser pulse as well as the number of layers and their properties. The PNNL model uses as well a fit of the raw data curve from the Netzsch software with the same information about the laser as the TUM model does, but the software treats the actual composite as an "effective" single layer. But applying a single layer model to a raw data curve of a multi-layer system does not fit well and results in a rather high uncertainty, see Figure 6.8.

Five-Layer System The resulting thermal diffusivity of this single layer model fit is then further used in the PNNL model to calculate the thermal diffusivity of one layer out of a three layer system. Here, one of the input parameters is again the laser pulse, so it is considered for the second time. Together with the uncertainty from the single layer model, this results in a slight variation between the two models, which can be neglected regarding the other uncertainties from the measurements.

Now, in the five layer system, the deviation between the two models increases. In this case, the TUM model again fits the raw data curves with the same input parameters as the three layer system. But now the model does not calculate with three, but with five layers directly in the fitting algorithm. So, the laser pulse propagates through five layers whereby the boundary conditions change for each layer intersection compared to the three layer case.
The PNNL model, in contrast, takes now the value resulting from the three layer model, i.e.

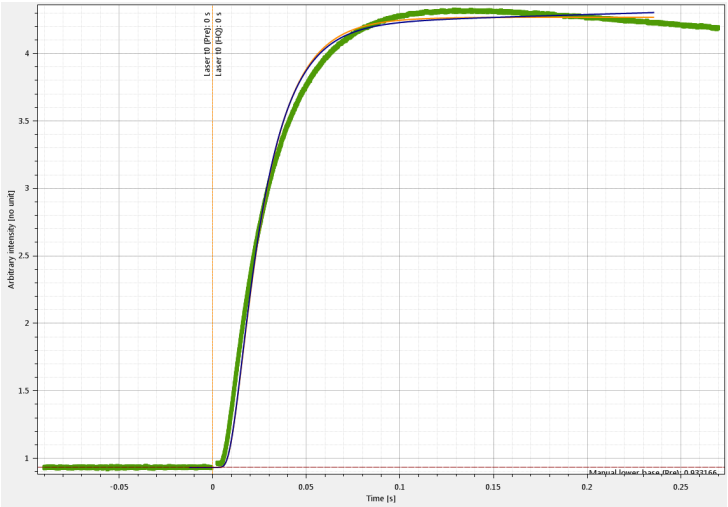


***Figure 6.8:*** *Fit of a single layer model to a raw data curve of a five layer system. The green curve is the raw data of a five layer system, the blue curve is the fit with a single layer model.*

the thermal diffusivity of the Zr + U-Mo layer. To eliminate the zirconium layer, the thermal diffusivity of the Zr + U-Mo layer is now used as input for the composite thermal diffusivity for a further three layer calculation. This time, the zirconium is treated like a cladding material. The model then calculates the meat, i.e. U-Mo layer, thermal diffusivity with the same boundary conditions and laser parameters as the previous three layer calculation. This way, the laser is considered a third time. Further, it is assumed that the laser directly hits the zirconium surface, but in fact, the laser first hits the aluminum cladding and its energy propagates through the cladding and then meets the zirconium surface. Thereby the "virtual" laser pulse parameters change, i.e. the initial heat peak is widened by the diffusion process through the cladding, but this change is not considered in the PNNL model.

Conclusion Finally, the multiple consideration of the laser pulse and the differing boundary conditions on the zirconium aluminum intersection in the PNNL model lead to a further deviation between the two models. However, considering the uncertainties of the multiple input parameters in the models, the deviation is roughly within the range of the measurement uncertainty. Both models are suitable for the calculation of a three layer system. To calculate the thermal diffusivity from a five layer system, in principle both models can be used, but the PNNL model has systematic errors in the calculation method.

# CHAPTER 7

## Constituents of the Thermal Conductivity: $\alpha$, $c_p$, $\rho$

The results of the measurements of the thermal properties, i.e. the thermal diffusivity, specific heat capacity, density and the resulting thermal conductivity of the different U-Mo fuels are presented in this chapter. Different types of dispersion U-Mo fuels are compared with each other, as well as irradiated and non-irradiated dispersion and monolithic U-Mo fuels.

### 7.1 Thermal Diffusivity $\alpha$

The thermal diffusivity $\alpha$ for fresh dispersion fuels has a significant variation between the different fuel types, especially comparing fresh and in-pile irradiated U-Mo fuels, see Figure 7.1.

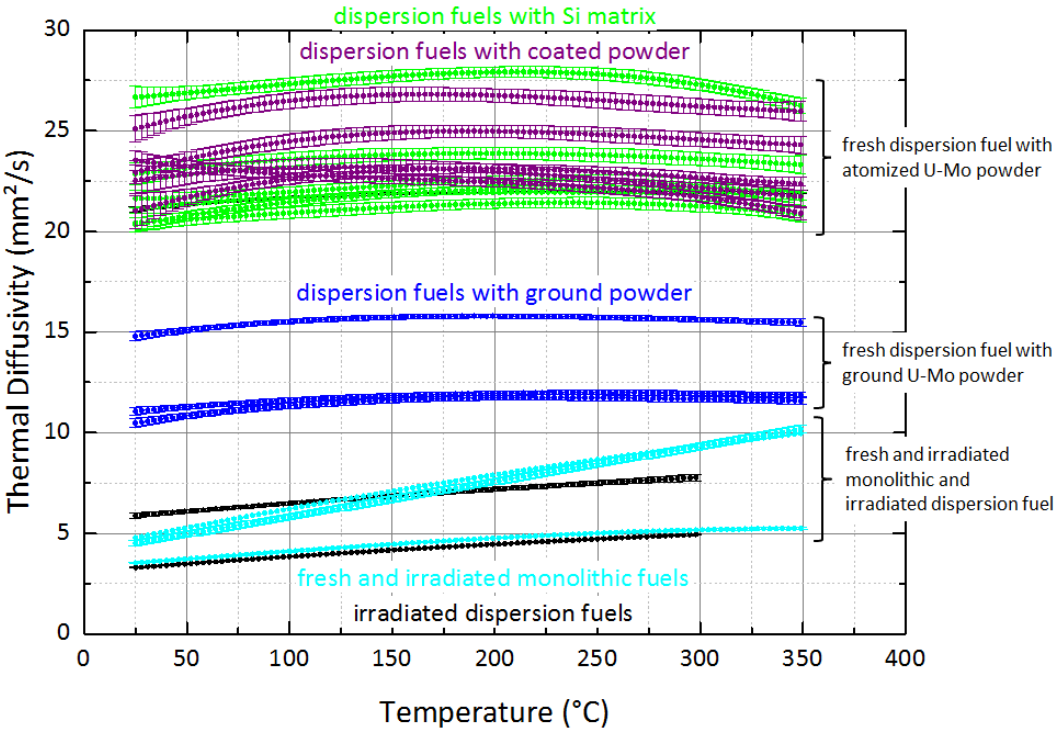


***Figure 7.1:*** *Thermal diffusivity of the different fresh and in-pile irradiated U-Mo fuel types.*

Table G.1 to G.20 in Appendix G.1 contains the parameters to calculate the thermal diffusivity of the curves in the following diagrams.

Figure 7.1 shows that the thermal diffusivity is a very sensitive parameter, strongly varying between the different types of U-Mo fuels.
Dispersion fuels containing atomized U-Mo powder vary within a band between 20 $mm^2/s$ to 30 $mm^2/s$, but dispersion fuels containing ground U-Mo powder have a significantly lower thermal diffusivity between 10 $mm^2/s$ and 15 $mm^2/s$. In-pile irradiation of dispersion fuel reduces its thermal diffusivity down to below 8 $mm^2/s$, which is in the range of monolithic U-Mo.

### 7.1.1 Dispersion Fuels with Atomized U-Mo Powder and Si-Matrix

In dispersion U-Mo fuels, the heat is mainly transferred through the highly conductive aluminum in the matrix material, as the U-Mo fuel particle's thermal diffusivity is very low, as already seen in the previous Chapter 6, as well as Figure 7.1 and 7.7. So, the matrix material's thermal diffusivity is an important factor. Pure Al has a thermal diffusivity of $\sim 100\ mm^2/s$, but as already discussed in Chapter 2.1, pure Al is not an adequate matrix material for uncoated U-Mo fuels. Thus, the Aluminum is alloyed or mixed with Silicon. Resultant, the thermal diffusivity of the matrix material strongly depends on the Silicon content of the Aluminum alloy. It lies for the alloys of interest for fuel fabrication between 60 $mm^2/s$ to 100 $mm^2/s$ [Wol14], see Figure 7.3. The green curves in Figure 7.2 show that a higher Si content reduces the thermal diffusivity of the fuel meat, accordingly.

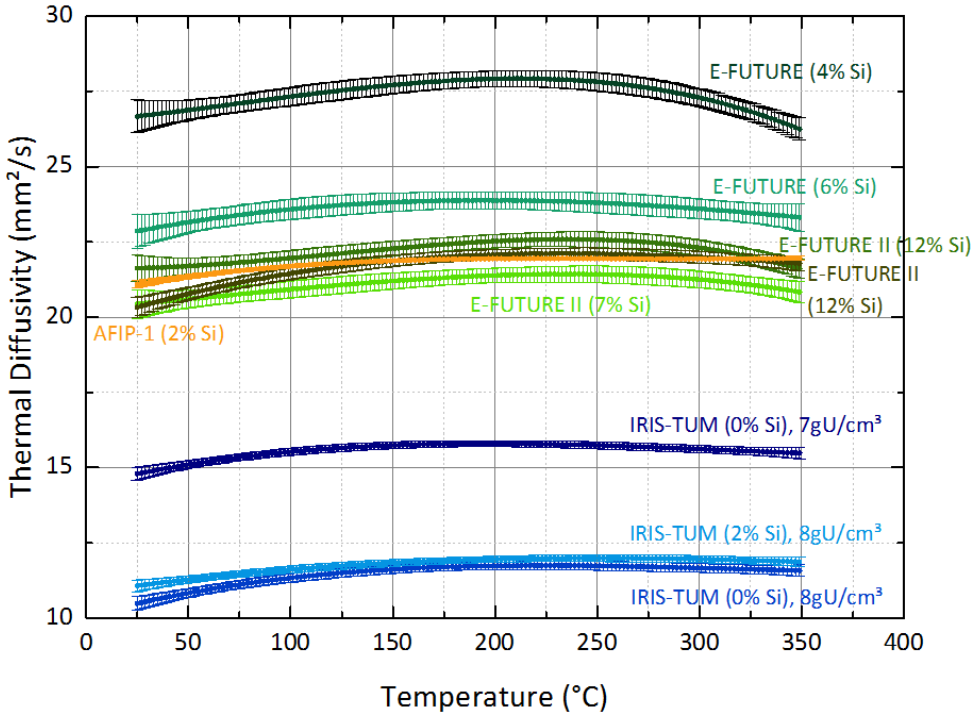


***Figure 7.2:*** *Summary of the thermal diffusivity of dispersion fuels with Si addition in the matrix. The green curves indicate dispersion fuels fabricated from atomized U-Mo powder, the blue indicate fabrication from ground U-Mo powder.*

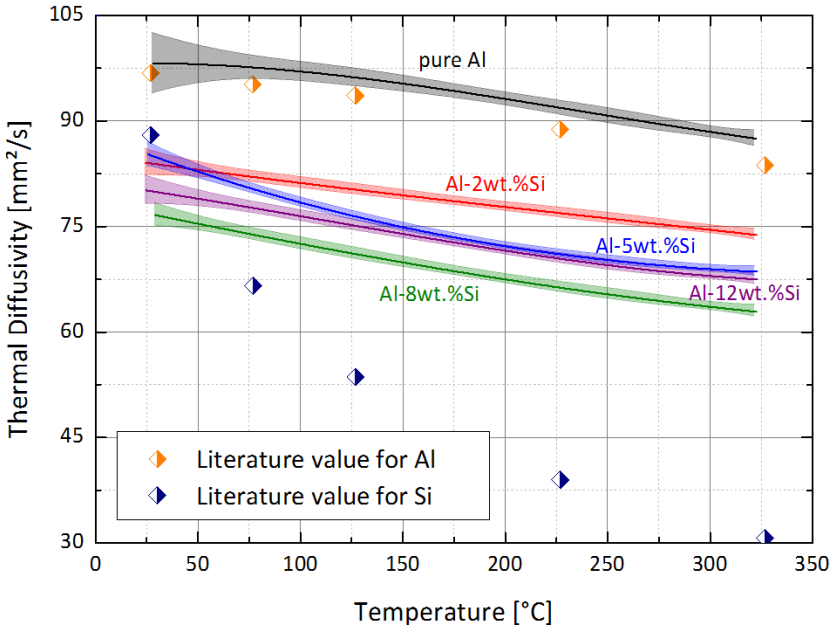


***Figure 7.3:*** *Summary of the thermal diffusivity of Al-Si alloys with different Si contents [Wol14].*

It can be observed that the thermal diffusivity of the AFIP-1 segment with 2 wt.%Si content lies in the range of the 12 wt.%Si content fuels. This is caused by the high Uranium loading of almost 9 $gU/cm^3$. This is almost 1 $gU/cm^3$ higher compared to the other fuels with Al-Si matrix. The high amount of low conductive Uranium reduces the thermal diffusivity of the fuel meat, see also Chapter 7.1.2. The E-FUTURE and E-FUTURE II fuels can be directly compared to each other, their Uranium loading does not differ significantly.

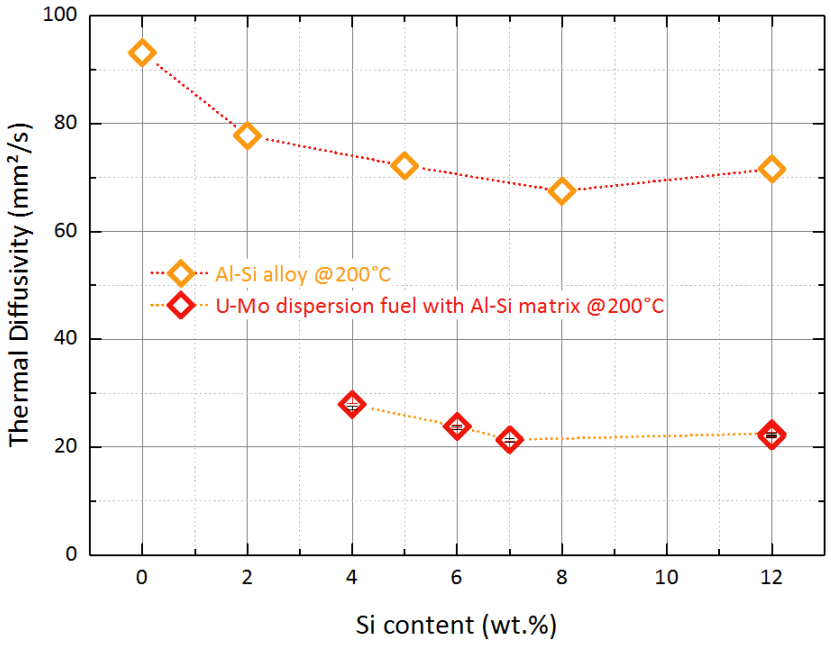


***Figure 7.4:*** *Thermal diffusivity of Al-Si alloys [Wol14] and U-Mo dispersion fuels with Al-Si matrix in dependence of the Si content.*

However, both Figures show that with increasing Si content, the thermal diffusivity decreases, but slightly increases again at $\sim 12$ wt.%Si content. This is illustrated in Figure 7.4. Here, the thermal diffusivity of Al-Si alloys and U-Mo dispersion fuels with Al-Si matrix is plotted against the Si content in the alloy, respectively matrix material. Also, here both curves indicate that the thermal diffusivity first decreases, but at about 6 wt.%Si content it starts to even slightly increase again.

A study was performed by [CHWT15], examining the microstructure and thermal conductivity of Al-Si alloys with Si additions between 0.5 wt.% to 14 wt.%Si content. Figure 7.5 shows SEM images of the different alloys.

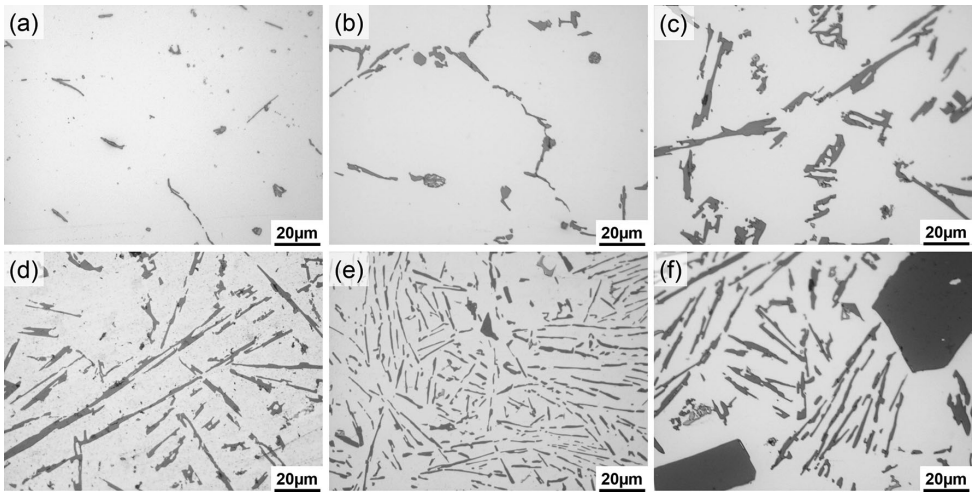


***Figure 7.5:*** *SEM images of Al-Si alloys with different Si contents: a) Al-*0.5 wt.%*Si, b) Al-*4 wt.%*Si, c) Al-*8 wt.%*Si, d) Al-*10 wt.%*Si, e) Al-*12 wt.%*Si and f) Al-*14 wt.%*Si [CHWT15].*

Until about 4 wt.% to about 6 wt.%Si content in the Al alloy, the Si is distributed over the material in the form of precipitates that grow with increasing Si content. [CHWT15] states that these precipitates serve as a series barrier for electron conduction and applies a series model of resistances to calculate the thermal conductivity for these alloys.
Above 6 wt.%Si content parallel eutectic lamellas grow. In general the thermal diffusivity would change to a tensor, but the lamellas are randomly distributed over the entire material, so that the thermal diffusivity can still be assumed as scalar.
The heat is then conducted along the lamellas, improving the overall heat transfer. For Si contents between 6 wt.% to about $\sim 12$ wt.%Si, [CHWT15] found that a parallel model of resistances (Maxwell model) best describes the heat conduction.
The eutectic phase at 12 wt.%Si content shows a full eutectic lamella microstructure. [CHWT15] applies here a combination of a series and parallel model that was originally developed for the simulation of the thermal conductivity of pearlite in cast iron.
Above 12 wt.%Si, the Si is distributed over the material in precipitates besides the lamella structure and [CHWT15] found that again the Maxwell model best describes the thermal conductivity of the alloy.

### 7.1.2 Dispersion Fuels with Ground U-Mo Powder and different Uranium Loading

In Figure 7.1, the green curves indicating fuels with atomized U-Mo powder, are significantly higher than the blue curves that indicate ground U-Mo powder. In these fuels, the heat transfer is restrained, due to the higher amount of porosity that is generated in the fuels during fabrication caused by the irregular particle shape of the ground powder. Additionally, the heat contact between the matrix material and the fuel particle is reduced due to the higher surface roughness of the ground powder compared to atomized powder that has a smoother surface providing better contact to the matrix material.

It can also be seen that the thermal diffusivity is very sensitive on uranium loading. The blue curves in Figure 7.2 show that the IRIS-TUM fuel with $7\,\mathrm{gU/cm^3}$ has a higher thermal diffusivity than the IRIS-TUM fuel with $8\,\mathrm{gU/cm^3}$. The thermal diffusivity of U-8 wt.%Mo ($5\,\mathrm{mm^2/s}$ [HBB+10]) is much lower than the thermal diffusivity of the matrix material with $60\,\mathrm{mm^2/s}$ to $100\,\mathrm{mm^2/s}$ [Wol14]. So, increasing the uranium loading, replaces parts of highly conductive matrix material by low conductive U-Mo and therefore, decreases the effective thermal diffusivity of the fuel meat.
Here, regarding IRIS-TUM7001 and IRIS-TUM 8003, that is fabricated from the same U-Mo ground powder, both with pure Al matrix, a difference of $1\,\mathrm{gU/cm^3}$ in the uranium loading causes a decrease of $\sim 4\,\mathrm{mm^2/s}$. Same effect was already observed for the AFIP-1 segment that only contains 2 wt.% Si in the Al alloy, but with a uranium content of almost $9\,\mathrm{gU/cm^3}$, see Table C.1 in Appendix A, it has a far higher uranium loading than the other fuels with $\sim 7\,\mathrm{gU/cm^3}$ to $\sim 8\,\mathrm{gU/cm^3}$.

### 7.1.3 Dispersion Fuels with Coated U-Mo Powder

Dispersion fuels fabricated from coated atomized U-Mo powder are in the same thermal diffusivity range as non-coated atomized U-Mo powder fuels. Figure 7.6 shows that the thermal diffusivity of dispersion fuels with different powder coatings only varies in a rather narrow band of $\sim 5\,\mathrm{mm^2/s}$.

Si has a higher thermal diffusivity than ZrN, which is a ceramic and consequently, the thermal diffusivity of the ZrN coated U-Mo powder fuels is lower than the Si coated U-Mo powder fuels. Those Si coated U-Mo powder fuels differ in the coating thickness, accordingly, the fuel with the thicker coating has a lower thermal diffusivity. The oxide coated U-Mo powder fuels are in the range of the ZrN coated U-Mo powder fuels, as uranium-oxide is as well a ceramic with low thermal diffusivity ($\sim 2\,\mathrm{mm^2/s}$ [RSMH99]).

### 7.1.4 In-pile Irradiated U-Mo Fuels

Figure 7.7 shows that the already low thermal diffusivity of monolithic U-Mo fuels further decreases during irradiation. On the one hand, the gaseous fission products form bubbles and more porosity is created that leads to a decrease of the thermal diffusivity. On the other hand, due to the high energy of the fission products (80 MeV) the crystal lattice of the fuel is destroyed in parts. As the heat is transferred via phonons and electrons, defects in the crystal lattice additionally lead to a higher thermal resistance.

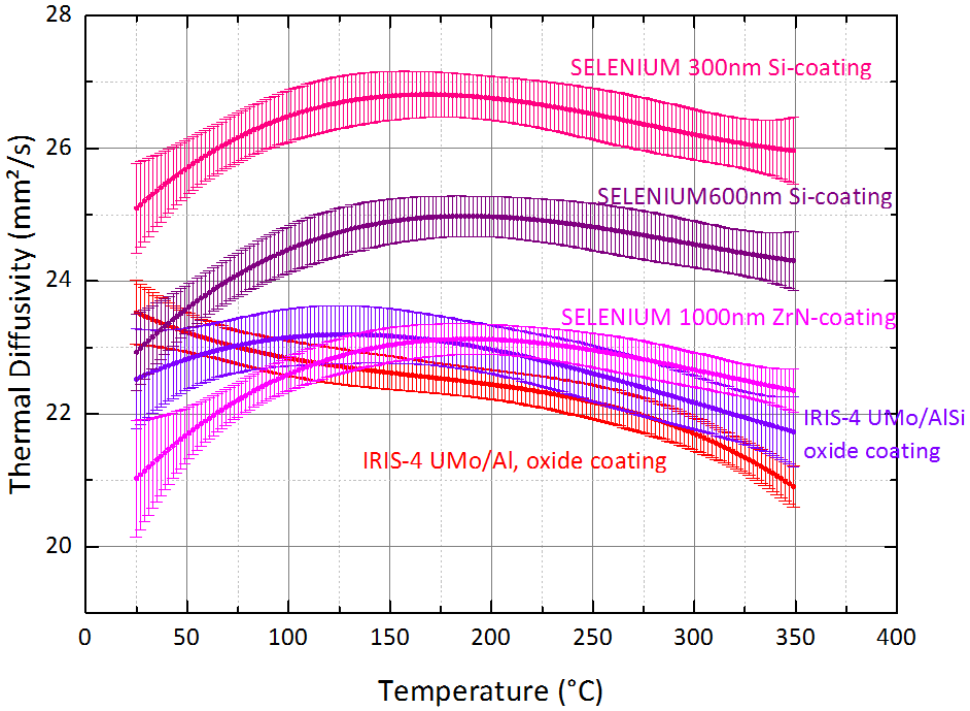


***Figure 7.6:*** *Thermal diffusivity of dispersion fuels containing coated atomized U-Mo powder.*

Figure 7.7 also shows that the thermal diffusivity of dispersion fuels stronger decreases during irradiation than the thermal diffusivity of monolithic fuels. In dispersion fuels, also the fission gas bubbles and lattice destruction in the fuel particles are an important factor that influence the thermal diffusivity of the entire fuel meat, but also the generation of the interaction layer around the fuel particles that consumes the matrix material. This layer has a very low thermal conductivity with about 15 $\mathrm{W/m{\cdot}K}$ and accordingly a very low thermal diffusivity. Therefore, it further reduces the effective thermal diffusivity of the fuel meat. More details on the calculation of the thermal conductivity of this interaction layer are presented in Chapter 8.4.

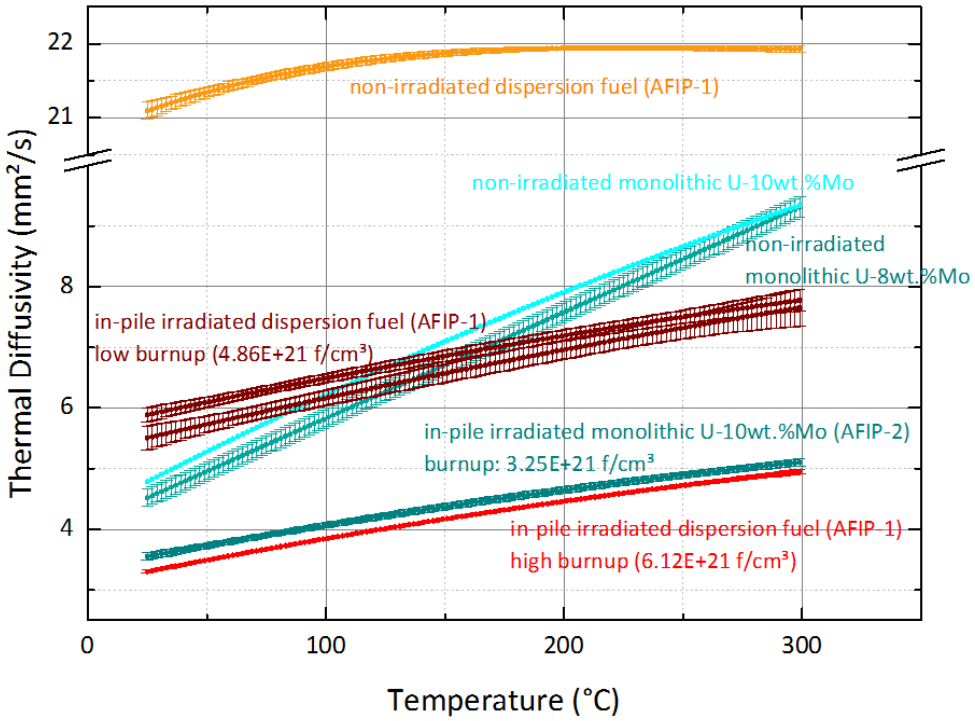


***Figure 7.7:*** *Comparison of the thermal diffusivity of fresh and in-pile irradiated dispersion and monolithic fuels.*

## 7.2 Specific Heat Capacity $c_p$

Figure 7.8 shows that the specific heat capacity $c_p$ of the fresh dispersion fuels lies in a narrow band between 0.2 J/gK and 0.3 J/gK with only very small variation between the different fuels. Table G.21 to G.39 in Appendix G.2 contains the parameters to calculate the specific heat capacity of the curves in the diagram.

The dispersion fuels have in general a similar composition and the particle shape or porosity do not directly impact the specific heat capacity. So, the specific heat capacity does not vary significantly between the fresh fuels, as it is mainly dependent on the material composition, see Figure 7.9.

The specific heat capacity of the fresh AFIP-1 segment (orange curve in Figure 7.9) overlaps the other curve below 150 °C. As already mentioned in Chapter 4.2, this segment was measured with a different DSC instrument. The operating temperature of this instrument starts at room temperature and the measurement is performed in one temperature step, which is different to the temperature cycles of the power-compensating DSC. So starting at room temperature, the DSC needs a certain time for the transient effect until about 100 °C to 150 °C. The larger error bars in the range from room temperature to about 100 °C indicate the inferior quality of the data compared to the quality of the data of the rest of the curve.

There is also just a small difference in the specific heat capacity between the fresh and irradiated dispersion fuels, see Figure 7.10. It is not impacted by most of the changes that happen to the material during irradiation except a small change in the material composition that results from

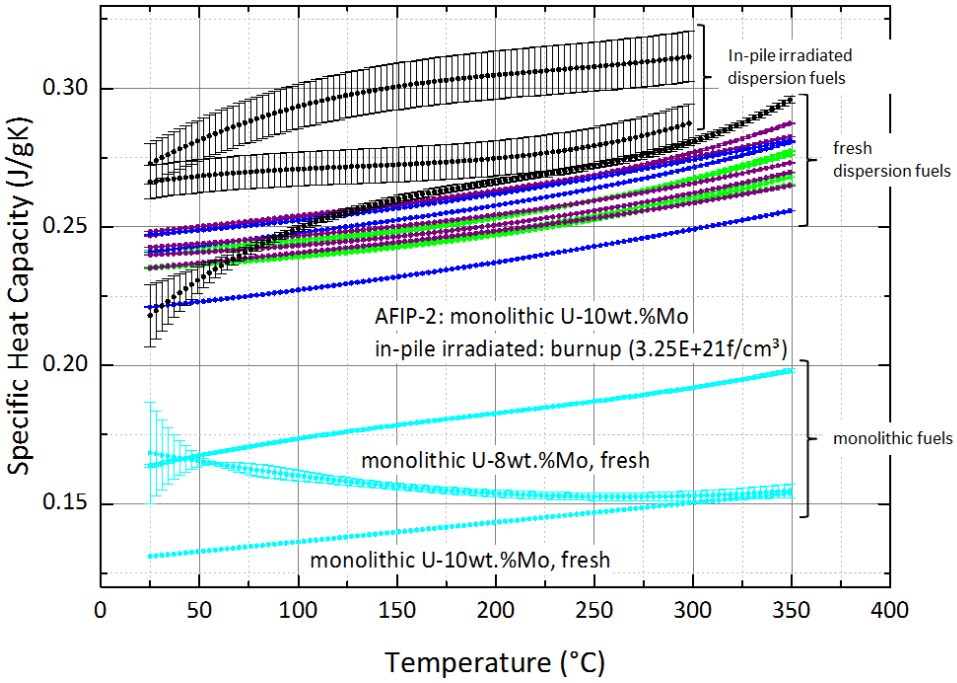


***Figure 7.8:*** *Summary of the specific heat capacity of fresh and in-pile irradiated dispersion and monolithic fuels.*

the solid fission products. But the fraction of generated fission products is about 5 % of the entire fuels atomic composition, which is very low for the sensitivity of the DSC. Another rather small impact comes from the change in the crystal lattice, which is (partially) destroyed during irradiation. The energy that is stored in the materials crystal lattice is part of the materials specific heat capacity and changes in the lattice have an impact on this property, accordingly.

The specific heat capacity of monolithic U-8 wt.%Mo [HBB+10] and U-10 wt.%Mo [BPM+10] is significantly lower than the specific heat capacity of dispersion fuels, see Figure 7.10. This is caused by the lack of matrix material, which mainly consists of materials with high specific heat capacities, like pure aluminum with about 0.9 J/gK [Tou70a].
The specific heat capacity of U-8 wt.%Mo is in the same range as the specific heat capacity of U-10 wt.%Mo, but is rather decreasing, while the specific heat capacity of U-10 wt.%Mo increases with increasing temperature. This may come from a different fabrication method of the two samples. The crystal lattice structure that is important for the specific heat capacity, is influenced by the fabrication process, especially the pressure and temperature. The U-8 wt.%Mo originates from machined sputter targets, while the U-10 wt.%Mo samples are produced from ingots. The different fabrication conditions are very likely to cause the deviation of the two curves.
Irradiation increases the specific heat capacity of the monolithic fuel in the same way as dispersion fuels does.

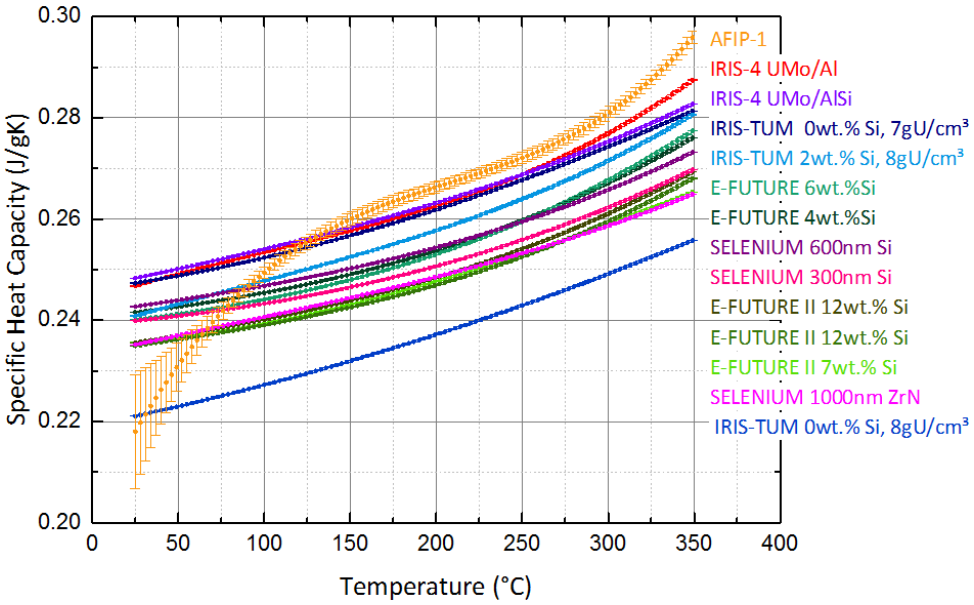


***Figure 7.9:*** *Comparison of the specific heat capacity of fresh dispersion fuels. The green colored curves are atomized powder fuels with Si in the matrix, the purple colored curves contain coated atomized fuel particles and the blue curves indicate fuels, fabricated from ground powder.*

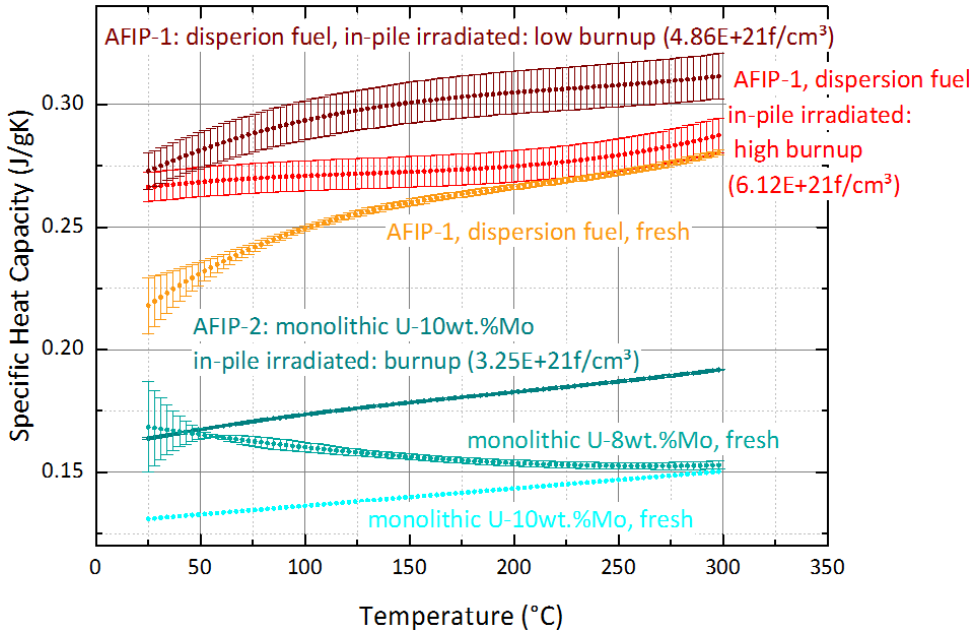


***Figure 7.10:*** *Comparison of the specific heat capacity of irradiated U-Mo fuels. The red colored curves indicate dispersion U-Mo fuels, the blue colored curves represent monolithic U-Mo.*

## 7.3 Density $\rho$

Figure 7.11 shows a summary of the density $\rho$ of fresh and irradiated dispersion and monolithic fuels. The density of fresh dispersion fuels lies in a narrow band around 10 $g/cm^3$. Small deviations in the porosity and uranium loading cause these small variations. The AFIP-1 sample shows the impact of irradiation on the density. With increasing burnup, more fission products are generated, of those mainly the gaseous products increase the fuels volume, leading to a decrease of the density.

The monolithic fuel has a significantly higher density than the dispersion fuels due to the lack of matrix material, which mainly consists of aluminum with a density of 2.7 $g/cm^3$. During irradiation, again mainly the generation of the gaseous fission products leads to a decrease of the fuels' density.

The values from Figure 7.11 can be found in Table G.40 in Appendix G.
Densities were only measured at room temperature ($\sim 25\,°C$). Temperature-dependent $\rho$-values were calculated as discussed in Chapter 3.3.

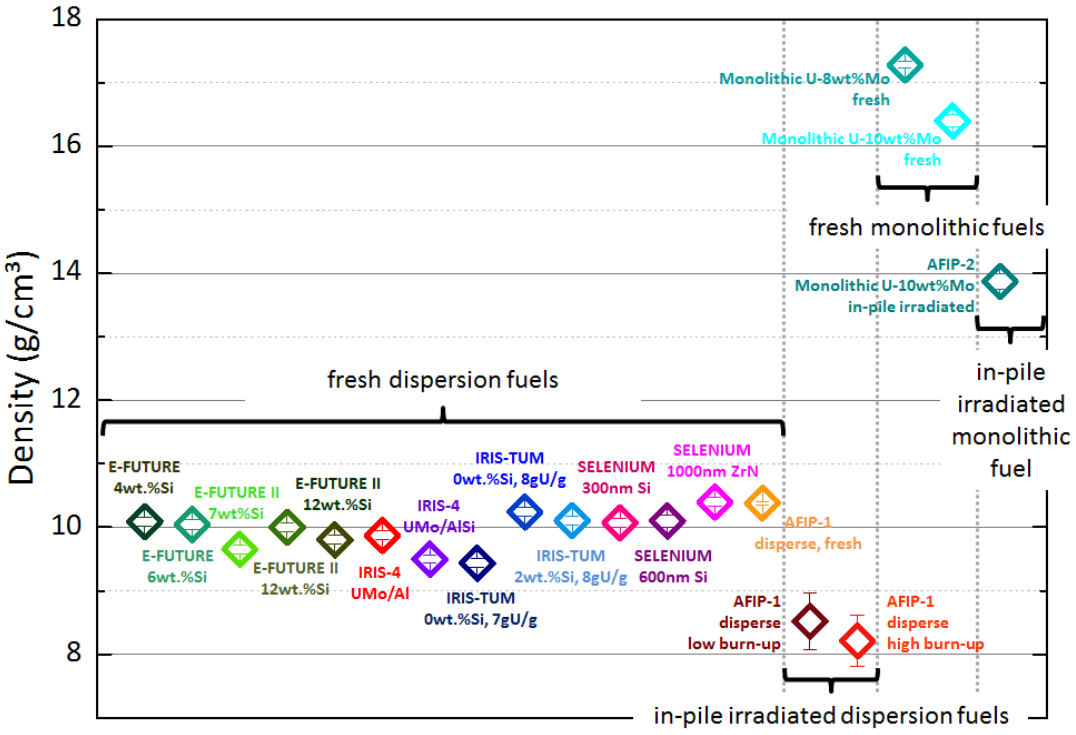


***Figure 7.11:*** *Summary of the density of fresh and irradiated dispersion and monolithic U-Mo fuels.*

# CHAPTER 8

## Thermal Conductivity

The thermal conductivity $\lambda$ is the product of the thermal diffusivity $\alpha$, the specific heat capacity $c_p$ and the density $\rho$, as shown in Chapter 3 in Equation 3.1:

$$\lambda = \alpha \cdot c_p \cdot \rho \tag{8.1}$$

Figure 8.1 shows a summary of the thermal conductivity of all investigated U-Mo fuels.

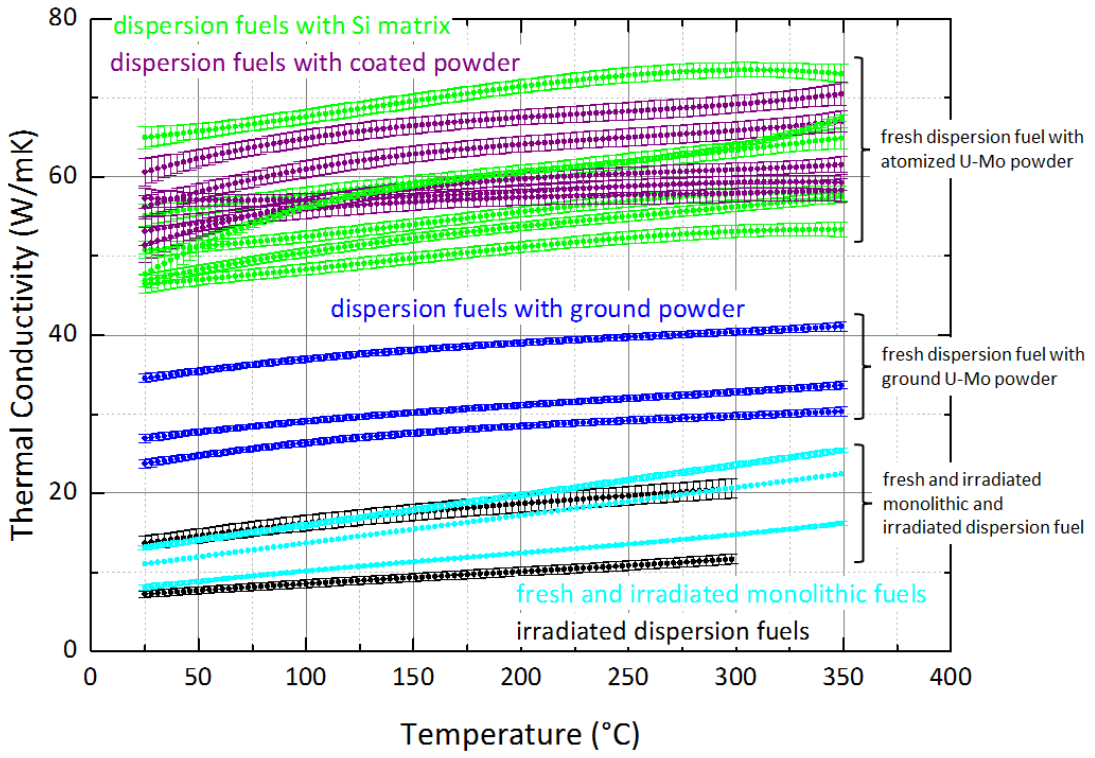


***Figure 8.1:*** *Thermal conductivity of fresh and irradiated dispersion and monolithic U-Mo fuels.*

The thermal conductivity has a similar variation for the different fuels (fresh and in-pile irradiated) as already the thermal diffusivity in Chapter 7.1, Figure 7.1. The thermal conductivities in the

following are all relating to a temperature of 50 °C, exceptions are explicitly denoted.
Fresh dispersion fuels fabricated from atomized powder, with or without particle coating, are in the range between 40 W/m·K and 80 W/m·K, while ground powder fuels are in a lower range between 20 W/m·K and 40 W/m·K. In-pile irradiated dispersion fuels is in the same range as monolithic U-Mo between 3 W/m·K and 20 W/m·K.

In the following, the thermal conductivity of the fuels will be discussed separately according to their type and differentiating fresh and irradiated fuel. The measured values are compared to theoretical values, calculated from the models in Chapter 3.4.2. Although the U-Mo alloy of dispersion fuels mostly contains 7 wt.% Mo, the thermal conductivity of U-8 wt.%Mo was used for calculation which should be close, as only the values for this composition and U-10 wt.%Mo are known.

## 8.1 Dispersion Fuels with Atomized U-Mo Powder and Si-Matrix

Figure 8.3 shows the thermal conductivity of fresh dispersion fuels with Al-Si matrix materials with differing Si content.

E-FUTURE and E-FUTURE II are dispersion fuels containing atomized powder with a uranium loading of 8 gU/cm³. The matrix materials consist of Al-Si alloys with 4 wt.% to 12 wt.% Si content.

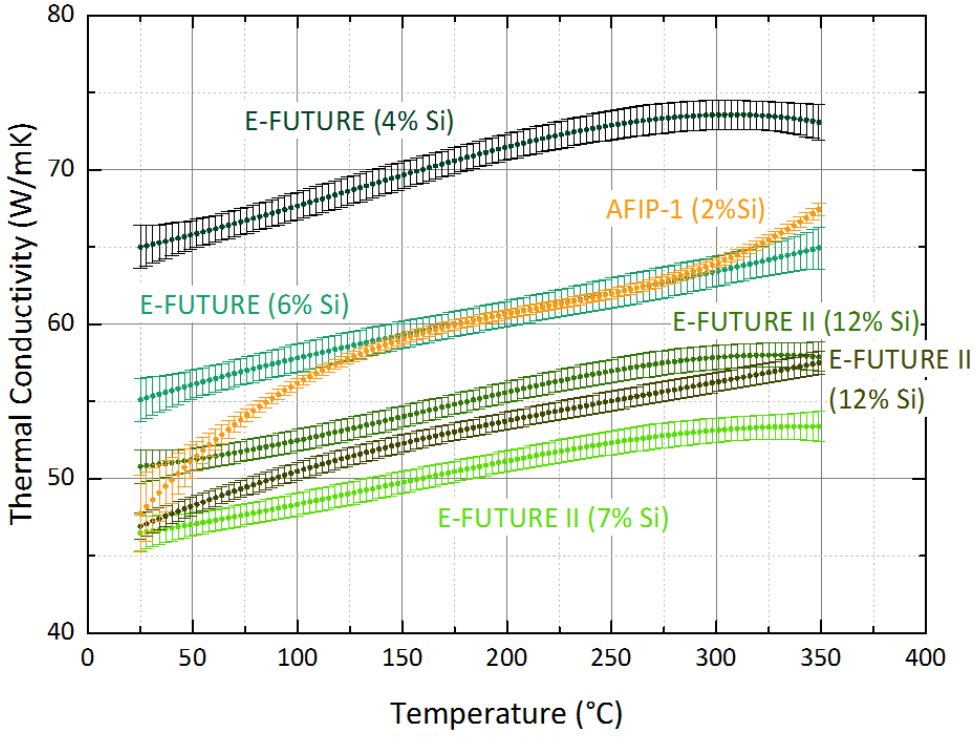


***Figure 8.2:*** *Summary of the thermal conductivity of dispersion fuels with Si addition in the matrix.*

Pure Al has a thermal conductivity of about 240 W/m·K [Tou70b], which is significantly higher than the thermal conductivity of Si with about 150 W/m·K [Tou70b]. So, the thermal conductivity

of these fuels is expected to be mainly dependent on the Si content, as the uranium loading and composition is almost constant, see Table C.1 in Appendix A.

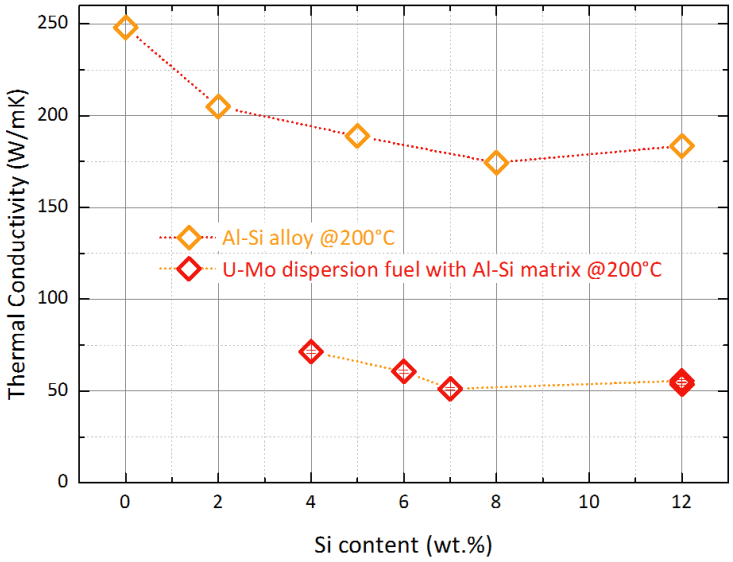


***Figure 8.3:*** *Thermal conductivity of Al-Si alloys [Wol14] and U-Mo dispersion fuels with Al-Si matrix in dependence of the Si content.*

For perfect mixtures, the thermal conductivity of the fuels should decrease with increasing Si content. A deviation from this behavior can be again observed regarding the 7 wt.% and 12 wt.% Si E-FUTURE II fuel, see Figure 8.3. The thermal conductivity of the 12 wt.% Si fuel is higher than the thermal conductivity of the 7 wt.% fuel. This behavior has already been observed for the thermal diffusivity in Chapter 7.1. The reference measurements of Al-Si alloys with similar Al-Si composition showed exactly the same behavior for the thermal conductivity, as the specific heat capacity and density did not show any abnormalities, see Figure 8.4 and 8.5 [Wol14]. The red lines are fitted straights to the data at 200 °C. They show that the density and specific heat capacity decrease steadily with increasing Si content. But the decrease in the specific heat capacity and density does not compensate the behavior of thermal diffusivity and its behavior is reflected in the thermal conductivity of the Al-Si alloys, as well as the dispersion fuels containing these alloys as matrix material.

It has been mentioned earlier in Chapter 3.4.2 that the thermal conductivity of dispersed materials can be calculated with the Hsu model (Equation 3.26). Figure 8.6 shows a comparison between the measured and the calculated values for the temperature range from 50 °C to 300 °C. The porosity has been included by repeating the calculation with the porosity as dispersed phase. Its thermal conductivity is assumed to be 0 $^{W}/_{m \cdot K}$.

For the calculation, the thermal conductivity of U-8 wt.%Mo [HBB+10] has been used for the fuel particle. The thermal conductivity for the matrix with the different Si contents was taken accordingly for each fuel from [Wol14]. As fuel particle geometry, a sphere was assumed to calculate the function of eccentricity.

It can be seen that the calculated and measured values for AFIP-1 with 2 wt.%Si in the matrix and E-FUTURE with 4 wt.%Si in the matrix are in very good accordance. Both dispersion fuels

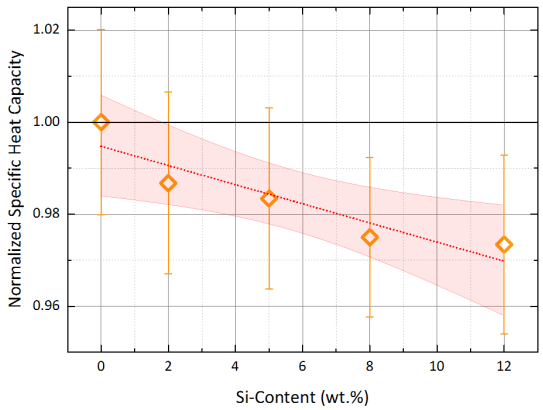


***Figure 8.4:*** *Specific heat capacity of Al-Si alloys, normalized to pure Al in dependence of the Si content at* 200 °C *[Wol14].*

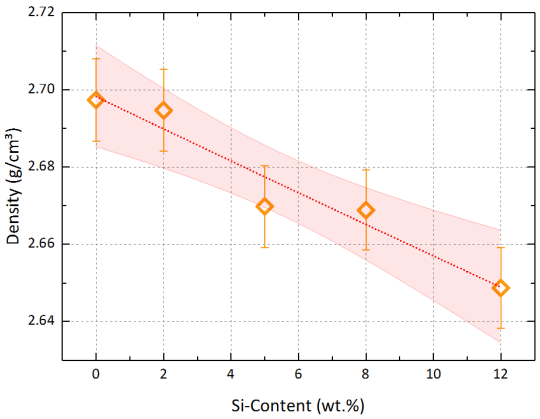


***Figure 8.5:*** *Density of Al-Si alloys in dependence of the Si content at* 200 °C *[Wol14].*

contain atomized U-Mo powder, which is very close to the spherical shape that the theoretical model assumes.

But for fuels with higher Si content than 4 wt.%, the calculated and measured values start to deviate beyond the 10 % line. The calculated thermal conductivity value of E-FUTURE with 6 wt.%Si in the matrix already deviates about 15 %, the value of E-FUTURE II with 7 wt.%Si and 7 wt.%Si in the matrix deviate more than 20 % from the measured thermal conductivity value.

In this case, the formation of the Si rich layer around the U-Mo particle during fabrication has to be taken into account. This Si rich layer consists of different phases: $U(Al,SI)_3$, $UMo_2Al_{20}$ and $U_3Si_5$ [API$^+$10]. The thermal conductivity of these phases is unknown and the thickness of this layer varies. So, the thermal conductivity of dispersion fuels with atomized U-Mo particles with a Si content above 4 wt.% in the matrix is overestimated by this model. It can be used to give an estimation for thermal conductivity, but a measurement is mandatory to obtain accurate values.

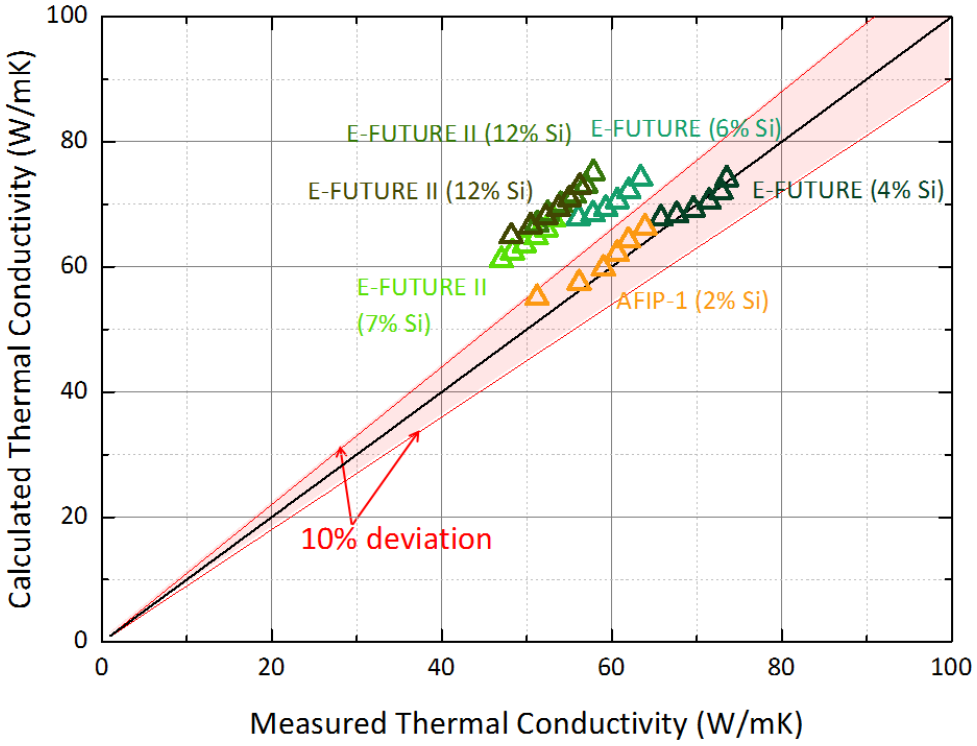


***Figure 8.6:*** *Comparison of the thermal conductivity between* 50 °C *and* 300 °C *obtained by measurement and calculation of dispersion fuels containing atomized U-Mo powder. The black line represents perfect agreement, the red lines represent a* 10 % *deviation between measured and calculated values.*

## 8.2 Dispersion Fuels with Ground U-Mo Powder and different Uranium loading

Figure 8.7 shows the thermal conductivity of the IRIS-TUM fuels that are fabricated from ground powder.

As already seen in Chapter 7.1 in Figure 7.1, the thermal diffusivity is strongly impacted by the particle shape and accompanying porosity, and is simultaneously the parameter with the highest impact on the thermal conductivity. Accordingly, the thermal conductivity of the ground powder fuel is lower than the thermal conductivity of the atomized powder fuel.
Additionally, the impact of the uranium loading can be observed. Due to the low thermal conductivity of U-Mo, the fuel with higher uranium loading has a significantly lower thermal conductivity. Here, the fuel with 8.5 $\mathrm{gU/cm^3}$ has a 10 $\mathrm{W/m{\cdot}K}$ lower thermal conductivity than the fuel with 7.3 $\mathrm{gU/cm^3}$. This is a relative decrease of almost 30 %.
In Figure 8.7 the thermal conductivity of the IRIS-TUM fuel without Si in the matrix is higher than the thermal conductivity of the fuel with 2 wt.%Si. But here, the Uranium loading of the 2 wt.%Si plate is also 0.2 $\mathrm{gU/cm^3}$ higher than the fuel without Si. So, the Uranium loading has a higher impact on the thermal conductivity than the Si content, as the thermal conductivity of Si is closer to the thermal conductivity of the Al than the uranium.

The thermal conductivity of the dispersion fuels fabricated from ground powder is again calculated with Equation 3.26, but this time the U-Mo particles cannot be assumed to be spheres, see

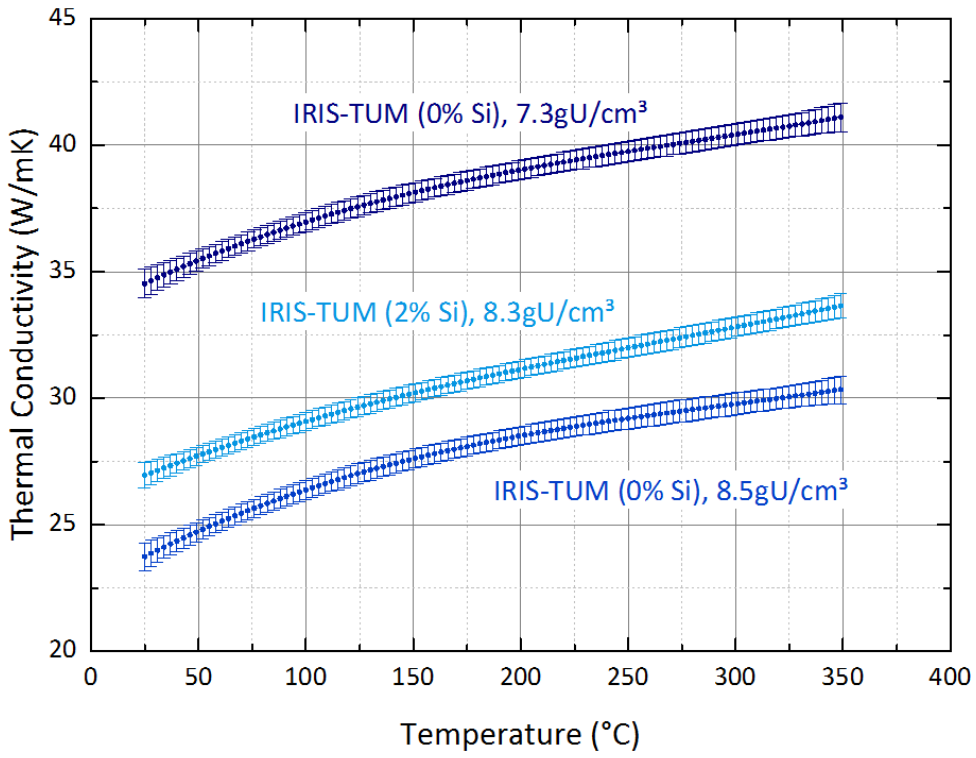


***Figure 8.7:*** *Summary of the thermal conductivity of dispersion fuels containing ground powder with different Uranium loading (the exact values can be found in Table C.1 in Appendix A.*

Figure 8.9. So, the function of eccentricity for prolate spheres has been used, assuming a fraction of approximately $\frac{1}{3}$ for the semi-minor axis to the semi-major axis. Again the porosity has been considered as an additional dispersed phase.

Figure 8.8 shows that the calculation for segment with $8\,\mathrm{gU/cm^3}$ and 2 wt.% Si in the matrix is in quite good agreement with measurement for low temperatures, but for temperatures above 50 °C, the calculated values are increasingly above the red 10 % deviation line.
The other two segments are completely out of the 10 % deviation range, also with increasing deviation for increasing temperature.
A reason for this temperature dependent deviation can come from the temperature dependence of the density. The calculation of the thermal conductivity of the Al already includes the temperature dependence of the density, but for the calculation of the U-Mo thermal conductivity, the temperature dependence can neglected, as the volume expansion based on the thermal expansion coefficient of $12 \cdot 10^{-6}/\mathrm{K}$ [BPM+10] is low compared to Al with $26 \cdot 10^{-6}/\mathrm{K}$ [HK52] for the temperature range of 20 °C to 300 °C.
With increasing temperature, the Al expands also into the porosity, so that it is not obvious that the density, contemplated over the entire volume of the fuel segment, decreases corresponding to the linear expansion. In case the density does not decrease as much as expected by calculation, the calculation overestimates the thermal conductivity for higher temperatures.

One major reason for general high deviation of these two segments without Si in the matrix may come from impurities in the aluminum of the matrix. The calculation has been performed for pure Al, but during the fabrication process in oxygen atmosphere, the Al powder reacts with the oxygen and forms Aluminum oxides with reduced thermal conductivity. The thermal conductivity

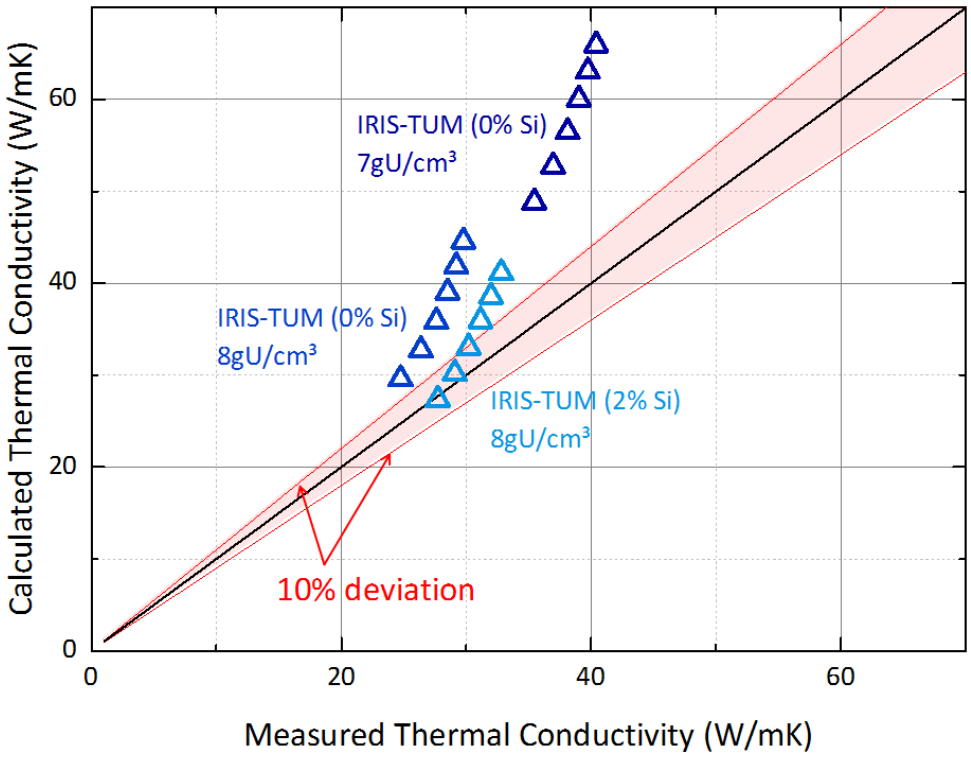


***Figure 8.8:*** *Thermal conductivity of the ground powder U-Mo fuels between* 50 °C *and* 300 °C *obtained by measurement and calculation based on prolate spheres. The black line represents perfect agreement, the red lines represent a* 10 % *deviation between measured and calculated values.*

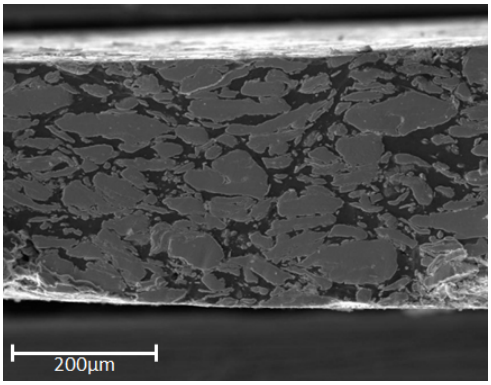


***Figure 8.9:*** *Scanning electron microscope image of an as-fabricated IRIS-TUM fuel segment.*

is very sensitive on impurities and decreases significantly already for marginal additions, as observed for 2 wt.%Si in [Wol14].
Further, Uranium oxides have a thermal conductivity of $\sim$ 7 $^{W}/_{m\cdot K}$ [Fin00], compared to U-8 wt.%Mo with $\sim$ 14 $^{W}/_{m\cdot K}$ [HBB+10] at 50 °C, and therefore reduces the effective thermal conductivity of the U-Mo particles. As the exact amount of Uranium oxide cannot be determined, it is not possible to consider this in the calculation.

So, due to the irregular shape of the particles that only can be described approximately, the inhomogeneous size distribution and the above-average unknown oxide content due to the

fabrication process, it is not feasible to calculate the thermal conductivity of dispersion fuels containing ground powder accurately and a measurement is mandatory.

## 8.3 Dispersion Fuels with Coated U-Mo Powder

Figure 8.10 shows the thermal conductivity of dispersion fuels fabricated from atomized powder with different particle coatings.

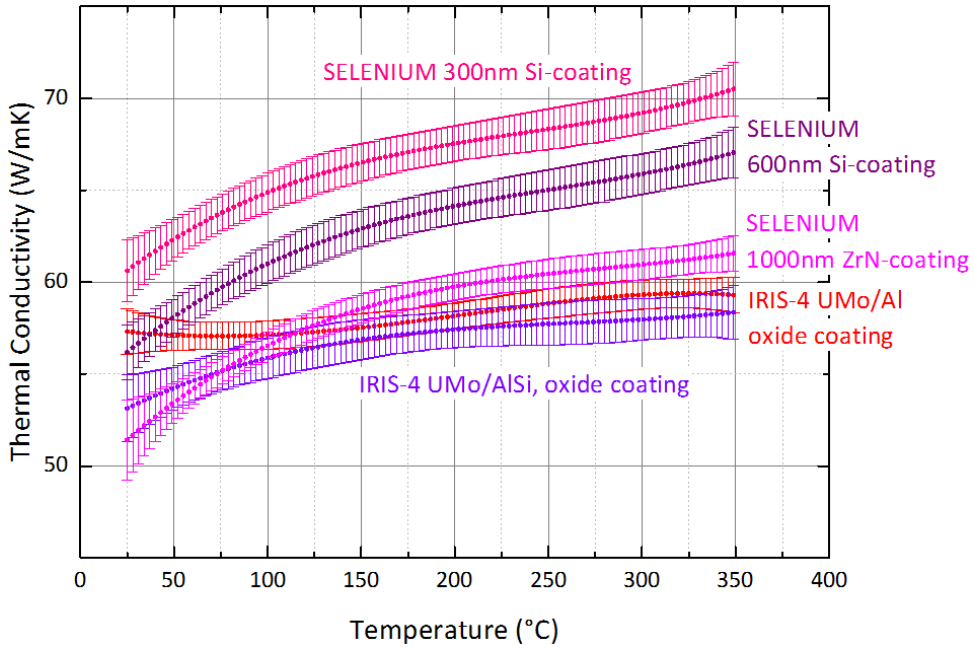


***Figure 8.10:*** *Thermal conductivity of dispersion fuels containing coated atomized U-Mo powder.*

The thermal conductivity of the Si coated fuels is comparable to the thermal conductivity of fuels with Si in the matrix material. Consistently, the fuel with thicker Si coating has a lower thermal conductivity. The fuels with oxide and ZrN coating have a similar thermal conductivity that is lower than the Si coated particle fuels thermal conductivity. Both coatings are ceramics with a low thermal conductivity of $\sim 7\,\mathrm{W/m{\cdot}K}$ [Fin00] for uranium oxide and $\sim 14\,\mathrm{W/m{\cdot}K}$ for ZrN, compared to Si.

For the calculation of the coated atomized powder fuels, first the effective thermal conductivity of the coated U-Mo particle with spherical shape is calculated with Equation 3.28 in Chapter 3.4.2. This effective thermal conductivity for the coated U-Mo particle is then used to calculate the meat thermal conductivity for dispersion fuels containing atomized powder (without coating) with Equation 3.26 in Chapter 3.4.2, analogous to Chapter 8.1.
In this case, the particle radius is needed for the calculation. For the SELENIUM fuel (Si and ZrN coating), the U-Mo powder was sieved before coating, so that the mainly smaller particles are sorted out and the resulting fuel particle diameter ranges from 60$\mu$m to 80$\mu$m. Accordingly, For the SELENIUM fuels, a mean particle diameter of 70$\mu$m was used in the calculation [Lee14]. The mean particle diameter for the IRIS-4 fuel (oxide coating) is assumed to be smaller, as the particles are not sorted before plate fabrication and therefore contain a certain fraction of particles with a diameter smaller than 60$\mu$m. As there is actually no information about the

particle size distribution of this fuel, based on this information, a mean particle diameter of 60$\mu$m was used for calculation. However, the model is not very sensitive on the fuel particle diameter, as a difference of 10$\mu$m for the fuel particle diameter results in a difference of 1 $^{W}/_{m\cdot K}$ of the thermal conductivity of the entire fuel meat.
Figure 8.11 shows the result of the calculation for all dispersion fuels with coated powder.

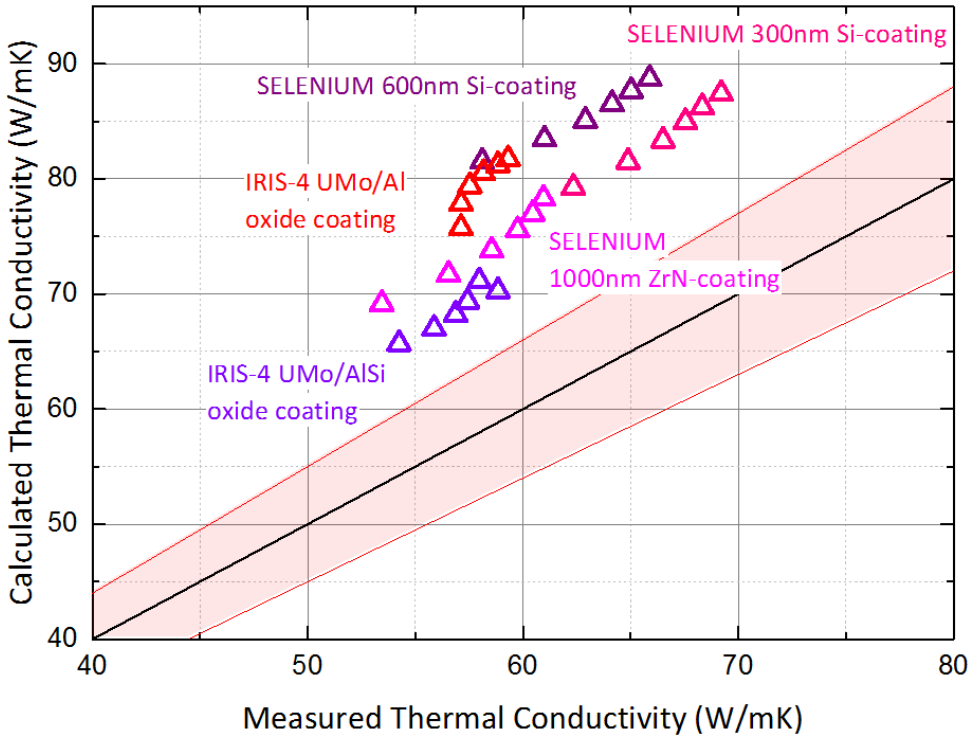


***Figure 8.11:*** *Thermal conductivity of dispersion fuels containing coated atomized U-Mo powder between* 50 °C *and* 300 °C *obtained by measurement and calculation. The black line represents perfect agreement, the red lines represent a* 10 % *deviation between measured and calculated values.*

The results of the calculations based on the nominal fuel composition from the fabrication certificates deviate between 15 % to almost 30 % from the measured thermal conductivity values. The reasons for the deviation are different for each fuel type. In the following, the results will be discussed in detail separately for each coating.

### 8.3.1 Si-coating

One type of the SELENIUM fuel contains atomized powder with Si coating in a pure Al matrix. Si has a thermal conductivity of 150 $^{W}/_{m\cdot K}$ [Tou70b] that is high compared to the thermal conductivity of U-8 wt.%Mo (14 $^{W}/_{m\cdot K}$ [HBB+10]). Hence, the effective thermal conductivity of the coated U-Mo particle is higher than the thermal conductivity of the non-coated U-Mo particle. Consequently, a higher effective particle thermal conductivity for coated particles leads in the calculation of the meat thermal conductivity to higher values than for uncoated particles if the calculation is performed with the same thermal conductivity of the matrix material. But, the measured values of the meat thermal conductivity with coated particles are in the same range as the values of uncoated particles.
Investigating SEM images of the SELENIUM fuel (see Figure 8.12), it can be observed that the

Si is not only confined in a layer around the U-Mo particle, but is also distributed in compounds as well as precipitates all over the matrix material. So, the first applied thermal conductivity of a pure Al for the matrix material needs to be adjusted, as impurities in general reduce the thermal conductivity of Al. A reduction of the matrix thermal conductivity of 20 %, decreases the thermal conductivity of the meat, so that the calculated thermal conductivity is well within the 10 % deviation boundary with the measured thermal conductivity, see Figure 8.14.
However, the calculated thermal conductivity of the 300 nm Si coated fuel still deviates slightly more than 10 % from the measured values. As a detailed fabrication certificate was not available, the same fuel composition has been chosen as for the 600 nm Si coated fuel for the calculation of the thermal conductivity, but with a 300 nm Si layer instead of a 600 nm Si. As both fuels have been fabricated from the same U-Mo powder by the same manufacturer, the composition can be assumed to be very similar. However, the calculation shows quite a small difference that most probably can be explained by a slightly different fuel composition.

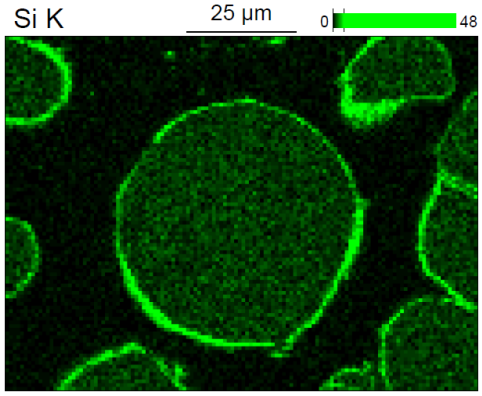


***Figure 8.12:*** *SEM image of the Si coated SELENIUM fuel [JZC+ 13].*

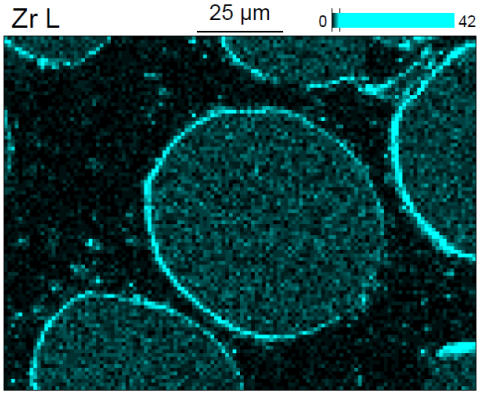


***Figure 8.13:*** *SEM image of the ZrN coated SELENIUM fuel [JZC+ 13].*

### 8.3.2 ZrN-coating

ZrN has a thermal conductivity of 14 $W/m \cdot K$, which is similarly low thermal conductivity as the thermal conductivity of U-8 wt.%Mo. Hence, the effective thermal conductivity of the coated sphere is roughly the same as for non-coated spheres. Also here, based on the information from the fabrication certificate, the thermal conductivity of pure Al has been used for the matrix material for the calculation of the meat thermal conductivity. Again, the calculated value is much higher than the measured value, see Figure 8.11.

The examination of SEM images (see Figure 8.13) shows that Zr, like the Si in the previous case, can be found in the matrix as compounds and precipitates that reduce the thermal conductivity of the Al in the matrix. The SEM images do not show the nitride, as it is very difficult to detect with SEM and EDX, but it can be assumed that the nitride is distributed over the matrix together with the Zr. It can be assumed that ZrN with its low thermal conductivity of 14 $W/m \cdot K$ reduces the thermal conductivity of the Al in a similar manner as the Si does. But, there is no exact information about the amount of Zr in the matrix, how it is composed with the Al and also about the thermal conductivity of the Al-Zr compositions.
During Focused Ion Beam (FIB) examination that the ZrN coating partly peels off the matrix material, which reduces the thermal contact between fuel particle and matrix leading to a decrease

of the thermal conductivity. Further, the actual ZrN layer has not the nominal thickness of 1$\mu$m. the actual thickness lies between 0.4$\mu$m and 0.5$\mu$m. This does not significantly influence the calculation. The effective thermal conductivity of the coated particle does not change, due to the similar thermal conductivity of the coating and the fuel particle. Therefore, in the fuel meat calculation only the particle diameter is influences. It is reduced by maximum 0.5$\mu$m. As already mentioned before, a difference of 10$\mu$m in the particle diameter causes a difference of 1 $^{W}/_{m\cdot K}$ in the thermal conductivity. So, the thermal conductivity is not very sensitive on the coating thickness.
Thus, mainly the matrix reduces the thermal conductivity of the meat and the calculation showed that a reduction the thermal conductivity of the matrix of 20 %, reduces the average meat thermal conductivity in a way that the calculated values are within the 10 % boundary of the measured values, see Figure 8.14.

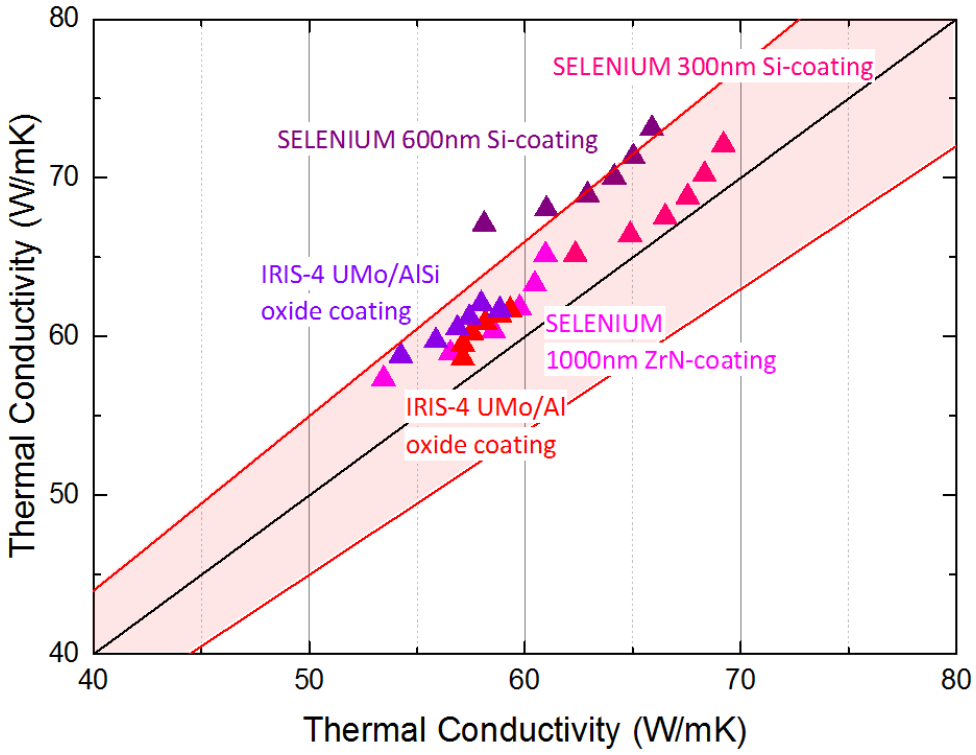


***Figure 8.14:*** *Thermal conductivity of dispersion fuels containing coated atomized U-Mo powder between* 50 °C *and* 300 °C *obtained by measurement and calculation. The black line represents perfect agreement, the red lines represent a* 10 % *deviation between measured and calculated values.*

### 8.3.3 Oxide-coating

A different problem can be observed regarding the oxide coated IRIS-4 fuels. Uranium oxide has about half the thermal conductivity of U-8 wt.%Mo: 7 $^{W}/_{m\cdot K}$ [Fin00]. The consequence is that the effective thermal conductivity of the coated U-Mo spheres is lower than the thermal conductivity of non-coated U-Mo spheres. But, the calculation of the thermal conductivity of the meat with a pure Al matrix for the IRIS-4 UMo/Al fuel or Al-2 wt.%Si matrix for the IRIS-4 UMo/AlSi fuel results in significantly higher values than the measurement, see Figure 8.11.

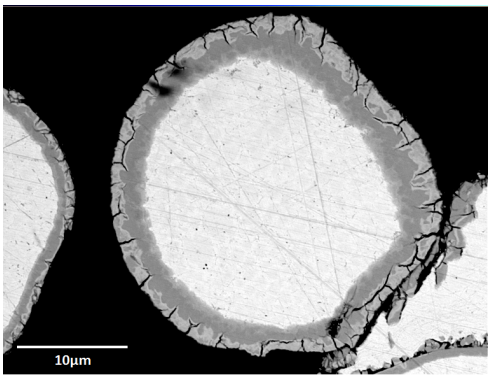


***Figure 8.15:*** *SEM image of the oxide coated IRIS-4 fuel [Zwe14].*

Due to the brittleness of the Uranium oxide, during fabrication parts of the oxide layer can break away from the fuel particles and get distributed over the matrix material causing impurities. In contact with air, the Al powder that is used for the matrix material, forms Al oxides that have a low thermal conductivity (46 $^{W}/_{m \cdot K}$ at room temperature for Corundum [MW]), reducing the thermal conductivity of the matrix material. Analogous to the SELENIUM fuels, a reduction of the matrix thermal conductivity of 20 % was used for the recalculation. But the calculated values were still more than 10 % higher than the measured values.
An examination of SEM images of the IRIS-4 fuel (see Figure 8.15) shows multiple cracks all around the oxide coating. Those cracks reduce the thermal conductivity in a similar manner as porosity. As the cracks are radial to the fuel particle, while the LFA measures only the heat flow in one direction, so that the thermal diffusivity would be a tensor with different values for the different directions. But as the LFA measurement averages over millions of particles, it is valid to calculate with a scalar thermal diffusivity. A short note besides the actual problem: During irradiation, the heat flux from the fuel particle to the matrix is not vectored in one direction, but is rather a radial flux, parallel to the cracks. In this case more surface is available for the heat transfer and the average fuel meat thermal diffusivity and therefore conductivity, assuming no change in the density and specific heat capacity, may be increased.
Reducing now the thermal conductivity of the oxide layer down to 1 $^{W}/_{m \cdot K}$ and recalculate the fuel meat with the adapted parameters, the calculated thermal conductivity of the fuel meat is within the 10 % range of the measured values, see Figure 8.14.

### 8.3.4 Si-rich layer

In Chapter 8.1, the calculation of the thermal conductivity of the E-FUTURE dispersion fuels with atomized powder and Si content above 4 wt.%Si showed significant deviations above 10 % from the measured values. As these fuels are known to form a Si rich layer around the fuel particles, the assumption stands to reason that the thermal conductivity can be calculated for a coated sphere. But the Si does not form a homogeneous well defined layer around the particles resulting in large deviations in the layer thickness. Further, it is not known how much of Si stays distributed over the Al matrix material, as the density of the Si rich layer is unknown. So, it is not possible to accurately calculate the thermal conductivity of these fuels this way.

### 8.3.5 Conclusion

In general, the thermal conductivity values calculated with the model are higher than the measured values. In the calculation, the parameters are given by the fabrication certificates that give information about the nominal fuel composition, like for example the amount of U-Mo powder and Al or Al-Si powder that is used for the fabrication process. Theoretically, the composition does not change, but in the real fabrication process, the different materials for example form compounds or are not homogeneously distributed over the entire fuel plate leading to deviations in the composition of single segments out of the entire fuel plate.
Further, the values for the pure aluminum as matrix material origin from measurements of 99.998 % pure Al [Wol14]. But considering the chemical analysis of the Al powder, used for the production of the fuel plates, the Al contains up to 0.5 % impurities, mainly Iron and Silicon. As the thermal conductivity of Al is very sensitive on already small amounts of impurities, the thermal conductivity of the actual matrix material is lower than theoretically assumed. Additionally, Al alloys are sensitive on heat treatment. Al alloys with the same alloy composition but different temper have different thermal conductivities. An example is the Al alloy 6061 used for the cladding of the US test plates. Al 6061 with temper O, i.e. the annealed alloy, has a thermal conductivity of 180 $^{W}/_{m\cdot K}$, while thermal conductivity of Al 6061 alloys with temper T that are heat treated and cold worked in different ways, have thermal conductivities between 150 $^{W}/_{m\cdot K}$ and 170 $^{W}/_{m\cdot K}$ [MW].

## 8.4 In-pile Irradiated U-Mo Fuels

Figure 8.16 shows a comparison of fresh and in-pile irradiated dispersion U-Mo fuels in relation to fresh and in-pile irradiated monolithic U-Mo fuels.

The thermal conductivity of the fresh AFIP-1 dispersion fuel containing atomized powder in Al-2 wt.%Si matrix is in the same range as the other investigated dispersion fuels, see Chapter 8.1. But during irradiation, the thermal conductivity strongly decreases over the temperature range from 25 °C to 300 °C with increasing burnup from $(50-65)$ $^{W}/_{m\cdot K}$ down to $(14-20)$ $^{W}/_{m\cdot K}$ at $4.86\cdot10^{21}$ $^{f}/_{cm^3}$, which is comparable with fresh monolithic U-8 wt.%Mo [HBB+10] and U-10 wt.%Mo [BPM+10]. With further irradiation to a burnup of $6.12\cdot10^{21}$ $^{f}/_{cm^3}$ the thermal conductivity further decreases down to $(7-13)$ $^{W}/_{m\cdot K}$ which is about 15 % of the original value of the fresh fuel.

The thermal conductivity of irradiated monolithic fuel only decreases from $(12-20)$ $^{W}/_{m\cdot K}$ to $(8-15)$ $^{W}/_{m\cdot K}$, which is about 75 % of the original value of the fresh fuel at a burnup of $3.25\cdot10^{21}$ $^{f}/_{cm^3}$ [BCB+13].

Figure 8.17 shows the trend of the thermal conductivity during irradiation for dispersion and monolithic fuel at a exemplary temperature of 200 °C.
The thermal conductivity of dispersion fuel decreases about 70 % until a burnup of $4.86\cdot10^{21}$ $^{f}/_{cm^3}$, but only further 15 % to a burnup of $6.12\cdot10^{21}$ $^{f}/_{cm^3}$ . This shows that the thermal conductivity decreases very fast at the beginning of irradiation, but with ongoing irradiation, the decrease is decelerated.
The thermal conductivity of monolithic fuel only decreases about 25 % until a burnup of $3.25\cdot10^{21}$ $^{f}/_{cm^3}$. Although the thermal conductivities of monolithic and dispersion fuel are

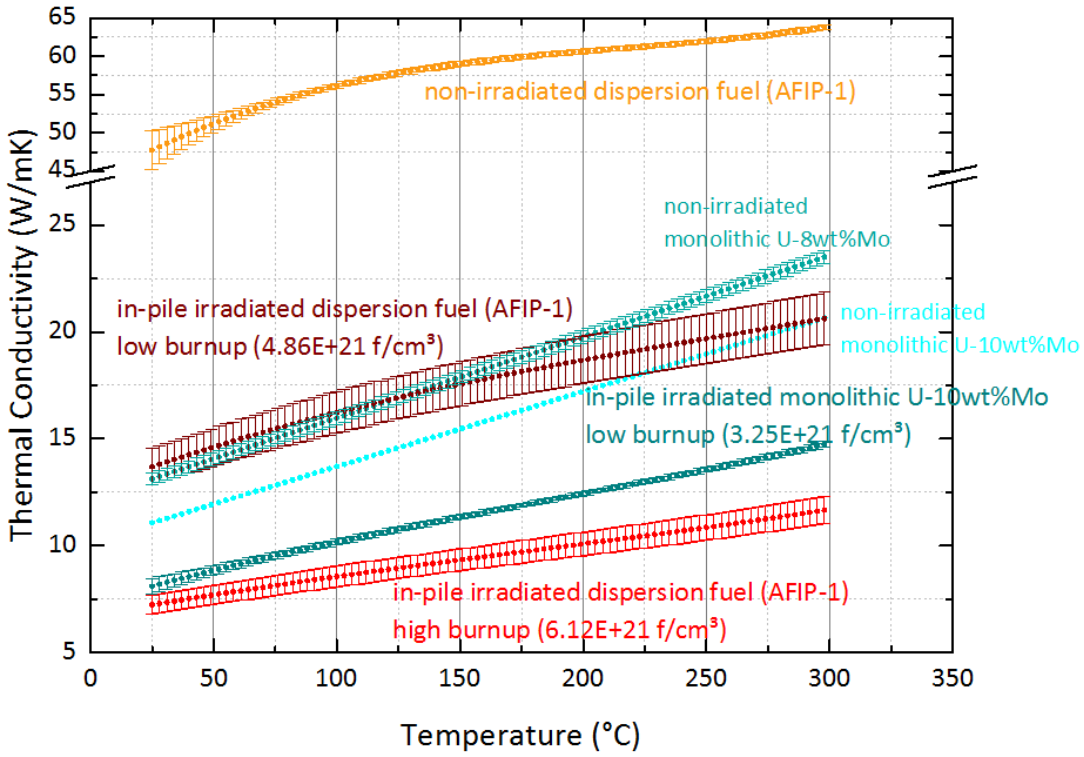


***Figure 8.16:*** *Comparison of the thermal conductivity of fresh and in-pile irradiated dispersion and monolithic fuels.*

not directly comparable, they clearly show that the thermal conductivity of dispersion fuel decreases at least at the beginning faster than the monolithic fuel.

In both fuels, monolithic and dispersion, the fission-induced formation of fission gas bubbles and the decomposition of the U-Mo crystal lattice lead to a decrease in the thermal conductivity. But, in the case of the dispersion fuel, additionally, the matrix material is more and more consumed by the inter-diffusion layer (IDL) that is generated during irradiation due to the reaction of the uranium in the fuel particles with the aluminum matrix. Further, the range of the fission products is due to their high kinetic energy, in average 80 MeV, longer than the average distance between the U-Mo particles. So, the matrix material gets cumulatively doped with fission products, which leads to a hardening of the matrix material during irradiation [BL14]. The hardening reduces the creeping of the Al that causes the formation of microscopic cracks. These impede the heat transfer and consequently reduce the average thermal conductivity of the meat.

Figure 8.18 is an optical microscopy image of the low burnup dispersion fuel segment. The formation of the IDL has already started, which can be seen at the dark gray areas around the fuel particles. The black spots in the fuel particle are the fission gas bubbles. The few light gray areas represent the remaining Al matrix material. Figure 8.19 is an optical microscopy image of the high burnup fuel segment. The size fission gas bubbles increased and the dark gray IDL has completely consumed the matrix.
Considering these observations from the optical microscopy images for the evolution of the thermal conductivity in Figure 8.17, the inter-diffusion layer must have a very low thermal conductivity that is comparable to the U-Mo thermal conductivity. So, during irradiation, the

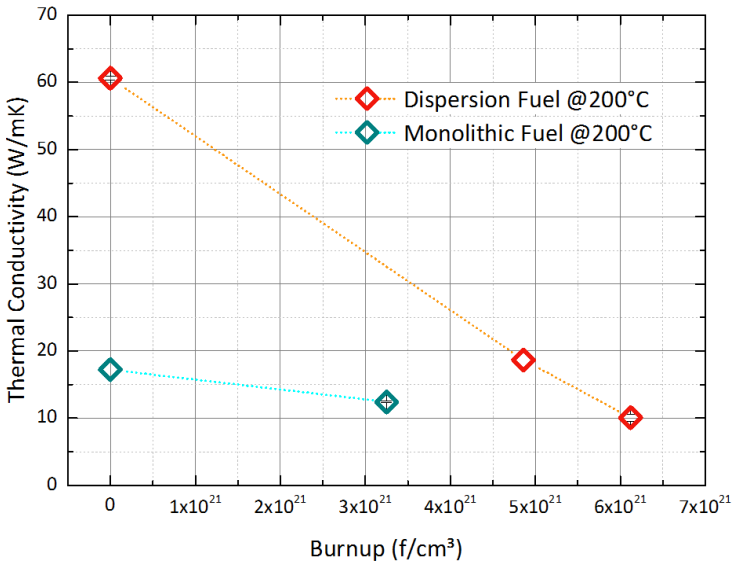


***Figure 8.17:*** *Comparison of the thermal conductivity of fresh and in-pile irradiated dispersion and monolithic fuels at* 200 °C *over burnup.*

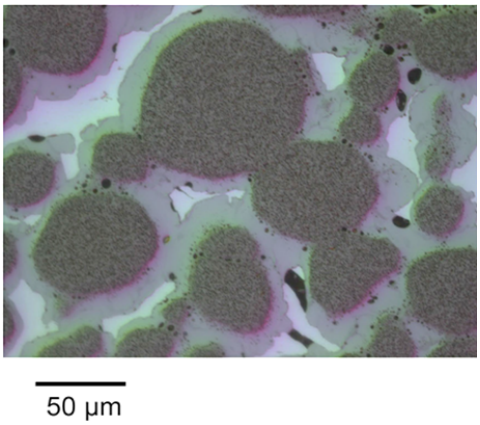


***Figure 8.18:*** *Microscopy image of the segment AFIP-1 TL [BCB⁺14a] at a burnup of* $4.86 \cdot 10^{21}$ f/cm³.

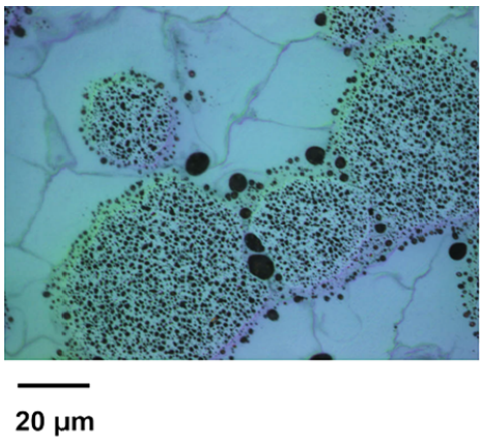


***Figure 8.19:*** *Microscopy image of the segment AFIP-1 TK [BCB⁺14a] a burnup of* $6.12 \cdot 10^{21}$ f/cm³.

high conductive Al matrix material is successively replaced by low conductive IDL material, leading to a decrease of the thermal conductivity of the entire fuel meat.

In Chapter 3.4.2, a model for the calculation of the thermal conductivity of coated spheres dispersed in a matrix material has been described. This model has already been used in the previous chapters to calculate the thermal conductivity of fresh dispersion fuels with different matrix material compositions as well as for coated fuel particle dispersion fuels. It could be shown that this model fits well for adapted input parameters.
Now, the model is used to calculate the unknown thermal conductivity of the interaction layer from the measured value of the in-pile irradiated meat of the two investigated dispersion fuel segments. In this case, the thermal conductivity of the fuel meat is known, as well as the thermal conductivity of all other components (i.e. the irradiated U-10 wt.%Mo fuel particles and the

Al-2 wt.%Si matrix alloy), except the wanted thermal conductivity of the IDL.
The model needs the thickness of the IDL that be obtained from the optical microscopy images, as described in Chapter 3.4.2. The examination results in $(5.8 \pm 0.3)\,\mu$m for segment TL and $(7.7 \pm 0.4)\,\mu$m for segment TK. The fuel particle diameter of the fresh dispersion plate was obtained from the size distribution of the the U-Mo powder before fabrication resulting in 67$\mu$m [KJR+12].
So, based on spherical irradiated U-10 wt.%Mo fuel particles, coated with IDL material with the according thickness for each segment, dispersed in an Al-2 wt.%Si matrix, the thermal conductivity of the IDL can be calculated from fuel meat composite by iteration of the model in Chapter 3.4.2 until the thermal conductivity of the IDL is in best agreement with both fuel segments.

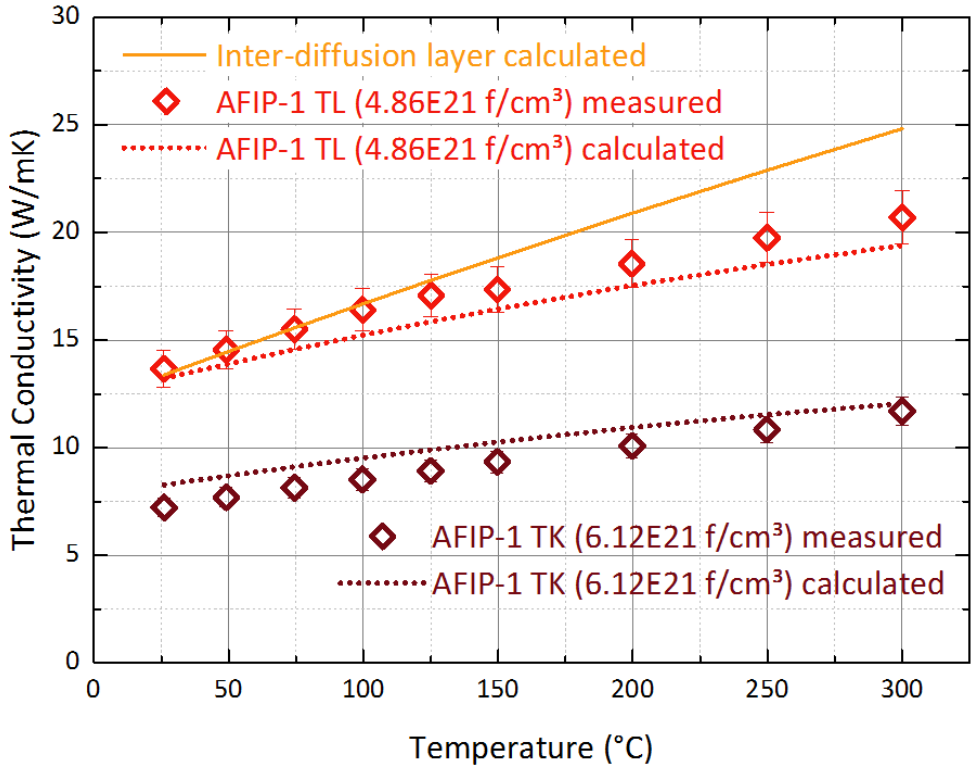


***Figure 8.20:*** *Comparison of the calculated and measured thermal conductivity of the two in-pile irradiated dispersion fuel segments. The solid orange line represents the calculated thermal conductivity of the inter-diffusion layer. The dotted lines represent the calculated thermal conductivity of the two irradiated AFIP-1 segments with the IDL thermal conductivity of* 14.6 $^{W}/_{m\cdot K}$ *at* 50 °C *[BHC15].*

A first approximation of the IDL thermal conductivity can be based on its material composition. According to out-of-pile studies [PE10], the IDL is composed of mostly (U,Mo)$Al_x$ intermetallics, with x being generally 2,3 or 4. So, the thermal conductivity of the IDL is expected to be close to the thermal conductivity of $UAl_x$ compounds, ranges for $UAl_3$ and $UAl_4$ from 11 $^{W}/_{m\cdot K}$ to 28 $^{W}/_{m\cdot K}$ [MS92].
Now, from the model results that the calculated thermal conductivity of the fuel meat of the two fuel segments, are in best agreement with the measured values for an IDL thermal conductivity

of 14.6 W/m·K at 50 °C [BHC15], see the solid lines in Figure 8.20. This value is well within the range of the estimated values of the $UAl_x$ compounds.
With this IDL thermal conductivity, the calculated values for the irradiated dispersion fuel meat of the low burnup segment TL are on the entire investigated temperature range in average ±14 %, of the high burnup segment TK in average ±7 %. Over the temperature range between 100 °C and 200 °C, which is roughly the operating temperature range for dispersion fuels, the model is for both fuel segments within ±12 % of the measured values.

Using Equation 3.31 to 3.35 in Chapter 3.4.2, the evolution of the thermal conductivity during the entire reactor operation can be calculated [BHC15]. The model includes the growth of the IDL under consideration of the operational temperature in the fuel meat, the fission density as well as the Si content in the matrix material and the Mo content in the fuel particles and their average diameter.
The thermal conductivity of the fuel particles at the beginning of reactor operation, i.e. non-irradiated U-10 wt.%Mo, was for consistency reasons not obtained from the measurement, but calculated with Equation 3.31 in Chapter 3.4.2 by setting $f_d$, the fission density, to zero. It is to remark that Equation 3.31 is derived from the measured values. The resulting value was then used as thermal conductivity of the fresh fuel particle in the model for the simulation of the evolution of the thermal conductivity during in-pile irradiation.

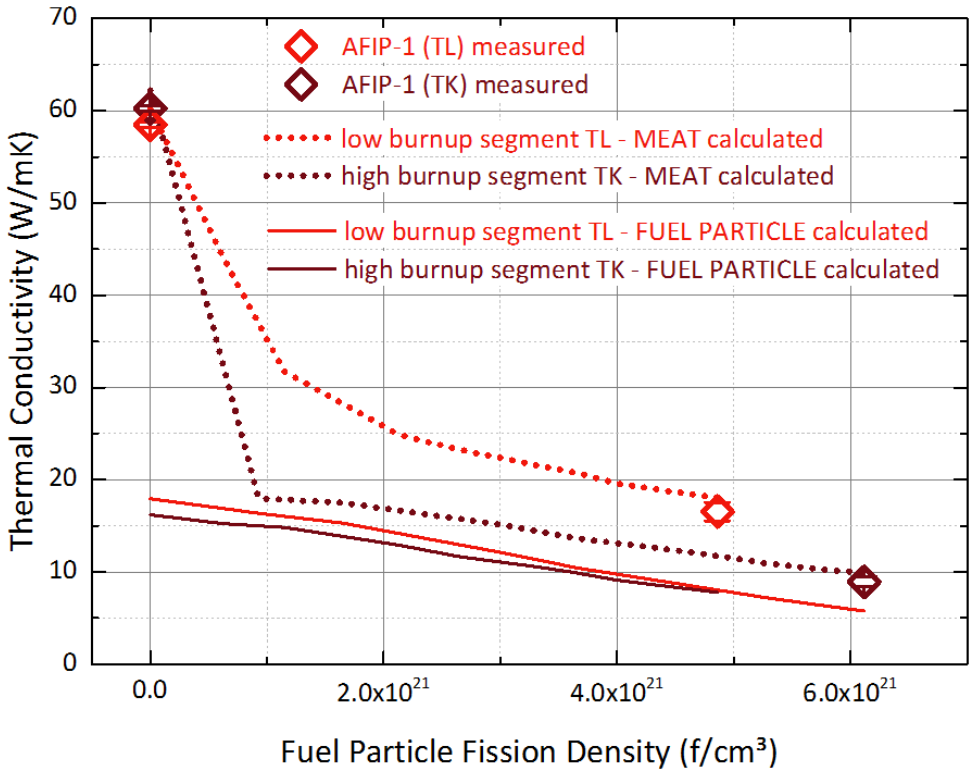


***Figure 8.21:*** *The dotted lines show the evolution of the thermal conductivity of the meat and the straight lines of the fuel particle, i.e. U-10 wt.%Mo, of segment TL and TK from the as-fabricated state to the EOL state after irradiation. The data points at the beginning and end of each curve represent the measured thermal conductivity for the actual operational temperature of the fuel segment at the beginning and end of cycle, see Figure 8.22.*

Figure 8.21 shows the calculated evolution of the thermal conductivity of the segments TL and TK for the as-fabricated state and end of life state after in-pile irradiation, based on the model in Chapter 3.4.2. Due to the differing irradiation history (operational temperature, surface heat flux etc.), caused by the different locations on the fuel plate, both segments behave differently. The calculated thermal conductivity at beginning of life of segment TL and TK, results in 60.2 $^{W}/_{m \cdot K}$ and 62.2 $^{W}/_{m \cdot K}$, which agrees well with the results from the measurements of the fresh AFIP-1 fuel segment in Chapter 8.1. The beginning of life fuel temperature was determined to be 138 °C for segment TL and 185 °C for segment TK [BHC15]. The two data points at the beginning and end of each in Figure 8.21 represent the measured thermal conductivity for the actual operational temperature of the fuel segment at the beginning and end of cycle, see Figure 8.22 [BHC15]. The measured thermal conductivity is in very good agreement with the calculated value of the thermal conductivity at the beginning as well as at the end of reactor operation.

Figure 8.21 also shows that at the beginning of reactor operation the thermal conductivity of the fuel particle, i.e. U-10 wt.%Mo, does not decrease as fast as the thermal conductivity of the meat. But for the high burnup segment TK, at already low fission density (about $1 \cdot 10^{21}$ $^{f}/_{cm^3}$)the steepness of the decrease the meat thermal conductivity gets conform with the fuel particle thermal conductivity. For the low burnup segment, the steepness of the meat thermal conductivity gets later (at about $2 \cdot 10^{21}$ $^{f}/_{cm^3}$) conform with the fuel particle thermal conductivity.
It stands to reason that the fast decrease of the meat thermal conductivity is caused by the matrix degradation at the beginning of irradiation. Figure 8.22 shows that exactly at $1 \cdot 10^{21}$ $^{f}/_{cm^3}$ and $2 \cdot 10^{21}$ $^{f}/_{cm^3}$ for the high and low burnup segments accordingly, most or all of the matrix material is consumed by the IDL. Above these fission densities, the decrease of the fuel particle thermal conductivity drives the fuel meat thermal conductivity.
But, Figure 8.22 also shows that the IDL growth is not only dependent on the fission density. It is also dependent on the operational temperature. The high burnup segment has been irradiated at the beginning at an in average 40 °C higher temperature, which resulted in a faster IDL growth and therefore faster decrease of the thermal conductivity.

In general, the model reproduces the measured values very well. But for a better justification of the model, more data is mandatory. On the one hand, further segments with different burnup of the same fuel plate would help to validate the model for this fuel type. On the other hand, further segments with different burnup from other dispersion fuel types, for example different Si content in the matrix, coated fuel particles or even ground powder fuel would help to understand the general behavior under in-pile irradiation of U-Mo dispersion fuels.

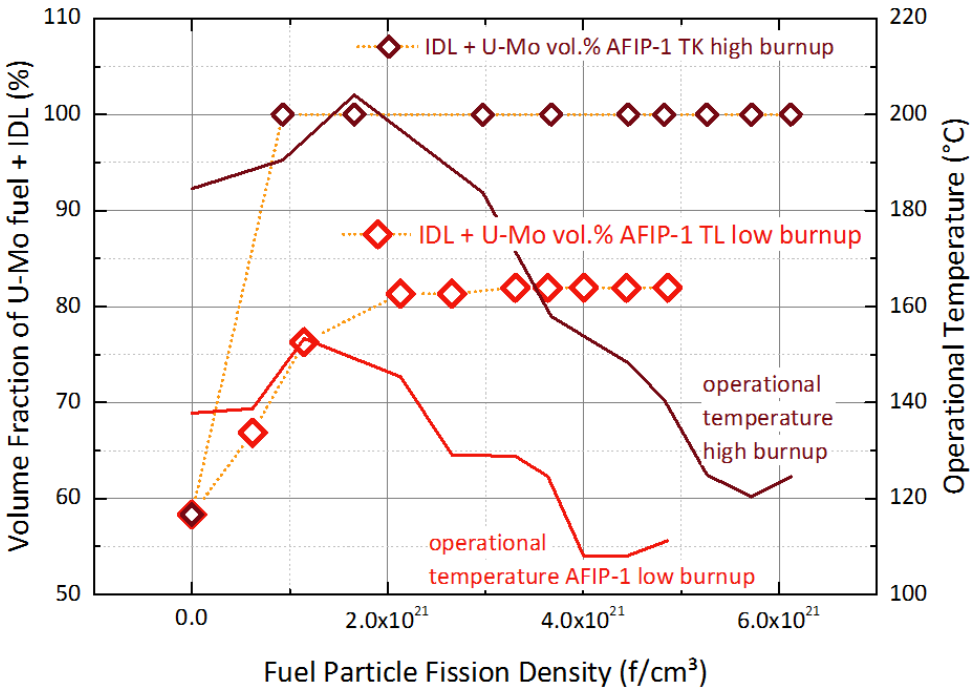


***Figure 8.22:*** *Left axis: Volume fraction of IDL and U-Mo over burnup. Right axis: operational temperature over burnup.*

## 8.5 Comparison with $U_3Si_2$ Dispersion Fuel

Figure 8.23 shows a summary of the thermal conductivity of the as-fabricated U-Mo fuels, measured in this work and $U_3Si_2$ dispersion fuels, the current reactor fuel of the FRM II.

The investigated U-Mo fuels have a fuel volume loading of roughly 50 vol.%. The thermal conductivity of $U_3Si_2$ dispersion fuel with a fuel volume loading of 46.6 vol.% [Com88] can therefore be directly compared with the measured U-Mo fuels. So, $U_3Si_2$ dispersion fuel is in the same range of about 60 $W/m \cdot K$ as the U-Mo dispersion fuels with coated or non-coated atomized powder and Al-Si matrix.

The current fuel element of the FRM II has a cylindrical geometry with 113 involute fuel plates. Each fuel plate has a step in fuel volume loading from 26.5 vol.% in the inner zone (about 5 cm width) to 13.3 vol.% in the narrow outer zone (about 1 cm width) of the fuel plate to facilitate cooling. The two available data points for the thermal conductivity of $U_3Si_2$ dispersion fuel for 32.3 vol.% and 13.7 vol.% are very close to the actual fuel element's fuel loading. One can see that the thermal conductivity in the inner zone is still almost within the range of the investigated U-Mo dispersion fuels with atomized powder. Although, due to the irregular shape of the $U_3Si_2$ particles, it would be expected that the thermal conductivity of the $U_3Si_2$ dispersion fuel is closer to the thermal conductivity of ground powder fuels. But the porosity of the $U_3Si_2$ fuel is given as 4 vol.% [Com88], while the here investigated ground powder fuels have a porosity of 7 vol.% to 9 vol.% This is about twice the porosity of the $U_3Si_2$ fuel and significantly reduces the thermal conductivity. The thermal conductivity of the outer zone is much higher due to the low Uranium content and therefore provides a good heat transfer to the coolant.

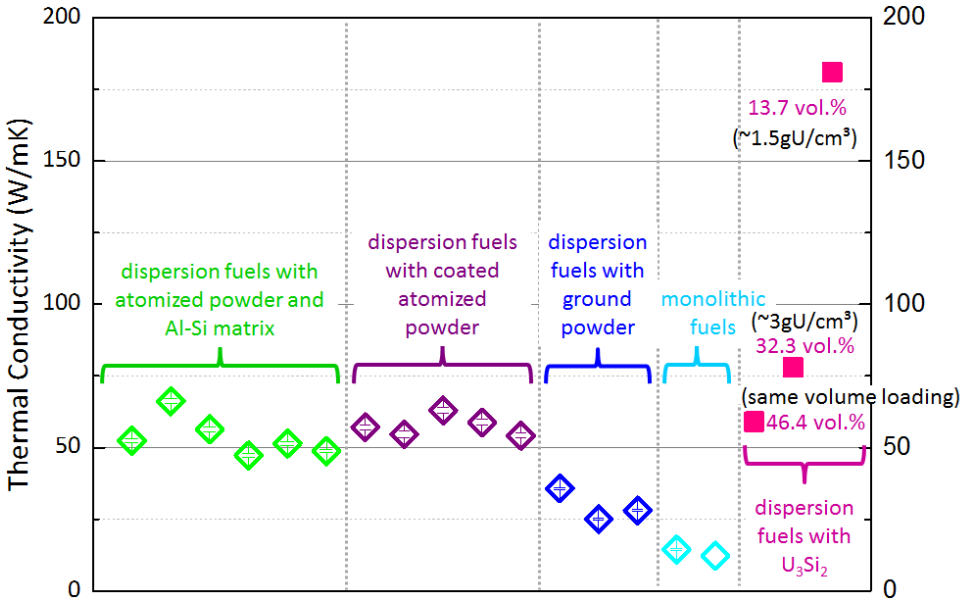


***Figure 8.23:*** *Comparison of the thermal conductivity of U-Mo fuels with* $U_3Si_2$ *dispersion fuels with different fuel volume loadings at* 60 °C *[Com88].*

Up to now, no data has been published about the thermal conductivity of in-pile irradiated $U_3Si_2$ dispersion fuel. During irradiation, $U_3Si_2$ dispersion fuels are also impacted from the fission gas bubbles, crystal lattice decomposition and matrix hardening. But, due to the highly enriched uranium, the fuel loading is lower than for the low enriched U-Mo fuels and the average distance between the fuel particles is longer. So, the meat contains almost only about half of the fuel and these effects might not have as much impact as for U-Mo fuels. Further, the inter-diffusion layer between fuel particle and Al matrix is much thinner as for U-Mo fuels, see Figure 1.1 in Chapter 1.2. As the thermal conductivity of the IDL in U-Mo dispersion fuels is very low and assuming the IDL in $U_3Si_2$ dispersion fuels is in the same range, based on the fact that the IDL of the $U_3Si_2 - Al$ dispersion fuel should be composed of $UAl_x$ compounds as well, the thermal conductivity of $U_3Si_2$ dispersion fuels is expected to also decrease during irradiation, but not as strong as the thermal conductivity of U-Mo dispersion fuels does.

# Part IV

# Summary and Outlook

# CHAPTER 9

## Summary

In this work, the thermal properties of as-fabricated as well as in-pile irradiated dispersion and monolithic U-Mo fuels have been investigated. The thermal conductivity $\lambda$ was not assessed directly, but it was obtained by the measurement of the thermal diffusivity $\alpha$, the specific heat capacity $c_\mathrm{p}$ and the density $\rho$.

$$\lambda = \alpha \cdot c_\mathrm{p} \cdot \rho \tag{9.1}$$

## 9.1 Thermal Diffusivity

The thermal diffusivity was measured with the Laser Flash Method (LFA). Two models have been compared for the evaluation of the thermal diffusivity of layered materials, namely the TUM and the PNNL model. The PNNL model is only valid for a three layer material, while the TUM model is adequate to evaluate any multi-layer material.

The thermal diffusivity strongly depends on the material's microstructure and is the parameter with the largest deviation between the different fuels. Therefore, it has the highest impact on the thermal conductivity, compared to the specific heat capacity and density.

The thermal diffusivity of dispersion fuels fabricated from atomized powder with Si matrix or particle coated ranges between $20\,\mathrm{mm^2/s}$ and $26\,\mathrm{mm^2/s}$. It was shown that the thermal diffusivity decreases for atomized powder dispersion fuels with increasing Si content in the matrix until about 6 wt.%Si and then gets almost constant due to different microstructures in the Al-Si alloy. For coated atomized powder dispersion fuels, the thermal diffusivity is in the range of the fuels with atomized powder and Al-Si matrix and behaves according to the thermal diffusivity of the coating material and the coating layer thickness.
Ground powder fuels have a thermal diffusivity in the range of $11\,\mathrm{mm^2/s}$ to $17\,\mathrm{mm^2/s}$, which is in general lower than the thermal diffusivity of the atomized powder fuels, due to the higher amount of porosity that is generate during fabrication caused by the irregular shape of the fuel particles.

During in-pile irradiation, the crystal lattice is destroyed by the fission products that have an average kinetic energy of 80 MeV. This impacts the microstructure of the fuel and leads together with the growth of fission gas bubbles and the interaction layer between the fuel particles and

the Al matrix to a decrease of the thermal diffusivity depending on the fission density down to about $3\,\mathrm{mm^2/s}$ to $7\,\mathrm{mm^2/s}$.

Monolithic fuels have with about $5\,\mathrm{mm^2/s}$ to $9\,\mathrm{mm^2/s}$ in the as-fabricated state a thermal diffusivity far below the thermal diffusivity of as-fabricated dispersion fuels. During irradiation, the thermal diffusivity further decreases down to about $4\,\mathrm{mm^2/s}$ to $5\,\mathrm{mm^2/s}$ due to the formation of fission gas bubbles and damages in the crystal lattice caused by the fission products. But the decrease is not as strong as for dispersion fuels, as monolithic fuels are not impacted by additional effects, like interaction action layer growth, due to the lack of an Al matrix.

## 9.2 Specific Heat Capacity

The specific heat capacity was obtained with a Differential Scanning Calorimeter (DSC) and is mainly dependent on the atomic, i.e. material, composition and the energy stored in the crystal lattice. As the dispersion fuels do not significantly differ in the material composition, the specific heat does not show high variations between the different fuel types. So, the specific heat capacity is in the range of $0.2\,\mathrm{J/g{\cdot}K}$ and $0.3\,\mathrm{J/g{\cdot}K}$.

In-pile irradiated fuels have slightly higher specific heat capacity that can be caused by the higher energy that is stored in the crystal lattice due to stresses induced by the damage of the crystal lattice from the fission products.

The specific heat capacity of monolithic fuels is in average $0.15\,\mathrm{J/g{\cdot}K}$ and is therefore lower than for dispersion fuels. Also here, as already observed for dispersion fuels, irradiation slightly increases the specific heat capacity.

## 9.3 Density

The density has been determined by using Immersion Method and Pycnometry. It varies in general around $10\,\mathrm{g/cm^3}$ for as-fabricated dispersion fuels. During irradiation, mainly the gaseous fission products lead to a decrease of the density depending on the fission density down to about $8.5\,\mathrm{g/cm^3}$.

Monolithic fuels have with about $17\,\mathrm{g/cm^3}$ a higher density due to the lack of an Al matrix. Analogous to dispersion fuels, the density decreases mainly due to the gaseous fission products down to about $14\,\mathrm{g/cm^3}$.

## 9.4 Thermal Conductivity

From the parameters above, the thermal conductivity was calculated with Equation 9.1 for the different as-fabricated and in-pile irradiated fuels.

### 9.4.1 Dispersion Fuels with Atomized U-Mo Powder

The thermal conductivity of dispersion fuels containing atomized powder and Si in the matrix is in the range of 45 $W/m \cdot K$ to 75 $W/m \cdot K$.
It decreases with increasing Si content, but does not further decrease for Al-Si matrices with more than 6 wt.%Si content, as already observed for the thermal diffusivity. Although both, the specific heat capacity and density, decrease accordingly with increasing Si content up to 12 wt.%Si content, these two parameters cannot compensate the behavior of the thermal diffusivity, which further propagates to the thermal conductivity.

The Hsu model was used to calculate the thermal conductivity of dispersed materials from the composition of the single fuels as specified in the fabrication certificates. The calculated values are in good agreement with the measured values for Si contents up to 4 wt.%Si. Above, the model overestimates the thermal conductivity by more than 10 %.

### 9.4.2 Dispersion Fuels with Ground U-Mo Powder and different Uranium loading

Ground powder dispersion fuels have thermal conductivity of 25 $W/m \cdot K$ to 40 $W/m \cdot K$. It is in general a lower than the thermal conductivity of atomized powder fuels, as already observed for the thermal diffusivity.
Due to the irregular shape of the fuel particles, it is hardly possible to apply a common model for the calculation of the thermal conductivity based on the nominal composition. However, the Hsu model, adapted for prolate spheres, showed good agreement for the IRIS-TUM fuel with 8 $gU/cm^3$ and 2 wt.%Si in the matrix for low temperatures (below 150 °C). But for higher temperatures and no Si in the matrix, the calculated values are more than 10 % overestimated by the model. For the fuel with 7 $gU/cm^3$, the deviation is even higher.
The macroscopic structure of the fuel is too complex for the analyzed analytical models, so a measurement is mandatory to obtain accurate values.

It was further be observed on the IRIS-TUM fuels that the Uranium loading impacts the thermal conductivity. Here, an increase of the Uranium loading of 11 % reduces the thermal conductivity of almost 30 %.

### 9.4.3 Dispersion Fuels with Coated Atomized U-Mo Powder

For dispersion fuels consisting of coated atomized fuel particles, the thermal conductivity is in about the same range as the other dispersion fuels fabricated from atomized U-Mo particles with Al-Si matrix (50 $W/m \cdot K$ to 70 $W/m \cdot K$). The thermal conductivity depends on the coating material and coating thickness.
A model for coated spheres, dispersed in a matrix material, was applied to calculate the thermal conductivity from the nominal composition. Due to impurities in the matrix material that can be found with SEM examination of the fuels, the thermal conductivity is overestimated by the model. By adjusting the thermal conductivity of the matrix material, the calculated thermal conductivity can be brought into 10 % agreement with the measured values.
Besides, oxide coated fuels form cracks in the oxide layer that further reduce the effective thermal conductivity of the coated fuel particle and therefore also reduces the average thermal conductivity of the fuel meat.

### 9.4.4 In-pile irradiated U-Mo Fuels

During in-pile irradiation, the thermal diffusivity of dispersion fuels strongly decreases, see Figure 9.1. In the following, the thermal conductivities of the fuels are compared at a temperature of 200 °C.

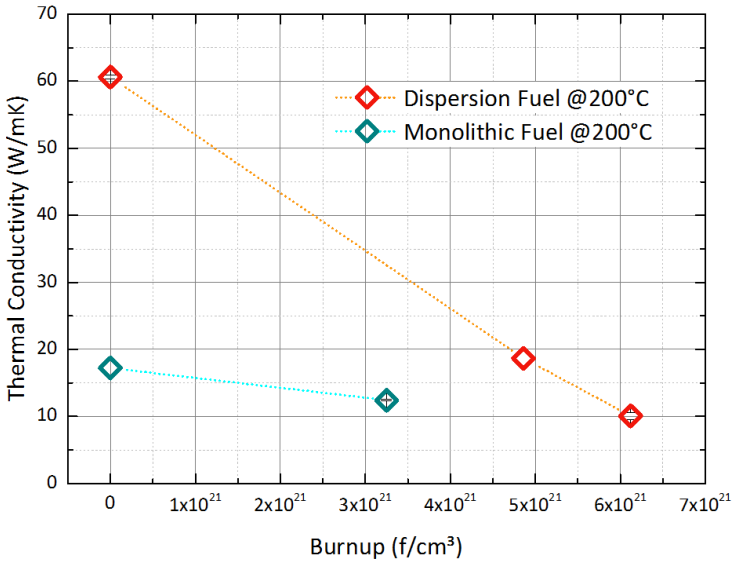


***Figure 9.1:*** *Comparison of the thermal conductivity of fresh and in-pile irradiated dispersion and monolithic fuels at* 200 °C *over burnup.*

In this work, two in-pile irradiated dispersion fuel segments with different burnup from the AFIP-1 irradiation campaign have been investigated. For the low burnup segment ($4.86 \cdot 10^{21}$ f/cm³), the thermal conductivity decreased from 60 W/m·K to 19 W/m·K, which is a relative reduction of almost 70 %. For the high burnup segment ($6.12 \cdot 10^{21}$ f/cm³), a thermal conductivity of 10 W/m·K was measured, which is relative reduction of more than 80 % compared to the fresh fuel.
In contrast, as-fabricated monolithic U-10 wt.%Mo has an already low thermal conductivity of 17 W/m·K that decreases for a burnup of $3.25 \cdot 10^{21}$ f/cm³ only down to 12 W/m·K, which is a relative reduction of about 30 %. Although the burnup of the monolithic and dispersion fuel segments cannot be compared directly, Figure 9.1 shows that the thermal conductivity of dispersion fuels decreases stronger than the thermal conductivity of monolithic fuels.

The reduction of the thermal conductivity in the U-Mo is mainly caused by the formation of fission gas bubbles and the decomposition of the U-Mo crystal lattice due to the high kinetic energy ($\sim$ 80 MeV) of the fission products.
It was already mentioned that the thermal conductivity of dispersion fuels stronger decreases than monolithic fuels. This is caused by the additional irradiation effects in the matrix, which do not exist for monolithic fuels.
In the case of dispersion fuels, two more mechanisms occur during irradiation: The cumulative hardening of the remaining matrix material caused by the high energetic fission products and the temperature and fission density dependent growth of the inter-diffusion layer between fuel particles and Al matrix, see Figure 9.2.

The thermal conductivity of the IDL in dispersion fuels has been derived by using the model described in Chapter 3.4.2 from the measurements of the two in-pile irradiated AFIP-1 dispersion

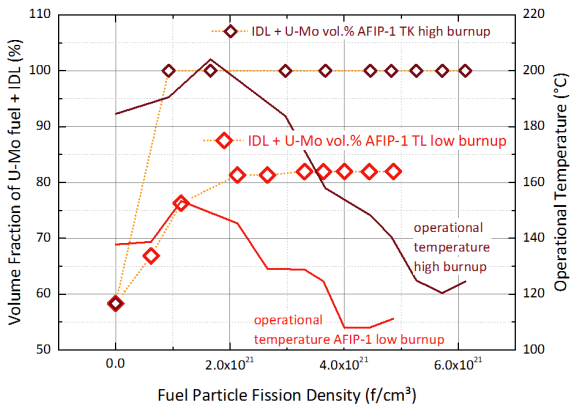


***Figure 9.2:*** *Left axis: Volume fraction of IDL and U-Mo over burnup. Right axis: operational temperature over burnup.*

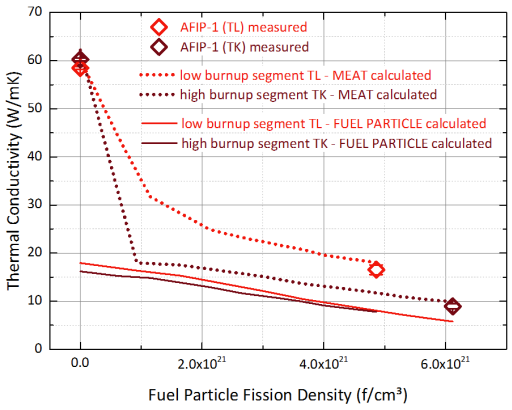


***Figure 9.3:*** *Results of the Calculation of the evolution of the thermal conductivity of segment TL and TK from the as-fabricated state to the EOL state after irradiation.*

fuel segments and results in 14.6 $\mathrm{W/m{\cdot}K}$. This is very low compared to the Al-Si alloy (about 200 $\mathrm{W/m{\cdot}K}$ for Al-2 wt.%Si), which is subsequently replaced during irradiation by the IDL.

At the beginning of reactor operation, the fast decrease of the thermal conductivity of the meat is mainly driven by the degradation of the matrix material, but once all matrix material is consumed by the IDL, the thermal conductivity of the meat is mainly driven by the thermal conductivity of the fuel particles themselves, see Figure 9.3.

## 9.5 Comparison with $U_3Si_2$ Dispersion Fuel

The thermal conductivity of $U_3Si_2$ dispersion fuel with roughly the same fuel loading as the here investigated U-Mo fuels is in the same range of about 60 $\mathrm{W/m{\cdot}K}$ as the dispersion U-Mo fuels with Al-Si matrix or coated particles.

Due to the high enrichment of the current fuel element of the FRM II, the fuel loading is only less than half of the low enriched U-Mo fuel loading. Thus, a much higher amount of highly thermal conductive matrix material is in the fuel, increasing the thermal conductivity to almost 80 $\mathrm{W/m{\cdot}K}$.
Replacing the high enriched $U_3Si_2$ dispersion fuel by low enriched U-Mo dispersion fuel in the current fuel element, the thermal conductivity of the fuel is reduced due to the higher fuel loading. Thus, during reactor operation, the heat transfer from the fuel particle to the cladding and finally the coolant is reduced, leading to a higher operational temperature in the fuel meat.

In this work, the thermal properties of the different types of dispersion and monolithic U-Mo fuels have been successfully investigated by measurement and calculation in respect of the matrix material, the U-Mo particle shape and coating, the U-Mo alloy itself and their behavior under in-pile irradiation, resulting in a thorough overview.

# CHAPTER 10

## Outlook

The different types of as-fabricated dispersion fuels and monolithic fuel have been characterized as far as possible. More interest should go into further investigations of in-pile irradiated fuels.

In the case of in-pile irradiated dispersion fuels, the thermal properties of only two segments with different burnup of dispersion fuel fabricated from atomized powder with a Al-2 wt.%Si matrix have been investigated and the evolution of the thermal conductivity was successfully described with a model. To confirm the model, the measurement of the thermal conductivity of more segments of the same fuel plate, but with different burnup and operational temperature would be mandatory, especially at a burnup below $2 \cdot 10^{21}$ f/cm³, in the region of the fast decrease.

Other types of irradiated dispersion fuels, like Si or ZrN coated atomized powder dispersion fuels have not been investigated yet. Post irradiation examinations showed that the growth of an interaction layer does not start before a burnup of $> 4.5 \cdot 10^{21}$ f/cm³ [BKH+15]. It would be of interest to investigate, if the thermal conductivity of this fuel also decreases as fast as the fuel with Al-Si matrix at the beginning of reactor operation or if the decrease starts at the time, when IDL formation starts. This way, it could be possible to get an indication of the impact of the matrix hardening.
Ground powder fuels already have more porosity than other dispersion fuels types that can assimilate the fission gases during irradiation and compensate the generation of fission gas bubbles. But, these fuels already have a lower thermal conductivity than the other dispersion fuels, so it is to investigate if the thermal conductivity decreases during irradiation as strong as the other atomized powder dispersion fuels down to an even lower thermal conductivity or if they end up at the same level.

In the case of monolithic fuels, there are only measurements of a few segments with a burnup around $3.3 \cdot 10^{21}$ f/cm³ to $4.5 \cdot 10^{21}$ f/cm³ [BCC+15b]. The evolution of monolithic fuel to high burnups and in dependence of the operational temperature is not known yet.

The thermal properties of the evolution of the thermal conductivity is mandatory for the simulation of the heat fluxes in the fuel element during reactor operation. Based on this, the cooling cycle is calculated with thermal-hydraulic models. So, once, a final fuel design is chosen for the reactor conversion to low enriched U-Mo fuel, it is advisable to investigate the thermal properties of this fuel during irradiation more in detail.

# Part V

# Appendix

# APPENDIX A

## As-fabricated U-Mo Fuel Selection

| Fuel Name | U-Mo Powder Type | Particle Coating | Uranium Loading [gU/cm$^3$] | Mo Content [wt.%] | Matrix Material | Porosity [vol.%] |
|---|---|---|---|---|---|---|
| E-FUTURE 4112 | atomized | — | 8.1 | 7.4 | Al + 4.2 wt.%Si | 2.1 |
| E-FUTURE 6101 | atomized | — | 8.1 | 7.6 | Al + 6.0 wt.%Si | 2.0 |
| E-FUTURE II 702 | atomized | — | 7.8 | 7.5 | Al + $\sim$ 7 wt.%Si | 5.6 |
| E-FUTURE II 1203 | atomized | — | 8.1 | 7.5 | Al + $\sim$ 12 wt.%Si | 1.6 |
| E-FUTURE II 1212 | atomized | — | 7.9 | 7.6 | Al + $\sim$ 12 wt.%Si | 3.5 |
| IRIS-4 U-Mo/Al | atomized | oxide | 7.9 | 7.3 | Al | 1.1 - 4.5 |
| IRIS-4 U-Mo/AlSi | atomized | oxide | 7.9 | 7.3 | Al + 2.1 wt.%Si | 1.1 - 4.5 |
| IRIS-TUM 7001 | ground | — | 7.3 | 7.3 | Al | 6.6 |
| IRIS-TUM 8003 | ground | — | 8.5 | 8.5 | Al | 7.8 |
| IRIS-TUM 8502 | ground | — | 8.3 | 8.3 | Al + 2.1 wt.%Si | 8.9 |
| SELENIUM A | atomized | 300 nm Si | $\sim$ 8 | 7.2 | Al | — |
| SELENIUM B | atomized | 600 nm Si | 8.1 | 7.2 | Al | 3.9 |
| SELENIUM C | atomized | 1000 nm ZrN | 8.2 | 7.2 | Al | 4.8 |
| AFIP-1 | atomized | — | 8.8 | 7.0 | Al + 1.9 wt.%Si | 3.1 |

***Table A.1:*** *Summary of the investigated fresh dispersion fuels, for details see Chapter 2.1 and 5.1.2.*

| Layer | Thickness [$\mu$m] AFIP-1 TL | Thickness [$\mu$m] AFIP-1 TK |
|---|---|---|
| Cladding | 310±15 | 307±21 |
| Meat | 700±33 | 692±33 |
| Total Plate | 1321±22 | 1306±22 |

***Table A.2:*** *Layer thicknesses of the investigated in-pile irradiated dispersion fuel segments from the AFIP-1 irradiation experiment. The thicknesses have been determined from optical microscopy [BCB+ 14a, BCB+ 14b].*

| Layer | Thickness [$\mu$m] |
|---|---|
| AA6061 (upper) | 443±20.6 |
| Zirconium (upper) | 31.5±7.02 |
| U-10 wt.%Mo | 391±15.6 |
| Zirconium (lower) | 34.7±8.75 |
| AA6061 (lower) | 445±46.4 |
| Total Plate | 1335±39.1 |

***Table A.3:*** *Layer thicknesses of the investigated in-pile irradiated monolithic fuel segment from the AFIP-2BZ irradiation experiment. The thicknesses have been determined from optical microscopy [BCC+ 15a].*

# APPENDIX B

## Scanning Thermal Diffusivity Microscope

The Scanning Thermal Diffusivity Microscope (STDM) was developed at Idaho National Laboratory (INL) to be remotely operated in a hot cell to measure the thermal diffusivity of irradiated fuels. [HFG+12] presents first experiments with the STDM instrument on irradiated monolithic and dispersion fuel samples.

### B.1 Operating Principle

When a pulsed LASER beam is incident on a material surface, the material absorbs some of the light and, in the process, converts light energy into thermal energy. This increase in thermal energy causes the material to undergo a local thermal expansion that is proportional to the energy absorbed. If the time between the laser pulses is sufficiently large, the locally absorbed thermal energy will diffuse throughout the body of the material according to the diffusion equation for heat conduction. As the volume of absorption cools, it undergoes thermal contraction, the inverse of thermal expansion.

If, on the other hand, the time between the LASER pulses is sufficiently small, the material will not be able to diffuse the thermal energy absorbed during each pulse before more energy is absorbed. This will result in a continued local thermal expansion. It is reasonable to postulate that there exists a unique pulse frequency, called the cut-off frequency, between these two extremes which will allow the material to maintain a balance between the diffusion of thermal energy from the preceding pulse, tending to cause thermal contraction, and the absorption of energy during the current pulse, tending to cause thermal expansion. In this equilibrium, the material will be in a quasi-steady thermally expanded state. It is this unique frequency that the STDM finds [KH11].
This process of expansion and contraction is controlled by a coupling of the thermal and elastic properties of the absorbing material. By solving the coupled equations and simplifying when necessary, it can be shown that the cut-off frequency ($f_c$) of the material is proportional to ratio of the thermal diffusivity ($D$) to the square of the laser spot size ($a$), and that the proportionality constant is independent of the material [KH11].

$$f_c = \frac{D}{a^2} \tag{B.1}$$

If the frequency of the LASER pulses is allowed to vary from a starting point of several hundred Hz upward, the cut-off frequency can be detected by a second LASER that measures the expansion and contractions of the material surface. If the cut-off frequency for several materials of known thermal diffusivity is obtained in this way by the STDM, a log-log plot of the above equation for all of the materials will be linear. This plot can then be used as a calibration curve for finding the thermal diffusivity of an unknown material [HFG$^+$12, KH11].

## B.2 Specimen - Characteristics and Irradiation Conditions

### B.2.1 Monolithic U-Mo Fuel Samples

For the STDM measurement, two monolithic mini plates (L1P12Z and L2P16Z) from the RERTR 10A experiment [PLC$^+$11b] were chosen for analysis. The RERTR-10A irradiation experiment was designed to evaluate the performance of monolithic fuel designs of various types under severe irradiation conditions (surface heat flux $> 400\,\mathrm{Wcm}^2$ and burnup $> 100\,\%$ LEU equivalent). The experiment was also designed to provide a basis to examine the performance of the fuel meat to cladding interface when a Zr interlayer with either 0.025 mm or 0.050 mm nominal fuel-foil thickness was inserted to mitigate U-Mo/Al inter-diffusion during irradiation. These two specific plates were selected because they offered the opportunity to examine the impact of a wide range of fission densities on thermal diffusivity.
Each plate is nominally 2.54 cm wide, 10.1 cm long, and 1.4 mm thick. All plates in the experiment were fabricated by first casting Uranium-molybdenum alloy ingots by arc melting, then hot rolling the ingots into thin foils and subsequently using the hot-isostatic-press (HIP) method to bond the cladding to the fuel core.

The Uranium-molybdenum fuel alloy of plate L1P12Z has an enrichment of 67.0 % U-235 and contains 10.1 wt.% Mo. The fuel foil with an average thickness of 0.310 mm has a co-rolled 0.025 mm Zr interlayer and is clad in Al-6061.
Plate L2P16Z contains a 33.4 % U-235 enriched fuel foil with 10.1 wt.% Mo, has a 0.025 mm co-rolled Zr interlayer and is also clad in Al-6061 [3]. The average foil thickness is 0.536 mm. This variation in thickness and enrichment allowed the plates to be irradiated at similar temperatures while simultaneously achieving different fission rates (which led to a variation in average fission density at the end of irradiation, see B.2.3).

### B.2.2 Dispersion U-Mo Fuel Sample

The R6R018 fuel plate [RWK$^+$10] of the RERTR-9B experiment [PLC$^+$11c] was chosen as a representative dispersion fuel-meat sample for STDM examination. The goal of this irradiation program was to investigate the impact of Si addition to the matrix material of dispersion U-7 wt.%Mo fuels under irradiation. Variations in the Si content in the fuel meat can substantially alter the volume fraction of U-Mo/Al interaction-product formation. As such, it is anticipated that significant variation in bulk thermal diffusivity will be observed. This plate has the same nominal dimensions as the RERTR-10A mini-plates.

The fuel powder was produced by first alloying a blend of highly enriched Uranium (HEU - 93.1 wt.% U-235), depleted Uranium (DU - 0.2 wt.% U-235) and Molybdenum by arc-melting, in

the end producing a total enrichment of 62.5 % U-235 and a molybdenum content of 6.99 wt.%. The alloy was subsequently atomized by the rotating-electrode atomization process. A blend of 5.540 g of fuel powder and 0.921 g gas-atomized Aluminum powder with 3.5 wt.% Si content was compacted in a hydraulic press. These fuel compacts were loaded into machined Al-6061 "picture frames" with cover plates and rolled in a two-high rolling mill. The rolling assembly was periodically reheated with a plate-heating furnace at 500 °C. Finally, the plate was annealed at 485 °C. for 30 minutes and, afterwards, cooled in air. During this process, Silicon in the matrix material accumulates around the fuel particles. This Si-rich layer was expected to reduce the diffusion of Uranium into the matrix during irradiation, which typically leads to the growth of a disadvantageous inter-diffusion layer around the U-Mo particles.

### B.2.3 Irradiation Conditions

RERTR mini-plate experiments [PLC+11b], [PLC+11c] consist of four capsules labeled from A to D, each containing eight mini-plates. RERTR-10A, consisted of the two capsules, A and C, with plate L1P12Z located in position C1 and plate L2P16Z in position C3. RERTR-9B consisted of the two capsules B and D, with plate R6R018 in position B7.
The plates are arranged in two rows of four in each capsule. Both experiments were irradiated in the B-11 position of the Advanced Test Reactor (ATR), with the capsule oriented such that one edge of the plates is facing the core center (see Figure B.1). The orientation combined with the higher enrichment leads to self-shielding and a subsequent large fission-density gradient across the 2.540 cm width of the plate [PLC+11b].

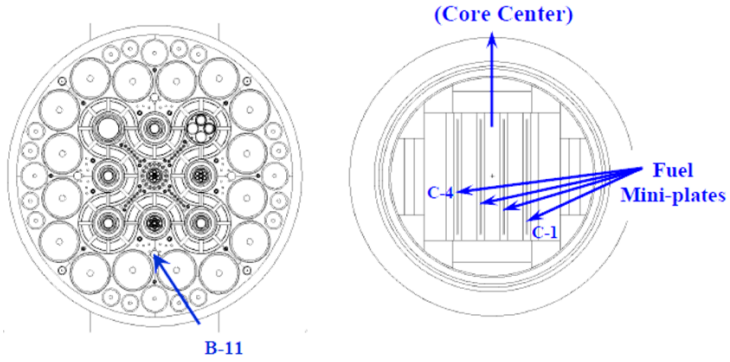


***Figure B.1:*** *(left) Radial cross section of ATR core, (right) assembly orientation in the irradiation position.*

The RERTR-10A plates were irradiated during cycles 142B and 143A for 52d and 26d [PLC+11b], respectively, and the RERTR-9B plates were irradiated during cycles 140A, 140B and 141A for 46.5d, 35d and 32d [PLC+11c], respectively. Table B.1 shows the plate-specific average fission density and U-235 burnup at the end of irradiation.

Figure B.2 and Figure B.3 show the power and fission density gradient across the width of the samples obtained by neutronic physics analysis.

Post-irradiation thickness measurements for plates all plates were performed as described in Figure B.4. Calculations [RWK+10] based on fission density across the plate width (nominal width, $10.15 \pm 0.05$ cm.) in the area of the STDM mount lead depending on the burnup to a fuel meat swelling of 15 % to 48 % due to gaseous and solid fission products.

| | Plate Average Fission Density in Meat [f/cm$^3$] | Plate Average U-235 Burnup [%] | |
|---|---|---|---|
| L1P12Z | $4.04 \cdot 10^{21}$ | 21.96 % | monolithic |
| L2P16Z | $1.91 \cdot 10^{21}$ | 19.14 % | monolithic |
| R6R018 | $3.49 \cdot 10^{21}$ | 34.02 % | disperse |

***Table B.1:*** *Average fission density and U-235 burnup after irradiation.*

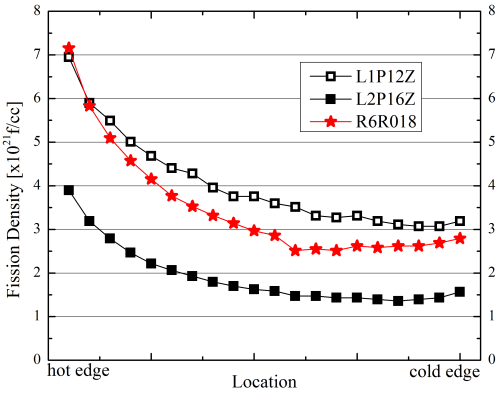


***Figure B.2:*** *Localized fission density across samples.*

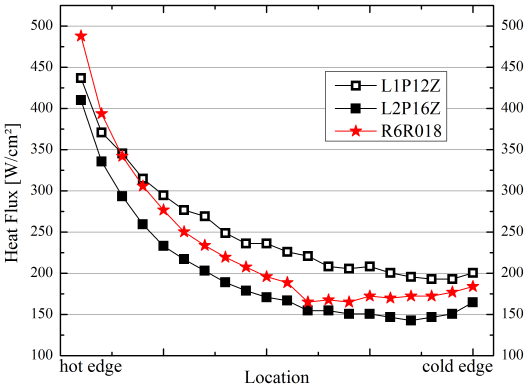


***Figure B.3:*** *Localized heat flux across samples.*

A cross section was taken through the mid-plane of each irradiated fuel plate for the further STDM examination (see Figure B.5).

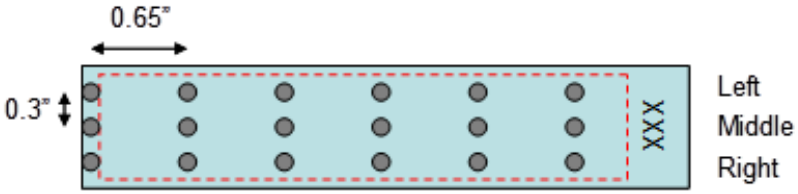


***Figure B.4:*** *Thickness measurement locations over fuel plates.*

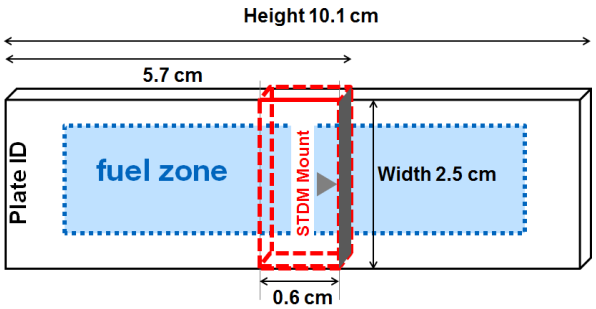


***Figure B.5:*** *Sectioning diagram for STDM samples.*

## B.3 Experimental

As part of the destructive post-irradiation examination, the thermal diffusivity of the three samples has been determined using the INL Scanning Thermal Diffusivity Microscope (STDM).

### B.3.1 Results

Due to the different material structure and behavior under irradiation, the monolithic and dispersion samples show different results in the STDM and are therefore examined in separate sections below.

#### B.3.1.1 Monolithic Sample

Figure B.6, Figure B.7 and Figure B.8 show a map of the measured thermal diffusivity across the width of both monolithic plates L1P12Z and L2P16Z. On the left and right side of the diagrams one can see the thermal diffusivity of the cladding material and of the fuel zone in the middle of the plates, with a characteristic low thermal diffusivity.

The L1P12Z sample was measured twice, and the values shown are the average of both measurements.

It is remarkable that the value for the fresh fuel, obtained by using the LASER-flash method, is lower than the one using the STDM. But the LASER-flash sample has a different fabrication history, as it was cut from a cast pin. Thus, it has a different microstructure and heat treatment than the plate-type samples used for STDM measurements. This impact of different heat treatment and microstructure on thermal diffusivity has been experimentally observed on pin-type samples [Cre11].

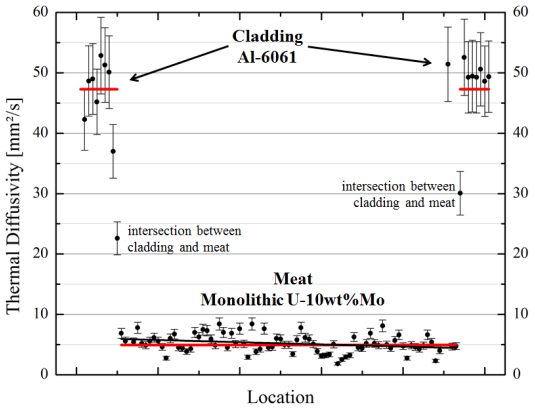


***Figure B.6:*** *First thermal diffusivity map across the width of plate L1P12Z. The red lines are the mean values of Al-6061 and U-10 wt.%Mo (see Table B.2). The black line is fitted to show the gradient in the thermal diffusivity of the meat along the width of the plate.*

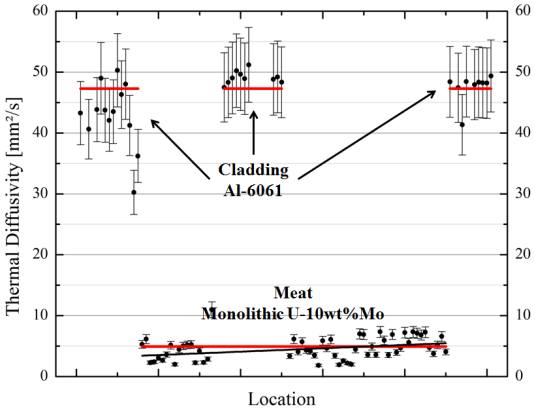


***Figure B.7:*** *Second thermal diffusivity map across the width of plate L1P12Z. The red lines are the mean values of Al-6061 and U-10 wt.%Mo (see Table B.2). The black line is fitted to show the gradient in the thermal diffusivity of the meat along the width of the plate.*

| | L1P12Z | L2P16Z | Fresh Material (STDM) | Fresh Material (Laser Flash) [RWK+10] |
|---|---|---|---|---|
| Al 6061 | $(47.3 \pm 0.9)$ $mm^2/s$ | $(45.7 \pm 1.3)$ $mm^2/s$ | $(50.3 \pm 6.0)$ $mm^2/s$ | |
| U-10 wt.%Mo | $(4.9 \pm 0.7)$ $mm^2/s$ | $(4.1 \pm 0.6)$ $mm^2/s$ | $(6.4 \pm 0.8)$ $mm^2/s$ | $(4.8 \pm 0.3)$ $mm^2/s$ |

***Table B.2:*** *Thermal diffusivity values for cladding and fuel zone of both monolithic plates compared to values of a previous STDM and LASER Flash measurement of a fresh U-10 wt.%Mo fuel plate sample. The uncertainty for each data point is 12 %. The average values have been weighted by the uncertainty of each data point.*

Regarding the thermal diffusivity of Al-6061 cladding, the values of the irradiated material are lower than for fresh material. Although aluminum is known for its low activation during irradiation, the highly energetic fission products and neutron irradiation, especially fast neutrons, cause microstructural damage in the cladding material and, thus, decrease its thermal diffusivity.

The map of plate L1P12Z shows data points around 20 $mm^2/s$ to 30 $mm^2/s$ at the intersection between cladding and fuel zone. There, at the boundary, the STDM measures a mixture of both materials, as the LASER beam encloses an area of $\sim$ 50 $\mu$m diameter. The signal determines a combined value for the highly conductive Al-6061 and the less conductive U-10 wt.%Mo, varying with the enclosed volume fraction of each material.
On the map of plate L2P16Z are three strongly deviating points in the meat zone. Taking into account the literature value for the thermal diffusivity of Zr (12.6 $mm^2/s$) [FL95], these points are, again, likely the result of a boundary measurement, namely between the Zr barrier and the cladding material. The reason for the deviations from the meat zone is that the measurement location is controlled through a lens that degrades and tarnishes due to radiation damage. Thus, the measurement location can drift to boundaries, smear over, and lead to deviations from the fuel zone. This can be clearly observed in Figure B.6, where the operator drifted into the cladding

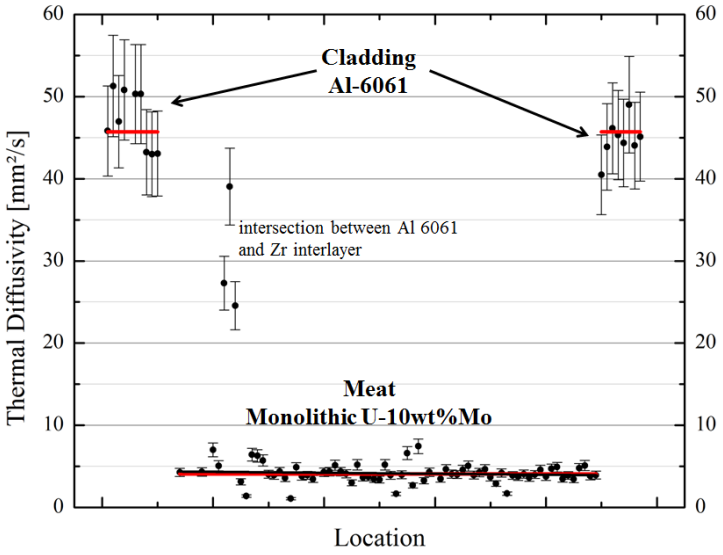


***Figure B.8:*** *Thermal diffusivity map across the width of plate L2P16Z. The red lines are the mean values of Al-6061 and U-10 wt.%Mo (see Table B.2). The black line is fitted to show the gradient in the thermal diffusivity of the meat along the width of the plate. But in contrast to plate L1P12Z, no significant gradient can be observed.*

zone on the rim of the meat zone.
Further, plate L1P12Z shows in the first measurement (Figure B.6) a clear gradient in the thermal diffusivity of the meat as a function of location. A slighter gradient can also be observed on the second measurement, while plate L2P16Z shows no significant gradient. Regarding the burnup, L1P12Z has a higher burnup in total and a steeper gradient than L2P16Z. It can therefore be assumed that thermal diffusivity depends on the burnup in the fuel. But which side of the sample experienced the high burnup is not known; thus, dependence on burnup cannot be proven at this point.

Besides the thermal diffusivity, the density and specific heat of the materials are factors that must be known for the calculation of thermal conductivity (see Table B.3). The density of the meat changes during irradiation (compare the hot and cold edges of the plates in Figure B.9 and Figure B.10). It is assumed that there is no significant change in the specific heat because no data exist as yet describing how it might change. Density change depending on the fission density fD was examined in the RERTR-12 experiment [RRM$^+$12] by weighing the fuel plate in air and in water before and after irradiation. The relative density change $\Delta\rho$ is calculated using Equation B.2 and leads to $-2.5\,\%$ for plate L1P12Z and $1.2\,\%$ for plate L2P16Z.

$$\Delta\rho = (-6.07 \pm 0.32) \cdot 10^{-24} \left[\frac{cm^3}{f}\right] \cdot f_{\mathrm{D}} \tag{B.2}$$

Using Equation B.1 and the information given in Table B.3, it is possible to estimate the thermal conductivity of the irradiated U-10 wt.%Mo fuel and Al-6061 cladding. When calculating the

| | Density at 300 K | Specific Heat Capacity at 300 K |
|---|---|---|
| Al 6061 | 2.7 $g/cm^3$ | 0.896 $J/g \cdot K$ |
| U-10 wt.%Mo | 16.8 $g/cm^3$ | 0.134 $J/g \cdot K$ |

***Table B.3:*** *Thermo-physical properties for Al 6061 [PLC+11c] and non-irradiated U-10 wt.%Mo [RWK+10].*

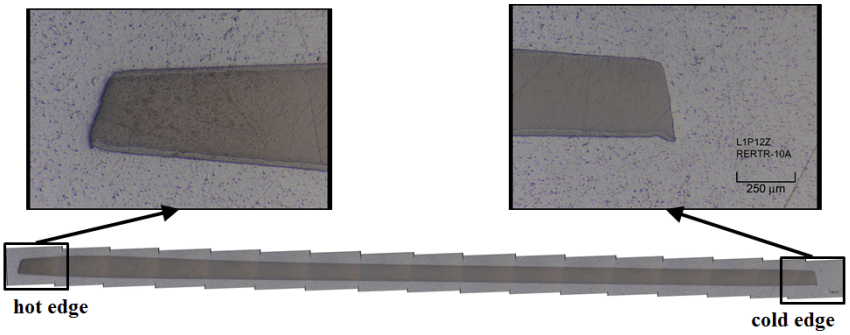


***Figure B.9:*** *Post-irradiation Optical Microscope picture of plate L1P12Z with magnification of the hot and cold edges of the meat zone.*

thermal conductivity of the irradiated meat, the change in the density has to be considered using formula B.3.

$$\rho_{\text{meat}} = \rho_{\text{U}-10\text{wt.\%Mo}} \cdot (1 + \Delta\rho) \tag{B.3}$$

| | U-10 wt.%Mo | Al 6061 |
|---|---|---|
| L1P12Z irradiated | $(9.0 \pm 1.5)$ $W/m \cdot K$ | $(114.4 \pm 2.1)$ $W/m \cdot K$ |
| L2P16Z irradiated | $(10.9 \pm 1.7)$ $W/m \cdot K$ | $(110.6 \pm 3.2)$ $W/m \cdot K$ |
| Non-irradiated (STDM) | $(14.4 \pm 1.9)$ $W/m \cdot K$ | $(121.6 \pm 15.0)$ $W/m \cdot K$ |
| Non-irradiated at 300 K [RWK+10], [PLC+11c] | 11.1 $W/m \cdot K$ | 167 $W/m \cdot K$ |

***Table B.4:*** *Thermal Conductivity for irradiated monolithic U-10 wt.%Mo and Al 6061 compared to non-irradiated STDM and literature data.*

The thermal conductivity of fresh Al-6061 measured by the STDM is far below the literature value. During the HIP process, the plates are heat treated and pressurized, which can have an impact on the thermal diffusivity and, consequently, on the thermal conductivity of the Aluminum alloy. Comparing the different tempers of Al-6061, the thermal conductivity ranges between $\sim 150$ $W/m \cdot K$ and $\sim 180$ $W/m \cdot K$.

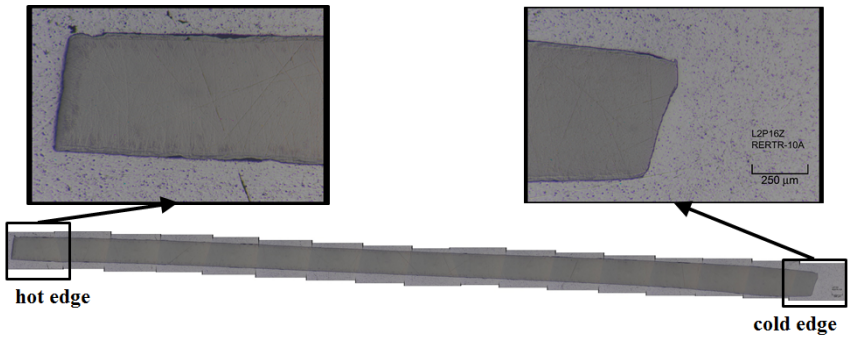


***Figure B.10:*** *Post-irradiation Optical Microscope picture of plate L2P16Z with magnification of the hot and cold edges of the meat zone.*

### B.3.1.2 Dispersion Sample

Figure B.11 presents a map of the thermal diffusivity across the width of the disperse fuel plate R6R018.

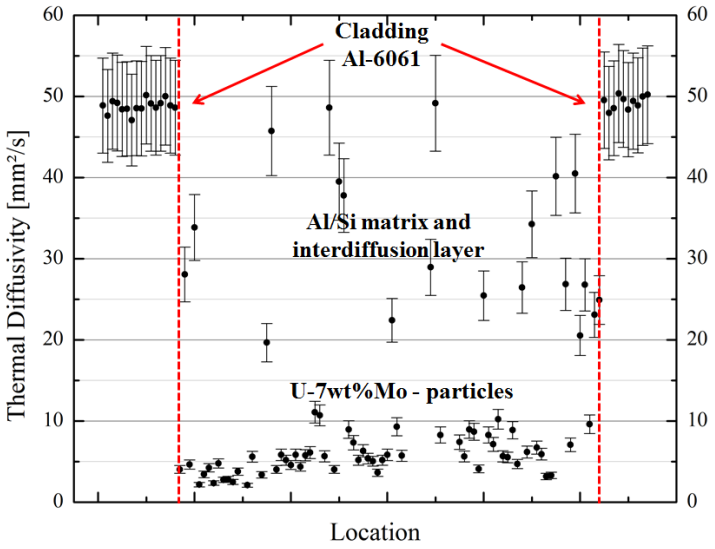


***Figure B.11:*** *Thermal diffusivity map across the width of plate R6R018.*

Again both sides of the diagram show the thermal diffusivity of the Al-6061 cladding. In the fuel-meat zone, the low diffusivity ($<10\,\mathrm{mm^2/s}$) indicates U-7 wt.%Mo particles. The spikes up to thermal diffusivity values of the cladding are caused by the fuel structure (see Figure B.12), an alternation of fuel particles and matrix material.

Compared to the measurement of the monolithic fuel plate L1P12Z, which has almost the same burnup but contains $\sim 3\,\%$ less highly conductive molybdenum ($138\,\mathrm{W/m{\cdot}K}$) [9], a thermal diffusivity of $<3.7\,\mathrm{mm^2/s}$ in the meat zone is expected. Indeed a few data points can be found within that low-diffusivity range. They result from measurements in which the LASER beam of the STDM directly hits a U-7 wt.%Mo particle such that the whole radius ( $\sim 50\ \mu$m) of the LASER beam covers the particle, which has a size of up to 106 $\mu$m. In this case, the thermal diffusivity of the fuel particle itself is measured.
As already mentioned in the description of fuel production, the Si rich layer around the fuel

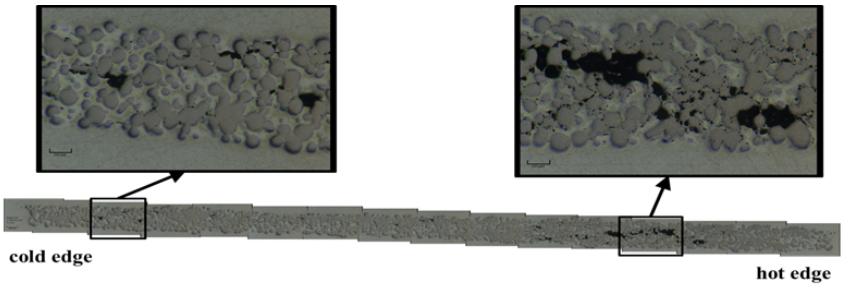


***Figure B.12:*** *Post-irradiation Optical Microscope picture of plate R6R018 with magnification of the hot and cold edges of the meat zone.*

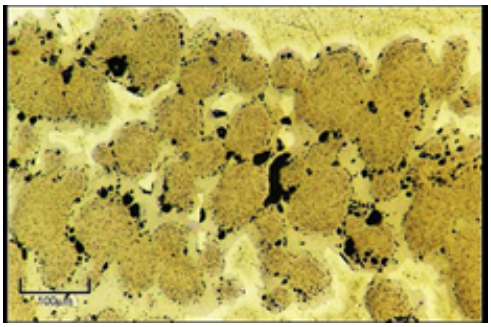

***Figure B.13:*** *Post-irradiation Optical Microscope magnification of the fuel particles with inter-diffusion layer and fission gas accumulations in the high burnup area.*

particles reduces, but does not completely prevent the growth of an inter-diffusion layer between the fuel particle and the Al matrix during irradiation. Figure B.13, a magnification of the high-burnup zone, clearly shows a layer around the fuel particles, together with a destabilizing and low- to non-thermal conductive conglomeration of fission-gas voids.
Regarding the scale on the microscope picture, there are few locations where the diffusion layer has a thickness of $> 50$ $\mu$m, which minimizes the chance to measure only this layer as is the case for the bigger fuel particles. Instead either a mixture of diffusion layer and fuel particle or diffusion layer and matrix is measured. As the matrix consists of pure Aluminum and Silicon, which are high thermal-conductivity materials with thermal diffusivities of $97\,\mathrm{mm^2/s}$ for pure Aluminum [JTS$^+$80] and $88\,\mathrm{mm^2/s}$ for Silicon [JTS$^+$80], the composite thermal diffusivity must be within that range. However, the diagram shows only diffusivities below $50\,\mathrm{mm^2/s}$, which indicates that only mixtures of the matrix with the less conductive diffusion layer or fuel particle have been measured.
Only taking into account the data points below $10\,\mathrm{mm^2/s}$, those which indicate fuel particles or mixtures containing mostly fuel particles, again a gradient exists that could indicate a fission-density-dependent thermal diffusivity, just as has been seen in monolithic fuel.
This measurement of the dispersion fuel can only give qualitative statements concerning general thermal diffusivity gradients depending on the burnup. It is not possible to calculate precise values for the fuel particles, inter-diffusion layer or matrix material as there is no information on the precise measurement location that could precisely identify the LASER-beam-enclosed materials.

### B.3.2 Thermal Diffusivity Variation

Figure B.14 shows the frequency of the data points according to a certain thermal diffusivity per fuel plate.

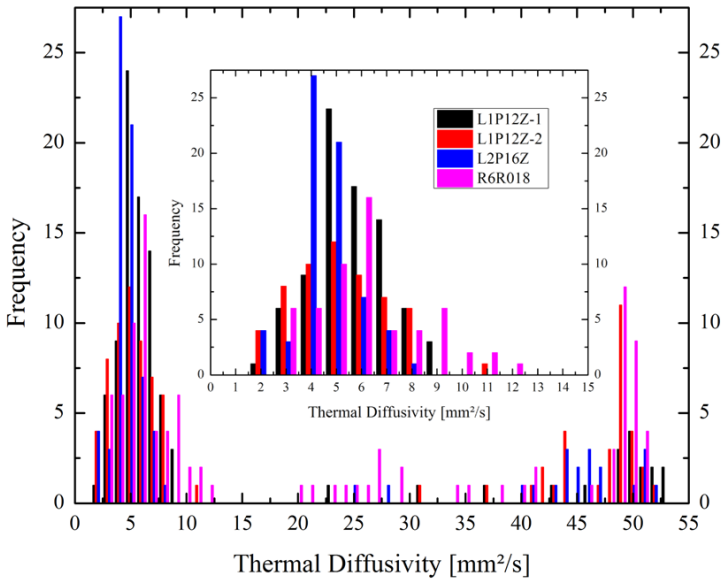


***Figure B.14:*** *Frequency of the number of data points for certain thermal diffusivities per plate with a zoom in the meat zone between* $0\,\mathrm{mm^2/s}$ *and* $15\,\mathrm{mm^2/s}$.

The monolithic samples show a clear maximum in the fuel zone with thermal diffusivities between $0\,\mathrm{mm^2/s}$ and $10\,\mathrm{mm^2/s}$ (see zoom in Figure B.14) and the cladding zone above $40\,\mathrm{mm^2/s}$ . The thermal diffusivity of the disperse sample is more scattered also between fuel and cladding zone due to the meat structure, where mixtures between the high conductive matrix material and the low conductive fuel have been measured.

## B.4 Conclusion

The measurements of the monolithic samples show a mean thermal diffusivity of $(4.5 \pm 0.7)\ \mathrm{mm^2/s}$, which is significantly lower than the STDM of fresh monolithic U-10 wt.%Mo of $(6.4 \pm 0.8)\ \mathrm{mm^2/s}$. A slight gradient has been observed over the width of plate L1P12Z, with, in total, a higher fission density and a steeper fission density gradient, which can be an indication of a fission density or burnup dependent thermal diffusivity. No gradient was observed for L2P16Z. Additional samples should be evaluated to further study this behavior.
The mean thermal conductivity of the irradiated monolithic fuel was estimated from the values determined from the STDM measurements to be $(9.9 \pm 1.6)\ \mathrm{W/m{\cdot}K}$, which is significantly lower than the thermal conductivity of fresh U-10 wt.%Mo $(14.4 \pm 1.9)\ \mathrm{W/m{\cdot}K}$, which is in good accordance with thermal conductivity measurements of fresh monolithic U-8 wt.%Mo obtained by using the LASER flash method [HBB+10].
Thermal diffusivity is not the only parameter in the thermal conductivity calculation that changes during irradiation. The main parameter with the highest deviation is density; this, therefore, has the highest impact on thermal conductivity. Again it is mandatory to have exact information

from the STDM measurement position combined with data on local fuel swelling to increase accuracy.

The change in specific heat during irradiation, which is currently assumed not to be significant, is still an unknown parameter without experimental determination. The measurements performed on the dispersion fuel plate shows the high resolution of the STDM instrument. It is possible to separate fuel particles from the matrix. However, due to the lack of information on exact measurement position, it is not possible to give exact values for the thermal conductivity of single materials as overlapping measurements between two materials can occur.

The STDM is a powerful instrument, with very high resolution and accuracy in thermal diffusivity. However, it is necessary to improve the exact determination of the measurement position on the sample, especially for work with dispersion fuels.

# APPENDIX C

## Thickness Values of Investigated Samples

The following tables give information to the the thickness and masses of the investigated LFA and DSC samples. The thickness value of the as-fabricated samples is the thickness of the fuel meat after removing the cladding. The thickness values of the in-pile irradiated samples are separated into cladding, meat and if existing diffusion barrier.

| Fuel Name | Thickness LFA sample [mm] | Mass DSC sample 1 [mg] | Mass DSC sample 2 [mg] | Mass DSC sample 3 [mg] |
|---|---|---|---|---|
| E-FUTURE 4112 | 0.46 | 29.89 | 48.76 | 49.25 |
| E-FUTURE 6101 | 0.42 | 55.79 | 42.98 | 31.90 |
| E-FUTURE II 702 | 0.42 | 62.63 | 38.40 | 53.44 |
| E-FUTURE II 1203 | 0.38 | 64.63 | 60.42 | 40.65 |
| E-FUTURE II 1212 | 0.44 | 47.2 | 58.72 | 36.03 |
| IRIS-4 U-Mo/Al | 0.45 | 61.05 | 44.97 | 48.01 |
| IRIS-4 U-Mo/AlSi | 0.42 | 59.56 | 48.11 | 63.30 |
| IRIS-TUM 7001 | 0.37 | 35.19 | 51.55 | 51.99 |
| IRIS-TUM 8003 | 0.27 | 25.03 | 27.16 | 33.4 |
| IRIS-TUM 8502 | 0.30 | 34.07 | 33.99 | 29.16 |
| SELENIUM A | 0.48 | 65.3 | 54.0 | 44.5 |
| SELENIUM B | 0.35 | 36.6 | 49.5 | 46.3 |
| SELENIUM C | 0.38 | 56.2 | 64.5 | 67.9 |
| AFIP-1 | 0.49 | 71.46 | 46.59 | 59.48 |

***Table C.1:*** *Thickness values and masses of the investigated as-fabricated LFA and DSC samples. The uncertainty of the thickness values is* 0.05 mm *and of the masses is* 0.01 mg

# APPENDIX D

## Sectioning Diagrams

Sectioning diagrams of the in-pile irradiated fuels.

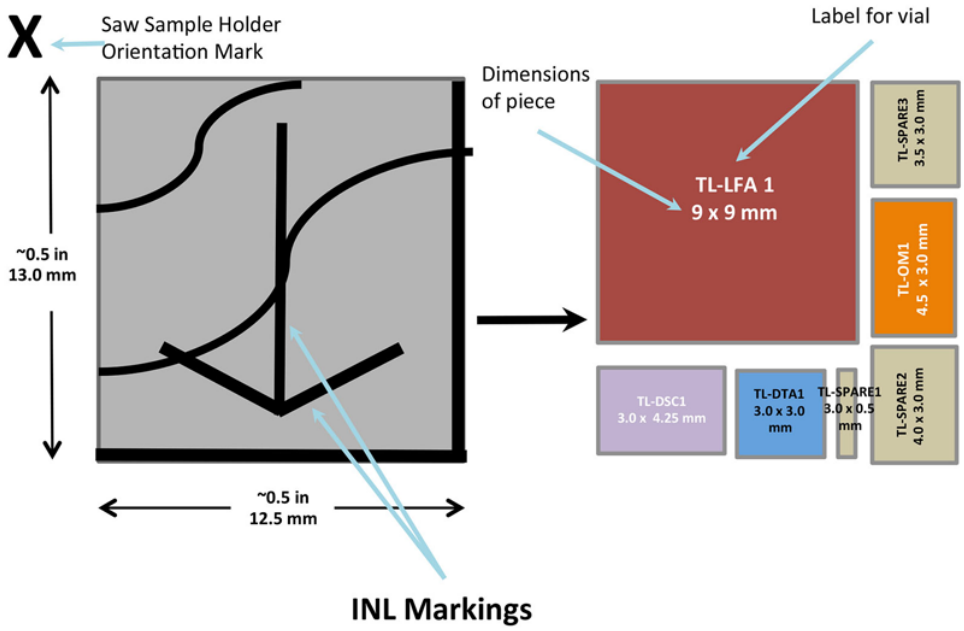


***Figure D.1:*** *Sectioning diagram of segment AFIP-1 TL [BCB+14a].*

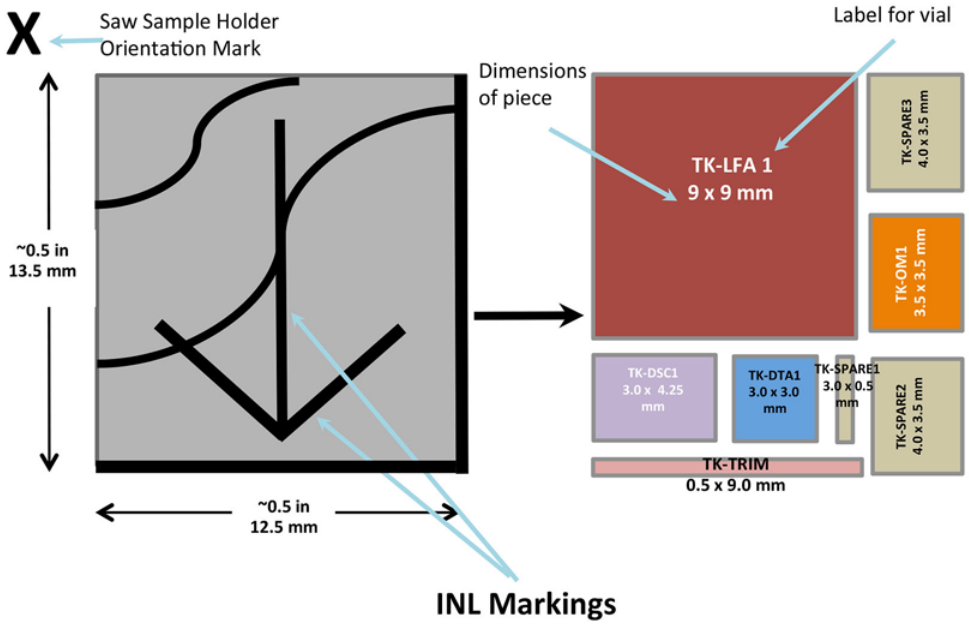


***Figure D.2:*** *Sectioning diagram of segment AFIP-1 TK [BCB+ 14a].*

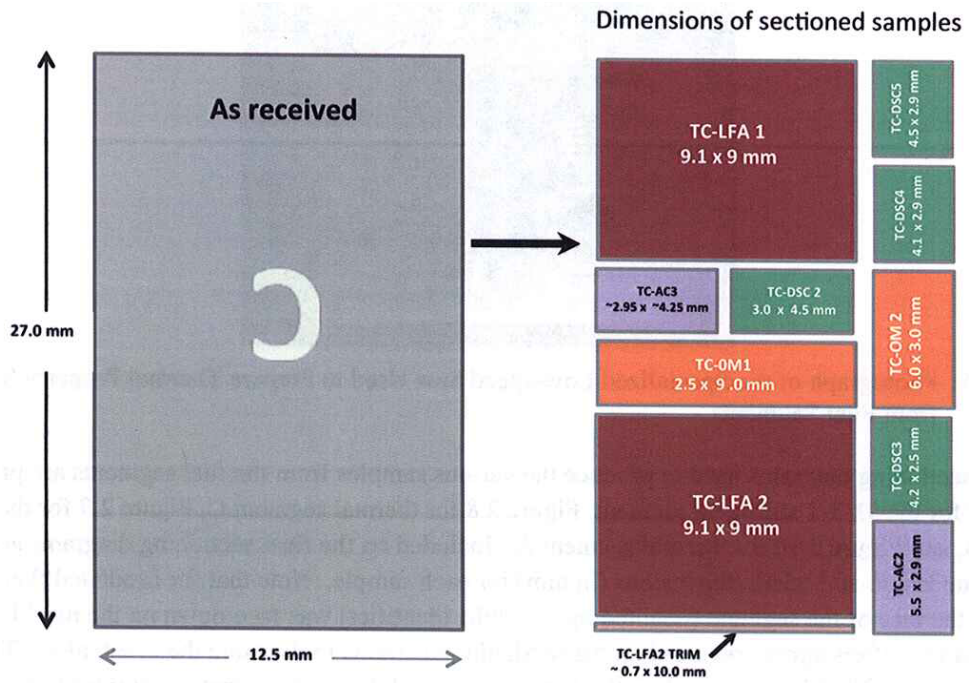


***Figure D.3:*** *Sectioning diagram of segment AFIP-2 TC [BCB+ 13].*

# APPENDIX E

## Polishing Recipe

The rear surface of a fresh met mount is usually bent. So in the step one, the rear surface of the met mount is polished with rough sandpaper to obtain a flat surface that is parallel to the front surface for a good polishing result.

| **Rotation** | | | **200 r/min** | | | **First Step** | | **Second Step** | |
|---|---|---|---|---|---|---|---|---|---|
| step | Mount Surface | Paper | FEPA Nr | Pressure | Suspension | Time | Rotation Direction | Time | Rotation Direction |
| 1 | back | SiC | 180 | 20 N | water | 1 min | →→ | 1 min | →← |
| 2 | front | SiC | 180 | 10 N | water | 30 sec | →→ | 30 sec | →← |
| 3 | front | SiC | 220 | 10 N | water | 30 sec | →→ | 30 sec | →← |
| 4 | front | SiC | 500 | 10 N | water | 30 sec | →→ | 30 sec | →← |
| 5 | front | SiC | 800 | 10 N | water | 30 sec | →→ | 30 sec | →← |
| 6 | front | SiC | 1000 | 10 N | water | 30 sec | →→ | 30 sec | →← |
| 7 | front | MD Dac | | 10 N | 9$\mu$m Dia Pro | 5 min | →→ | 5 min | →← |
| 8 | front | MD Dac | | 10 N | 3$\mu$m Dia Pro | 5 min | →→ | 5 min | →← |
| 9 | front | MD Dac | | 10 N | 1$\mu$m Dia Pro | 5 min | →→ | 5 min | →← |

***Table E.1:*** *Polishing parameters for SEM sample preparation.*

# APPENDIX F

## Parameters for TUM and PNNL Models

### F.1 Density

The density of the composite of cladding, Zr barrier and U-Mo has been measured using pycnometry, see Chapter 4.3.2.
By applying the rule of mixture (see Equation 3.14 in Chapter 3.3), the density of all single layers can be calculated with the knowledge of the density of the AA 6061 cladding and the Zr barrier, which are known from literature [FL95, Mil02] and are assumed not to be affected by irradiation. The volume fractions can be obtained from the thickness measurement: 66 vol.% AA 6061 and 34 vol.% Zr + U-Mo for the three layer system and 66 vol.% AA 6061, 5 vol.% Zr and 29 vol.% U-Mo for the five layer system.

| | Density [g/cm$^3$] |
|---|---|
| Composite | 6.14±0.036 |
| AA 6061 | 2.71 |
| Zr + U-Mo (3-layer) | 12.81±0.11 |
| Zirconium | 6.57 |
| U-Mo (5-layer) | 13.87±0.12 |

***Table F.1:*** *Density at room temperature of the Composite and the single layers of the irradiated monolithic AFIP-2BZ fuel segments [BCC+15a]. The values are averaged for segment TC LFA1 and TC LFA2.*

### F.2 Specific Heat Capacity

The specific heat capacity of the composite of cladding, Zr barrier and U-Mo has been measured using differential calorimetry, see Chapter 4.2.
By applying the Neumann-Kopp rule (see Equation 3.10 in Chapter 3.2), the specific heat capacity of all single layers can be calculated with the knowledge of the density of the AA 6061 cladding and the Zr barrier, which are known from literature [FL95, Mil02]. They are assumed not to be affected by irradiation, although there will be minor modifications to the chemical

composition of the constituents as a function of irradiation, e.g. transmutation of silicon in AA 6061. But the influence of these modifications is rather minor and well within the uncertainty of the measurement [BCC+15a]. The volume fractions can be converted into weight fractions via the density of the constituents: 29 wt.% AA 6061 and 71 wt.% Zr + U-Mo for the three layer system and 29 wt.% AA 6061, 5 wt.% Zr and 66 wt.% U-Mo for the five layer system.

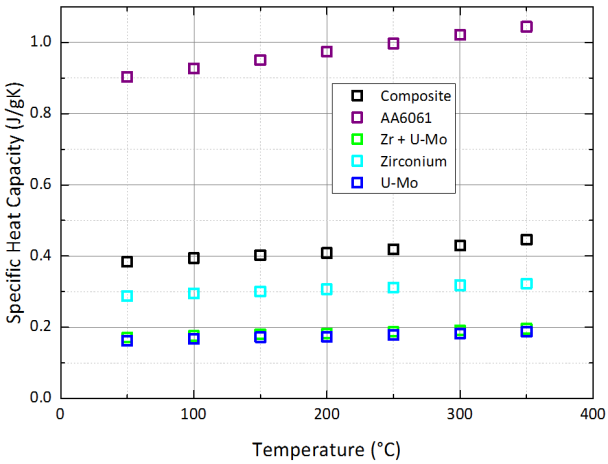


***Figure F.1:*** *Specific heat capacity data [BCC+15a, FL95, Mil02]. The values are averaged for segment TC LFA1 and TC LFA2.*

## F.3 Thermal Diffusivity

The thermal diffusivity of the composite of cladding, Zr barrier and U-Mo has been measured using the Laser Flash method, see Chapter 4.1.
The thermal diffusivity of the AA6061 and the Zr can be calculated from the thermal conductivity relations, provided in [Def98, FL95] and the density and specific heat capacity values from Appendix F.1 and F.2 by using Equation 3.1 in Chapter 3.
The TUM model calculates the thermal diffusivity of the U-Mo directly from the raw data, while the PNNL model needs the thermal diffusivity of the composite. This was obtained from the one-layer analysis of the Netzsch Proteus software Version 6.0.0, using the Cape-Lehman + pulse correction model that is based on [CL63, PJBA61].

For the calculation of the fuel meat thermal diffusivity, the thickness of the single layers is mandatory. Table F.2 gives the thickness values for all layer, which have been obtain by optical microscopy [BCC+15a]. For the three layer model, the thickness of the zirconium of the top and bottom have been added to the thickness of the U-Mo layer.

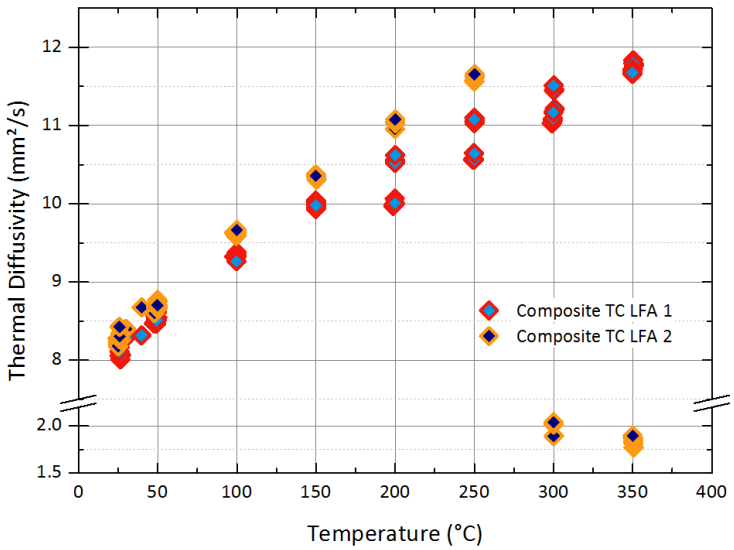


***Figure F.2:*** *Thermal diffusivity values of the composite are separated here for segment TC LFA1 and TC LFA2 [BCC+ 15a].*

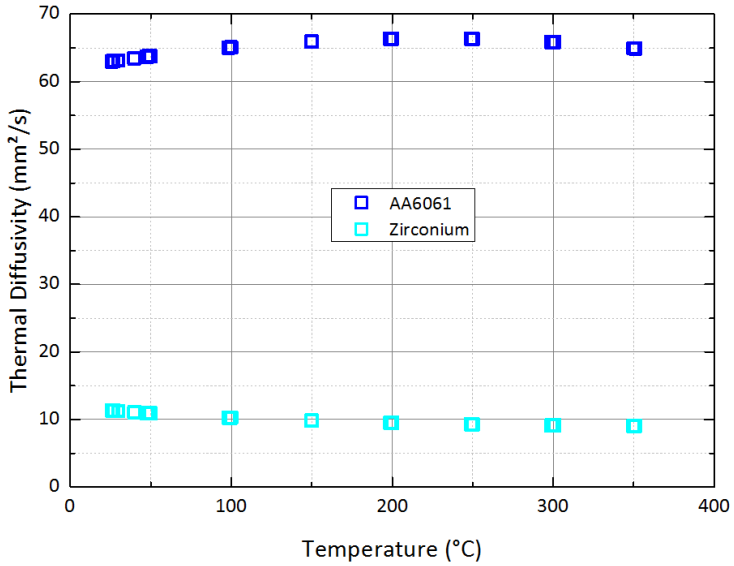


***Figure F.3:*** *Thermal diffusivity data from [Def98, FL95].*

| | Thickness [$\mu$m] |
|---|---|
| Composite | 1335±39.1 |
| AA 6061 (top) | 443±20.6 |
| Zirconium (top) | 31.5±7.02 |
| U-Mo | 391±15.6 |
| Zirconium (bottom) | 34.7±8.75 |
| AA 6061 (top) | 445±46.4 |

***Table F.2:*** *Thickness of the Composite and the single layers of the irradiated monolithic AFIP-2BZ fuel segments [BCC+ 15a].*

# APPENDIX G

## Thermal Properties Data

### G.1 Thermal Diffusivity

Table G.1 to G.20 show the fitting parameters with their standard error obtained from the analysis of the raw data following the procedure in Chapter 4.1.3. By inserting the parameters into Equation G.1, the temperature dependent thermal diffusivity $\alpha(T)$ can be calculated.

$$\alpha(T) = A + B \cdot T + C \cdot T^2 + D \cdot T^3 \tag{G.1}$$

| Parameter | Value | Unit |
|---|---|---|
| A | $26.49 \pm 0.45$ | $[\frac{\mathrm{mm}^2}{\mathrm{s}}]$ |
| B | $(6.28 \pm 9.90) \cdot 10^{-3}$ | $[\frac{\mathrm{mm}^2}{^\circ\mathrm{C}\cdot\mathrm{s}}]$ |
| C | $(3.67 \pm 5.82) \cdot 10^{-5}$ | $[\frac{\mathrm{mm}^2}{^\circ\mathrm{C}^2\cdot\mathrm{s}}]$ |
| D | $(-1.62 \pm 0.98) \cdot 10^{-7}$ | $[\frac{\mathrm{mm}^2}{^\circ\mathrm{C}^3\cdot\mathrm{s}}]$ |

***Table G.1:*** *E-FUTURE 4112*

| Parameter | Value | Unit |
|---|---|---|
| A | $22.50 \pm 0.47$ | $[\frac{\mathrm{mm}^2}{\mathrm{s}}]$ |
| B | $(1.53 \pm 1.11) \cdot 10^{-2}$ | $[\frac{\mathrm{mm}^2}{^\circ\mathrm{C}\cdot\mathrm{s}}]$ |
| C | $(-4.93 \pm 6.36) \cdot 10^{-5}$ | $[\frac{\mathrm{mm}^2}{^\circ\mathrm{C}^2\cdot\mathrm{s}}]$ |
| D | $(0.34 \pm 1.10) \cdot 10^{-7}$ | $[\frac{\mathrm{mm}^2}{^\circ\mathrm{C}^3\cdot\mathrm{s}}]$ |

***Table G.2:*** *E-FUTURE 6101*

| Parameter | Value | Unit |
|---|---|---|
| A | $20.29 \pm 0.40$ | $[\frac{mm^2}{s}]$ |
| B | $(5.75 \pm 8.89) \cdot 10^{-3}$ | $[\frac{mm^2}{°C \cdot s}]$ |
| C | $(1.29 \pm 5.27) \cdot 10^{-5}$ | $[\frac{mm^2}{°C^2 \cdot s}]$ |
| D | $(-7.13 \pm 8.96) \cdot 10^{-8}$ | $[\frac{mm^2}{°C^3 \cdot s}]$ |

***Table G.3:*** *E-FUTURE II 702*

| Parameter | Value | Unit |
|---|---|---|
| A | $21.61 \pm 0.37$ | $[\frac{mm^2}{s}]$ |
| B | $(-0.92 \pm 8.14) \cdot 10^{-3}$ | $[\frac{mm^2}{°C \cdot s}]$ |
| C | $(6.06 \pm 4.82) \cdot 10^{-5}$ | $[\frac{mm^2}{°C^2 \cdot s}]$ |
| D | $(-1.66 \pm 0.82) \cdot 10^{-7}$ | $[\frac{mm^2}{°C^3 \cdot s}]$ |

***Table G.4:*** *E-FUTURE II 1203*

| Parameter | Value | Unit |
|---|---|---|
| A | $19.80 \pm 0.28$ | $[\frac{mm^2}{s}]$ |
| B | $(2.27 \pm 0.63) \cdot 10^{-3}$ | $[\frac{mm^2}{°C \cdot s}]$ |
| C | $(-6.71 \pm 3.75) \cdot 10^{-5}$ | $[\frac{mm^2}{°C^2 \cdot s}]$ |
| D | $(5.28 \pm 6.39) \cdot 10^{-8}$ | $[\frac{mm^2}{°C^3 \cdot s}]$ |

***Table G.5:*** *E-FUTURE II 1212*

| Parameter | Value | Unit |
|---|---|---|
| A | $23.91 \pm 0.40$ | $[\frac{mm^2}{s}]$ |
| B | $(-1.76 \pm 0.86) \cdot 10^{-2}$ | $[\frac{mm^2}{°C \cdot s}]$ |
| C | $(8.50 \pm 5.04) \cdot 10^{-5}$ | $[\frac{mm^2}{°C^2 \cdot s}]$ |
| D | $(-1.70 \pm 0.85) \cdot 10^{-7}$ | $[\frac{mm^2}{°C^3 \cdot s}]$ |

***Table G.6:*** *IRIS-4 U-Mo/Al*

| Parameter | Value | Unit |
|---|---|---|
| A | $22.12 \pm 0.63$ | $[\frac{mm^2}{s}]$ |
| B | $(1.83 \pm 1.39) \cdot 10^{-2}$ | $[\frac{mm^2}{°C \cdot s}]$ |
| C | $(-9.00 \pm 8.17) \cdot 10^{-5}$ | $[\frac{mm^2}{°C^2 \cdot s}]$ |
| D | $(0.99 \pm 1.39) \cdot 10^{-7}$ | $[\frac{mm^2}{°C^3 \cdot s}]$ |

***Table G.7:*** *IRIS-4 U-Mo/AlSi*

| Parameter | Value | Unit |
|---|---|---|
| A | $14.42 \pm 0.18$ | $[\frac{\mathrm{mm}^2}{\mathrm{s}}]$ |
| B | $(1.65 \pm 0.40) \cdot 10^{-2}$ | $[\frac{\mathrm{mm}^2}{^\circ\mathrm{C}\cdot\mathrm{s}}]$ |
| C | $(-6.11 \pm 2.38) \cdot 10^{-5}$ | $[\frac{\mathrm{mm}^2}{^\circ\mathrm{C}^2\cdot\mathrm{s}}]$ |
| D | $(6.46 \pm 4.08) \cdot 10^{-8}$ | $[\frac{\mathrm{mm}^2}{^\circ\mathrm{C}^3\cdot\mathrm{s}}]$ |

***Table G.8:*** *IRIS-TUM 7001*

| Parameter | Value | Unit |
|---|---|---|
| A | $10.07 \pm 0.20$ | $[\frac{\mathrm{mm}^2}{\mathrm{s}}]$ |
| B | $(1.84 \pm 0.45) \cdot 10^{-2}$ | $[\frac{\mathrm{mm}^2}{^\circ\mathrm{C}\cdot\mathrm{s}}]$ |
| C | $(-6.33 \pm 2.70) \cdot 10^{-5}$ | $[\frac{\mathrm{mm}^2}{^\circ\mathrm{C}^2\cdot\mathrm{s}}]$ |
| D | $(6.62 \pm 4.62) \cdot 10^{-8}$ | $[\frac{\mathrm{mm}^2}{^\circ\mathrm{C}^3\cdot\mathrm{s}}]$ |

***Table G.9:*** *IRIS-TUM 8003*

| Parameter | Value | Unit |
|---|---|---|
| A | $10.83 \pm 0.16$ | $[\frac{\mathrm{mm}^2}{\mathrm{s}}]$ |
| B | $(1.04 \pm 0.37) \cdot 10^{-2}$ | $[\frac{\mathrm{mm}^2}{^\circ\mathrm{C}\cdot\mathrm{s}}]$ |
| C | $(-2.72 \pm 2.22) \cdot 10^{-5}$ | $[\frac{\mathrm{mm}^2}{^\circ\mathrm{C}^2\cdot\mathrm{s}}]$ |
| D | $(1.71 \pm 3.77) \cdot 10^{-8}$ | $[\frac{\mathrm{mm}^2}{^\circ\mathrm{C}^3\cdot\mathrm{s}}]$ |

***Table G.10:*** *IRIS-TUM 8502*

| Parameter | Value | Unit |
|---|---|---|
| A | $24.32 \pm 0.57$ | $[\frac{\mathrm{mm}^2}{\mathrm{s}}]$ |
| B | $(3.47 \pm 1.25) \cdot 10^{-2}$ | $[\frac{\mathrm{mm}^2}{^\circ\mathrm{C}\cdot\mathrm{s}}]$ |
| C | $(-1.48 \pm 0.74) \cdot 10^{-4}$ | $[\frac{\mathrm{mm}^2}{^\circ\mathrm{C}^2\cdot\mathrm{s}}]$ |
| D | $(1.79 \pm 1.26) \cdot 10^{-7}$ | $[\frac{\mathrm{mm}^2}{^\circ\mathrm{C}^3\cdot\mathrm{s}}]$ |

***Table G.11:*** *SELENIUM A*

| Parameter | Value | Unit |
|---|---|---|
| A | $22.11 \pm 0.49$ | $[\frac{\mathrm{mm}^2}{\mathrm{s}}]$ |
| B | $(3.62 \pm 1.10) \cdot 10^{-2}$ | $[\frac{\mathrm{mm}^2}{^\circ\mathrm{C}\cdot\mathrm{s}}]$ |
| C | $(-1.41 \pm 0.65) \cdot 10^{-4}$ | $[\frac{\mathrm{mm}^2}{^\circ\mathrm{C}^2\cdot\mathrm{s}}]$ |
| D | $(1.60 \pm 1.11) \cdot 10^{-7}$ | $[\frac{\mathrm{mm}^2}{^\circ\mathrm{C}^3\cdot\mathrm{s}}]$ |

***Table G.12:*** *SELENIUM B*

| Parameter | Value | Unit |
|---|---|---|
| A | $20.20 \pm 0.58$ | $[\frac{\mathrm{mm}^2}{\mathrm{s}}]$ |
| B | $(3.62 \pm 1.14) \cdot 10^{-2}$ | $[\frac{\mathrm{mm}^2}{^\circ\mathrm{C}\cdot\mathrm{s}}]$ |
| C | $(-1.38 \pm 0.26) \cdot 10^{-4}$ | $[\frac{\mathrm{mm}^2}{^\circ\mathrm{C}^2\cdot\mathrm{s}}]$ |
| D | $(1.48 \pm 1.01) \cdot 10^{-7}$ | $[\frac{\mathrm{mm}^2}{^\circ\mathrm{C}^3\cdot\mathrm{s}}]$ |

***Table G.13:*** *SELENIUM C*

| Parameter | Value | Unit |
|---|---|---|
| A | $18.53 \pm 0.15$ | $[\frac{\mathrm{mm}^2}{\mathrm{s}}]$ |
| B | $(1.73 \pm 0.33) \cdot 10^{-2}$ | $[\frac{\mathrm{mm}^2}{^\circ\mathrm{C}\cdot\mathrm{s}}]$ |
| C | $(-8.40 \pm 1.93) \cdot 10^{-5}$ | $[\frac{\mathrm{mm}^2}{^\circ\mathrm{C}^2\cdot\mathrm{s}}]$ |
| D | $(1.09 \pm 0.33) \cdot 10^{-7}$ | $[\frac{\mathrm{mm}^2}{^\circ\mathrm{C}^3\cdot\mathrm{s}}]$ |

***Table G.14:*** *AFIP-1 (disperse, fresh)*

| Parameter | Value | Unit |
|---|---|---|
| A | $5.59 \pm 0.08$ | $[\frac{\mathrm{mm}^2}{\mathrm{s}}]$ |
| B | $(1.15 \pm 0.20) \cdot 10^{-2}$ | $[\frac{\mathrm{mm}^2}{^\circ\mathrm{C}\cdot\mathrm{s}}]$ |
| C | $(-2.70 \pm 1.47) \cdot 10^{-5}$ | $[\frac{\mathrm{mm}^2}{^\circ\mathrm{C}^2\cdot\mathrm{s}}]$ |
| D | $(4.46 \pm 3.03) \cdot 10^{-8}$ | $[\frac{\mathrm{mm}^2}{^\circ\mathrm{C}^3\cdot\mathrm{s}}]$ |

***Table G.15:*** *AFIP-1 (disperse, low burnup), run1*

| Parameter | Value | Unit |
|---|---|---|
| A | $5.27 \pm 0.33$ | $[\frac{\mathrm{mm}^2}{\mathrm{s}}]$ |
| B | $(9.98 \pm 0.88) \cdot 10^{-3}$ | $[\frac{\mathrm{mm}^2}{^\circ\mathrm{C}\cdot\mathrm{s}}]$ |
| C | $(-1.10 \pm 0.63) \cdot 10^{-5}$ | $[\frac{\mathrm{mm}^2}{^\circ\mathrm{C}^2\cdot\mathrm{s}}]$ |
| D | $(1.22 \pm 1.31) \cdot 10^{-8}$ | $[\frac{\mathrm{mm}^2}{^\circ\mathrm{C}^3\cdot\mathrm{s}}]$ |

***Table G.16:*** *AFIP-1 (disperse, low burnup), run2*

| Parameter | Value | Unit |
|---|---|---|
| A | $3.12 \pm 0.01$ | $[\frac{\mathrm{mm}^2}{\mathrm{s}}]$ |
| B | $(7.59 \pm 0.39) \cdot 10^{-3}$ | $[\frac{\mathrm{mm}^2}{^\circ\mathrm{C}\cdot\mathrm{s}}]$ |
| C | $(-2.88 \pm 2.82) \cdot 10^{-6}$ | $[\frac{\mathrm{mm}^2}{^\circ\mathrm{C}^2\cdot\mathrm{s}}]$ |
| D | $(7.00 \pm 5.81) \cdot 10^{-9}$ | $[\frac{\mathrm{mm}^2}{^\circ\mathrm{C}^3\cdot\mathrm{s}}]$ |

***Table G.17:*** *AFIP-1 (disperse, high burnup)*

| Parameter | Value | Unit |
|---|---|---|
| A | $-2.30 \pm 1.00$ | $[\frac{\mathrm{mm}^2}{\mathrm{s}}]$ |
| B | $(2.75 \pm 0.31) \cdot 10^{-2}$ | $[\frac{\mathrm{mm}^2}{^\circ\mathrm{C}\cdot\mathrm{s}}]$ |
| C | $(-1.25 \pm 0.21) \cdot 10^{-5}$ | $[\frac{\mathrm{mm}^2}{^\circ\mathrm{C}^2\cdot\mathrm{s}}]$ |
| D | 0 | $[\frac{\mathrm{mm}^2}{^\circ\mathrm{C}^3\cdot\mathrm{s}}]$ |

***Table G.18:*** *Monolithic U-*10 wt.%*Mo (fresh) [BPM*$^+$ *10]*

| Parameter | Value | Unit |
|---|---|---|
| A | $4.08 \pm 0.14$ | $[\frac{\mathrm{mm}^2}{\mathrm{s}}]$ |
| B | $(175.0 \pm 0.97) \cdot 10^{-2}$ | $[\frac{\mathrm{mm}^2}{^\circ\mathrm{C}\cdot\mathrm{s}}]$ |
| C | 0 | $[\frac{\mathrm{mm}^2}{^\circ\mathrm{C}^2\cdot\mathrm{s}}]$ |
| D | 0 | $[\frac{\mathrm{mm}^2}{^\circ\mathrm{C}^3\cdot\mathrm{s}}]$ |

***Table G.19:*** *Monolithic U-*8 wt.%*Mo (fresh) [HBB*$^+$ *10]*

| Parameter | Value | Unit |
|---|---|---|
| A | $3.34 \pm 0.04$ | $[\frac{\mathrm{mm}^2}{\mathrm{s}}]$ |
| B | $(7.91 \pm 1.22) \cdot 10^{-3}$ | $[\frac{\mathrm{mm}^2}{^\circ\mathrm{C}\cdot\mathrm{s}}]$ |
| C | $(0.39 \pm 7.79) \cdot 10^{-6}$ | $[\frac{\mathrm{mm}^2}{^\circ\mathrm{C}^2\cdot\mathrm{s}}]$ |
| D | $(-2.11 \pm 1.37) \cdot 10^{-8}$ | $[\frac{\mathrm{mm}^2}{^\circ\mathrm{C}^3\cdot\mathrm{s}}]$ |

***Table G.20:*** *AFIP-2 Monolithic U-*10 wt.%*Mo (irradiated) [BCH15]*

## G.2 Specific Heat Capacity

Table G.21 to G.39 show the fitting parameters with their standard error obtained from the analysis of the raw data following the procedure in Chapter 4.2.4. By inserting the parameters into Equation G.2, the temperature dependent thermal diffusivity $C_\mathrm{p}\,(T)$ can be calculated.

$$C_\mathrm{p}\,(T) = A + B \cdot T + C \cdot T^2 + D \cdot T^3 \tag{G.2}$$

| Parameter | Value | Unit |
|---|---|---|
| A | $0.24 \pm (4.37 \cdot 10^{-5})$ | $[\frac{\mathrm{J}}{\mathrm{g \cdot K}}]$ |
| B | $(3.60 \pm 0.10) \cdot 10^{-5}$ | $[\frac{\mathrm{J}}{^\circ\mathrm{C \cdot g \cdot K}}]$ |
| C | $(9.79 \pm 0.57) \cdot 10^{-8}$ | $[\frac{\mathrm{J}}{^\circ\mathrm{C^2 \cdot g \cdot K}}]$ |
| D | $(2.56 \pm 0.10) \cdot 10^{-10}$ | $[\frac{\mathrm{J}}{^\circ\mathrm{C^3 \cdot g \cdot K}}]$ |

***Table G.21:*** *E-FUTURE 4112*

| Parameter | Value | Unit |
|---|---|---|
| A | $0.24 \pm (4.94 \cdot 10^{-5})$ | $[\frac{\mathrm{J}}{\mathrm{g \cdot K}}]$ |
| B | $(3.68 \pm 0.11) \cdot 10^{-5}$ | $[\frac{\mathrm{J}}{^\circ\mathrm{C \cdot g \cdot K}}]$ |
| C | $(1.05 \pm 0.06) \cdot 10^{-7}$ | $[\frac{\mathrm{J}}{^\circ\mathrm{C^2 \cdot g \cdot K}}]$ |
| D | $(2.98 \pm 0.11) \cdot 10^{-10}$ | $[\frac{\mathrm{J}}{^\circ\mathrm{C^3 \cdot g \cdot K}}]$ |

***Table G.22:*** *E-FUTURE 6101*

| Parameter | Value | Unit |
|---|---|---|
| A | $0.23 \pm (3.05 \cdot 10^{-5})$ | $[\frac{\mathrm{J}}{\mathrm{g \cdot K}}]$ |
| B | $(2.12 \pm 0.06) \cdot 10^{-5}$ | $[\frac{\mathrm{J}}{^\circ\mathrm{C \cdot g \cdot K}}]$ |
| C | $(2.47 \pm 0.04) \cdot 10^{-7}$ | $[\frac{\mathrm{J}}{^\circ\mathrm{C^2 \cdot g \cdot K}}]$ |
| D | $(-1.67 \pm 0.07) \cdot 10^{-10}$ | $[\frac{\mathrm{J}}{^\circ\mathrm{C^3 \cdot g \cdot K}}]$ |

***Table G.23:*** *E-FUTURE II 702*

| Parameter | Value | Unit |
|---|---|---|
| A | $0.23 \pm (3.04 \cdot 10^{-5})$ | $[\frac{\mathrm{J}}{\mathrm{g \cdot K}}]$ |
| B | $(4.71 \pm 0.07) \cdot 10^{-5}$ | $[\frac{\mathrm{J}}{^\circ\mathrm{C \cdot g \cdot K}}]$ |
| C | $(2.55 \pm 0.39) \cdot 10^{-8}$ | $[\frac{\mathrm{J}}{^\circ\mathrm{C^2 \cdot g \cdot K}}]$ |
| D | $(3.46 \pm 0.07) \cdot 10^{-10}$ | $[\frac{\mathrm{J}}{^\circ\mathrm{C^3 \cdot g \cdot K}}]$ |

***Table G.24:*** *E-FUTURE II 1203*

| Parameter | Value | Unit |
|---|---|---|
| A | $0.23 \pm (3.44 \cdot 10^{-5})$ | $[\frac{\mathrm{J}}{\mathrm{g \cdot K}}]$ |
| B | $(5.46 \pm 0.07) \cdot 10^{-5}$ | $[\frac{\mathrm{J}}{\circ\mathrm{C \cdot g \cdot K}}]$ |
| C | $(1.97 \pm 0.44) \cdot 10^{-8}$ | $[\frac{\mathrm{J}}{\circ\mathrm{C^2 \cdot g \cdot K}}]$ |
| D | $(3.23 \pm 0.08) \cdot 10^{-10}$ | $[\frac{\mathrm{J}}{\circ\mathrm{C^3 \cdot g \cdot K}}]$ |

***Table G.25:*** *E-FUTURE II 1212*

| Parameter | Value | Unit |
|---|---|---|
| A | $0.24 \pm (6.03 \cdot 10^{-5})$ | $[\frac{\mathrm{J}}{\mathrm{g \cdot K}}]$ |
| B | $(1.09 \pm 0.01) \cdot 10^{-4}$ | $[\frac{\mathrm{J}}{\circ\mathrm{C \cdot g \cdot K}}]$ |
| C | $(-2.61 \pm 0.08) \cdot 10^{-9}$ | $[\frac{\mathrm{J}}{\circ\mathrm{C^2 \cdot g \cdot K}}]$ |
| D | $(8.64 \pm 0.15) \cdot 10^{-10}$ | $[\frac{\mathrm{J}}{\circ\mathrm{C^3 \cdot g \cdot K}}]$ |

***Table G.26:*** *IRIS-4 U-Mo/Al*

| Parameter | Value | Unit |
|---|---|---|
| A | $0.25 \pm (2.92 \cdot 10^{-5})$ | $[\frac{\mathrm{J}}{\mathrm{g \cdot K}}]$ |
| B | $(7.28 \pm 0.07) \cdot 10^{-5}$ | $[\frac{\mathrm{J}}{\circ\mathrm{C \cdot g \cdot K}}]$ |
| C | $(7.43 \pm 4.00) \cdot 10^{-9}$ | $[\frac{\mathrm{J}}{\circ\mathrm{C^2 \cdot g \cdot K}}]$ |
| D | $(2.33 \pm 0.07) \cdot 10^{-10}$ | $[\frac{\mathrm{J}}{\circ\mathrm{C^3 \cdot g \cdot K}}]$ |

***Table G.27:*** *IRIS-4 U-Mo/AlSi*

| Parameter | Value | Unit |
|---|---|---|
| A | $0.25 \pm (2.43 \cdot 10^{-5})$ | $[\frac{\mathrm{J}}{\mathrm{g \cdot K}}]$ |
| B | $(4.56 \pm 0.05) \cdot 10^{-5}$ | $[\frac{\mathrm{J}}{\circ\mathrm{C \cdot g \cdot K}}]$ |
| C | $(1.75 \pm 3.21) \cdot 10^{-7}$ | $[\frac{\mathrm{J}}{\circ\mathrm{C^2 \cdot g \cdot K}}]$ |
| D | $(-4.77 \pm 0.56) \cdot 10^{-11}$ | $[\frac{\mathrm{J}}{\circ\mathrm{C^3 \cdot g \cdot K}}]$ |

***Table G.28:*** *IRIS-TUM 7001*

| Parameter | Value | Unit |
|---|---|---|
| A | $0.22 \pm (2.79 \cdot 10^{-5})$ | $[\frac{\mathrm{J}}{\mathrm{g \cdot K}}]$ |
| B | $(6.93 \pm 0.04) \cdot 10^{-5}$ | $[\frac{\mathrm{J}}{\circ\mathrm{C \cdot g \cdot K}}]$ |
| C | $(1.01 \pm 0.01) \cdot 10^{-7}$ | $[\frac{\mathrm{J}}{\circ\mathrm{C^2 \cdot g \cdot K}}]$ |
| D | 0 | $[\frac{\mathrm{J}}{\circ\mathrm{C^3 \cdot g \cdot K}}]$ |

***Table G.29:*** *IRIS-TUM 8003*

| Parameter | Value | Unit |
|---|---|---|
| A | $0.24 \pm (7.97 \cdot 10^{-5})$ | $[\frac{\mathrm{J}}{\mathrm{g \cdot K}}]$ |
| B | $(1.03 \pm 0.02) \cdot 10^{-4}$ | $[\frac{\mathrm{J}}{^{\circ}\mathrm{C \cdot g \cdot K}}]$ |
| C | $(-1.38 \pm 0.11) \cdot 10^{-7}$ | $[\frac{\mathrm{J}}{^{\circ}\mathrm{C^2 \cdot g \cdot K}}]$ |
| D | $(5.46 \pm 0.20) \cdot 10^{-10}$ | $[\frac{\mathrm{J}}{^{\circ}\mathrm{C^3 \cdot g \cdot K}}]$ |

***Table G.30:*** *IRIS-TUM 8502*

| Parameter | Value | Unit |
|---|---|---|
| A | $0.24 \pm (2.14 \cdot 10^{-5})$ | $[\frac{\mathrm{J}}{\mathrm{g \cdot K}}]$ |
| B | $(2.90 \pm 0.05) \cdot 10^{-5}$ | $[\frac{\mathrm{J}}{^{\circ}\mathrm{C \cdot g \cdot K}}]$ |
| C | $(1.13 \pm 0.03) \cdot 10^{-7}$ | $[\frac{\mathrm{J}}{^{\circ}\mathrm{C^2 \cdot g \cdot K}}]$ |
| D | $(1.58 \pm 0.05) \cdot 10^{-10}$ | $[\frac{\mathrm{J}}{^{\circ}\mathrm{C^3 \cdot g \cdot K}}]$ |

***Table G.31:*** *SELENIUM A*

| Parameter | Value | Unit |
|---|---|---|
| A | $0.24 \pm (2.53 \cdot 10^{-5})$ | $[\frac{\mathrm{J}}{\mathrm{g \cdot K}}]$ |
| B | $(4.69 \pm 0.06) \cdot 10^{-5}$ | $[\frac{\mathrm{J}}{^{\circ}\mathrm{C \cdot g \cdot K}}]$ |
| C | $(3.60 \pm 0.33) \cdot 10^{-8}$ | $[\frac{\mathrm{J}}{^{\circ}\mathrm{C^2 \cdot g \cdot K}}]$ |
| D | $(2.57 \pm 0.07) \cdot 10^{-10}$ | $[\frac{\mathrm{J}}{^{\circ}\mathrm{C^3 \cdot g \cdot K}}]$ |

***Table G.32:*** *SELENIUM B*

| Parameter | Value | Unit |
|---|---|---|
| A | $0.23 \pm (6.95 \cdot 10^{-5})$ | $[\frac{\mathrm{J}}{\mathrm{g \cdot K}}]$ |
| B | $(7.66 \pm 0.15) \cdot 10^{-5}$ | $[\frac{\mathrm{J}}{^{\circ}\mathrm{C \cdot g \cdot K}}]$ |
| C | $(-5.66 \pm 0.91) \cdot 10^{-8}$ | $[\frac{\mathrm{J}}{^{\circ}\mathrm{C^2 \cdot g \cdot K}}]$ |
| D | $(2.77 \pm 0.16) \cdot 10^{-10}$ | $[\frac{\mathrm{J}}{^{\circ}\mathrm{C^3 \cdot g \cdot K}}]$ |

***Table G.33:*** *SELENIUM C*

| Parameter | Value | Unit |
|---|---|---|
| A | $0.20 \pm (4.96 \cdot 10^{-3})$ | $[\frac{\mathrm{J}}{\mathrm{g \cdot K}}]$ |
| B | $(7.30 \pm 0.86) \cdot 10^{-4}$ | $[\frac{\mathrm{J}}{^{\circ}\mathrm{C \cdot g \cdot K}}]$ |
| C | $(-2.99 \pm 0.44) \cdot 10^{-6}$ | $[\frac{\mathrm{J}}{^{\circ}\mathrm{C^2 \cdot g \cdot K}}]$ |
| D | $(4.79 \pm 0.67) \cdot 10^{-9}$ | $[\frac{\mathrm{J}}{^{\circ}\mathrm{C^3 \cdot g \cdot K}}]$ |

***Table G.34:*** *AFIP-1 (disperse, fresh)*

| Parameter | Value | Unit |
|---|---|---|
| A | $0.26 \pm (0.39 \cdot 10^{-5})$ | $[\frac{\mathrm{J}}{\mathrm{g \cdot K}}]$ |
| B | $(5.67 \pm 0.04) \cdot 10^{-4}$ | $[\frac{\mathrm{J}}{^{\circ}\mathrm{C \cdot g \cdot K}}]$ |
| C | $(-2.14 \pm 0.01) \cdot 10^{-6}$ | $[\frac{\mathrm{J}}{^{\circ}\mathrm{C^2 \cdot g \cdot K}}]$ |
| D | $(2.96 \pm 0.10) \cdot 10^{-9}$ | $[\frac{\mathrm{J}}{^{\circ}\mathrm{C^3 \cdot g \cdot K}}]$ |

***Table G.35:*** *AFIP-1 (disperse, low burnup)*

| Parameter | Value | Unit |
|---|---|---|
| A | $0.26 \pm (0.72 \cdot 10^{-5})$ | $[\frac{\mathrm{J}}{\mathrm{g \cdot K}}]$ |
| B | $(2.48 \pm 0.08) \cdot 10^{-4}$ | $[\frac{\mathrm{J}}{^{\circ}\mathrm{C \cdot g \cdot K}}]$ |
| C | $(-12.40 \pm 0.02) \cdot 10^{-6}$ | $[\frac{\mathrm{J}}{^{\circ}\mathrm{C^2 \cdot g \cdot K}}]$ |
| D | $(2.59 \pm 0.09) \cdot 10^{-9}$ | $[\frac{\mathrm{J}}{^{\circ}\mathrm{C^3 \cdot g \cdot K}}]$ |

***Table G.36:*** *AFIP-1 (disperse, high burnup)*

| Parameter | Value | Unit |
|---|---|---|
| A | $0.11 \pm (4.28 \cdot 10^{-3})$ | $[\frac{\mathrm{J}}{\mathrm{g \cdot K}}]$ |
| B | $(7.05 \pm 0.52) \cdot 10^{-5}$ | $[\frac{\mathrm{J}}{^{\circ}\mathrm{C \cdot g \cdot K}}]$ |
| C | 0 | $[\frac{\mathrm{J}}{^{\circ}\mathrm{C^2 \cdot g \cdot K}}]$ |
| D | 0 | $[\frac{\mathrm{J}}{^{\circ}\mathrm{C^3 \cdot g \cdot K}}]$ |

***Table G.37:*** *Monolithic U-*10 wt.%*Mo (fresh) [BPM$^+$ 10]*

| Parameter | Value | Unit |
|---|---|---|
| A | $0.17 \pm (3.84 \cdot 10^{-3})$ | $[\frac{\mathrm{J}}{\mathrm{g \cdot K}}]$ |
| B | $(-1.40 \pm 0.55) \cdot 10^{-4}$ | $[\frac{\mathrm{J}}{^{\circ}\mathrm{C \cdot g \cdot K}}]$ |
| C | $(2.32 \pm 2.05) \cdot 10^{-7}$ | $[\frac{\mathrm{J}}{^{\circ}\mathrm{C^2 \cdot g \cdot K}}]$ |
| D | $(7.85 \pm 0.27) \cdot 10^{-10}$ | $[\frac{\mathrm{J}}{^{\circ}\mathrm{C^3 \cdot g \cdot K}}]$ |

***Table G.38:*** *Monolithic U-*8 wt.%*Mo (fresh) [HBB$^+$ 10]*

| Parameter | Value | Unit |
|---|---|---|
| A | $0.16 \pm (4.62 \cdot 10^{-4})$ | $[\frac{\mathrm{J}}{\mathrm{g \cdot K}}]$ |
| B | $(1.83 \pm 0.11) \cdot 10^{-4}$ | $[\frac{\mathrm{J}}{^{\circ}\mathrm{C \cdot g \cdot K}}]$ |
| C | $(-5.03 \pm 7.18) \cdot 10^{-7}$ | $[\frac{\mathrm{J}}{^{\circ}\mathrm{C^2 \cdot g \cdot K}}]$ |
| D | $(8.52 \pm 1.26) \cdot 10^{-10}$ | $[\frac{\mathrm{J}}{^{\circ}\mathrm{C^3 \cdot g \cdot K}}]$ |

***Table G.39:*** *AFIP-2 Monolithic U-*10 wt.%*Mo (irradiated) [BCH15]*

## G.3 Density

| Fuel | Density [g/cm$^3$] |
|---|---|
| E-FUTURE 4112 | $10.09 \pm 0.07$ |
| E-FUTURE 6101 | $10.04 \pm 0.07$ |
| E-FUTURE II 702 | $9.65 \pm 0.07$ |
| E-FUTURE II 1203 | $10.00 \pm 0.07$ |
| E-FUTURE II 1212 | $9.80 \pm 0.07$ |
| IRIS-4 U-Mo/Al | $9.87 \pm 0.07$ |
| IRIS-4 U-Mo/AlSi | $9.50 \pm 0.07$ |
| IRIS-TUM 7001 | $9.44 \pm 0.07$ |
| IRIS-TUM 8003 | $10.24 \pm 0.07$ |
| IRIS-TUM 8502 | $10.10 \pm 0.07$ |
| SELENIUM A | $10.07 \pm 0.07$ |
| SELENIUM B | $10.10 \pm 0.09$ |
| SELENIUM C | $10.40 \pm 0.07$ |
| AFIP-1 (disperse, fresh) | $10.38 \pm 0.03$ |
| AFIP-1 (disperse, low burnup) | $8.52 \pm 0.44$ |
| AFIP-1 (disperse, high burnup) | $8.21 \pm 0.41$ |
| Monolithic U-8 wt.%Mo (fresh) | $17.2 \pm 0.1$ |
| Monolithic U-10 wt.%Mo (fresh) | $16.4 \pm 0.1$ |
| AFIP-2 Monolithic U-10 wt.%Mo (irradiated) | $13.87 \pm 0.12$ |

***Table G.40:*** *Summary of the density of the investigated fuels [BPM$^+$10, BCC$^+$15b, HBB$^+$10].*

# Table of Symbols

| | |
|---|---|
| $a$ | cooling factor |
| $\alpha$ | thermal diffusivity |
| at. % | atomic percent |
| $\beta$ | time parameter |
| $C$ | heat capacity |
| $C_\mathrm{p}$ | isobaric heat capacity |
| $c_\mathrm{p}$ | isobaric specific heat capacity |
| $C_v$ | isochoric heat capacity |
| $c_v$ | isochoric specific heat capacity |
| $\gamma$ | isobaric thermal expansion |
| $d$ | thickness |
| $F$ | force |
| $F\,(e)$ | function of eccentricity |
| $f\,()$ | fitting function |
| $G$ | weight |
| $g$ | gravitational acceleration |
| $H$ | enthalpy |
| $\kappa_\mathrm{T}$ | isothermal compressibility |
| $L$ | length |
| $\lambda$ | thermal conductivity |
| $m$ | mass |
| $N$ | particle density |
| $p$ | pressure |
| $\pi$ | constant pi |
| $\phi$ | heat flux |
| $Q$ | heat |
| $\rho$ | density |
| $S$ | laser source |
| $T$ | temperature |
| $t$ | time |
| $t_0$ | laser pulse delay time |
| $t_1$ | laser pulse turnaround time |
| $\tau$ | laser pulse length |
| $U$ | inner energy |
| $V$ | volume |
| $\nu$ | volume fraction |

| | |
|---|---|
| $W$ | work |
| $\omega$ | mass fraction |
| $x$ | space |
| $x_1$ | laser pulse rise factor |
| $x_2$ | laser pulse decay factor |
| vol. % | volume percent |
| wt. % | weight percent |

# Table of Abbreviations

| | |
|---|---|
| AA6061 | Aluminum Alloy 6061 |
| AC | Analytical Chemistry |
| AFM | American Machine & Foundry Corporation, N.Y. |
| AFIP | The Advanced Test Reactor (ATR) Full size plate In center flux trap Position (AFIP) experiment |
| AlFeNi | Aluminum alloy with 1 wt.% Fe and 1 wt.% Ni and 1 wt.% Mg |
| ATR | Advanced Test Reactor |
| BOC | Beginning of Cycle |
| BOL | Beginning of Life |
| BR2 | Belgian Reactor-2 |
| CEA | Commissariat de l'Energie Atomique, France |
| DoE | Department of Energy |
| DSC | Differential Scanning Calorimeter |
| DTA | Differential Thermal Analysis |
| EOC | End of Cycle |
| EOL | End of Life |
| FRM | Forschungsreaktor |
| FRM II | Forschungsreaktor München II, i.e. Forschungs-Neutronenquelle Heinz Maier-Leibnitz |
| FUTURE | U-Mo Fuel Irradiation Experiment in the BR2 reactor (Belgium) |
| HEU | high enriched uranium |
| HFIR | High Flux Isotope Reactor |
| HFR | High Flux Reactor |
| HPPR | High Performance Research Reactor |
| IDL | interdiffusion layer |
| ILL | Intitut Laue Langevin |
| INFCE | International Nuclear Fuel Cycle Evaluation |
| INL | Idaho National Laboratory |
| IRIS | Irradiation Experiment in the OSIRIS Reactor at CEA Saclay Center |
| LEU | low enriched uranium |
| LFA | Laser Flash Apparatus |
| MCNP | Monte Carlo N-Particle code |
| MOC | Middle of Cycle |
| MTR | Material Test Reactor |
| NRC | US Nuclear Regulatory Commision |
| OM | Optical Microscopy |

| | |
|---|---|
| ORNL | Oak Rich National Laboratory |
| OSIRIS | French MTR Type Reactor at CEA-Saclay Center |
| PIE | post irradiation examination |
| PNNL | Pacific Northwest National Laboratory |
| RERTR | Reduced Enrichment for Research and Test Reactors |
| SELENIUM | Surface Engineered Low Enriched Uranium-Molybdenum fuel |
| SEM | Scanning Electron Microscope |
| TUM | Technische Universität München |
| U-Mo | Uranium-Molybdenum |
| US | United States |

# List of Figures

# List of Tables

# Bibliography


[A.G00] A.G., Sartorius: *Sartorius Basic Plus - Installation and Operating Instructions*, 2000

[A.G01] A.G., Sartorius: *YDK 01, YDK 01-0D, YDK 01-LP, Dichtebestimmung Betriebsanleitung*, 2001

[API+10] Allenou, J. ; Palancher, H. ; Iltis, X. ; Cornen, M. ; Tougait, O. ; Tucoulou, R. ; Welcomme, E. ; Martin, Ph. ; Valot, C. ; Charollais, F. ; Anselmet, M.C. ; Lemoine, P.: U-Mo/Al-Si interaction: Influence of Si concentration. In: *J. Nucl. Mat.* 399 (2010), S. 189–199

[BAS01] Böning, K. ; Axmann, A. ; Schreckenbach, K.: Die neue Forschungs-Neutronenquelle FRM II. In: *Jahrestagung Kerntechnik*, 2001

[BB90] Badrinarayan, B. ; Barlow, J.W.: Prediction of the Thermal Conductivity of Beds Which Contain Polymer Coated Metal Particles. In: *Solid Freeform Fabrication (SEF) Symposium*, 1990

[BCB+13] Burkes, D.E. ; Casella, A.M. ; Buck, E.C. ; Casella, A.J. ; Edwards, M.K. ; MacFarlan, P.J. ; Pool, K.N. ; Slonecker, B.D. ; Smith, F.N. ; Steen, F.H. ; Thornhill, R.E.: Fuel Thermo-physical Characterization Project: Fiscal Year 2013 Final Report / Pacific Northwest National Laboratory. 2013. – Technical Report

[BCB+14a] Burkes, D.E. ; Casella, A.J. ; Buck, E.C. ; Casella, A.M. ; Edwards, M.K. ; MacFarlan, P.J. ; Pool, K.N. ; Smith, F.N. ; Steen, F.H.: LEU-Mo Fuel Out-of-Pile Characterization for TUM: Final Report / Pacific Northwest National Laboratory. 2014. – Technical Report

[BCB+14b] Burkes, D.E. ; Casella, A.M. ; Buck, E.C. ; Casella, A.J. ; Edwards, M.K. ; MacFarlan, P.J. ; Pool, K.N. ; Smith, F.N. ; Steen, F.H.: Development and Validation of Capabilities to Measure Thermal Properties of Layered Monolithic U-Mo Alloy Plate-Type Fuel. In: *Int. J. Thermophys.* 35 (2014), S. 1476–1500

[BCC+15a] Burkes, D.E. ; Casella, A.J. ; Casella, A.M. ; Gardner, L.D. ; Huber, T.K. ; Breitkreutz, H.: Fuel Thermo-physical Characterization Project: Evaluation of Models to Calculate Thermal Diffusivity of Layered Composites / Pacific Northwest National Laboratory. 2015. – Technical Report

[BCC+15b] Burkes, D.E. ; Casella, A.M. ; Casella, A.J. ; Buck, E.C. ; Pool, K.N. ; MacFarlan, P.J. ; Edwards, M.K. ; Smith, F.N.: Thermal properties of U-Mo alloys irradiated to moderate burnup and power. In: *J. Nucl. Mater.* 464 (2015), S. 331–341

[BCH15] Burkes, D.E. ; Casella, A.M. ; Huber, T.K.: Modeling the influence of interaction layer formation on thermal conductivity of U-Mo dispersion fuel. In: *Journal of Alloys and Compounds* 618 (2015), S. 7–13

[BGR95] Böning, K. ; Gläser, W. ; Röhrmoser, A.: Attachment to Comparison of the FRM-II HEU Design With an Alternative LEU Design. In: *Proceedings of the International Meeting on Reduced Enrichment for Research and Test Reactors (RERTR).* Paris, France, September 1995

[BHC15] Burkes, D.E. ; Huber, T.K. ; Casella, A.M.: Validation of a model to predict thermal conductivity of irradiated U-Mo dispersion fuel. In: *J. Nucl. Mater.* (2015). – submitted

[BKH+15] Breitkreutz, H. ; Keiser, D. D. ; Hofman, G. ; Leenaers, A. ; Berghe, S. van d.: Fuel Development Expert Group (FDEG) Report. 2015. – Technical Report

[BL14] Berghe, S. van d. ; Lemoine, P.: Review of 15 Years of High-Density Low-Enriched UMo Dispersion Fuel Development For Research Reactors in Europe. In: *Nuclear Engineering and Technology* 46 (2014), S. 125–146

[BPM+10] Burkes, D.E. ; Papesch, C.A. ; Maddison, A.P. ; Hartmann, T. ; Rice, F.J.: Thermo-physical properties of DU-10wt.%Mo alloys. In: *J. Nucl. Mater.* 403 (2010), S. 160–166

[Bru35] Bruggeman, D.A.G.: Berechnung verschiedener physikalischer Konstanten von heterogenen Substanzen. I. Dielektrizitätskonstanten und Leitfähigkeiten der Mischkörper aus isotropen Substanzen. In: *Ann. Phys.* 416 (1935), S. 636–664

[CDP+14] Chiang, H.-Y. ; Döblinger, M. ; Park, S.-H. ; Beck, L. ; Petry, W.: Ion Beam Induced Spinodal Decomposition and Amorphization in the Immiscible Bilayer System UMo/Mg. In: *Journal of Nuclear Materials* 453 (2014), S. 41

[Chi14] Chiang, H.-Y.: *Material Selection of UMo Fuel for Research Reactors: Swift Heavy Ion Irradiation Studies*, Technische Universität München, Diss., 2014

[CHWT15] Chen, J.K. ; Hung, H.Y. ; Wang, C.F. ; Tang, N.K.: Thermal and electrical conductivity in Al-Si/Cu/Fe/Mg binary and ternary Al alloys. In: *J. Mater. Sci.* 50 (2015), S. 5630–5639

[CJ59] Carslaw, H.S. ; Jaeger, J.C.: *Conduction of Heat in Solids.* Oxford University Press, 1959. – 421–428 S.

[CJ73] Cohen, M.H. ; Jortner, J.: Effective Medium Theory for the Hall Effect in Disordered Materials. In: *Phys. Rev. Lett.* 30 (1973), S. 696

[CL63] Cape, J.A. ; Lehman, G.W.: Temperature and Finite Pulse-Time Effects in the Flash Method for Measuring Thermal Diffusivity. In: *J Appl Phys* 34 (1963), S. 1909–1913

[Com88] Commission, U. S. Nuclear R.: Safety Evaluation Report / Office of Nuclear Reactor Regulation. 1988. – Technical Report

[CRA+09] Charollais, F. ; Ripert, M. ; Anselmet, M.C. ; Boulcourt, P. ; Tiratay, X. ; Lemoine, P. ; Jarousse, C.: IRIS Program: IRIS 4 First Results. In: *Proceedings of the European Research Reactor and Fuel Conference (RRFM)*, 2009

[Cre11] Creasy, J. T.: *Thermal Properties of Uranium-Molybdenum Alloys: Phase Decomposition Effects of Heat Treatments*, Texas A&M University, Diplomarbeit, 2011

[Def98] Defense, DOD U.S. D.: Metallic Materials and Elements for Aerospace Vehicle Structures / U.S. Department of Defense. Washington D.C., 1998. – Technical Report

[Eis14] Eisenhower, D. D.: *Atoms for Peace Speech*. `http://www.iaea.org/About/atomsforpeace_speech.html`. Version: Jan. 2014

[Fin00] Fink, J.K.: Thermophysical properties of uranium dioxide. In: *J. Nucl. Mat.* 279 (2000), S. 1–18

[FL95] Fink, J.K. ; Leibowitz, L.: Thermal Conductivity of Zirconium. In: *J. Nucl. Mater.* 226 (1995), S. 44–50

[GKM+12] Gan, J. ; Keiser, D.D. ; Miller, B.D. ; Robinson, A.B. ; Jue, J.-F. ; Medvedev, P. ; Wachs, D.M.: TEM characterization of U-7Mo/Al-2Si dispersion fuel irradiated to intermediate and high fission densities. In: *J. Nucl. Mater.* 424 (2012), S. 43–50

[HB85] Hsu, W.Y. ; Berzins, T.: Percolation and effective-medium theories for perfluorinated ionomers and polymer composites. In: *J. Polym. Sci. Polym. Phys. Ed.* 23 (1985), S. 933–953

[HBB+10] Hengstler, R.M. ; Beck, L. ; Breitkreutz, H. ; Jarousse, C. ; Jungwirth, R. ; Schmid, W. PetW. P. ; Schneider, J. ; Wieschalla, N.: Physical Properties of monolithic U8wt.In: *J. Nucl. Mater.* 402 (2010), S. 74–80

[HDC87] Hofman, G.L. ; Domagala, R.F. ; Copeland, G.L.: Irradiation Behavior of $U_6Fe - Al$ Dispersion Fuel Elements. In: *J. Nucl.Mat.* 238 (1987), S. 43

[HFG+12] Huber, T. K. ; Fig, M. K. ; Garrett, D. ; Kennedy, J. R. ; Petry, W. ; Robinson, A. B. ; Wachs, D. M.: First Results of Scanning Thermal Diffusivity Microscope (STDM) Measurements on Irradiated Monolithic and Disperse Fuel. In: *Proceedings of the International Meeting on Reduced Enrichment for Research and Test Reactors (RERTR)*, 2012

[HHF96] Höhne, G. ; Hemminger, W. F. ; Flammersheim, H.-J.: *Differential Scanning Calorimetry*. Springer Verlag, 1996

[HHKS13] Huang, K. ; Heinrich, H. ; Keiser, D.D. ; Sohn, Y.H.: Fuel-Matrix Chemical Interaction Between U-7wt.In: *Defect and Diffusion Forum* 333 (2013), S. 199–206

[HK52] Hidnert, P. ; Krider, H. S.: Thermal Expansion od Aluminum and Some Aluminum Alloys. In: *Journal of Research of the National Bureau of Standards* 48 (1952), S. 209–220

[HSK13] Hurley, D. H. ; Schley, R. S. ; Khafizov, M.: Scanning Thermal Diffusivity Microscope Status Report / Idaho National Laboratory. 2013. – Technical Report

[JTS+80] Jensen, J. E. ; Tuttle, W. A. ; Stewart, R. B. ; Brechna, H. ; Prodell, A. G. ; Energy, United States D. (Hrsg.): *Brookhaven National Laboratory Selected Cryogenic Data Notebook*. Brookhaven National Laboratory Associated Universities Inc., 1980

[Jun11] Jungwirth, R.: *Irradiation Behavior of Modified High-Performance Nuclear Fuels*, Technische Universität München, PhD Thesis, 2011

[JZC+13] Jungwirth, R. ; Zweifel, T. ; Chiang, H.-Y. ; Petry, W. ; Berghe, S. van d. ; Leenaers, A.: Heavy ion irradiation of UMo/Al samples PVD coated with Si and ZrN layers. In: *J. Nucl. Mater.* 434 (2013), S. 296–302

[KH10] Kim, Y. S. ; Hofman, G. L.: Performance comparison between various U-Mo powders. In: *Proceedings of the European Research Reactor and Fuel Conference (RRFM)*, 2010

[KH11] Khafizov, M. ; Hurley, D. H.: Measurement of thermal transport using time-resolved thermal wave microscopy. In: *J. Appl. Phys.* 110 (2011), S. 083525

[KHJ11] Keiser, D. ; Hess, J. ; Jue, J.-F.: AFIP-1 Charakterization Summary Report / Idaho National Laboratory. 2011. – Technical Report

[KHR+13] Kim, Y.S. ; Hofman, G.L. ; Ryu, H.J. ; Park, J.M. ; Robinson, A.B. R. ; Wachs, D.M.: Modeling of Interaction Layer Growth Between U-Mo Particles and an Al Matrix. In: *Nucl. Eng. Tech.* 45 (2013), S. 827–838

[Kir73] Kirkpatrick, S.: Percolation and Conduction. In: *Rev. Mod. Phys.* 45 (1973), S. 574

[KJR+12] Keiser, D. D. ; Jue, J.-F. ; Robinson, A. B. ; Medvedev, P. ; Wachs, D. M. ; Moore, G. A. ; Clark, C. R. ; Meyer, M. K. ; Finlay, M. R.: Effects of irradiation on the microstructure of U-7Mo dispersion fuel with Al-2Si matrix. In: *J. Nucl. Mater.* 425 (2012), S. 156–172

[KP97] Koester, L.K. ; Pabst, M.: *40 Jahre Atom-Ei Garching.* October 1997

[KWR+12] Keiser, D.D. ; Wachs, D.M. ; Robinson, A.B. ; Medvedev, P. ; Moore, G. A.: Microstructural Ananlysis of Irradiated U-Mo Fuel Plates: Recent Results. In: *Proceedings of the European Research Reactor and Fuel Conference (RRFM)*, 2012

[LBD13] Leenaers, A. ; Berghe, S. van d. ; Detavernier, C.: Surface Enginieering of Low Enriched Uranium-Molybdenum. In: *J. Nucl. Mater.* 440 (2013), S. 220–228

[Lee77] Lee, T.Y.R.: *Thermal Diffusivity of Dispersed and Layered Composites*, Purdue University, Diss., 1977

[Lee14] Leenaers, A.: *Surface-engineered low-enriched Uranium-Molybdenum fuel for research reactors*, Universiteit Gent, Diss., 2014

[Mar63] Marquardt, D.W.: An Algorithm for Least-Squares Estimation of Nonlinear Parameters. In: *SIAM J. Appl. Math.* 11 (1963), S. 431–441

[MHM95] Mo, S.C. ; Hanan, N.A. ; Matos, J.E.: Comparison of the FRM-II HEU Design With an Alternative LEU Design. In: *Proceedings of the International Meeting on Reduced Enrichment for Research and Test Reactors (RERTR)*. Paris, France, September 1995

[MHS+00] Meyer, M. K. ; Hofman, G. L. ; Strain, R. V. ; Clark, C. R. ; Stuart, J. R.: Metallographic Analysis of Irradiated RERTR-3 Fuel Test Specimens. In: *Proceedings of the International Meeting on Reduced Enrichment for Research and Test Reactors (RERTR)*. Las Vegas, Nevada, October 1-6 2000

[Mil02] Mills, K.C.: *Recommended Values of Thermophysical Properties for Selected Commercial Alloys*. Cambridge, England : Woodhead Publishing Limited, 2002

[Moo10] Moore, G.A.: AFIP-2 Fabrication Summary Report / Idaho National Laboratory. 2010. – Technical Report

[MRW+08] Moore, G.A. ; Rice, F.J. ; Woolstenhulme, N.E. ; Swank, W.D. ; Haggard, D.C. ; Jue, J.-F. ; Park, B.H. ; Steffler, S.E. ; Hallinan, N.P. ; Chapple, M.D. ; Burkes, D.E.: Monolithic Fuel Fabrication Process Development at the Idaho National Laboratory / Idaho National Laboratory. 2008. – Technical Report

[MRW+09] Moore, G. A. ; Rice, F. J. ; Woolstenhulme, N. E. ; Jue, J.-F. ; Park, B. H. ; Steffler, S. E. ; Hallinan, N. P. ; Chapple, M. D. ; Marshall, M. C. ; Mackowiak, B. l. ; Clark, C. R. ; Rabin, B. H.: Monolithic Fuel Fabrication Process Development at the Idaho National Laboratory / Idaho National Laboratory. 2009 (INL/CON-09-17298). – Technical Report

[MS92] Matos, J. E. ; Snelgrove, J. L.: Selected thermal properties and uranium density relations for alloy, aluminide, oxide, and silicide fuels. In: *Research Reactor Core Conversion Guidebook. Vol. 4: Fuels (Appendices I-K)* (1992), S. 13–29

[MW] `www.mathweb.com`

[MWHH00] Meyer, M.K. ; Wiencek, T.C. ; Hayes, S.L. ; Hofman, G.L.: Irradiation Behavior of $U_6Mn - Al$ Dispersion Fuel Elements. In: *J. Nucl.Mat.* 278 (2000), S. 358–363

[NG14a] Netzsch-Gerätebau, GmbH: *Laser Flash Analysis - LFA*. Brochure, Dec. 2014

[NG14b] Netzsch-Gerätebau, GmbH: *Laserser Flash Apparatus LFA 457 MicroFlash*. Brochure, Dec. 2014

[NG14c] Netzsch-Gerätebau, GmbH: *Principle of the LFA Method*. Homepage. `http://holding.netzschcdn.com//uploads/pics/LFA467-FlashTech.jpg?1377851710`. Version: Dec. 2014

[PE10] Porter, D.L. ; Ewh, A.: Interaction Layer Characteristics in U-xMo Dispersion/-Monolithic Fuels / Idaho National Laboratory. 2010. – Technical Report

[PJBA61] Parker, W.J. ; Jenkins, R.J. ; Butler, C.P. ; Abbott, G.L.: Flash Method of Determining Thermal Diffusivity, Heat Capacity, and Thermal Conductivity. In: *Journal of Applied Physics* 32 (1961), S. 1679–1684

[PLC+11a] Perez, D. M. ; Lillo, M. A. ; Chang, G. S. ; Roth, G. A. ; Woolstenhulme, N. E. ; Wachs, D. M.: AFIP-1 Irradiation Summary Report / Idaho National Laboratory. 2011. – Technical Report

[PLC+11b] Perez, D. M. ; Lillo, M. A. ; Chang, G. S. ; Roth, G. A. ; Woolstenhulme, N. E. ; Wachs, D. M.: RERTR-10 Irradiation Summary Report / Idaho National Laboratory. 2011. – Technical Report

[PLC+11c] Perez, D. M. ; Lillo, M. A. ; Chang, G. S. ; Roth, G. A. ; Woolstenhulme, N. E. ; Wachs, D. M.: RERTR-9 Irradiation Summary Report / Idaho National Laboratory. 2011. – Technical Report

[PLC+11d] Perez, D.M. ; Lillo, M.A. ; Chang, G.S. ; Roth, G.A. ; Woolstenhulme, N.E. ; Wachs, D.M.: AFIP-2 Irradiation Summary Report / Idaho National Laboratory. 2011. – Technical Report

[RCK+09] Robinson, A.B. ; Chang, G.S. ; Keiser, D.D. ; Wachs, D.M. ; Porter, D.L.: Irradiation Performance of U-Mo Based 'Monolithic' Plate-Type Fuel - Design Selection / Idaho National Laboratory. 2009 (INL/EXT-09-16807). – Technical Report

[Rei13] Reiter, C.: *Methodenentwicklung, Kalorimetrie und Messung der Dichte von hochdichten Kernbrennstoffen*, Technische Universität München, Diploma Thesis, 2013

[RRM+12] Robinson, A. B. ; Rice, F. J. ; Meyer, M. K. ; Wachs, D. M. ; Keiser, D. D. ; Perez, D. M.: Post Irradiation Examination Results of the RERTR-12 Campaign. In: *Proceedings of the International Meeting on Reduced Enrichment for Research and Test Reactors (RERTR)*, 2012

[RSMH99] Ronchi, C. ; Sheindlin, M. ; Musella, M. ; Hyland, G.J.: Thermal conductivity of uranium dioxide up to 2900K from simultaneous measurement of the heat capacitiy and thermal diffusivity. In: *J. Appl. Phys.* 85 (1999), S. 776

[RWK+10] Robinson, A. B. ; Wachs, D. M. ; Keiser, D. D. ; Medvedev, P. G. ; Clark, C. R. ; Chang, G. S. ; Lillo, M. A. ; Jue, J. F. ; Moore, G. A. ; Wight, J. M.: Results of the Irradiation of R6R018 in the Advanced Test Reactor / Idaho National Laboratory. 2010. – Technical Report

[SGC+14] Stepnik, B. ; Grasse, M. ; Coullomb, C. ; Geslin, D. ; Jarousse, C. ; Petry, W. ; Jungwirth, R. ; Breitkreutz, H. ; Röhrmoser, A. ; Huber, T. K. ; Zweifel, T. ; Wachs, D. M.: UMo monolithic fuel development progress in ARVA-CERCA. In: *Proceedings of the European Research Reactor and Fuel Conference (RRFM)*, 2014

[SHMR98] Sheindlin, M. ; Halton, D. ; Musella, M. ; Ronchi, C.: Advances in the use of laser-flash techniques for thermal diffusivity measurement. In: *Rev. Sci. Instrum.* 69 (1998), S. 1426

[SPS+13] Schenk, R. ; Petry, W. ; Stepnik, B. ; Jarousse, C. ; Bourdat, G. ; Moyroud, C. ; Grasse, M.: FRM-II / CERCA UMo Atomizer Project Status. In: *Proceedings of the European Research Reactor and Fuel Conference (RRFM)*, 2013

[SSP+15] Schenk, R. ; Schauer, R. ; Petry, W. ; Stepnik, B. ; Moyroud, C. ; Grasse, M. ; Coullomb, C. ; Bourdat, G. ; Jarousse, C.: UMo Fuel-Powder Production Process and Results. In: *Proceedings of the European Research Reactor and Fuel Conference (RRFM)*. Bucharest, Romania, April 19-23 2015

[Str75] Strout, D.: Generalized effective-medium approach to the conductivity of an inhomogeneous material. In: *Phys. Rev. B* 12 (1975), S. 3368–3373

[Tou70a] Touloukian, Y.S.: *Specific Heat: Metallic elements and alloys.* IFI-Plenum, 1970

[Tou70b] Touloukian, Y.S.: *Thermal Conductivity: Metallic elements and alloys.* IFI-Plenum, 1970

[Tou70c] Touloukian, Y.S.: *Thermal Diffusivity: Metallic elements and alloys.* IFI-Plenum, 1970

[Wac07] Wachs, D. M.: RERTR Fuel Development and Qualification Plan / Idaho National Laboratory. 2007 (INL/EXT-05-01017 Rev.3). – Technical Report

[Wol14] Wolf, A.: *Einfluss des Si-Anteils im Matrix-Material hinsichtlich der Wärmeleitfähigkeit von dispersen UMo-Brennstoffen*, Technische Universität München, Bachelor Thesis, 2014

[WW99] Weise, K. ; Wöger, W.: *Messunsicherheit und Meßdatenauswertng.* Wiley-VCH, 1999

[Zwe14] Zweifel, T.: *Fission Gas Behaviour and Interdiffusion Layer Growth in in-pile and out-of-pile Irradiated U-Mo/Al Nuclear Fuels*, Technische Universität München, Diss., 2014

## Acknowledgement

There are many people I'd like to thank, not only for technical support.

Prof. Dr. Winfried Petry Thank you for motivating me to this work and my stay at the Idaho and Pacific Northwest National Laboratories, it was a great experience for me. But most of all, thank you for all your trust and support throughout my entire PhD work!

Dr. Rainer Jungwirth Thanks for the excellent introduction into uranium handling, for sharing all your knowlegde about U-Mo metallography, all the endless literature research and most important all the fun we had as office-mates. I will always remember this!

Dr. Harald Breitkreutz A special thank for "ThermoProp", this is really good stuff! But also thank you for the great time as a colleague and friend and all the good advice, you always had for me.

Christian Reiter, Alexander Wolf and Thomas Huber A big thank to my diploma and bachelor students. Especially to Christian, for all the investigations with the DSC and the excellent software you provided to me for the data analysis. Great work!

My colleagues: Bruno Baumeister, Tobias Chemnitz, Dr. Hsin-Yin Chiang, Luise Fiedler, Dr. Tobias Hollmer, Dr. A. Röhrmoser, Steffen Säubert, Rupert Schauer, Robert Schenk, Christian Steyer and Dr. Tobias Zweifel You are a wonderful team to work with. Thank you for the great time!

HEUMEU radiation protection team: Alexandra Egle and Dr. Rainer Grossmann It has not been easy with me and my special wishes and ideas, but we always found a way together! Thanks for the excellent collaboration!

Idaho National Laboratory: Dr. Daniel M Wachs, Dr. Dennis D Keiser, Cynthia A Papesch and M Craig Marshall, Adam B Robinson, Dr. James A King and Dr. Brandon D Miller and all co-workers Thank you all for hosting me for almost a year at INL. Although, it was sometimes difficult, I always got all possible support. Thank you for the great time in Idaho!

**Acknowledgment**

Pacific Northwest National Laboratory: Dr. Douglas E Burkes, Dr. Amanda J Casella and Jake Bohlke, Dr. Andrew M Casella, Dr. Frances N Smith and Nicole Green, Edgar C Buck and Paul J Mac Farlan It was a great pleasure to work with you at the Pacific Northwest National Laboratory. I learned a lot and got excellent help to gain very precious data for this work. Many thanks to Doug and Andy for the excellent publications!

SCK-CEN: Dr. Sven van den Berghe Thank you for all your excellent advices.

Max-Planck Insitute for Plasma Physics: Stefan Elgeti Thanks for all the patience with my measurements at the LFA with all my special wishes!

AREVA-CERCA: Bertrand Stepnik Most of my investigated fuels were fabricated by AREVA-CERCA. Thank you for providing them!

My family Thanks to my parents, Nicolette and Herbert Huber and my grandparents, Katharina and Erich Stettner, for giving me all possible support for my education.

Sandra Blankenburg-Sailer and Andreas Sailer No big words, just thank you!

Jackie Hafla and Whitney Stoddard Both of you made my stays in Idaho to an unforgettable adventure. Especially, Whit, you're a great room mate! Thank you!

Michael Schmidt Tu siempre crees a mi... Gracias!